



HAL
open science

Radiofrequency readout of hole spins confined in semiconductor quantum dots

Estelle Vincent

► **To cite this version:**

Estelle Vincent. Radiofrequency readout of hole spins confined in semiconductor quantum dots. Physics [physics]. Université Grenoble Alpes [2020-..], 2023. English. NNT : 2023GRALY069 . tel-04523264

HAL Id: tel-04523264

<https://theses.hal.science/tel-04523264v1>

Submitted on 27 Mar 2024

HAL is a multi-disciplinary open access archive for the deposit and dissemination of scientific research documents, whether they are published or not. The documents may come from teaching and research institutions in France or abroad, or from public or private research centers.

L'archive ouverte pluridisciplinaire **HAL**, est destinée au dépôt et à la diffusion de documents scientifiques de niveau recherche, publiés ou non, émanant des établissements d'enseignement et de recherche français ou étrangers, des laboratoires publics ou privés.

THÈSE

Pour obtenir le grade de

DOCTEUR DE L'UNIVERSITÉ GRENOBLE ALPES

École doctorale : PHYS - Physique

Spécialité : Physique de la Matière Condensée et du Rayonnement

Unité de recherche : PHotonique, Electronique et Ingénierie QuantiqueS

**Lecture radiofréquence de spins de trou confinés dans des boîtes
quantiques semiconductrices**

**Radiofrequency readout of hole spins confined in semiconductor
quantum dots**

Présentée par :

Estelle VINCENT

Direction de thèse :

Silvano DE FRANCESCHI

DIRECTEUR DE RECHERCHE, CEA CENTRE DE GRENOBLE

Directeur de thèse

Romain MAURAND

INGENIEUR HDR, CEA CENTRE DE GRENOBLE

Co-directeur de thèse

Rapporteurs :

ALEXEI ORLOV

FULL PROFESSOR, UNIVERSITY OF NOTRE DAME

EDWARD LAIRD

FULL PROFESSOR, LANCASTER UNIVERSITY

Thèse soutenue publiquement le **8 novembre 2023**, devant le jury composé de :

OLIVIER BUISSON,

DIRECTEUR DE RECHERCHE, CNRS DELEGATION ALPES

Président

ALEXEI ORLOV,

FULL PROFESSOR, UNIVERSITY OF NOTRE DAME

Rapporteur

EDWARD LAIRD,

FULL PROFESSOR, LANCASTER UNIVERSITY

Rapporteur

HERMANN SELLIER,

MAITRE DE CONFERENCES HDR, UNIVERSITE GRENOBLE
ALPES

Examineur

EVA DUPONT-FERRIER,

ASSOCIATE PROFESSOR, UNIVERSITE DE SHERBROOKE

Examinatrice



Abstract

Holes in the valence band of group-IV semiconductors benefit from natural spin-orbit interactions. Consequently, holes spins can be manipulated with the electric field offering prospects for quantum information processing. Among the different semiconducting materials, silicon and germanium stand out for the fabrication of quantum dot devices hosting a single spin. On one hand, isotopically purified silicon offers a clean magnetic environment together with very mature fabrication processes. On the other hand, germanium shows high mobilities and low effective masses in Ge/SiGe quantum well heterostructures, offering great freedom in device design. In this manuscript, we explore the spin physics of holes confined in semiconductor quantum dots focusing on readout techniques allowing for spin states detection. We first investigate the dispersive readout of holes in silicon-on-insulator nanowires. For this purpose, we design and fabricate niobium nitride superconducting microwave resonators, and implement a gate-sensing setup operating at a few gigahertz. Second, we focus on the charge sensing of double quantum dots (DQDs) in Ge/SiGe heterostructures. We implement a radiofrequency setup on a single quantum dot charge sensor that allows the differentiation of DQD charge states in less than a microsecond. Combined with a measured charge noise around $0.2 \mu\text{eV}/\sqrt{\text{Hz}}$, this setup enables to reach the last hole regime of the DQD. Eventually, we demonstrate the detection of Pauli Spin Blockade. Using this spin-to-charge conversion mechanism, we access the spin states of the DQD and report on their energy relaxation rates.

Résumé

Les trous dans la bande de valence des semi-conducteurs du groupe IV bénéficient d'une interaction spin-orbite naturelle. Par conséquent, les spins de ces trous peuvent être manipulés avec le champ électrique, ce qui offre d'intéressantes perspectives pour la réalisation de processeurs quantiques. Parmi les différents matériaux semiconducteurs, le Silicium et le Germanium se distinguent pour la fabrication de dispositifs à boîtes quantiques. D'une part, le Silicium isotopiquement purifié offre un environnement magnétique propre ainsi que des processus de fabrication très matures. D'autre part, le Germanium présente des mobilités élevées et de faibles masses effectives dans des hétérostructures à puits quantiques, offrant une grande liberté dans la conception des dispositifs. Dans ce manuscrit, nous explorons la physique des spins de trous confinés dans des boîtes quantiques semiconductrices, en nous concentrant sur les techniques de lecture permettant la détection des états de spins. Nous investiguons dans un premier temps la lecture dispersive de trous piégés dans des nanofils de Silicium sur isolant. À cette fin, nous concevons et fabriquons des résonateurs micro-ondes supraconducteurs en Nitrure de Niobium et mettons en œuvre un setup de lecture de grille fonctionnant à quelques gigahertz pour sonder leur réponse en fréquence. Dans un deuxième temps, nous nous concentrons sur la détection de charges dans des doubles boîtes quantiques (DQD) fabriquées dans des hétérostructures en Ge/SiGe. Nous implémentons un setup radiofréquence sur un capteur de charge constitué d'une seule boîte quantique, permettant la différenciation des états de charge du DQD en moins d'une microseconde. Associé à un bruit de charge mesuré autour de $0.2 \mu\text{eV}/\sqrt{\text{Hz}}$, le setup permet d'atteindre le régime du dernier trou du DQD. Finalement, nous démontrons la détection du blocage de spin de Pauli. En utilisant ce mécanisme de conversion spin-charge, nous accédons aux états de spin du DQD et rapportons leurs taux de relaxation.

Acknowledgements

First of all I would like to thank my PhD supervisors **Romain Maurand** and **Silvano De Franceschi**. I have learnt a lot on your side and it has been a real pleasure to work with both of you. Thank you Silvano for the scientific exchange we had. Your deep understanding of spin systems makes all the great experiments we are doing possible! Thank you Romain for being so present throughout my PhD and for teaching me all the skills of the laboratory. Your curiosity and your know-how make you a very good researcher, while your pedagogy and your kindness make you a very good supervisor. I've come out of this PhD a much bigger person, thanks in part to you!

Thank you **Boris Brun-Barrière** for assisting me in the final stages of my measurements. Your expertise in measuring instruments was a great help. I congratulate you on obtaining your position and wish you all the best for the future! I also congratulate **Simon Zihlmann** and **Vivien Schmitt** for their positions. Thank you Simon for your expertise on spin-photon interactions and thank you Vivien for all the valuable advice you have given me on microwave setups. Many thanks also to **Etienne Dumur** who taught me a lot about resonators and helped me to model my high-frequency circuits.

I would like to thank **Jean-Luc Thomassin** and **Frédéric Gustavo** for their invaluable help on the fabrication of the superconducting resonators. Your expertise was essential for the smooth running of the fabrication processes. I would also like to thank **Michel Bougeard** for his humour and the many mechanical parts he has made for my various projects.

A big thank you also to my great co-workers **Gonzalo Troncoso Fernandez Bada**, who entrusted me with his precious germanium samples, and **Cécile Yu**, who opened the way to the nobium nitride resonators. It has been a great pleasure to share these years with you and to spend so much time outside the lab!

I would like to thank the generation of PhD students who preceded me for their warm welcome when I joined the laboratory and for the knowledge they passed on to me. I would like to thank **Anthony Amisse**, **Loïck Le Guevel**, **Rami Ezzouch**, **Agostino Apra** and **Tom Vethaak**. Special thanks to **Thomas Jalabert**, **Romain Albert**, **Estelle Mazalera**, **Florie Mesple** and **Nicolas Piot** for the many mountain bivouacs that followed my arrival at the laboratory.

I would like to thank the generation of PhD students who will follow me with the same fervour and wish them every success in their research. I wish **Oliver Gallego Lacey**, **Nathan Aubergier**, **Nesrine Chaaben**, **Thomas Hourriez**, **Elyjah Kiyooka** and **Chotivut Tangchingchai** the best of luck. Special thanks also to **Marion Bassi**, **Victor Millory**, **Axel Leblanc**, **Victor Champain**, **Diego Fossion** and **Léo Noirot** for the friendships we have made over the years. I'm sure they will continue to follow us!

I thank the permanent researchers of **Lateqs** who guided me throughout my PhD. Thus, I would like to thank **François Lefloch**, **Xavier Jehl**, **Louis Jansen**, **Claude Chapelier**, **Vincent Renard** and **Clemens Winkelmann**. I would also like to thank the post-docs **Maria D'Antuono** and **Zoltan Scherubl**, with whom I regret not having had more interaction.

I would particularly like to thank **Yann-Michel Niquet** for taking the time to explain to me

the physics of the devices I measured, always with clarity and pedagogy. I also thank his team **L-SIM lab**, and in particular **Michele Filippone**, **Biel Martinez Diaz**, **Esteban Rodriguez Mena** and **Alessandro Chessari** with whom I have had the pleasure of interacting on many occasions.

I would also like to thank the researchers and engineers at **CEA Leti**, without whom there would be no devices to measure. In particular, I would like to thank **Jean-Michel Hartmann** for fabricating the germanium heterostructures, **Candice Thomas** and **Edouard Deschaseaux** for supplying me with very high quality niobium nitride wafers, and **Benoît Bertrand**, **Maud Vinet** and **Louis Hutin** for supervising the fabrication of the silicon devices.

Finally, I would like to thank my parents **Pascale Vincent** and **Thierry Vincent**, who have supported me throughout my PhD and all my long studies. A big thank you for that! Thanks also to my best friend **Anne Coloigner**, who did her PhD at the same time as me. Thank you for your mutual support, especially during the writing period! Last but not least, I would like to extend my warmest thanks to my boyfriend **Dorian Fraudet** who shared my life during the years of my PhD. We have both been through the long ordeal of doing PhDs, and we have always been there for each other. Sharing this with you has for sure strengthened our bond!

CONTENTS

	Page
List of Figures	xiii
List of Tables	xv
Introduction	1
0.1 Context	2
0.1.1 From spin discovery to spintronics	2
0.1.2 Hole spins in semiconductors	3
0.1.3 Quantum computing with hole spins	4
0.2 Manuscript outline	5
0.3 Author's contribution	5
1 Hole spins confined in semiconductors	7
1.1 Holes in group-IV semiconductors	8
1.1.1 Luttinger-Kohn band model	8
1.1.2 Band structure in bulk Ge and bulk Si	9
1.2 Holes confined in Ge heterostructures	11
1.2.1 Ge heterostructures	11
1.2.2 Band structure in Ge heterostructures	12
1.2.3 Device fabrication	13
1.3 Holes confined in Si nanowires	15
1.3.1 Si nanowires	16
1.3.2 Band structure in Si nanowires	16
1.3.3 Semi-industrial device processing	17
1.4 Spins and charges in quantum dots	18
1.4.1 Charges in quantum dots	19
1.4.2 Spins in quantum dots	23
1.4.3 Spin-to-charge conversion	25
1.5 Conclusion	27
2 Radiofrequency readout of hole spins confined in semiconductors	29
2.1 Charge sensing of hole spins	30
2.1.1 Quantum conductance	30
2.1.2 Radiofrequency readout	31

2.1.3	Recent achievements and limitations	33
2.2	Dispersive readout of hole spins	35
2.2.1	Quantum capacitance	35
2.2.2	Dispersive response	37
2.2.3	Resonators	38
2.3	Choice of the readout method	39
2.4	Conclusion	39
3	Superconducting inductors for dispersive readout of Si Quantum dots	43
3.1	Design of superconducting inductors	44
3.1.1	Lumped-element resonators	44
3.1.2	Microstrip design	47
3.1.3	Finite-element simulations	48
3.2	Niobium nitride superconducting films	52
3.2.1	Niobium nitride sputtering	52
3.2.2	Film properties	53
3.2.3	Magnetic field resilience	55
3.2.4	Crystallographic structure and phases	58
3.3	Fabrication of niobium nitride inductors	61
3.3.1	Fabrication recipe	61
3.3.2	Result of the different batches	63
3.3.3	Inductors properties	64
3.4	Dispersive readout of charges confined in silicon nanowires	65
3.4.1	Experimental setup	65
3.4.2	Tank circuit characteristics	69
3.4.3	Dispersive charge readout	73
3.5	Conclusion	77
4	Charge sensing readout of Ge quantum dots	81
4.1	Charge sensing readout circuit	82
4.1.1	Device and experimental setup	82
4.1.2	Simulations of the readout circuit	84
4.1.3	Circuit matching and sensitivity	87
4.1.4	Properties of the measured readout circuit	89
4.2	Charge sensing measurements and performances	90
4.2.1	Charge sensor tuning	90
4.2.2	Charge sensitivity of the sensor	91
4.2.3	Sensor signal and charge noise	93
4.3	Charge sensing of a double quantum dot	97
4.3.1	Double quantum dot design and experimental setup	97
4.3.2	Double quantum dot tuning and stability diagram	99
4.3.3	Charge sensitivity to the double quantum dot	101
4.3.4	Double quantum dot charge noise	102
4.4	Conclusion	102

5 Spins in Ge quantum dots	105
5.1 Last holes regime	106
5.1.1 Stability diagram	106
5.1.2 Lever arms and interdot properties	108
5.2 Pauli Spin Blockade signature	109
5.2.1 Pulse sequence	110
5.2.2 Video mode scanning	111
5.3 Spin states and relaxation	112
5.3.1 Relaxation time T_1	112
5.3.2 Landau-Zener spectroscopy	115
5.4 Conclusion	119
Conclusion	123

LIST OF FIGURES

1.1	Band structure of group-IV semiconductors	10
1.2	Heterostructure stack and surface roughness	12
1.3	Effects of strain on Ge	13
1.4	Band structure of relaxed and strain Ge	14
1.5	Device fabrication process	15
1.6	SEM and TEM images of SOI nanowires	16
1.7	Band structure in Si nanowires	17
1.8	Fabrication process of the SOI nanowire devices	17
1.9	Two different device geometries	18
1.10	Si nanowire devices	19
1.11	Single quantum dot and Coulomb blockade	20
1.12	Double quantum dot and stability diagram	22
1.13	Energy diagram of a single charge in a double quantum dot	23
1.14	Energy diagram of a double quantum dot with two charges	24
1.15	Pauli Spin Blockade signature measured by charge sensing	26
2.1	Charge sensing with a quantum point contact	31
2.2	Radiofrequency readout principle	32
2.3	SETs integrated with quantum dot devices	34
2.4	Dispersive readout of a DQD with two charges	36
3.1	Coil inductors used in reflectometry setups	46
3.2	Coil inductors coupled to a microstrip	47
3.3	Microstrip geometry	48
3.4	Finite element simulations using Sonnet	49
3.5	Simulations results using Sonnet	50
3.6	Evolution of the inductors design with the different batches	51
3.7	PPMS measurement of critical temperature and sheet resistivity	53
3.8	Resilience of a 50nm-thick NbN film with the magnetic field	56
3.9	Resilience of a 10nm-thick NbN film with the magnetic field	57
3.10	Evolution of the film phases with the nitrogen percentage	59
3.11	Evolution of the film phases with the substrate	60
3.12	Fabrication process and dose tests	62
3.13	SEM images of NbN inductor and NbN microstrip	63
3.14	Optical images of NbN inductors and Au microstrips.	64

LIST OF FIGURES

3.15	Setup PCB	67
3.16	4K Helium probe	68
3.17	Dilution refrigerator	69
3.18	Loaded inductor properties	70
3.19	Superconducting meanders for on-chip bias-tees	72
3.20	Stability diagram of a single quantum dot probed with a coil inductor	74
3.21	SNR of a Coulomb peak with the integration time	75
3.22	Evolution of the SNR with the integration time	75
3.23	Interdot charge transitions of DQDs probed with coil inductors	76
4.1	Gate layers and layer stack of the charge sensor	82
4.2	Experimental setup	83
4.3	Ohmic and accumulation approaches	84
4.4	Equivalent readout circuit for the ohmic and accumulation approaches	86
4.5	Circuit matching and sensitivity to the QW resistance	87
4.6	Evolution of the sensitivity with the resonant frequency	89
4.7	Resonance of the readout circuit	90
4.8	Tuning of the charge sensor	91
4.9	SNR optimisation and charge sensitivity	92
4.10	Maximum SNR and lever-arm	94
4.11	Time measurement of the charge	95
4.12	Low-frequency charge noise	96
4.13	Gate layers and layer stack of the DQD devices	97
4.14	Experimental setup	98
4.15	Double quantum dot tuning	99
4.16	Stability diagram of the DQD	100
4.17	Signal difference between two charge states of the DQD	101
4.18	Tunnelling noise and sensor noise	103
5.1	Evolution of the stability diagram with the tunnel barrier BT	106
5.2	The last hole regime	107
5.3	Stability diagram recorded with two different measurement methods	108
5.4	Tunability of the interdot tunnelling rate	109
5.5	Bias triangles	110
5.6	PSB signature and pulse sequence	111
5.7	PSB signature with the Video Mode	112
5.8	Pulse sequence for the measurement of T1	113
5.9	T1 as a function of the angle of the in-plane magnetic field	114
5.10	Landau-Zener interferometry applied to a singlet-triplet qubit	115
5.11	Landau-Zener spectroscopy of an interdot	116
5.12	Energy levels and wave function of a single hole	118
5.13	Landau-Zener spectroscopy on different interdots	119

LIST OF TABLES

3.1	Sputtering parameters	53
3.2	NbN films properties	54
3.3	LETI NbN film properties	55
3.4	Fabrication results.	65
3.5	Unloaded inductors properties.	66
3.6	Loaded properties of the coil inductor measured on Figure 3.18.	71
4.1	Several couples of L and C_{match} allowing for the maximum sensitivity.	88
4.2	State-of-the-art charge sensitivities	93
4.3	State-of-the-art charge noise for SETs or SHTs	97

INTRODUCTION

Contents

0.1	Context	2
0.1.1	From spin discovery to spintronics	2
0.1.2	Hole spins in semiconductors	3
0.1.3	Quantum computing with hole spins	4
0.2	Manuscript outline	5
0.3	Author's contribution	5

Ascent of Petit Pelvoux by S ridge, with V. Pahon and A. Gallet

Écrins massif, France - June 26th 2021

0.1 Context

0.1.1 From spin discovery to spintronics

In 1902, P. Zeeman was awarded the Nobel Prize in Physics for his discovery of the hyperfine structure of the energy levels of atoms. He observed experimentally that the spectral rays of a light source under a magnetic field have a discrete number of components, each of them being polarised. The lifting of the degeneracy induced by the magnetic field, later called Zeeman effect, provided an experimental proof of the electromagnetic theory of light. However, there was still an unsolved mystery: the anomalous Zeeman effect. Indeed, depending on the initial conditions, the number of spectral rays was odd or even, which could not be explained by the only quantum numbers n and l already discovered. This problem was solved by W. Pauli in 1924 [Pauli 1925], with the introduction of a third quantum number: the spin s . Together with the so-called Pauli exclusion principle stating that two electrons cannot have the same quantum state in the same quantum system, an explanation was found.

In the years 1920s, other works suggested the existence of the spin, with notably R. Kronig, S. Goudsmit and G. Uhlenbeck [Uhlenbeck and Goudsmit 1925]. It was first thought as a self-rotation of the electron giving it the name of «spin». This classical picture was abandoned, since the rotation speed of the electron on itself would exceed the speed of light. Spin is therefore one of the observables for which there is no classical equivalent. Besides the anomalous Zeeman effect, the introduction of the spin enabled the resolution of other key problems in Physics such as the Stern and Gerlach experiment of 1922 [Gerlach and Stern 1922], and a problem of factor 2 in the spectrum of hydrogen long studied by W. Heisenberg. The theory of the spin then quickly spread among the scientific community, and in 1928 P. Dirac demonstrated its adequacy with the theory of relativity [Dirac 1928].

Since then, nuclear and electronic spins have been the subject of many studies and have led to several useful applications. Among them, an imaging method based on nuclear magnetic resonance [Lauterbur 1973] has revolutionised the field of medical imaging. It uses the relaxation of the different nuclear spins composing a body to map its anatomy and access its physiological processes, allowing precise medical diagnosis with very harmless side effects. In parallel with the work carried on nuclear spins, the observation of spin-dependent electron transport phenomena in the 1980s gave birth to a new field of physics: spintronics. Among the founding experiments, we can cite the discovery of the giant magnetoresistance in 1988 by the groups of A. Fret [Baibich et al. 1988] and P. Grünberg [Binasch et al. 1989].

The use of semiconductors for spintronics was developed in the 1990s, after S. Datta and B. Das proposed to build a spin field effect transistor [Datta and B. Das 1990] based on electric dipole spin resonance [E. I. Rashba 1960]. The first experimental realisations that followed are reported in a review published in 2001 [L. P. Kouwenhoven et al. 2001]. There, we learn that it is experimentally possible to confine single charges in nanoscale semiconducting structures called quantum dots. Although the experiments that revealed the existence of spin were carried out on large ensembles of particles, the ability we now have to isolate a single electron spin or a single hole spin allow us to further investigate the spin dynamics and think to new applications.

0.1.2 Hole spins in semiconductors

As mentioned above, single spintronics is based on quantum dots. Quantum dots are boxes defined in a semiconducting host material with nanoscale dimensions. The confinement in such structures is so strong that the energy levels are quantized and follow the shell filling rules of atomic physics. Electrons or holes can be trapped within quantum dots by repelling the electric fields arising from all confinement directions. It is possible to precisely control the filling of quantum dots by using external gates to control their electrochemical potential. Additional electrical contacts on both side of quantum dots act as reservoirs and enable to determine the charge states through transport measurements. Quantum dots are 0D-objects that can be formed in various semiconductor platforms that can have higher dimensions. Thus, quantum dots have been reported in 0D-structures as core-shell points [Dabbousi et al. 1997], 1D-structures as nanowires [Björk et al. 2004] and 2D-structures as planar heterostructures [Ciorga et al. 2000]. In the following, we will focus on 1D-nanowires and 2D-heterostructures, since these platforms offer the modularity to build complex architectures including multiple quantum dots and gates.

Quantum dot devices have been fabricated from many different semiconductor hosts but gallium arsenide, silicon and germanium stand as the most widely used. GaAs was one of the first materials to be used in the form of GaAs/AlGaAs heterostructures. There, free electrons accumulate at the GaAs/AlGaAs interface, forming a two dimensional electron gas. The latter benefits from high mobilities $\sim 10^5 - 10^7 \text{ cm}^2/\text{V s}$ and low electron densities $\sim 1 - 5 \times 10^{15} \text{ m}^{-2}$, allowing to locally deplete the electron gas by applying an electric field with electrostatic gates [Hanson, L. P. Kouwenhoven, et al. 2007]. The main drawback of GaAs lattices is the presence of many nuclear spins degrading the coherence of the electron spins trapped in the quantum dots. As a consequence, GaAs was gradually abandoned in favour of group IV-semiconductors which have isotopes with zero nuclear spins. Silicon was then brought to the fore, combining the absence of nuclear spins in isotopically purified lattices with mature fabrication processes thanks to the parallel development of the microelectronics industry. Quantum dots in silicon generally take the form of Si/SiGe heterostructures [Simmons et al. 2010] or nanowires. The latter can be designed to trap either electrons [Voisin et al. 2014] or holes [Zwanenburg et al. 2009]. The development of hole spin physics has recently brought another material to light: germanium. Used in the form of hut wires [Gao et al. 2020], core-shell nanowires [Hu et al. 2012] or Ge/SiGe heterostructures [N. W. Hendrickx, D. Franke, et al. 2018], germanium benefits from mobilities comparable to GaAs $\sim 10^5 - 10^6 \text{ cm}^2/\text{V s}$ [Dobbie et al. 2012] together with few nuclear spins and isotopic purification capabilities.

Hole spins in group-IV semiconductors are expected to have long lifetimes due to the almost complete absence of nuclear spins in isotopically purified lattices. The few remaining nuclear spins have a reduced hyperfine interaction with the hole spins. The hyperfine interaction is an important source of decoherence in confined spin systems [Hanson, L. P. Kouwenhoven, et al. 2007]. It derives from the coupling of the electronic spin with the nuclear spins present in the host material. In contact hyperfine interactions, the coupling strength is proportional to the overlap squared between the particle wave function and the nucleus. The contribution of each nuclear spin can be treated as an apparent magnetic field \vec{B}_N , called Overhauser field. First, it has a longitudinal component, oriented parallel or opposed to the external applied magnetic field \vec{B}_0 , that changes the precession frequency by $g\mu_B B_N$. Second, it has a transverse component able to change the precession frequency and tilt the precession axis, as a function of the ratio B_N/B_0 . As \vec{B}_N ran-

domly evolves with time, the spin phase will also randomly evolve with time. This phenomenon is responsible for decoherence, transforming a pure spin state into a statistical mixture of states. The p-orbital symmetry of the holes in the valence band produces a node at the atomic site, reducing in principle the contact hyperfine interaction to zero. Even if other hyperfine terms can contribute significantly to the hole hyperfine interaction, holes generally benefit from longer hyperfine limited dephasing times than electrons.

Unlike electron spins, hole spins can also be manipulated by the electric field through a combination of both electric-dipole and spin-orbit interactions. This last arises from the fact that a hole spin moving in an electric field \vec{E} experiences an internal magnetic field, depending on the orbital the hole occupies. The resulting spin-orbit interaction can be treated as a small perturbation of the Hamiltonian, coupling different orbital and spin parts. Consequently, the energy states are no longer pure spin up or spin down states, but admixtures of spin and orbital states. Two main phenomena contribute to the spin-orbit interaction. The first one, the Rashba contribution, is the consequence of an intrinsic and spin-dependent magnetic field \vec{B}_{SO} able to induce a spin rotation [Bychkov and É. I. Rashba 1984]. \vec{B}_{SO} depends on the motion of the hole and on the geometry of the device. It was observed to be particularly large in 1D geometries. The second phenomenon contributing to spin-orbit interaction is known as the Dresselhaus contribution [Dresselhaus 1955]. It arises from the electric fields of the charged atoms composing the environment of the spin. Consequently, it strongly depends on the crystal structure of the bulk semiconductor. Depending on the crystal structure, Dresselhaus contribution can be larger or smaller than the Rashba contribution. They can add or subtract along different crystal orientations, making the spin-orbit interaction anisotropic. As a result, the gyromagnetic factor governing the Zeeman effect of spin-orbit states is likely to be anisotropic for holes.

0.1.3 Quantum computing with hole spins

Many applications rely on hole spins confined in semiconductors. Among these, quantum computing has received the most attention. After D. Loss and D. DiVincenzo [Loss and DiVincenzo 1998] proposed to use the spin of electrons as a physical system to encode elementary bits of quantum information (qubits), many qubit experiments based on electron spins in quantum dots were published. The first qubit involving hole spins in silicon was demonstrated in 2016 by R. Maurand [Maurand et al. 2016]. He worked on a Si nanowire double quantum dot device populated with a few tens of charges and demonstrated that electrically coherent spin manipulation is possible. Indeed, hole spin qubits benefit from all advantages mentioned above, including long spin lifetimes and manipulation with the electric field, which means that there is no need to integrate micro-magnets for manipulation as is the case with electron spin qubits.

Recent achievements on Si nanowires include the demonstration of coherent spin manipulation at 1.5K and 4.2K [Camenzind et al. 2022]. The ability to work at such temperatures is a veritable asset as an increased cooling power can facilitate the integration of numerous qubits together with their control electronics. If the manipulation of hole spins via the electric field is another great advantage, it also renders the spins sensitive to electrical noise. N. Piot [Piot et al. 2022] recently observed the anisotropy of the gyromagnetic factor and the spin susceptibility for different directions of the magnetic field. He found that for certain field directions the longitudinal contribution of the charge noise cancels out, strongly improving the coherence time. Similar observations have recently been published for hole spins in Ge/SiGe heterostructures [N. W. Hendrickx, Massai, et

al. 2023]. The fast development of hole spin qubits in Ge/SiGe heterostructures started with N. Hendrickx in 2020 [N. W. Hendrickx, Lawrie, et al. 2020] and within the same year a two-qubit gates was shown [N. W. Hendrickx, D. P. Franke, et al. 2020]. The following year, the first singlet-triplet qubit in planar Ge [Jirovec et al. 2021] was published, as well as an operating four quantum processor [Nico W. Hendrickx et al. 2021].

The desire to increase the number of qubits is linked to the need for compact architectures allowing the simultaneous readout of many quantum dots. Scalability also rhymes with readout rapidity, especially since we expect that increasing the number of qubits in a lattice will decrease their single shot coherence times. Although it is possible to perform single-shot readout with transport [Hanson, Beveren, et al. 2005] with high charge sensitivities, classical transport readout is starting to show its limits. Indeed, the implementation of a fast and scalable current-based readout scheme on a large matrix of qubits seems challenging. As an alternative, radiofrequency-based sensing techniques seem to open the way for scalability [Borsoi et al. 2023], high sensitivity [Connors, J. Nelson, et al. 2022] and fast readout [Vukušić et al. 2018].

0.2 Manuscript outline

In this Manuscript, we explore the implementation of radiofrequency setups for the dispersive readout of Si nanowire quantum dot devices and the charge sensing of Ge/SiGe heterostructure quantum dot devices. In [Chapter 1](#), we review the fabrication of such devices and their hole band-structures. Moreover, we present the charge and spin states in quantum dots. In [Chapter 2](#), we motivate the choice of charge sensing for Ge/SiGe heterostructures and gate-based dispersive sensing for Si nanowire devices. For the latter, we present the design and fabrication of NbN superconducting lumped element resonators in [Chapter 3](#). We discuss materials issues and show the dispersive measurement of Si nanowire double quantum dot devices. In [Chapter 4](#), we focus on the implementation of a radiofrequency setup for the readout of charge sensors integrated in Ge/SiGe architectures. We evaluate their charge sensitivity and discuss noise sources. Finally, in [Chapter 5](#), we present measurement results of Ge/SiGe double quantum dot devices. These include the stability diagram in the last hole regime, the signature of Pauli-Spin-Blockade and the relaxation time of the blockade spin states. We finished with a [Conclusion](#) summarising the main highlights of this PhD work and outlining its perspectives.

0.3 Author's contribution

The experiments and results presented in this Manuscript are the outcome of collaboration between researchers, engineers and technicians from different laboratories. In this section I will try to clarify my own contribution to this work.

In terms of measurement setups, I was able to take advantage of the different cryogenic systems we have in the laboratory. I took care of the wiring and thermalisation of the 4K-stick I used, and I modified the measurement lines and the amplification chain of the dilution refrigerator I was working on. I was able to reuse existing printed circuit boards by soldering electronic components according to the resonant circuits I wanted to designed. The semiconductor devices I worked with were fabricated by the CEA Leti for the silicon ones and by G. Troncoso for the germanium ones.

INTRODUCTION

I was responsible for testing and microbonding them.

Concerning the superconducting resonators, I can fairly attribute to myself all the work on the design of the inductors and on the characterisation of the many batches. I also did all the fabrication except for the EBEAM lithography, which was done by J-L. Thomassin. For the fabrication of my samples, I had access to the facilities of the upstream technological platform (PTA) and to some fabrication recipes provided by F. Gustavo.

For the measurement of the germanium devices, I can claim the work on the optimisation of the radiofrequency circuit for the readout of the charge sensors and its experimental implementation. For the measurement campaigns, I was assisted by B. Brun-Barrière, with whom I worked in pairs. We also received punctually some help from V. Millory and E. Dumur for the Python scripts. I took care of all the data processing, which Y-M. Niquet supplemented with simulations. For the interpretation of the results, I could benefit from many exchanges with my PhD supervisors and the other members of the Lateqs group and L-SIM theory group.

Chapter 1

HOLE SPINS CONFINED IN SEMICONDUCTORS

Contents

1.1	Holes in group-IV semiconductors	8
1.1.1	Luttinger-Kohn band model	8
1.1.2	Band structure in bulk Ge and bulk Si	9
1.2	Holes confined in Ge heterostructures	11
1.2.1	Ge heterostructures	11
1.2.2	Band structure in Ge heterostructures	12
1.2.3	Device fabrication	13
1.3	Holes confined in Si nanowires	15
1.3.1	Si nanowires	16
1.3.2	Band structure in Si nanowires	16
1.3.3	Semi-industrial device processing	17
1.4	Spins and charges in quantum dots	18
1.4.1	Charges in quantum dots	19
1.4.2	Spins in quantum dots	23
1.4.3	Spin-to-charge conversion	25
1.5	Conclusion	27

First ascent of a multi-pitch in Maja Cokistes, with G. Bonton

Prokletije massif, Montenegro - August 18th 2021

Holes in group-IV semiconductors can benefit from a reduced hyperfine interaction together with a strong spin-orbit coupling. These particularities motivate us to explore the physics of hole spins in quantum dots. In this Chapter, we review the the band structure of holes in silicon nanowires and in planar germanium heterostructures. We detail their fabrication process and present the samples used during this PhD project. In a second time, we explain how to form quantum dots in such structures and study the spin states of double quantum dots. Finally, we describe a method enabling for spin-to-charge conversion, for the readout of the spin states.

1.1 Holes in group-IV semiconductors

The valence bands of group-IV semiconductors originate from atomic p-orbitals. Consequently, holes have an angular momentum $l = 1$ and a spin $s = 1/2$, giving a total angular momentum $J = 3/2$. Unlike electrons, with total angular momentum $J = 1/2$, hole bands do not exhibit valley degeneracy as the valleys are only found in the conduction band. The $J=3/2$ valence band splits into heavy and light hole bands, each with different effective masses depending on the spatial direction. In this Part, we review the band structure of holes in group-IV semiconductors, and compute the effective masses of light and heavy holes in bulk silicon and bulk germanium.

1.1.1 Luttinger-Kohn band model

Luttinger-Kohn Hamiltonian

In a bulk group-IV semiconductor, the light and heavy hole bands can be described by the four-band model of Kohn and Luttinger [Luttinger and Kohn 1955]. Formula 1.1 gives the Luttinger-Kohn Hamiltonian, where m_0 is the free electron mass, \vec{k} is the wave vector and \vec{J} is the angular momentum vector. γ_1 , γ_2 and γ_3 are the Luttinger parameters proper to each semiconductor and characterising the anisotropy of the hole mass.

$$H_{\text{LK}} = -\frac{\hbar^2}{2m_0} \left[\left(\gamma_1 + \frac{5}{2}\gamma_2 \right) \vec{k}^2 - 2\gamma_2 \left(\vec{k} \cdot \vec{J} \right)^2 - 2\gamma_3 \sum_{m \neq n} J_m J_n k_m k_n \right] \quad (1.1)$$

Group-IV semiconductors have total angular momentum $J = 3/2$, consequently the projections of J along the z-axis are $J_z = \pm 3/2$ for the heavy holes and $J_z = \pm 1/2$ for the light holes. Thus, we can write the Hamiltonian Formula 1.1 in the $\{ |+\frac{3}{2}\rangle, |+\frac{1}{2}\rangle, |-\frac{1}{2}\rangle, |-\frac{3}{2}\rangle \}$ basis as [Venitucci and Niquet 2019] :

$$H_{4\text{kp}} = \frac{\hbar^2}{2m_0} \begin{pmatrix} P+Q & -S & R & 0 \\ -S^* & P-Q & 0 & R \\ R^* & 0 & P-Q & S \\ 0 & R^* & S^* & P+Q \end{pmatrix} \quad (1.2)$$

Where :

$$\left\{ \begin{array}{l} P = \gamma_1(k_x^2 + k_y^2 + k_z^2) \\ Q = \gamma_2(k_x^2 + k_y^2 - 2k_z^2) \\ R = \sqrt{3}[-\gamma_3(k_x^2 - k_y^2) + 2i\gamma_2k_xk_y] \\ S = 2\sqrt{3}\gamma_3(k_x - ik_y)k_z \end{array} \right. \quad (1.3)$$

Heavy holes and light holes

The previous Hamiltonian takes into account the electrostatic interaction between the holes and their lattice, as well as their spin-orbit interaction resulting from the coupling between the hole spins and lattice-generated magnetic fields. The presence of off-diagonal terms in the Hamiltonian highlights the existence of light/heavy hole mixing. From the diagonal terms referring to heavy holes ($J_z = \pm 3/2$) and light holes ($J_z = \pm 1/2$), we can extract the Hamiltonians of the heavy holes H_{HH} and light holes H_{LH} (see Formulas 1.4 and 1.5). In the case of heavy holes, the spin is parallel or antiparallel to the the direction of motion of the hole given by \vec{k} . The effective mass of the heavy holes is given by $m_{\text{HH}} = m_0/(\gamma_1 - 2\gamma_2)$ and the eigenenergy by $-\hbar^2k^2/2m_{\text{HH}}$. In the case of light holes, the effective mass is $m_{\text{LH}} = m_0/(\gamma_1 + 2\gamma_2)$ and the eigenenergy is $-\hbar^2k^2/2m_{\text{LH}}$.

$$H_{\text{HH}} = P + Q = -\frac{\hbar^2}{2m_0} [(\gamma_1 + \gamma_2)k_x^2 + (\gamma_1 + \gamma_2)k_y^2 + (\gamma_1 - 2\gamma_2)k_z^2] \quad (1.4)$$

$$H_{\text{LH}} = P - Q = -\frac{\hbar^2}{2m_0} [(\gamma_1 - \gamma_2)k_x^2 + (\gamma_1 - \gamma_2)k_y^2 + (\gamma_1 + 2\gamma_2)k_z^2] \quad (1.5)$$

Band diagram

Figure 1.1 (a) presents the general band structure of group-IV semiconductors around the Γ -point, showing the light hole and heavy hole bands, the split-off band and the first conduction band. The first conduction band is separated from the LH and HH bands by the semiconducting gap Δ . The latter is material dependent and can be direct or indirect depending on the case. In bulk materials, LH and HH bands are degenerate at the Γ -point. They are separated by the spin-orbit gap Δ_0 from the split-off band [Winkler 2003] deriving from the the spin-orbit interaction.

1.1.2 Band structure in bulk Ge and bulk Si

Bulk germanium

Germanium is a group-IV semiconductor with a diamond lattice. It is the 32th element of the periodic table, displaying an atomic mass of 72.64u. It belongs to the p-block, since its electronic

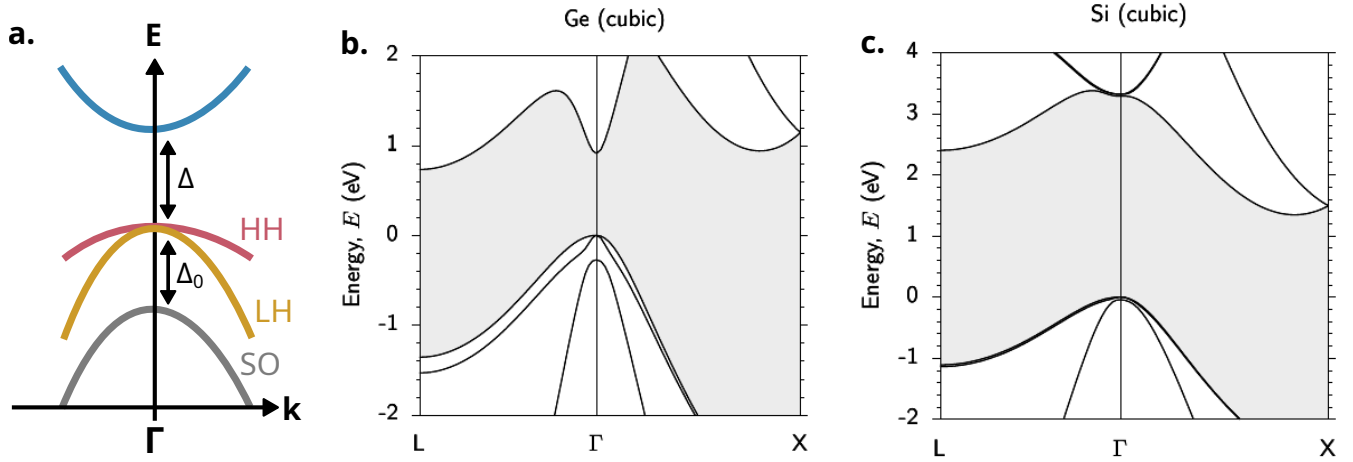


Figure 1.1 – **Band structure of group-IV semiconductors.** Figure adapted from C. Broderick [Broderick 2020]. (a) Schematic representation of the band structure of a group-IV semiconductor near the Γ -point, showing the conduction band (blue), the heavy holes band (red), the light-hole band (yellow) and the split-off band (grey). (b) Calculated band structure of cubic Ge near the Γ -point. (c) Calculated band structure of cubic Si near the Γ -point.

structure is $[\text{Ar}]3d^{10}4s^24p^2$. The Luttinger parameters in Ge are $\gamma_1 = 13.38$, $\gamma_2 = 4.24$ and $\gamma_3 = 5.69$. Referring to Equations 1.4 and 1.5, in absence of strain, we obtained the effective masses given in Equation 1.6. We observe that the heavy holes are almost 5 times heavier than the light holes. A calculated band diagram of the bulk Ge [Broderick 2020] is shown in Figure 1.1 (b). There, we observe a remarkable difference between the curvature of the HH and LH hole bands, resulting from their large difference in effective mass. The spin-orbit gap for bulk Ge is relatively large ($\Delta_0 \approx 0.3 \text{ eV}$), resulting in a very distinct separation between the HH and LH bands ($j=3/2$) and the split-off band ($j=1/2$).

$$\begin{cases} m_{\text{HH}} = 0.204 m_0 \\ m_{\text{LH}} = 0.046 m_0 \end{cases} \quad (1.6)$$

Bulk silicon

Silicon is the 14th element of the periodic table. It belongs to the p-block, with an atomic mass of 28,085u and the electronic structure $[\text{Ne}]3s^23p^2$. The Luttinger parameters in Si are $\gamma_1 = 4.285$, $\gamma_2 = 0.339$ and $\gamma_3 = 1.446$. Referring to Equations 1.4 and 1.5, in absence of strain, we obtain the effective masses given in Equation 1.7. For bulk silicon, the heavy hole and light hole effective masses anisotropy is less pronounced than for bulk germanium. Figure 1.1 (c) shows a calculated band diagram of bulk Si [Broderick 2020]. Compared to bulk Ge, the difference in curvature between the HH and LH bands is much less pronounced, since the HH and LH effective masses are of the same order. The split-off band is also closer since the spin-orbit gap is smaller for Si ($\Delta_0 \approx 0.044 \text{ eV}$) than for Ge.

$$\begin{cases} m_{\text{HH}} = 0.277 m_0 \\ m_{\text{LH}} = 0.201 m_0 \end{cases} \quad (1.7)$$

1.2 Holes confined in Ge heterostructures

In recent years, germanium has emerged as a promising concurrent to silicon in the field of CMOS-compatible quantum dot devices. Ge quantum dot devices can be divided into three main categories : Ge/Si core-shell nanowires, Ge hut wires and Ge/SiGe planar heterostructures. This last platform offers a large freedom in device design, and therefore the best prospects in terms of scalability. Ge quantum wells benefit from very high mobilities up to $10^6 \text{cm}^2/\text{Vs}$ [Dobbie et al. 2012], enabling the formation of clean and well-controlled quantum dots [Scappucci et al. 2021]. The holes at the top of the valence band also benefit from very low in-plane effective masses down to $0.05 m_0$ [M. Lodari et al. 2019], which provide to the quantum dots a large energy level spacing. In this Part, we discuss the band structure of holes in planar Ge heterostructures and the fabrication of quantum dot devices from a Ge/SiGe heterostructure.

1.2.1 Ge heterostructures

In a planar Ge heterostructure, a thin layer of pure Ge is encapsulated between two layers of another semiconductor, generally an alloy of SiGe. The lattice mismatch between the two materials ensures the compressive strain of the Ge well. Here, we report on Ge/SiGe heterostructures fabricated by J.M. Hartmann [Hartmann et al. 2023] at the CEA Leti in Grenoble.

Ge/SiGe heterostructure fabrication

The Ge/SiGe heterostructure is grown on a 200mm Si(001) wafer. The whole deposition process occurs in a chemical vapor deposition (CVD) machine at high temperature $T = 850^\circ \text{C}$ and at low pressure $P = 20$ milliTorr. First, a linear gradient of $\text{Si}_{1-x}\text{Ge}_x$ is deposited over a few microns, starting from Si_1Ge_0 until reaching $\text{Si}_{0.21}\text{Ge}_{0.79}$. The slow variation of the lattice parameter reduces the formation of dislocations and defects but increases surface strain. The latter is counterbalanced at step of chemical mechanical planarization (CMP). Figures 1.2 (b) and (c) show the sample surface before and after CMP, highlighting the positive effects of CMP on surface roughness.

After the planarization, three layers are grown on top of each other to form the Ge quantum well : a 100 nm layer of $\text{Si}_{0.21}\text{Ge}_{0.79}$, a thin 16 nm layer of pure Ge and a 44 nm layer of $\text{Si}_{0.21}\text{Ge}_{0.79}$. The lattice parameter of $\text{Si}_{0.21}\text{Ge}_{0.79}$ and Ge being different, respectively 5.61 \AA and 5.66 \AA , a compressive strain of the Ge layer is observed and results in the separation of the light and heavy hole energy bands (see the following section). At the end of the process, the surface of the heterostructure is protected with a 2 nm Si cap layer.

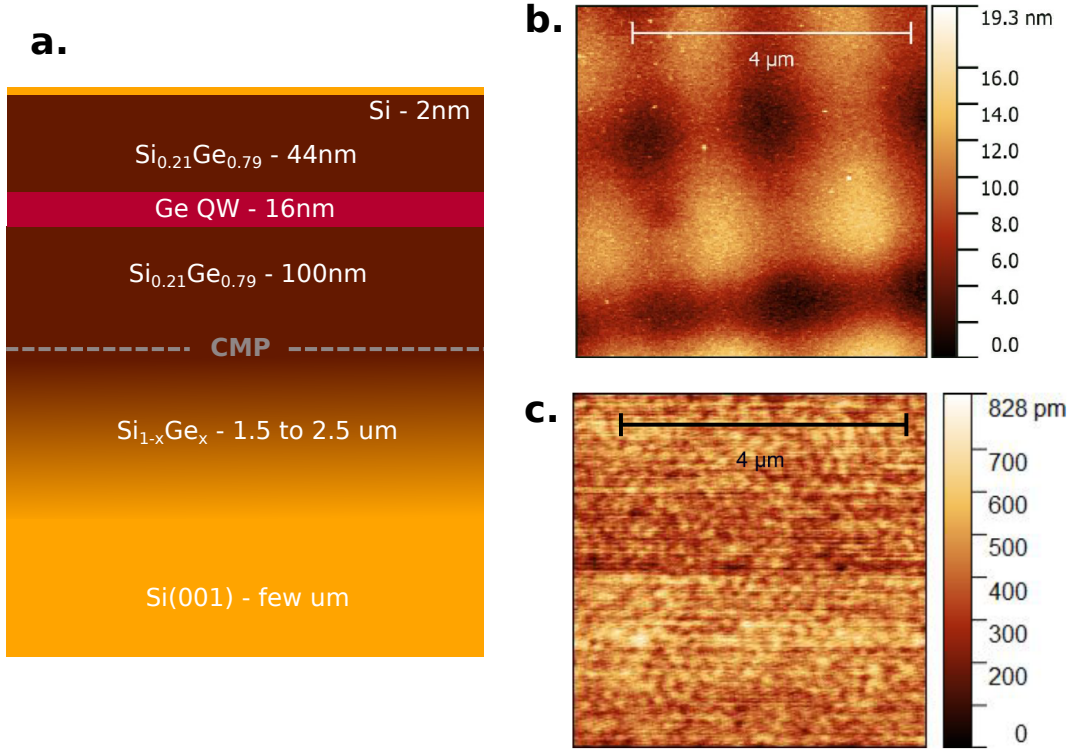


Figure 1.2 – **Heterostructure stack and surface roughness.** (a) Schematic of the heterostructure stack. (b) AFM image of the $\text{Si}_{0.21}\text{Ge}_{0.79}$ surface before CMP. We observe that the surface has a grain structure, creating local variations (10-15 nm) that are comparable to the Ge well thickness. (c) AFM image of the $\text{Si}_{0.21}\text{Ge}_{0.79}$ surface after CMP. We notice the net reduction of the surface roughness.

1.2.2 Band structure in Ge heterostructures

Effective masses in planar heterostructures

The valence-band offset at the interfaces between Ge and SiGe results in the confinement of the holes within the Ge well. Then, the heterostructure can be considered as a 2D-structure, since the confinement along the out-of-plane direction z is much stronger than the confinement in the plane (x,y) . As a consequence, the eigenenergy for the HH can be simplified as $-\hbar^2(k_x^2 + k_y^2)/2m_{\parallel}^{\text{HH}}$, with $m_{\parallel}^{\text{HH}} = m_0/(\gamma_1 + \gamma_2)$. For the LH, the eigenenergy becomes $-\hbar^2(k_x^2 + k_y^2)/2m_{\parallel}^{\text{LH}}$, with $m_{\parallel}^{\text{LH}} = m_0/(\gamma_1 - \gamma_2)$. Eventually, we obtained for Ge the effective masses expressed in Formula 1.8. Here we see that the heavy holes are about twice as light as the light holes in the plane.

$$\begin{cases} m_{\parallel}^{\text{HH}} = 0.057m_0 \\ m_{\parallel}^{\text{LH}} = 0.109m_0 \end{cases} \quad (1.8)$$

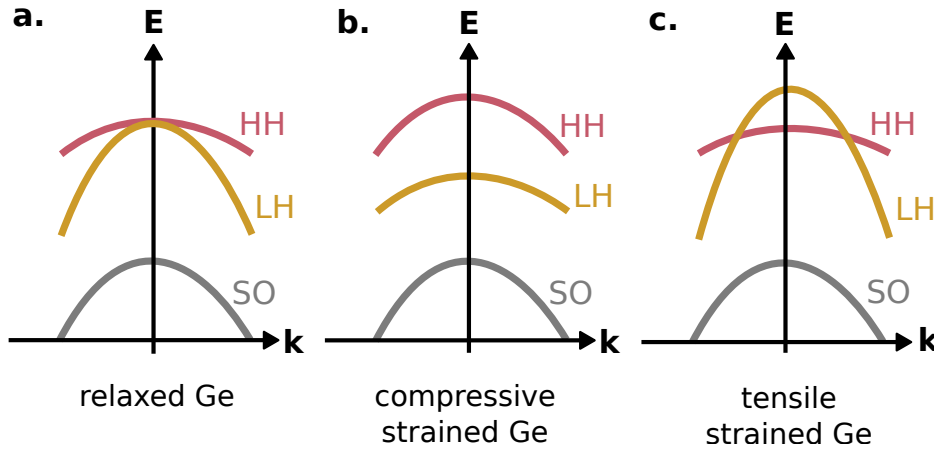


Figure 1.3 – **Effects of strain on Ge.** Figure adapted from J. Foronda [Foronda et al. 2014]. (a) Schematic of the light-hole (yellow), heavy-hole (red) and split-off (grey) bands of relaxed Ge. (b) Same for compressive strained Ge. We observe a separation of the light hole and heavy hole bands. (c) Same for tensile strained Ge. The light hole band passes above the heavy hole one.

Effects of strain

The electronic band structure of the heavy and light holes strongly varies with the strain. In bulk germanium, the two light hole and the two heavy hole bands are degenerated at the Γ point where $\hbar\vec{k} = 0$. Figure 1.3 schematises the change in band structure for compressive or tensile strain. Under compressive strain, heavy and light hole bands separate at the Γ point, and it's the heavy holes that are favoured. Under tensile strain, the light hole band bends and pass over the heavy hole band. This time, it is the light holes that are favoured at the Γ point. In planar Ge heterostructures, compressive strain occurs when the Ge is stretched between two layers having a smaller lattice parameter. This is the case when considering Ge/SiGe heterostructures. Contrariwise, tensile strain happen when the Ge is compressed between two layers with a larger lattice parameter. It is the case for Ge/GeSn heterostructures, often used in the field of optics.

Figure 1.4 shows the valence band difference between cubic bulk Ge and tetragonal strained Ge. We clearly observe the splitting of the heavy and light hole bands when straining the Ge. The calculations have been made for a Ge layer of 20 nm compressively strained between two layers of $\text{Si}_{0.25}\text{Ge}_{0.75}$. This heterostructure is very close to the one involved in the fabrication process described below.

1.2.3 Device fabrication

Single and double dot devices have been fabricated on Ge/SiGe heterostructures. The fabrication recipe of such devices is synthesised in the following. The detailed recipe and the electrical characterisation of the devices can be found in the PhD manuscript of G. Troncoso [Fernandez-Bada 2023].

Quantum dot devices

In order to correctly align the different lithography steps required all along the fabrication process, markers have to be deposited on the heterostructure surface. A first set of $\text{Ti}(5\text{ nm}):\text{Pt}(100\text{ nm})$

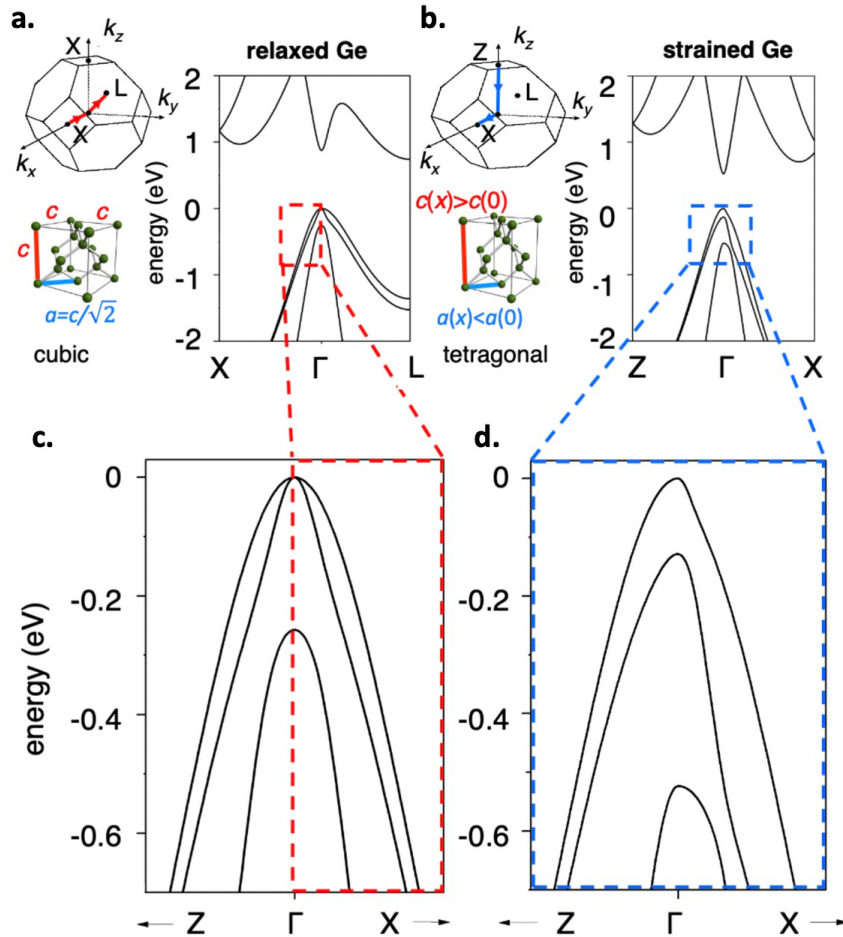


Figure 1.4 – **Band structure of relaxed and strain Ge.** Figure taken from L. Terrazos [Terrazos et al. 2021]. (a) Band structure calculation of bulk Ge using the Density Functional Theory. The schematic represents the real and reciprocal space crystal structures. (b) Same for a 20nm-thick layer of Ge compressively strained in a Ge/Si_{0.25}Ge_{0.75} planar heterostructure. (c) Zoom on (a) focusing on the [100](x) and [001](y) axis. (d) Zoom on (b). We clearly see the splitting of the heavy hole and light hole bands at the Γ point.

markers is exposed with UV-lithography straight after the heterostructure CVD. These markers have to be thick enough as their contrast is attenuated by the electronic signal of the Ge well. The next step of the process is the deposition of the Al ohmic contacts. The Si cap layer and the Si_{0.21}Ge_{0.79} are etched until reaching the Ge well. The aluminium is then deposited, and lift-off. Afterwards, an annealing step is needed to create a pure ohmic contact between the Al and the Ge well, with a contact resistance ranging from hundreds Ohms to kOhms depending on the fabrication process quality.

The fabrication process continues with the definition of the mesa. The heterostructure is etched away leaving only a $60\ \mu\text{m} \times 60\ \mu\text{m}$ square defining the location of the 2D hole gas. This leaves a free space around the device for the bonding pads to avoid the shorting of the 2DHG with the gates when microbonding. The mesa is defined by UV-lithography. Etching was initially performed in a solution of HF:HNO₃:H₂O, but a lack of reproducibility and significant variations on the surface profile lead to a dry etching solution. The mesa is etched in an inductively coupled plasma reactive

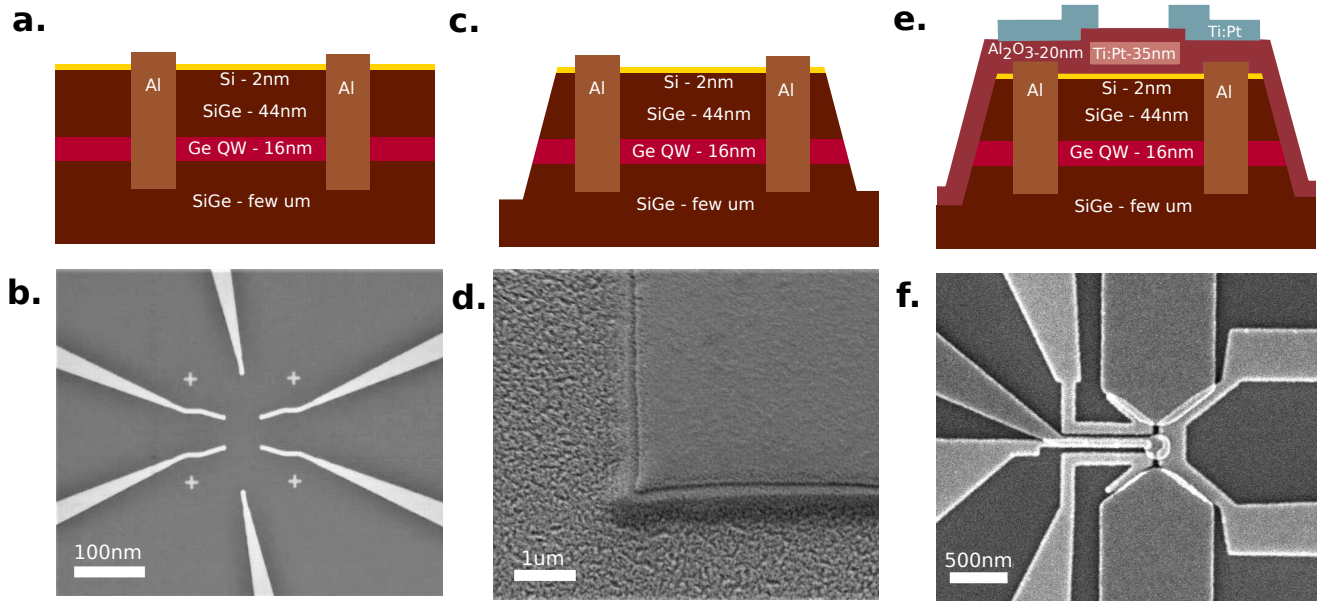


Figure 1.5 – **Device fabrication process.** (a) Schematic of the device stack after the ohmic contact deposition. (b) SEM picture taken by G. Troncoso showing markers and ohmic contacts. (c) Device stack after mesa etching. (d) SEM picture taken by G. Troncoso showing the mesa edges. (e) Device stack after the deposition of two layers of dielectric and gates. (f) SEM picture taken by G. Troncoso showing a device with two layers of gates.

ion etching (ICP-RIE) machine, with a plasma of $\text{SF}_6:\text{O}_2:\text{CH}_2\text{O}_2$. The various parameters (plasma ratios, plasma power, chamber pressure, ...) have been optimised to obtain the most isotropic etching possible.

The fabrication process ends with the deposition of the gates and their dielectric. A first layer of Al_2O_3 dielectric is grown in an atomic layer deposition (ALD) machine, in an O_2 plasma at 280°C . The heterostructure is pre-treated in-situ with an O_2 plasma, that reduces the risks of shorted contacts. Most device designs required two gate layers. To properly align them, a second set of $\text{Ti}(3\text{nm}):\text{Pt}(32\text{nm})$ markers is deposited. The $\text{Ti}(3\text{nm}):\text{Pt}(32\text{nm})$ gates are evaporated after exposure by electron beam lithography (EBEAM). The proximity effect slightly changes the gate dimensions compared to the original design, up to a few tens of nm. These changes were measured and corrections made in the final gate design. To complete the process, a second layer of dielectric is deposited and then the second layer of gates after a careful alignment. Figure 1.5 shows an overview of the whole fabrication process and SEM images of samples at different key steps.

1.3 Holes confined in Si nanowires

Silicon has been used for decades in the microelectronics industry, resulting in mature fabrication processes and widespread foundries. In this highly purified and isotopically enriched material, spins can benefit from a particularly clean magnetic environment. These two remarkable advantages, make silicon one of the most considered candidates for building spin-based quantum processors [Maurand et al. 2016]. Such processors require the integration of millions of qubits together, which spotlights the silicon metal-oxide-semiconductor (Si-MOS) technology and the

silicon-on-insulator (SOI) nanowire architecture. In this Part, we detail the band structure of holes in SOI nanowires and describe the semi-industrial fabrication process leading to the devices measured later in this manuscript.

1.3.1 Si nanowires

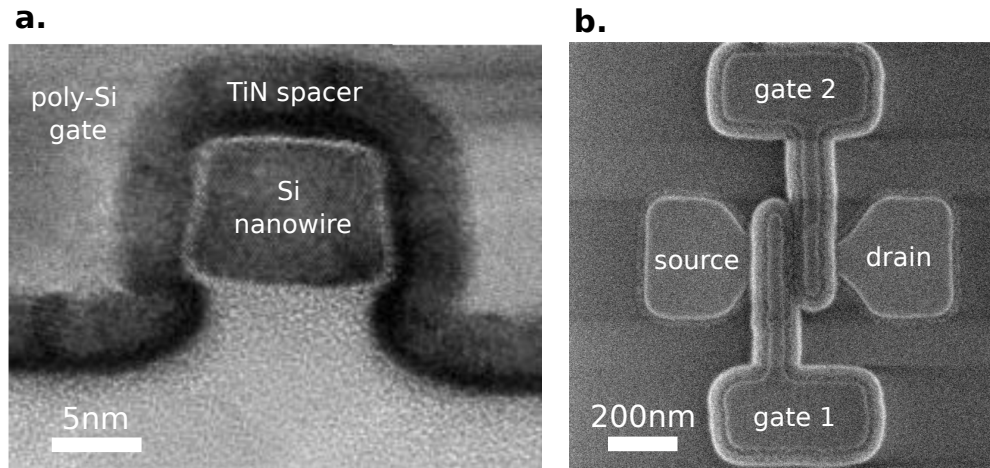


Figure 1.6 – **SEM and TEM images of SOI nanowires.** Figure taken from L. Hutin [Hutin et al. 2017] and R. Maurand [Maurand et al. 2016]. (a) TEM image of the cross-section of a Si nanowire device. (b) SEM image of a Si nanowire device with two gates.

Silicon nanowires consist of thin undoped silicon channels with typical widths varying from 100 nm down to 20 nm. The length of the channel is on the order of a few hundred nm. On both sides of the nanowire, p-doped contact regions called source and drain serve as reservoirs. Several gates perpendicular to the nanowire axis wrap around the nanowire, allowing a fine control of the confinement underneath. This enables the formation of a quantum dot with a single charge or a few charges under each gate. Figure 1.6 shows SEM and TEM images of a Si nanowire single dot device. We can observe the large wrapping of the gates around the nanowire. Figure 1.8 shows a schematic representation of the device layer stack.

1.3.2 Band structure in Si nanowires

In Si nanowire, the very strong confinement given by the 1D geometry leads to a strong mixing of the HH and LH states even for the low energy eigenstates. Consequently a simple description of the states in terms of HH and LH is no longer possible. In the Luttinger-Kohn Hamiltonian, J_z is then replaced by the operator $F_z = J_z + L_z$, where L_z is the orbital angular momentum given by the envelope functions [Kloeffel, Trif, et al. 2011]. Figure 1.7 (a) presents a schematic of the low energy band of a Si nanowire using F_z as states index. C. Kloeffel [Kloeffel, Rančić, et al. 2018] computed the band structure of Si nanowires for different crystallographic orientations. He found that the effective mass varies strongly with the nanowire orientation. He further shows that the spin-orbit interaction also depends on the crystalline orientation of the nanowire (see Figure 1.7 (b)).

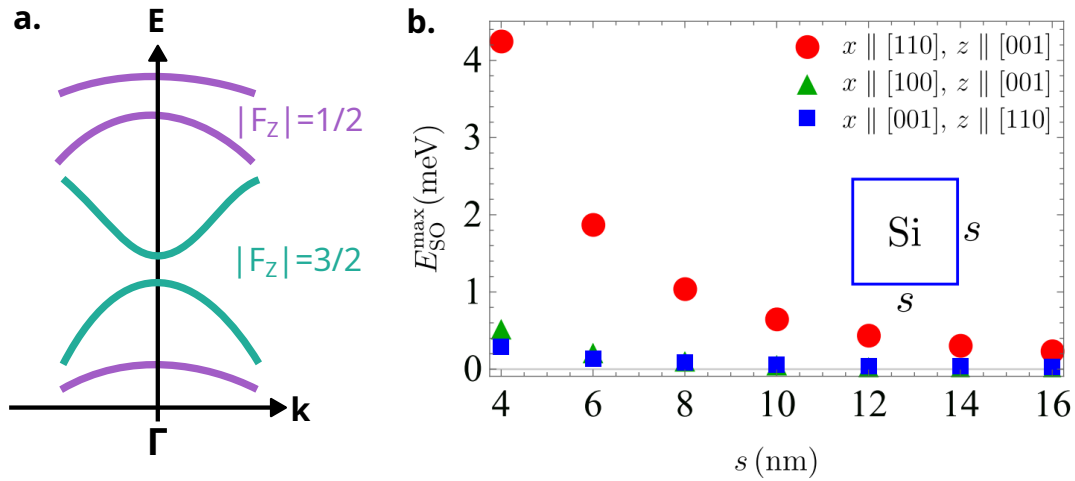


Figure 1.7 – **Band structure in Si nanowires.** Figure adapted from G. Scappucci [Scappucci et al. 2021] and C. Kloeffel [Kloeffel, Rančić, et al. 2018]. (a) Illustration of the holes band structure in a Si nanowire. The purple bands correspond to $F_z = \pm 1/2$, while the green bands correspond to $F_z = \pm 3/2$. (b) Calculated evolution of the maximum spin-orbit energy as a function of the nanowire width. For very thin nanowires, we observe strong differences depending on the crystalline orientation.

1.3.3 Semi-industrial device processing

The Si nanowire devices described below are processed on 300 mm silicon-on-insulator wafers at the CEA Leti. They are fabricated under the supervision of M. Vinet and L. Hutin.

Fabrication process

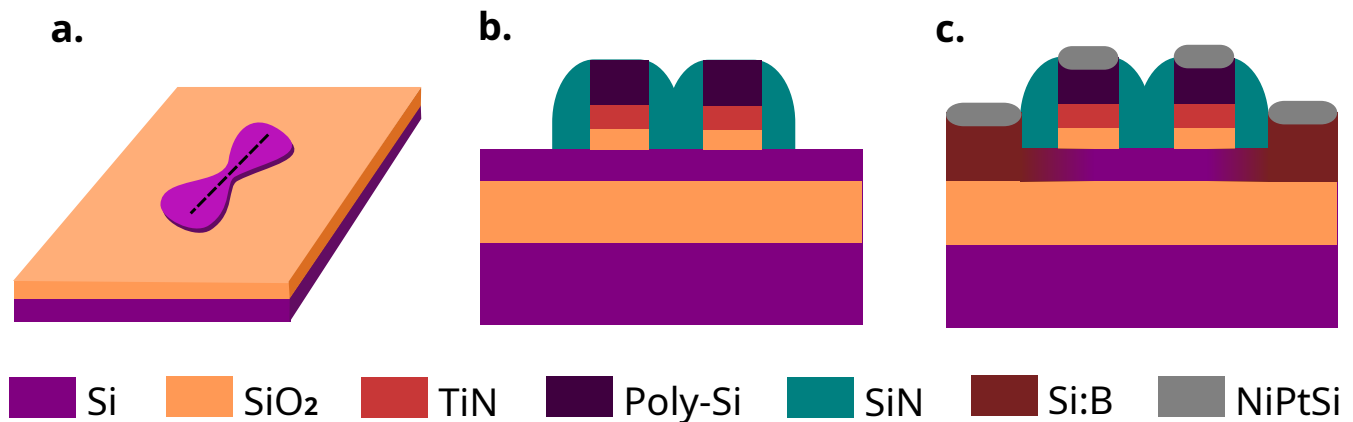


Figure 1.8 – **Fabrication process of the SOI nanowire devices.** (a) 3D view of the SOI wafer after patterning. The black dashed line indicate the cutting plan of the representations (b) and (c). (b) 2D cut of the gate stack, after deposition and patterning of the gates and spacers. (c) 2D cut of the final devices, after epitaxy and thermal activation of the source and drain, and the salicidation of the contacts.

The wafers used for the fabrication are 300 mm SOI wafers. They consist of three layers : a thick bulk Si substrate, a 145 nm thick SiO_2 buried on oxide layer, and a thin Si layer typically

8 nm to 20 nm thick. This last layer is patterned into nanowires using deep ultraviolet lithography and plasma etching. To further reduce the lateral size of the nanowires, the resist is over-etched. Using this trimming method, narrow channels of 20 nm to 100 nm width can be achieved. The gate stack is deposited above the nanowires. It also consist of three layers : a 5 nm thermal SiO₂ layer, a 5 nm TiN layer and a 60 nm heavily doped poly-Si layer. The gates are patterned into 80-100 nm pitch using electron beam lithography and dry etching. They are isolated from each other by 31 nm wide SiN spacers. The channel is contacted at both extremities, defining the source and the drain. An in-situ doped Si epitaxy is formed by the diffusion of boron dopants at the source and the drain. The dopants are thermally activated at $\sim 1030^\circ\text{C}$ for 30 s. A final salicidation step allows to form low resistance NiPtSi contacts on top of the gates, the source and the drain. Figure 1.8 schematises the different fabrication steps described in this paragraph.

Geometries available

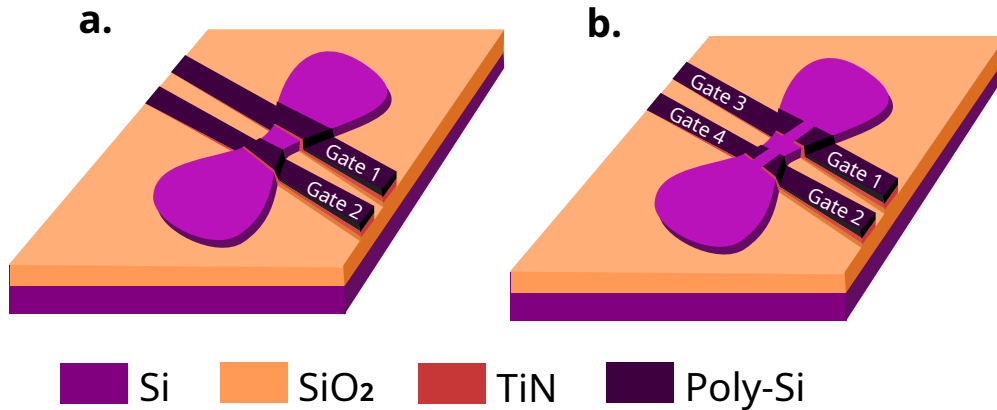


Figure 1.9 – **Two different device geometries.** (a) Representation of a pump device after the gate patterning. Two gates in series are wrapping around the Si channel. (b) Representation of a face-to-face device after the gate patterning. Two pairs of gates are facing each other and are partially wrapping around the Si channel.

Among all gates geometries, the pump and the face-to-face stand out. In the pump or series geometry, the gates overlap over the channel width and are distributed in series along the nanowire. In such a design, all gates must be simultaneously in accumulation mode in order for the source-drain current to circulate. In the face-to-face or split gate approach, the gates are split down the centre by an additional etching step. As a result, they partially overlap the channel facing each other. A source-drain current can flow with only one of the upper or lower gate arrays in accumulation mode.

1.4 Spins and charges in quantum dots

Charge states in semiconductor quantum dots can be used as building blocks for qubit-based quantum processors. However, spins in quantum dots appear to be even more promising candidates benefiting from longer coherence times than charges, exceeding $T_2^E = 1.2\text{ ms}$ for electron spins [Veldhorst et al. 2014] and $T_2^E = 88\text{ }\mu\text{s}$ for hole spins [Piot et al. 2022]. The readout of the spin

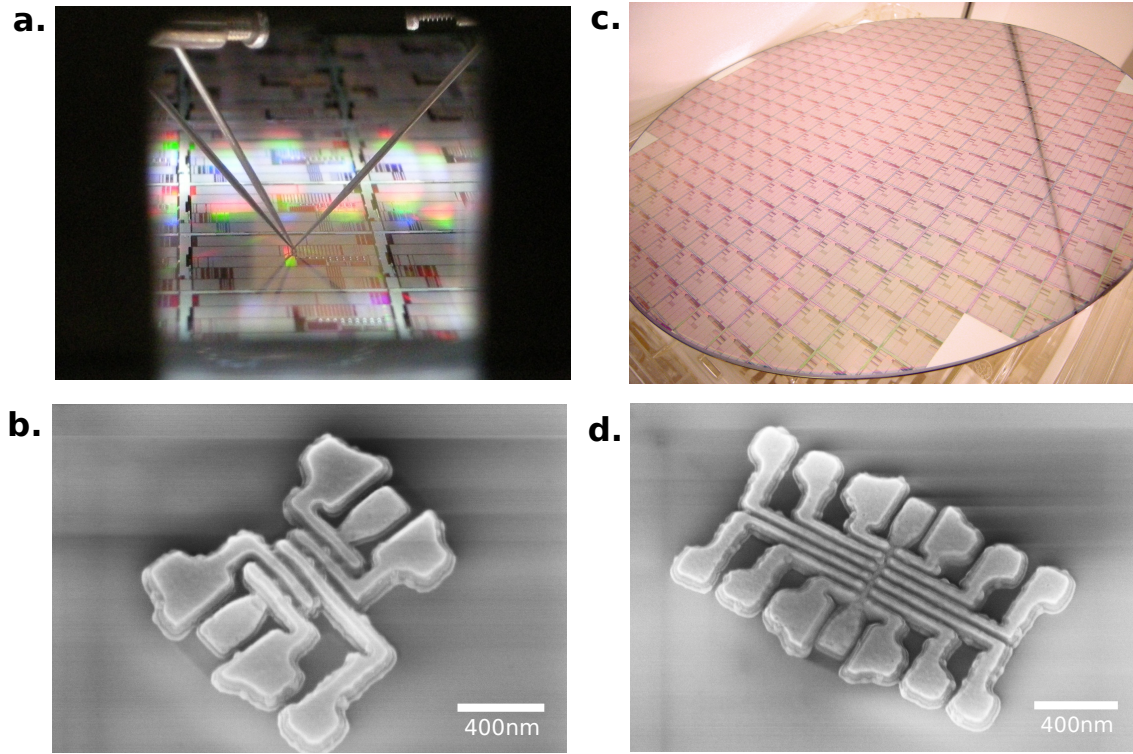


Figure 1.10 – **Si nanowire devices.** (a) Picture of a device chip under the probe station. (c) Picture of a processed 300 mm Si wafer, which will be cut into smaller device chips. (b) SEM picture of a 5 gates pump device. (d) SEM picture of a 12 gates face-to-face device.

states can be ensured thanks to a spin-to-charge conversion technique, enabling to get rid of the complicated measurement of small spin magnetic moments. In this Part, we present the basic physics of charges and spins in single and double quantum dots and describe a spin-to-charge conversion technique based on the Pauli exclusion principle.

1.4.1 Charges in quantum dots

Coulomb blockade

In a quantum dot, the first interaction between carriers to be considered is Coulomb repulsion. If several carriers already occupy a highly confined space, the addition of an extra carrier comes at a cost. To enter the quantum dot, it must have the energy corresponding to the repulsion between the charges of the carriers present so far in the QD. This charging energy $E_C = e^2/C$ results from the modification of the electrostatic potential when adding a charge e [Leo P. Kouwenhoven et al. 1997]. The Coulomb repulsion therefore opposes the entry of carriers into the QD and this is why we speak of Coulomb blockade. This phenomenon is also called sequential tunnelling effect, as it is equivalent to a regime of weak tunnelling where the carrier stays inside the QD longer than it tunnels in or out ($R_S, R_D > 1 \text{ M}\Omega$). Two conditions have to be satisfied in order to observe Coulomb blockade :

- The electronic temperature have to be low enough, such that the thermal energy does not provide enough energy to the carriers to counter Coulomb repulsion ($k_b T \ll E_C$).

- The Heisenberg uncertainty relation relates the energy and time involved in a tunnelling process as $\Delta t \Delta E > h$. In our case, ΔE is the charging energy E_C and Δt is the RC time constant of the tunnel junction. Thus, we obtain that the tunnel junction contact resistance has to be large enough ($R \gg h/e^2$).

Single quantum dot

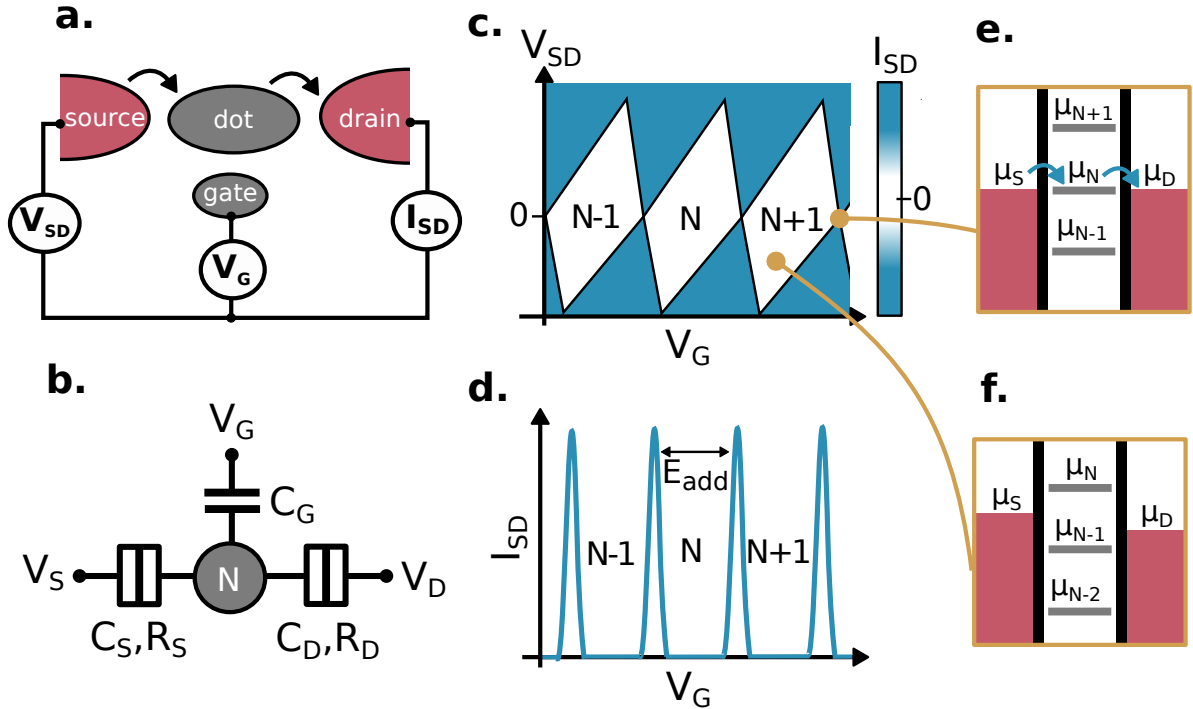


Figure 1.11 – **Single quantum dot and Coulomb blockade.** (a) Schematic of a single quantum dot and its associated gate and reservoirs. (b) Schematic of the capacitances and resistances to consider to apply the constant interaction model to the single quantum dot. (c) Schematic of the current Coulomb diamonds formed by sweeping both V_G and V_{SD} . Inside each diamond the current is zero and the charge state of the QD remains unchanged. (d) Schematic of the current Coulomb peaks obtained in the low bias regime (V_{SD} small). Like for the Coulomb diamonds, in the region where $I_{SD} = 0$, the charge state of the QD remains unchanged. (e) Schematic of the electrochemical potentials of the system at a charge degeneracy point. (f) Schematic of the electrochemical potentials of the system at a blockade region.

A simplified schematic of a single quantum dot system can be found Figure 1.11 (a). The potential of the quantum dot can be tuned by the gate G . The coupling between the dot and the gate is modelled by a capacitance C_G . The dot can be filled thanks to the Fermi reservoirs called source S and drain D . The tunnel barrier between the dot and the source is modelled as a capacitance C_S in parallel with a resistance R_S . In a similar manner, the tunnel barrier between the dot and the drain is modelled by C_D in parallel with R_D .

Transport through the QD can be modelled using the constant interaction model [L. P. Kouwenhoven et al. 2001]. It assumes that the single particle energy level spectrum is independent of the number of carriers. It also assumes that the coupling between the dot, the gates and the reservoirs can be modelled by a constant capacitance C . For the case presented Figure 1.11 (b),

$C = C_G + C_S + C_D$. Then, the total energy of the quantum dot filled with N carriers is given Formula 1.9. The term eN_0 compensates the parasitic charges of the environment. The energy $E_n(B)$ corresponds to the energy of an occupied level under a magnetic field B .

$$U(N) = \frac{[-e(N - N_0) + C_S V_S + C_D V_D + C_G V_G]^2}{2C} + \sum_{n=1}^N E_n(B) \quad (1.9)$$

The electrochemical potential of the dot is defined as $\mu(N) \equiv U(N) - U(N - 1)$. When it is aligned with the electrochemical potentials of the source and drain, carriers have the proper energy to tunnel in or out of the dot. When we apply a bias voltage $V_{SD} = V_S - V_D$, we open a bias window such that $\mu_S - \mu_D = -eV_{SD}$. If the electrochemical potential of the dot falls within this window, a carrier can tunnel from the source to the dot, and then from the dot to the drain, creating a source-drain current. Otherwise, the tunnelling is Coulomb blocked and no current flows across the dot.

The electrochemical potential of the dot can be tuned by applying a voltage V_G to the gate. In order to increase the filling of the dot from N to $N+1$, the potential to apply to the gate should correspond to the energy $E_{\text{add}} = \mu(N + 1) - \mu(N) = E_C + \Delta E$, where ΔE is the energy level spacing between the levels N and $N+1$. The lever arm of the gate α is defined as the ratio between the voltage applied to the gate and the energy it brings to the dot.

Figure 1.11 (c) shows the source-drain current peaks, also called Coulomb peaks, appearing when the gate voltage is swept so that the dot potential falls in the bias window. By further increasing the bias voltage, ground and excited levels can live within the same bias window. It opens new parallel paths for the carrier to tunnel, reducing the blockade regions. A 2D map of the source-drain current, sweeping both the gate and bias voltages, will show blockade regions that shrink as the bias window is increased. Figure 1.11 (d) shows these blockade regions, called Coulomb diamonds because of their shape.

Double quantum dot

A simple DQD system is presented Figure 1.12 (a). This time, two dots are coupled together by a tunnel barrier modelled as a capacitance C_M in parallel with a resistance R_M . The left dot is coupled to the source, while the right dot is coupled to the drain. Both dots have a gate enabling the tuning of their electrochemical potential. The gates have some cross capacitances which are represented in Figure 1.12 (b).

The stability diagram of a DQD gives valuable information about the DQD filling and the coupling between the dots and the leads [Wiel et al. 2002]. Figures 1.12 (c) and (d) schematise the stability diagram of a DQD filled with holes. It is obtained by measuring the source-drain current while sweeping both V_{GL} and V_{GR} . The transition lines obtained correspond to values of the gate voltage at which a charge can tunnel from a lead to the dot. As a consequence, each time one of these lines is crossed, the DQD filling increases. In the case presented Figure 1.12 (c), the dots are uncoupled with no cross capacitances. Thus, a change in V_{GL} only affects the left dot filling and a change in V_{GR} the right dot filling. This explains why the lines are exactly vertical and horizontal. In Figure 1.12 (d), the dots are capacitively coupled, taking into account the cross capacitances.

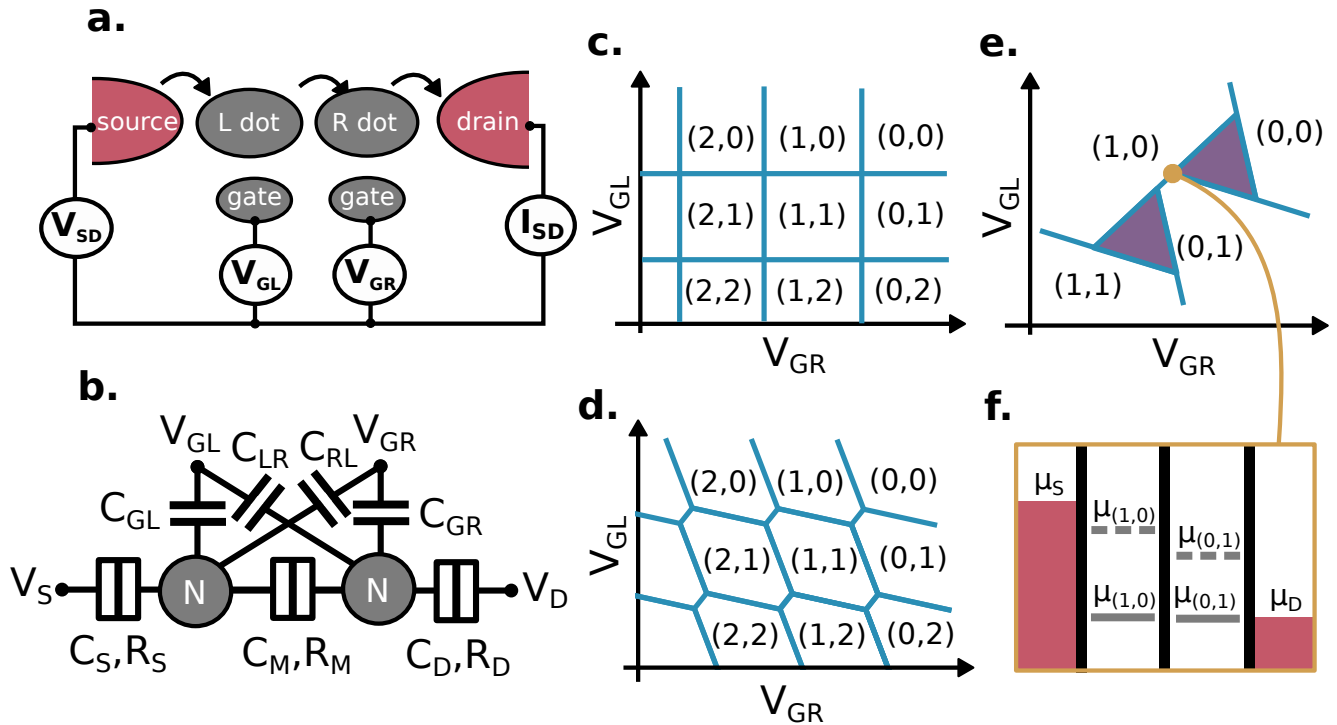


Figure 1.12 – **Double quantum dot and stability diagram.** (a) Schematic of a double quantum dot and its gates and reservoirs. (b) Schematic of the capacitances and resistances to consider to apply the constant interaction model to the double quantum dot. (c) Schematic of the stability diagram for uncoupled dots where $C_M = 0$. The filling of the two dots is indicated as (N_L, N_R) . (d) Schematic of the stability diagram for coupled dots such that $0 < C_M < C_{GL,GR}$. (e) Schematic of the bias triangles around the interdot charge transition $(1,0) - (0,1)$, appearing for $V_{SD} \neq 0$. The regions where the current is not zero are indicated in violet. (f) Schematic of the electrostatic potentials of the system at the point indicated by the gold arrow.

This time, the addition of a hole in one dot affects the electrostatic potential of the other dot. It results in an hexagonal honeycomb pattern, in which the dot-lead transitions have a finite slope.

At the intersection of two dot-lead transition lines, an interdot charge transition line appears. It corresponds to the transition of a charge from a dot to the other, without changing the total number of holes in the DQD. The length of the interdot charge transition line scales with the interdot capacitance C_M . In this configuration, the electrochemical potential of the left dot is given by $\mu_L(N_L, N_R) \equiv U_L(N_L, N_R) - U_L(N_L - 1, N_R)$ with N_L and N_R the number of holes occupying the left and right dots respectively.

Increasing the bias voltage allows higher energy levels to fit within the bias window. At a triple point, this allows the charge to take multiple paths to transit from the source to the drain through the two dots. This results in the appearance of so-called bias triangles presented in Figure 1.12 (e). These bias triangles are the charge signature of a DQD when performing current measurements.

1.4.2 Spins in quantum dots

Odd charge configuration

Here, we focus on the spin physics of a DQD with an odd charge configuration. It is driven by four different mechanisms [Mutter and Burkard 2021]:

- The Zeeman splitting described by $\mathcal{H}_Z = \frac{1}{2}\mu_B g_{L/R} B \sigma$, that lifts the degeneracy of the spin up and spin down states when an external magnetic field B is applied.
- The detuning contribution, expressed as $\mathcal{H}_\epsilon = \frac{\epsilon}{2}\tau_z$.
- The spin-conservative tunnelling between the two dots, expressed as $\mathcal{H}_t = t\tau_x$.
- The spin-flip tunnelling, made possible by the spin-orbit coupling and modelled by $\mathcal{H}_{t_{SO}} = t_{SO}\tau_y\sigma_y$.

For these Hamiltonians, σ is the Pauli spin operator, τ is the Pauli position operator and $g_{L/R}$ is the g-matrix of the left and right dots respectively. The g-matrix is a 3×3 matrix characterising the gyromagnetic response of the hole. This response is anisotropic due to the anisotropy of the hole confinement, the SOC mixing orbitals and spins and the magnetic field also acting on the spin and orbital degrees of freedom [Crippa et al. 2018]. The total Hamiltonian of the DQD with one spin is finally given by the Formula 1.10.

$$\mathcal{H} = \mathcal{H}_\epsilon + \mathcal{H}_Z + \mathcal{H}_t + \mathcal{H}_{t_{SO}} \quad (1.10)$$

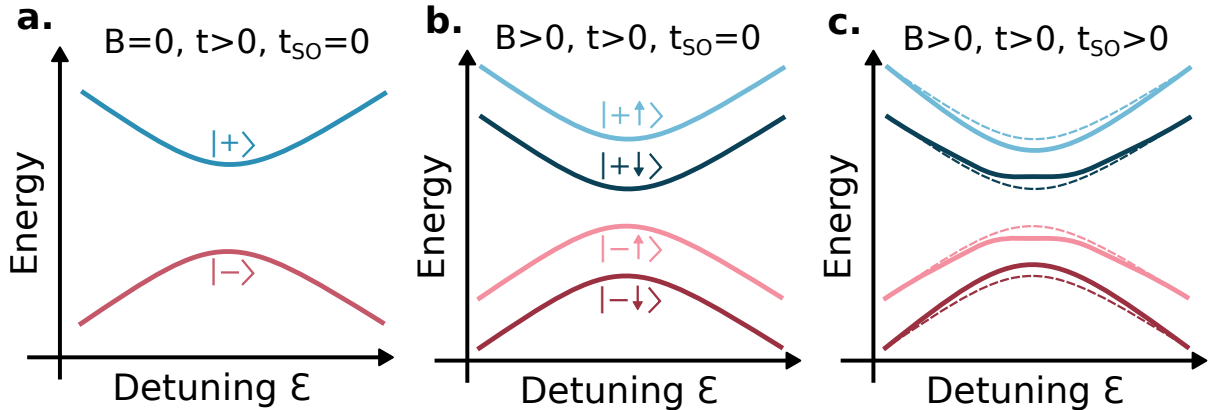


Figure 1.13 – **Energy diagram of a single charge in a double quantum dot.** (a) Energy diagram of a single charge in a DQD with $B = 0$. (b) Same with $B > 0$. The magnetic field lifts the degeneracy of $|+\rangle$ and $|-\rangle$. As a result $|+\downarrow\rangle$ and $|+\uparrow\rangle$, as well as $|-\downarrow\rangle$ and $|-\uparrow\rangle$, are split by the Zeeman energy $\Delta E_Z = g\mu_B B$. (c) Same with $t_{SO} > 0$. The spin-orbit coupling mixes $|-\uparrow\rangle$ and $|+\downarrow\rangle$ through t_{SO} .

For a DQD filled with a single charge spin¹ there is four possible eigenstates. Either the hole is in the left dot with a spin down $|L \downarrow\rangle$ or a spin up $|L \uparrow\rangle$, or it is in the right dot with a spin down $|R \downarrow\rangle$ or a spin up $|R \uparrow\rangle$. In the basis $\{|L \downarrow\rangle, |L \uparrow\rangle, |R \downarrow\rangle, |R \uparrow\rangle\}$, the Hamiltonian 1.10 rewrites as 1.11.

$$\mathcal{H}_{\text{odd}} = \begin{pmatrix} \frac{\epsilon}{2} - \frac{1}{2}g_L\mu_B B & 0 & t & -t_{SO} \\ 0 & \frac{\epsilon}{2} + \frac{1}{2}g_L\mu_B B & t_{SO} & t \\ 0 & t_{SO} & -\frac{\epsilon}{2} - \frac{1}{2}g_R\mu_B B & 0 \\ -t_{SO} & t & 0 & -\frac{\epsilon}{2} + \frac{1}{2}g_R\mu_B B \end{pmatrix} \quad (1.11)$$

Even charge configuration

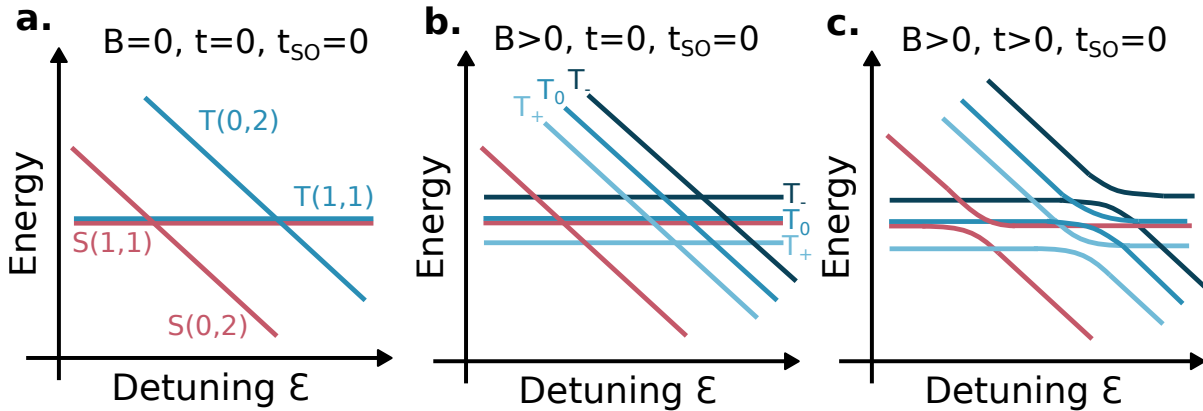


Figure 1.14 – **Energy diagram of a double quantum dot with two charges.** (a) Energy diagram of a DQD with two charges with $B = 0$ and no tunnelling events. (b) Same with $B > 0$. Under magnetic field, the triplet states $T(1,1)$ and $T(0,2)$ split in three, giving new energy states T_+ , T_0 and T_- . T_+ and T_- are energetically separated by the Zeeman energy. (c) Same with $t > 0$. The singlets $S(1,1)$ and $S(0,2)$ anticross, as well as $T_-(1,1)$ with $T_-(0,2)$, $T_0(1,1)$ with $T_0(0,2)$ and $T_+(1,1)$ with $T_+(0,2)$. If we would add $t_{SO} > 0$, then every time two states intersect there would be an anticrossing.

If we now focus on a DQD with two holes or an even number of holes, the eigenstates are different. At zero magnetic field, the ground state corresponding to the charge filling $(0,2)$ is the the singlet $S(0,2)$ and its excited state is the triplet $T(0,2)$. The states corresponding to the charge configuration $(1,1)$ are $S(1,1)$ and $T(1,1)$. Under a magnetic field, the Zeeman effect splits $T(1,1)$ into triplets $T_{-/0/+}(1,1)$. They are defined as in Formula 1.12.

1. A DQD charge configuration with an odd number of spins is equivalent to a DQD filled with one spin.

$$\left\{ \begin{array}{l} S(1, 1) = \frac{1}{\sqrt{2}}(|\downarrow\uparrow\rangle - |\uparrow\downarrow\rangle) \\ T_-(1, 1) = |\downarrow\downarrow\rangle \\ T_0(1, 1) = \frac{1}{\sqrt{2}}(|\downarrow\uparrow\rangle + |\uparrow\downarrow\rangle) \\ T_+(1, 1) = |\uparrow\uparrow\rangle \end{array} \right. \quad (1.12)$$

At finite magnetic field, because of the anisotropy of the g-matrix, $S(1, 1)$ and $T_0(1, 1)$ are no longer eigenstates of the system. A better description of the spin states can be done using the basis $\{|\downarrow\downarrow\rangle, |\uparrow\downarrow\rangle, |\downarrow\uparrow\rangle, |\uparrow\uparrow\rangle, S(0, 2)\}$. Then, the Hamiltonian 1.10 rewrites as in 1.13. Figure 1.14 shows the energy diagram of the doubly occupied DQD depending on the detuning for different regimes of magnetic field and tunnelling.

$$\mathcal{H}_{even} = \begin{pmatrix} -\frac{1}{2}(g_L + g_R)\mu_B B & 0 & 0 & 0 & t_{SO} \\ 0 & \frac{\epsilon}{2} - \frac{1}{2}(g_L - g_R)\mu_B B & 0 & 0 & t \\ 0 & 0 & \frac{\epsilon}{2} + \frac{1}{2}(g_L - g_R)\mu_B B & 0 & t \\ 0 & 0 & 0 & \frac{\epsilon}{2} + \frac{1}{2}(g_L + g_R)\mu_B B & t_{SO} \\ t_{SO} & t & t & t_{SO} & -\frac{\epsilon}{2} \end{pmatrix} \quad (1.13)$$

1.4.3 Spin-to-charge conversion

A direct measurement of the spin magnetic moment is difficult to establish and would require a long measurement time. Instead of measuring the spin directly, Loss and Di Vincenzo [Loss and DiVincenzo 1998] proposed to measure the charge, that can be mapped to the spin states using various schemes. The historical way to perform spin-to-charge conversion is to use the Pauli Spin Blockade (PSB) principle. This is still one of the most widely used methods and is the focus of this Section. There are alternative methods, the most common being the energy selective readout known as the Elzerman readout [Elzerman, Hanson, Willems van Beveren, et al. 2004].

Pauli Spin Blockade

The Pauli exclusion principle states that two carriers occupying the same orbital cannot have the same spin. As a consequence, if we consider a quantum dot occupied with a single carrier and try to load a second carrier having the same spin state, the transition will be blocked. This phenomenon is known as Pauli Spin Blockade. If we now consider a QD occupied by an odd number of charges, the result is the same. If the QD is already occupied by an even number of charges, the incoming carrier will occupy a new orbital and no blockade will occur, regardless of its spin state.

The first experimental observation of PSB in a DQD was made by K. Ono [Ono et al. 2002]. He showed that the transition $(1, 1) \rightarrow (0, 2)$ is blocked when $(1, 1)$ is a triplet state, while the

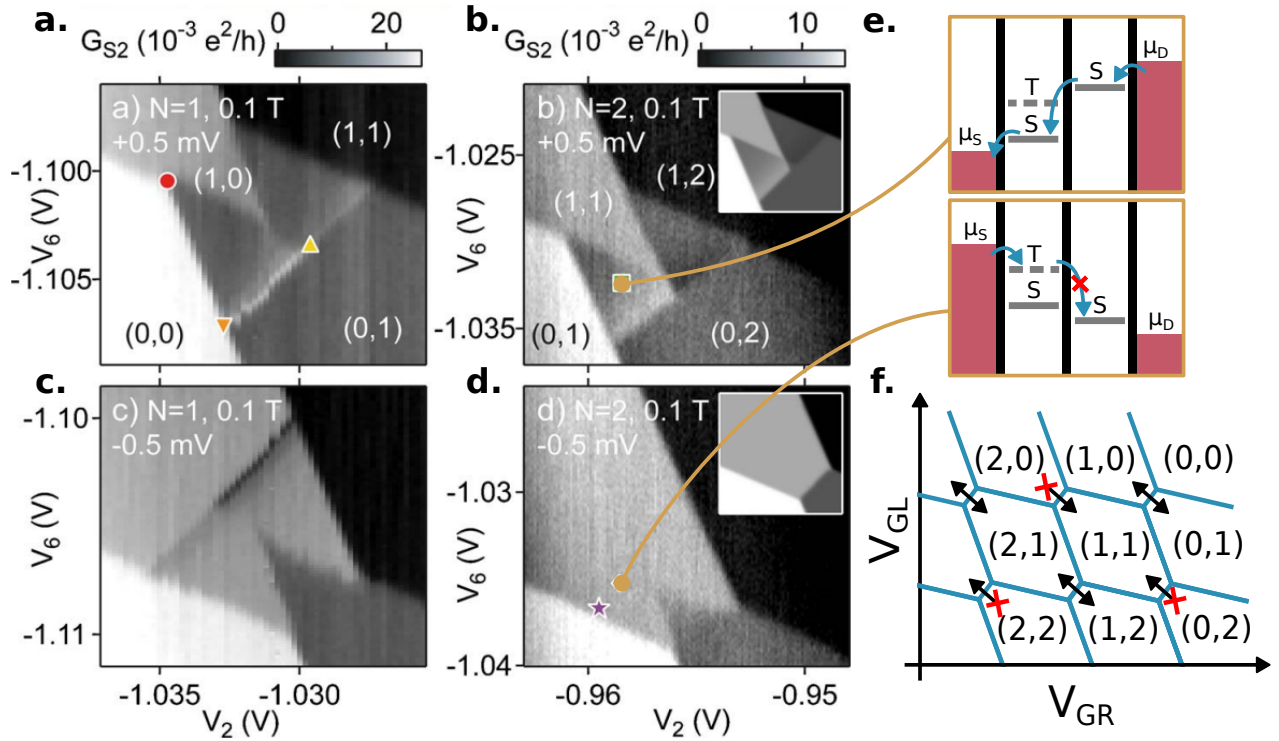


Figure 1.15 – **Pauli Spin Blockade signature measured by charge sensing.** Figure adapted from A. Johnson [Johnson et al. 2005]. (a) Charge sensor signal G_{S2} obtained when measuring the $(0,1) \rightarrow (1,0)$ transition at positive bias. (b) G_{S2} when measuring the $(1,1) \rightarrow (0,2)$ transition at positive bias. (c) The same than (a) at negative bias. The result is symmetrical compared to (a). (d) The same than (b) at negative bias. This time, we observe a blockade at the level of the bias triangles. (e) Electrostatic potentials inside the bias triangles schematised in the non-blockade case and in the blockade case. (f) Representation of the blockade transitions of a DQD stability diagram.

transition $(0,2) \rightarrow (1,1)$ is never blocked. Indeed, the transition $(0,2) \rightarrow (1,1)$ consists in separating two carriers initially in the same dot, so no blockade is expected. Contrariwise, the transition $(1,1) \rightarrow (0,2)$ consists in gathering two carriers in the same dot in the same orbital. The transition is then possible only if both carriers have opposite spins.

Figure 1.15 shows the Pauli Spin Blockade signature on interdot charge transitions, measured by charge sensing. Sub-figures (a) and (c) focus on the $(0,1) \rightarrow (1,0)$ transition. By opening a positive or a negative bias window, we observe the appearance of symmetrical bias triangles. Subfigures (b) and (d) focus on the $(1,1) \rightarrow (0,2)$ transition. This time, applying a positive bias voltage prepares a singlet state while applying a negative bias voltage prepares a triplet state. As a consequence, the transition is blocked for negative bias windows but not for positive ones. The symmetry is broken and this is how PSB is evidenced. In a more general manner, the blockade only concerns transitions involving an even total number of charges.

Unlike the Elzermann technique, Pauli Spin Blockade offers many readout possibilities, such as transport, charge sensing or dispersive readout. It does not require the proximity of reservoirs near the dot, but does require a second dot only dedicated to the readout. However, from a quantum

processor perspective, it remains the preferred route to scalability.

1.5 Conclusion

In this Chapter, we first studied the band structure of holes in bulk germanium and silicon. We then observed that the band structure evolves with the strain and the confinement. In Ge heterostructures, the strain is responsible for the separation of the heavy and light hole bands at the Γ -point. The heavy holes become lighter than the light holes in the plane, they are energetically favoured. In Si nanowires, the confinement is so strong that the heavy hole and light hole states are heavily mixed even for the lowest energy states. This time, the light holes are energetically favoured. In addition to the study of the band structure, we also reviewed the fabrication of quantum dot devices starting from Ge heterostructures or Si nanowires. Afterwards, we saw that Coulomb repulsion is the phenomenon responsible for the formation of quantum dots. We studied the transport in single and double quantum dots. We highlighted the role of the stability diagram, which gives information on the DQD filling and the couplings between dots and leads. Formerly, we studied the physics of spins in DQDs and discussed on the differences between the odd and even charge configurations. Finally, we have shown that Pauli spin blockade can be used to perform spin-to-charge conversion to read out the spin states.

TAKEAWAY MESSAGES:

- Holes in group-IV semiconductors can be described by the four-band model of Kohn and Luttinger. The $J=3/2$ valence band splits into heavy holes and light holes, both having anisotropic effective masses.
- For holes in planar germanium heterostructures, strain is the main responsible for the separation of the light and heavy hole bands. The heavy holes are energetically favoured.
- For holes in silicon nanowires, confinement is mainly responsible for the separation of the light and heavy hole bands. LH and HH are heavily mixed.
- The stability diagram of a DQD gives information about the filling of the dots and their coupling to the leads.
- The spin physics of a DQD is driven by the Zeeman splitting, the detuning, and the conservative and spin flip tunnelling events.
- The eigenstates of the Hamiltonian differ when the total number of carriers inside the DQD is odd or even.
- Pauli Spin Blockade allows spin-to-charge conversion to read the spin states.

RADIOFREQUENCY READOUT OF HOLE SPINS CONFINED IN SEMICONDUCTORS

Contents

2.1	Charge sensing of hole spins	30
2.1.1	Quantum conductance	30
2.1.2	Radiofrequency readout	31
2.1.3	Recent achievements and limitations	33
2.2	Dispersive readout of hole spins	35
2.2.1	Quantum capacitance	35
2.2.2	Dispersive response	37
2.2.3	Resonators	38
2.3	Choice of the readout method	39
2.4	Conclusion	39

First ascent of an icefall in Akka mountains, with T. Cattelain

Sarek massif, Sweden - March 10th 2022

If the existence of hole spin angular momentum is no longer to be proven, the direct readout of this tiny magnetic moment would not be fast enough to allow spin qubit applications. An alternative readout method is based on the spin-to-charge conversion technique reviewed in Chapter 1.4.3, and allows to access the spin states of double quantum dots through charge detection. The charge states are then read thanks to local charge sensors integrated as close as possible to the quantum dot to probe. This method called charge sensing is detailed in a first Part. Even though the charge sensors can be read with the current, radiofrequency-based readout setups benefit from reduced noise and larger bandwidth, offering faster readout together with multiplexing possibilities. Another method called dispersive sensing is detailed in a second Part. The latter also relies on a radiofrequency setup enabling to probe the quantum capacitance of a quantum dot with a resonator. Depending on the geometry of the devices, one of the readout methods may or may not be preferred. This will be the subject of a third Part.

2.1 Charge sensing of hole spins

Charge sensing is the most widely used technique for probing the charge states of quantum dot devices. The charge sensors can take the form of quantum point contacts (QPCs) [Wees et al. 1988], single electron transistors (SETs) [Averin and Likharev 1986] or other quantum dots dedicated to the readout [Colless et al. 2013]. In such systems, the conductance of the charge sensor shifts if the number of electrons on their nearby quantum dots changes [Elzerman, Hanson, Greidanus, et al. 2003], even if the tunnel coupling is too small to allow transport detection. To use a local charge sensor to determine the charge states of quantum dots, the tunnelling times have to be smaller than the measurement times. Consequently, having tunable tunnel barrier¹ is of importance. With charge sensing, it is therefore possible to observe electron tunnelling in real time. For this purpose, the bandwidth of the charge detection must be larger than the tunnel rate and the charge signal must exceed the noise level over the bandwidth [Schoelkopf et al. 1998]. In this Part, we present the working principle of QPCs and SETs and discuss on their integration on quantum dots architectures. We further review recent achievements in term of charge sensitivity and matching of the radiofrequency readout circuits.

2.1.1 Quantum conductance

Quantum point contacts (QPCs) were the first structures used as local charge sensors [Sprinzak et al. 2002]. They consist of narrow constrictions having a quantized conductance [Wees et al. 1988]. Between two quantized conductance plateaus, where the slope of the conductance is maximum, G_{QPC} is highly sensitive to its induced potential. Formula 2.1 gives the relation between the QPC electrostatic potential Φ_{QPC} and the electrostatic potential of the dot Φ_{QD} , with C_{QPC} the self capacitance of the QPC, and $C_{\text{QPC-QD}}$ the mutual capacitance between the QPC and the dot. Hence, we observe that the greater the capacitive coupling between the QPC and the dot, the more the electrostatic potential of the QPC is affected by small variations in the dot potential. As the gate voltage is swept, this potential Φ_{QD} gradually increases until it reaches the point where an additional carrier can enter the dot. There, Φ_{QD} and therefore the conductance G_{QPC} follow a sawtooth behaviour, the sharpness of which can be attenuated by the electronic temperature or the broadening of the energy levels. To detect the signal, one will generally prefer to look at the derivative of the conductance, whose signal is a deep instead of a sawtooth. Figure 2.1 shows the

1. This is the case for our Ge heterostructure quantum dot devices.

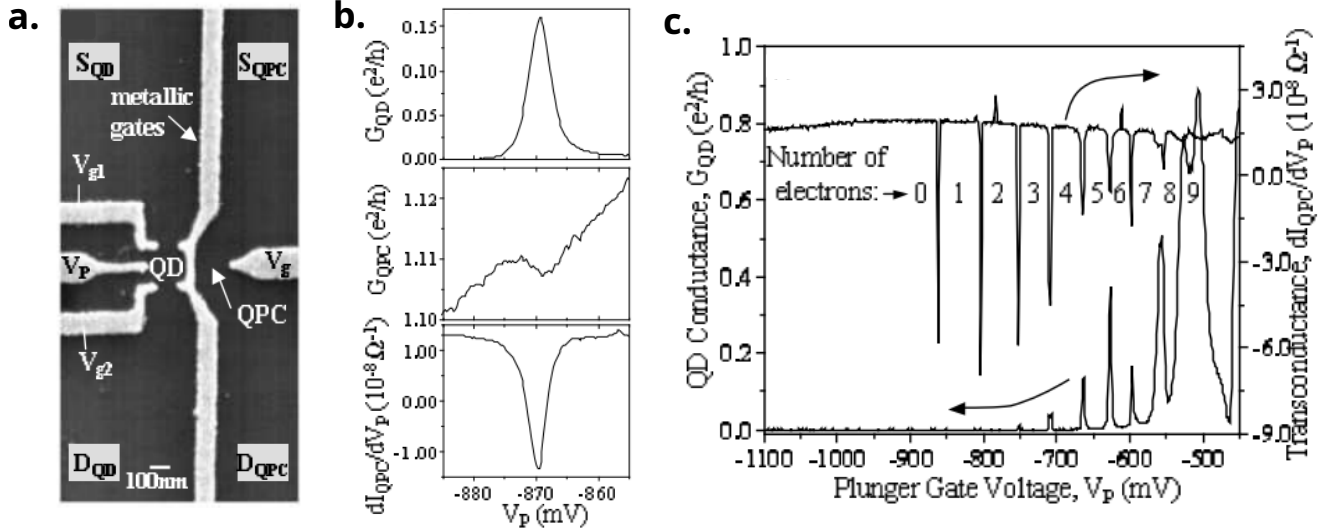


Figure 2.1 – **Charge sensing with a quantum point contact.** Figure adapted from D. Sprinzak [Sprinzak et al. 2002]. (a) SEM image of a GaAs quantum dot device, including a quantum point contact. (b) (top) Coulomb peak measured in transport through the QD. (middle) The same Coulomb peak measured with the conductance of the QPC. (bottom) The same Coulomb peak measured with the derivative of the QPC conductance. (c) Comparison between the signals obtained with the conductance of the QD and the derivative conductance of the QPC, for the measurement of the first charges populating the QD.

integration of a QPC to sense a single quantum dot device.

$$\Phi_{\text{QPC}} = \Phi_{\text{QD}} \frac{C_{\text{QPC-QD}}}{C_{\text{QPC}}} \quad (2.1)$$

2.1.2 Radiofrequency readout

Historically, charge sensors have been read by measuring the current flowing through them [Wees et al. 1988]. Although many setups still rely on current readout, the use of radiofrequency circuits instead has offered many advantages. Introduced by S. Schoelkopf in 1998 [Schoelkopf et al. 1998], RF-readout has enabled high charge sensitivities [Brenning et al. 2006], single-shot readouts [Takeda et al. 2023] and multiplexing possibilities [Borsoi et al. 2023]. For this purpose, a resonator is connected to the charge sensor to probe. The frequency response of this resonator depends on the conductance of the charge sensor. It is probed either with a reflectometry configuration, or with a transmission configuration.

Reflectometry or transmission readout

Figure 2.2 (a) illustrates the differences between a radiofrequency readout circuit setup in a reflectometry configuration or in a transmission configuration. For the case of the reflectometry configuration, the RF-signal is sent to a resonator through a 50Ω -line and the coupled port of a

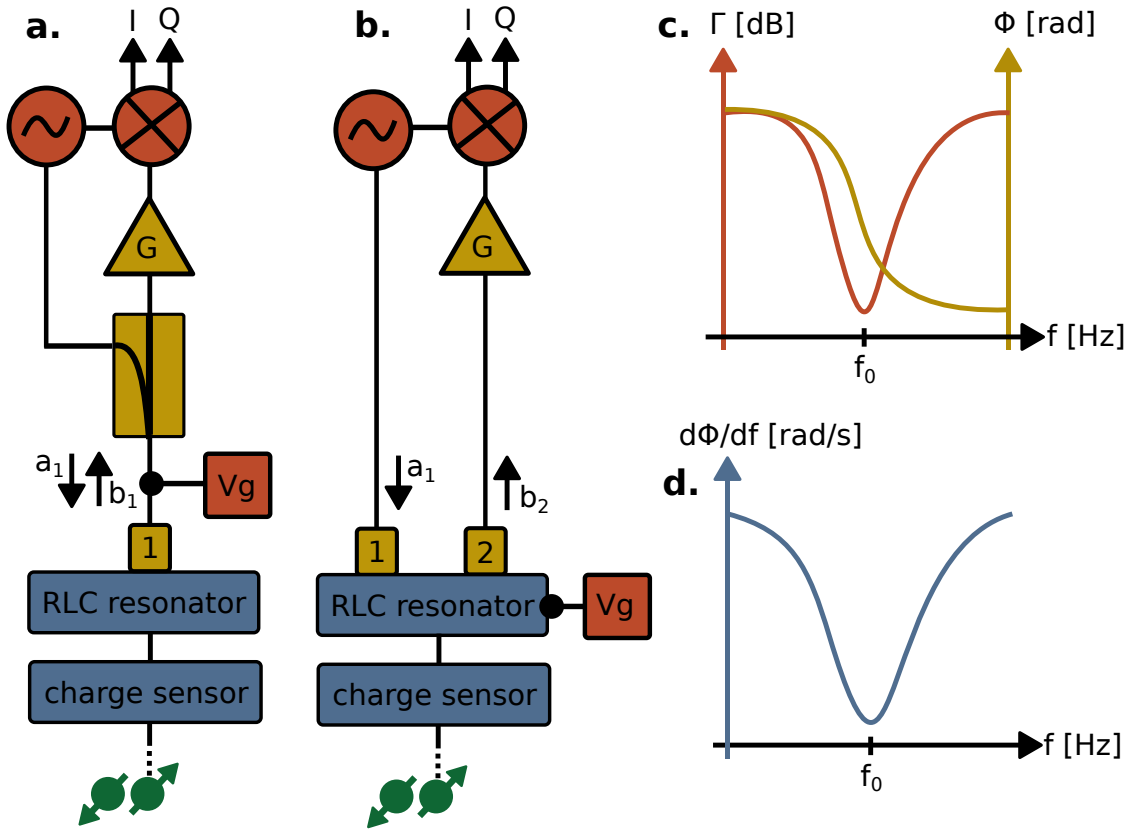


Figure 2.2 – **Radiofrequency readout principle.** (a) Illustration of a basic reflectometry setup, including a directional coupler separating the incident and reflected signals at port 1. (b) Equivalent setup in transmission with the resonator coupled to the feedlines. (c) Schematic frequency response of the amplitude Γ and phase ϕ of the reflected or transmitted signal. (d) Schematic phase derivative as a function of the frequency.

directional coupler. After reaching the resonator coupled to the charge sensor, part of the signal is reflected back through the main port of the directional coupler and amplified before being read. Figure 2.2 (b) shows an equivalent setup on a transmission configuration. This time, the input signal is sent through a 50Ω -line, passes through the resonator coupled to the charge sensor and exits through an output line where the signal is amplified before being analysed.

The resonator gives the circuit a resonant behaviour. Its frequency response is characterised by a deep in the amplitude of the reflected or transmitted signal at its so-called resonant frequency. It is accompanied by a shift of the phase, as illustrated Figure 2.2 (c) and (d). The simplest lumped-element model that can be made of such resonant circuit close to resonance is a series or parallel RLC circuit. The latter consists of a capacitor C representing the electric field, an inductor L representing the magnetic field and a resistor R associated with the losses. Its resonant frequency is then expressed as in Formula 2.2. A more complete description of the RLC model can be found in Part 3.1.1.

$$f_0 = \frac{1}{2\pi\sqrt{LC}} \quad (2.2)$$

Scattering parameters

The scattering parameters give the relationship between the input radiofrequency signal and the reflected and transmitted signals. If we define a_i as the incident signal of port i and b_i as its reflected signal, then the scattering matrix of a two-port system is defined as in Formula 2.3. In a reflectometry setup we will consider the equation $b_1 = S_{11}a_1$ involving the signals incident and reflected on the port 1. Consequently, we will measure the phase of the reflection coefficient S_{11} . In a transmission configuration, we will consider the equation $b_2 = S_{21}a_1$ involving the signal entering on port 1 and the signal leaving on port 2. Hence, we will study the phase of the transmission coefficient S_{21} .

$$\begin{pmatrix} b_1 \\ b_2 \end{pmatrix} = \begin{pmatrix} S_{11} & S_{12} \\ S_{21} & S_{22} \end{pmatrix} \begin{pmatrix} a_1 \\ a_2 \end{pmatrix} \quad (2.3)$$

2.1.3 Recent achievements and limitations

In 2007, two notable achievements were published involving QPCs read with radiofrequency setups. On one hand, D. Reilly [Reilly et al. 2007] demonstrated a high-bandwidth measurement with a charge sensitivity of $\sim 1 \text{ me}/\sqrt{\text{Hz}}$. In the other hand, M. Cassidy [Cassidy et al. 2007] showed single-shot charge readout with a charge sensitivity of $\sim 0.2 \text{ me}/\sqrt{\text{Hz}}$. For both experiments, the QPC is integrated into a GaAs quantum dot architecture and consists of an elongated gate capacitively coupled to the quantum dot device. The radiofrequency readout is based on a reflectometry setup, including a surface mount inductor used as resonator. The latter is connected on an ohmic contact of the QPC. For the setup of D. Reilly, the value of the resonator inductance is $L = 820 \text{ nH}$ and the value of its capacitance is $C_p = 0.63 \text{ pF}$, corresponding to the parasitic capacitance of the inductor to ground. For the setup of M. Cassidy, the inductor value is $L = 490 \text{ nH}$ and its parasitic capacitance is $C_p = 0.47 \text{ pF}$.

Single electron transistors

After the 2010s, QPCs were gradually abandoned in favour of single electron transistor (SETs) for the detection of charge states. In such system, the slope of the conductance between two plateaus of a QPC is replaced by the slope of a Coulomb peak of a quantum dot placed close to the quantum dot device to sense. In the few electron regime, this slope can be very sharp and offers higher sensitivities than QPCs can. Among the work carried out on SET charge sensors, we can cite three recent cases of successful integration with quantum dot devices (see Figure 2.3) :

- **High sensitivity charge sensor** : D. Keith and co-workers [Keith et al. 2019] worked on the integration of the charge sensor and in particular on optimising the capacitive coupling between the SET and the probed quantum dot. They achieved a strong coupling between the SET and the probed quantum dot resulting in a charge sensitivity of $\sim 0.9 \mu\text{e}/\sqrt{\text{Hz}}$, greatly exceeding that of the other setups. For this measurement, a reflectometry circuit was

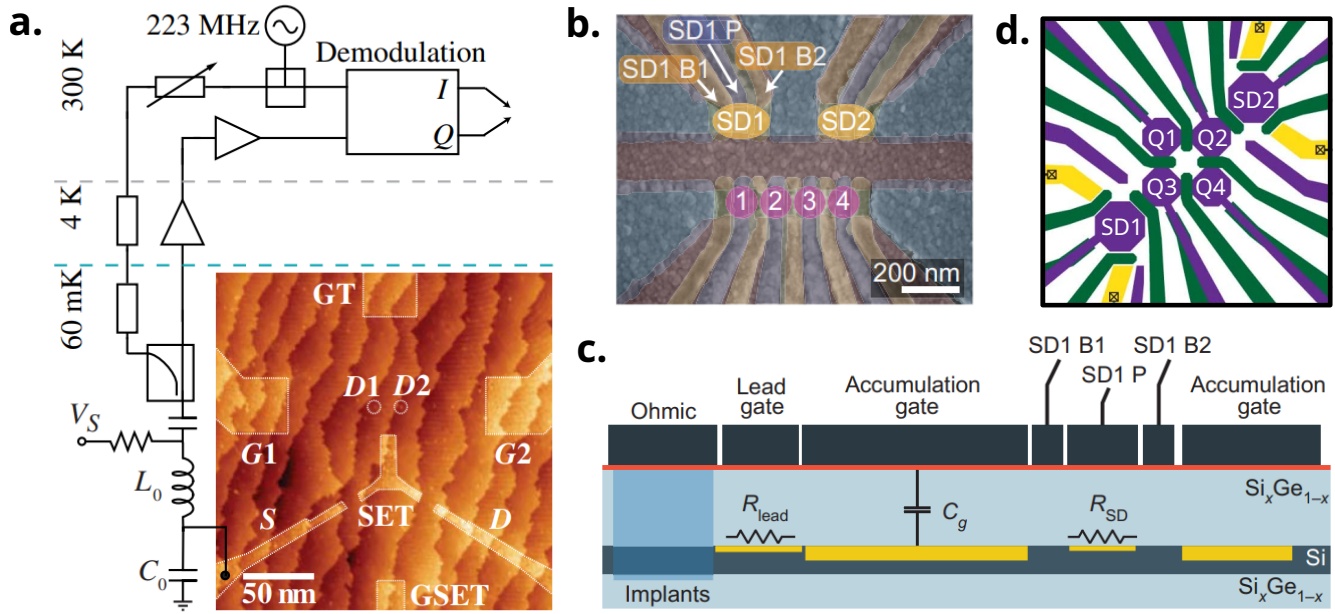


Figure 2.3 – **SETs integrated with quantum dot devices.** Figure adapted from D. Keith [Keith et al. 2019], Y. Liu [Liu et al. 2021] and N. Hendrickx [Nico W. Hendrickx et al. 2021]. (a) STM image of a Si device including a double quantum dot and a SET charge sensor. The external reflectometry circuit is schematised. (b) False-colour SEM image of a Si/SiGe device including four quantum dots and two SET charge sensors. (c) Schematic of the cross section of sample (b), showing the quantum well and the different gates. The quantum well regions drawn in yellow have a finite electron density. (d) Schematic representation of the layer stack of a four qubit processor fabricated in a Ge heterostructure. It includes four quantum dots and two single hole transistors for the charge sensing.

set up on the source of the SET and composed by an inductor $L = 1200$ nH and its parasitic capacitance $C_p = 0.4$ pF. They additionally presented a theoretical work on the shot-noise sensitivity limit for the strong-response regime, and figured out that the sensitivity they measured is only one order of magnitude above the theoretical shot-noise limit.

- **RF readout circuit matching :** Y. Liu and co-workers [Liu et al. 2021] proposed on-chip and off-chip solutions in order to match the feedlines with the LC circuit and mitigate the effects of the parasitic capacitance. They further discussed on which gate or ohmic contact it is suitable to set the radiofrequency readout circuit. Among the solutions enabling a better control of the matching, they proposed in particular to add a matching capacitor to the usual LC resonator composed of an inductor and its parasitic capacitance. Thanks to their work on the readout, they achieved a fidelity of 99.9% in $1 \mu\text{s}$ for the measurement of a Si/SiGe heterostructure double quantum dot device.
- **Integration in Ge heterostructures :** N. Hendrickx and co-workers [Nico W. Hendrickx et al. 2021] used a single hole transistor (SHT) to probe the states of a four qubit processor fabricated in a Ge/SiGe heterostructure. In this respect, they have set up a reflectometry circuit including an NbTiN resonator on one of the ohmic contacts of the SHT. They demonstrated the single-shot readout of the spin-up probability for each of the four qubits.

Limitations in term of integration

While charge sensors have been widely used to read spin qubits for almost two decades, their integration into complex qubit architectures is a matter of debate. Indeed, the addition of charge sensors requires a significant space in the quantum dot architecture and they must be numerous as their sensitivity is only limited to their nearby quantum dots. In addition, we have to consider that some spin-to-charge conversion methods, such as Pauli spin blockade, require two quantum dots to form an effective qubit. The use of charge sensing to readout many spin qubits seems then particularly bulky. However, several geometries including charge sensors with quantum dot matrices have recently been proposed [Borsoi et al. 2023].

2.2 Dispersive readout of hole spins

To avoid the addition of local charge sensors in quantum dot architectures, it has been proposed to connect the radiofrequency readout setup directly on the gate under which the quantum dot to probe is formed [Pettersson et al. 2012]. It is then possible to sense the variations of the device capacitance during a state transition [Mizuta et al. 2017]. This gate-based dispersive readout method enables to probe the stability diagram of a quantum dot device at zero bias and access its excited quantum states. It has demonstrated high readout fidelities [Zheng et al. 2019], single-shot readouts [Pakkiam et al. 2018] and multiplexing possibilities [Hornibrook et al. 2014]. In this Part, we first review the origin of the capacitive variations. We then present the dispersive readout method enabling for their measurement. Finally, we document on the latest achievements in dispersive readout of quantum dot devices.

2.2.1 Quantum capacitance

Origin of the quantum capacitance

Figures 2.4 (a) and (b) show the schematic of a double quantum dot device and the capacitances and resistances involved. The gate charges Q_1 and Q_2 of the two quantum dots can be expressed as in Formula 2.4. There, Q_1 and Q_2 are decomposed into a first term, which depends on the geometry of the device, and a second term, which depends on the charging of the quantum dots. $\langle N_1 \rangle$ and $\langle N_2 \rangle$ are the average electron or hole occupation probabilities of the two dots.

$$\begin{cases} Q_1 = \alpha_1(C_S V_{G1} + e \langle N_1 \rangle) \text{ with } \alpha_1 = \frac{C_{G1}}{C_S + C_M + C_{G1} + C_{12}} \\ Q_2 = \alpha_2(C_D V_{G2} + e \langle N_2 \rangle) \text{ with } \alpha_2 = \frac{C_{G2}}{C_D + C_M + C_{G2} + C_{21}} \end{cases} \quad (2.4)$$

The gate current can be expressed as a function of the gate charges Q_1 and Q_2 [Vigneau, Fedele, et al. 2023], as in Formula 2.5. There, $\alpha = (\alpha_2 - \alpha_1)$ and $C_{\text{geom}} = \alpha_1 C_S + \alpha_2 C_D$ represent the capacitances due to the geometry of the device.

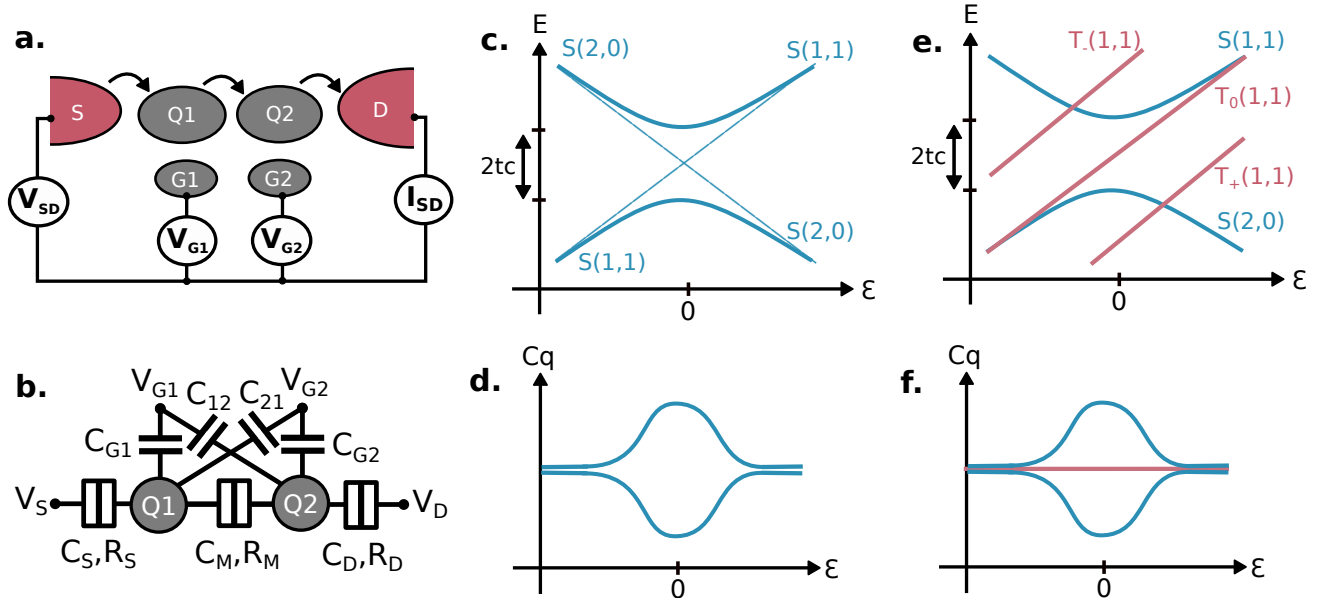


Figure 2.4 – **Dispersive readout of a DQD with two charges.** (a) Schematic of a DQD device. (b) Capacitances and resistances of the DQD device schematised in (a). (c) Energy diagram of the charge states of a DQD filled with two charges around a charge transition. (d) Evolution of the quantum capacitance with the detuning. The two blue curves represent the quantum capacitance associated to the two energy levels represented in (c). (e) Energy diagram of the spin states of a DQD filled with two charges around a charge transition. (f) Evolution of the quantum capacitance with the detuning. The two blue curves correspond to the quantum capacitance when the the system is in a singlet state. The pink curve corresponds to the quantum capacitance when the system is in a triplet state.

$$I_G = \frac{d(Q_1 + Q_2)}{dt} = \left[C_{\text{geom}} - e^2 \alpha^2 \frac{d\langle N_2 \rangle}{d\epsilon} \right] \times \frac{dV_G}{dt} \quad (2.5)$$

The average electron or hole occupation probability is defined in Formula 2.6 as the average number of carriers in the ground state $\langle N_2^- \rangle$ and the excited state $\langle N_2^+ \rangle$ weighted by the probability of being in the corresponding state P_{\pm} . We can define $\chi = P^- - P^+$ as the polarisation of the system and develop $\langle N_2^{\pm} \rangle = (1 \pm \epsilon/\Delta E)/2$ (see [Gonzalez-Zalba et al. 2016]). Here $\Delta E = E_+ - E_-$ is the energy difference between the excited and the ground states and ϵ is the energy detuning.

$$\langle N_2 \rangle = \langle N_2^- \rangle P^- + \langle N_2^+ \rangle P^+ = \frac{1}{2} \left[1 + \frac{\epsilon}{\Delta E} \chi \right] \quad (2.6)$$

The derivative of $\langle N_2 \rangle$ with respect to ϵ can be found in Formula 2.7. We see the appearance of two terms, one corresponding to the curvature of the energy levels with respect to the detuning, the other resulting from inelastic tunnelling processes.

$$\frac{d\langle N_2 \rangle}{d\epsilon} = \frac{1}{2} \left[\frac{\partial^2 E_-}{\partial^2 \epsilon} \chi + \frac{\epsilon}{\Delta E} \frac{\partial \chi}{\partial \epsilon} \right] \quad (2.7)$$

The term resulting from the curvature of the energy levels with the detuning is associated with the quantum capacitance C_Q which represents the electron or hole compressibility at zero temperature. Its expression can be found in Formula 2.8. By inserting the eigenenergies of the system $E_{\pm} = \pm(\sqrt{\epsilon^2 + t_c^2})/2$, we can rewrite the quantum capacitance as a function of the tunnel coupling rate of the energy levels t_c , the energy level spacing at zero detuning ΔE_0 and the polarisation at equilibrium χ^0 .

$$C_Q = \frac{e^2 \alpha^2}{2} \frac{\partial^2 E_-}{\partial^2 \epsilon} \chi = \frac{e^2 \alpha^2}{2} \frac{t_c^2}{\Delta E_0^3} \chi^0 \quad (2.8)$$

Application to a DQD occupied with two charges

Let's first consider the charge states of a double quantum dot occupied with two charges. The accessible energy levels are the singlet S(2,0) or the singlet S(1,1). Around a charge transition, these energy states hybridise resulting in a avoided anticrossing as schematized in Figure 2.4 (c). As a consequence, the energy levels present a certain curvature with the detuning and so the quantum capacitance will be non-zero around the charge transition as shown in Figure 2.4 (d).

If we add to consideration the spin, the possible states for the charge configuration (1,1) are remembered in Formula 2.9. The corresponding energy diagram can be found in Figure 2.4 (e). There we observe that the triplet states do not show any curvature with detuning. Consequently, when the system is in a triplet state, the quantum capacitance will be zero whatever the detuning, as illustrated in 2.4 (d). In this way it is possible to access the spin states of the system by reading the quantum capacitance. This is possible because of the strong coupling between the spin and the orbital states, since we are not directly probing the spin but spin-dependent orbital states.

$$\left\{ \begin{array}{l} S(1, 1) = \frac{1}{\sqrt{2}}(|\downarrow\uparrow\rangle - |\uparrow\downarrow\rangle) \\ T_-(1, 1) = |\downarrow\downarrow\rangle \\ T_0(1, 1) = \frac{1}{\sqrt{2}}(|\downarrow\uparrow\rangle + |\uparrow\downarrow\rangle) \\ T_+(1, 1) = |\uparrow\uparrow\rangle \end{array} \right. \quad (2.9)$$

2.2.2 Dispersive response

To measure the quantum capacitance of a DQD, we connect a resonant circuit to one of the gates under which the DQD is formed. The circuit contains a resonator designed so that its resonant frequency shifts as much as possible when the quantum capacitance of the device varies. By exciting the resonator near its resonant frequency, a dispersive shift in the amplitude or phase of the signal can be measured. The frequency response of the resonator is studied in either a reflectometry configuration or a transmission configuration (see above). The reflectometry setup

is the most common in the literature, with typical resonator frequencies around a few 100MHz. To work at higher frequencies, it seems more relevant to use a transmission configuration. It allows to get rid of the directional coupler whose bandwidth is very limited, especially for frequencies of a few GHz.

Either the amplitude or the phase of the reflected or transmitted signal can be used to probe the stability diagram of quantum dot devices. The amplitude will be preferred for the study of dot-lead transitions as it affects the device admittance. For the detection of interdot charge transitions, we will generally focus on the phase shifts induced by the parametric capacitance. Figure 2.2 shows the phase derivative as a function of the resonant frequency. We observe a maximum at the resonant frequency, which means that the dispersive shift induced by the parametric capacitance is maximum when the readout circuit is operated close to its resonant frequency. The dispersive shift of the resonant frequency with the quantum capacitance can be calculated using Formula 2.10. The induced phase shift [West et al. 2019] is given by the Formula 2.11, where Q is the total quality factor of the resonance.

$$\Delta f = f_q - f_0 = \frac{1}{2\pi} \frac{1}{\sqrt{L(C + C_Q)}} - \frac{1}{2\pi} \frac{1}{\sqrt{LC}} \quad (2.10)$$

$$\Delta\Phi = -2Q \frac{C_Q}{C} \quad (2.11)$$

To maximise the phase signal, we need the sum of all the capacitances composing the circuit C to be as small as possible. We also need the quality factor Q of the circuit to be as large as possible. We are therefore interested in resonators with a high quality factor and a low self-capacitance. For this purpose, it is interesting to work with superconducting resonators, where the absence of resistance helps to achieve very high quality factors. In terms of design, the use of coil inductors or $\lambda/2$ -resonators is generally favoured, as they can have very low self-capacitance for quite large inductance.

2.2.3 Resonators

Among the many developments in gate-based dispersive sensing, three recent achievements involving different types of resonators can be highlighted:

- **Surface mount inductors** : M. Urdampilleta and co-workers [Urdampilleta et al. 2019] showed electron spin readout fidelity of 99% in 1 ms on Si nanowire devices from CEA Leti². In this respect, they implemented a reflectometry setup based on a LC resonator composed by a surface mounted inductor soldered on the PCB ($L = 820$ nH) and its parasitic capacitance to ground ($C_p = 0.75$ pF). They obtained a resonant frequency $f_0 = 234$ MHz and an overall quality factor $Q \approx 50$.

2. These devices are N-types, similar to the P-types used in this PhD project.

- **On-chip superconducting resonator** : G. Zheng and co-workers [Zheng et al. 2019] showed the single-shot readout of a two-electron spin state with a fidelity better than 98 % in 6 μs . Their LC circuit consists of an NbTiN high-impedance $\lambda/2$ -resonator, capacitively coupled to a 50 Ω -feedline probed in transmission. The resonator is galvanically connected to the two gates under which the double quantum dot is formed. The resonant frequency is $f_0 = 5.71$ GHz and the total quality factor is $Q \approx 2600$.
- **Separate-chip superconducting inductors** : D. Ibberson and co-workers [Ibberson et al. 2021] measured a dispersive shift on the order of the resonator linewidth, resulting from the large coupling between a Si nanowire device and a superconducting coil inductor ($g_0/2\pi = 204$ MHz). For this purpose, they fabricated on a separate chip an NbN coil inductor coupled to a 50 Ω -microstrip probed by reflectometry. The coil inductor is bonded to one of the device gates. It has an inductance of $L = 47$ nH and a parasitic capacitance to ground of $C_p = 0.15$ pF, giving a resonant frequency of $f_0 = 1.88$ GHz and an overall quality factor of $Q \approx 600$.

2.3 Choice of the readout method

Depending on the geometry of the devices, one or the other readout method will be preferred. The silicon nanowire devices described in Part 1.3 are particularly suited to the implementation of a dispersive readout circuit. In such structures, the large wrapping of the gates around the channels together with the limited cross-capacitances between the gates make the gates lever-arms remarkably large³. As a consequence, the gates are very sensitive to any capacitive change in the channels below, which should allow dispersive detection of small quantum capacitances. In Chapter 3, we will present the implementation of a dispersive circuit for the readout of our Si nanowire devices. We will describe in detail the fabrication of superconducting coil inductors, which are designed to have small parasitic capacitances and large quality factors to increase the dispersive shifts.

The geometry of the germanium heterostructure devices described in Part 1.2.1 results in small gate lever-arms⁴, due to the large cross-capacitances between the numerous gates and the considerable distance between the gates and the 2D hole gases where the quantum dots are formed. As a consequence, the readout of small quantum capacitances would be difficult and the implementation of a gate-based sensing is not suitable. Hence, we will prefer a charge sensing method using a sensing dot integrated near the double quantum dot to probe. The charge sensing of our Ge heterostructure devices is presented in Chapter 4. A particular attention has been paid in order to improve the sensitivity of the radiofrequency readout circuit to the charge state signals.

2.4 Conclusion

In this chapter, we have reviewed two different methods that allow the readout of quantum dot devices. For Si nanowire devices, which benefit from a large wrapping of the gates around the channel, a gate-based readout technique can allow the quantum capacitance to be measured

3. On the order of $\alpha \sim 0.7$ eV/V.

4. On the order of $\alpha \sim 0.15$ eV/V.

and thus access to the qubit states. The choice of the resonator implemented in the readout circuit is particularly important. The use of superconducting inductors, which exhibit low parasitic capacitances and low losses, seems to be the way forward. Gate based sensing can offer fast readout capabilities together with scalability advantages as it does not require the integration of local charge sensors. However, for planar geometries such as the Ge heterostructure devices, gate-based sensing is difficult to apply due to the large cross-capacitance between the gates and the distance between the gates and the 2D hole gas. Charge sensing using a single-hole transistor can then offer competitive sensitivities at the cost of an additional dot on the quantum dot architecture. The integration of the charge sensor within the design needs to be properly studied, as the charge sensitivity will depend on the capacitive coupling between the quantum dot and its sensor. Additional work on the matching between the radiofrequency readout circuit and the charge sensor is required to obtain the best possible signal.

TAKEAWAY MESSAGES:

- For Si nanowire devices, the large wrapping of the gates around the channel allows gate-based sensing.
- The quantum capacitance results from the curvature of the energy levels and allows us to access the spin states of a DQD.
- The quantum capacitance can be sensed using a high-frequency readout circuit, either in reflectometry mode or in transmission mode. In this case, the resonant frequency of an LC circuit connected to one of the device gates shifts as the quantum capacitance varies.
- To increase the dispersive shift, we must increase the quality factor of the resonator and reduce its parasitic capacitance. For this purpose, we can use superconducting inductors as LC circuits.
- For Ge heterostructure devices, gate-based sensing is not adapted and can be replaced by the use of a single-hole transistor as a local charge sensor.
- The integration of a charge sensor into the quantum dot architecture must be such that the capacitive coupling between the sensor and the dot to be sensed is maximised.
- The use of tunable barriers is a real advantage for charge sensing, as tunnelling times must be shorter than measurement times.
- The use of a suitable matching capacitor to match the radiofrequency readout circuit to the charge sensor allows better performance to be achieved.

SUPERCONDUCTING INDUCTORS FOR DISPERSIVE READOUT OF SI QUANTUM DOTS

Contents

3.1	Design of superconducting inductors	44
3.1.1	Lumped-element resonators	44
3.1.2	Microstrip design	47
3.1.3	Finite-element simulations	48
3.2	Niobium nitride superconducting films	52
3.2.1	Niobium nitride sputtering	52
3.2.2	Film properties	53
3.2.3	Magnetic field resilience	55
3.2.4	Crystallographic structure and phases	58
3.3	Fabrication of niobium nitride inductors	61
3.3.1	Fabrication recipe	61
3.3.2	Result of the different batches	63
3.3.3	Inductors properties	64
3.4	Dispersive readout of charges confined in silicon nanowires	65
3.4.1	Experimental setup	65
3.4.2	Tank circuit characteristics	69
3.4.3	Dispersive charge readout	73
3.5	Conclusion	77

Ascent of Aiguille Purtscheller by the S ridge, with M. Lorcery

Mont-Blanc massif, Switzerland - June 18th 2022



By coupling a resonator to a Si nanowire quantum dot device, it is possible to dispersively read the parametric capacitance. This technique, reviewed in detail in Chapter 2.2, requires the use of low loss resonators capable of detecting capacitive changes. For this purpose, superconducting coil inductors are good candidates, benefiting from many advantages described in this Chapter. Notably, it has been shown that coupling several coil inductors to a 50Ω -microstrip allow to simultaneously readout different devices using a single transmission setup. Here, we discuss the realisation of superconducting coil inductors embedded in microstrip designs for the dispersive readout of Si nanowire quantum dot devices. We first discuss the geometry and the design of such resonators, based on electromagnetic simulations. Then we motivate the choice of the superconducting material, which fell on niobium nitride, and explain the sputtering process allowing for the growth of NbN thin films. In a third part, we detail the fabrication recipe of the resonators and comment on the results obtained gradually with the different batches. Finally, we describe the experimental setup used for the measurement of coil inductors coupled to Si nanowire devices, and show the measurement results.

3.1 Design of superconducting inductors

In this Part, we mainly focus on the design of superconducting coil inductors embedded in microstrip designs. We introduce the physical quantities describing the resonant circuits such as the resonant frequency, the impedance and the quality factors. We study the evolution of these quantities with different design parameters using finite element simulations.

3.1.1 Lumped-element resonators

The lumped-element model proposes to describe a circuit with ideal electrical components such as resistors R , inductors L and capacitors C joined by a network of perfectly conducting wires. This model can be applied for the condition $L_c \ll \lambda$, where L_c is the characteristic length of the circuit and λ is the operating wavelength of the circuit. Thus, the more a circuit is operated at high frequency, the smaller it must be to maintain lumped element behaviour. If the circuit size compares or exceeds the wavelength, then we must use the distributed element model described by Maxwell's equations.

RLC circuits

The simplest lumped-element description that can be made of a resonant circuit close to resonance is to model it using a series or parallel RLC circuit. In such circuit, the electromagnetic energy oscillates between its electric form, represented by the charging of a capacitor C , and its magnetic form, represented by the current flowing through an inductor L . These oscillations may have losses, represented by a resistor R . Such an RLC circuit has the ability to resonate at a certain frequency when the impedance of the inductor matches the impedance of the capacitor. The resonant frequency is expressed in Formula 3.1.

$$f_0 = \frac{1}{2\pi\sqrt{LC}} \quad (3.1)$$

The quality factor Q of a resonator is the ratio between the initial energy stored in the resonator and the energy lost in one radian of one oscillation cycle. A high quality factor is therefore an indication of low energy loss. The quality factor can be expressed as the ratio between the resonant frequency f_0 , and the bandwidth Δf describing the range of frequencies for which the oscillator resonates (see Formula 3.2). Thereby, a high quality factor also indicated an higher selectivity around the resonant frequency. This can be an advantage for many applications such as the detection of small frequency shifts.

$$Q = \frac{f_0}{\Delta f} \quad (3.2)$$

For a RLC series circuit, the impedance $Z(f)$ and the impedance at resonance Z_0 are given in Formula 3.3.

$$\begin{cases} Z(f) = R + 2i\pi fL + \frac{1}{2i\pi fC} \\ Z_0 = R \end{cases} \quad (3.3)$$

Superconducting coil inductors

Superconducting coil inductors can be described with a lumped-element model if their dimensions are small enough. They have the particularity to be non-resistive and their capacitance can be small and controlled by design. Their main capacitance to ground C_p arises from the capacitance between the surface of the pads and the metallic backplane that is grounded. This is generally very small and can be as low as 0.1 pF per pad. The cross-capacitance of the coil conductor between its different turns and the capacitance of the conductor to the ground plane are generally neglected. The inductance of the coil can be easily tuned by design and mainly determines the resonant frequency and the impedance of the resonator. It has two different origins:

- The geometric inductance, which is the same regardless of the metal used. This inductance results from the Ampere's law which states that a current flowing in a conductor creates a circular magnetic field around the conductor. When using a coil inductor, the magnetic fields generated separately by the different turns of the coil all pass through the centre of the coil and overlap, producing a stronger field. Therefore, the geometric inductance increases with the number of turns the coil have. It can further vary with other design parameters such as the ratio of the conductor width to the spacing.
- The kinetic inductance, that is proper to the material used. This physical quantity, comparable to an inductance, takes into account the inertia of charge carriers in the high-frequency transport of electric current [Watanabe et al. 1994]. If it is negligible compared to the Joule effect in normal conductors, this is not the case for superconducting materials. It is particularly marked for thin films of disordered type-II superconductors such as NbN, and increases with thinner films [Kamlapure, T. Das, et al. 2013].

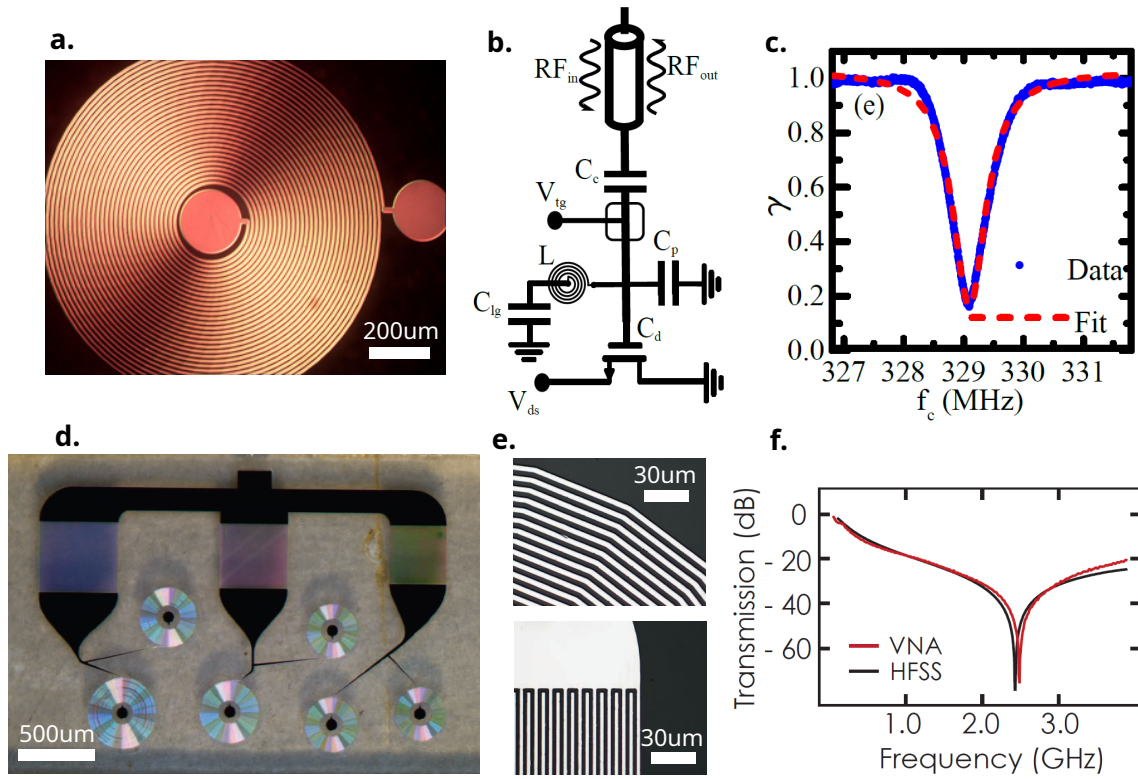


Figure 3.1 – **Coil inductors used in reflectometry setups.** Figure adapted from I. Ahmed [Ahmed et al. 2018] and J. Hornibrook [Hornibrook et al. 2014]. (a) Optical image of an NbN coil inductor. Both the conductor width and spacing is $8\ \mu\text{m}$. (b) Circuit diagram of the reflectometry setup used to read the inductor. This last is bonded to the top-gate of a Si nanowire field-effect transistor on one side, and to a DC entry on the other side. (c) Amplitude γ of the reflection coefficient as a function of the frequency. (d) Optical image of a multiplexing chip including several coil inductors and interdigitated capacitors made of Nb on sapphire. Three inductors are connected to GaAs double quantum dot devices, while the other three couples of L and C are used to bias the devices. (e) Optical images zoomed on the features composing the inductors and the capacitors. (f) Measured transmission through the bias tee components, as a function of the frequency.

Because of their sensitivity to small capacitive changes, superconducting coil inductors have been proposed to measure the parametric capacitance of semiconductor double quantum dot devices, whose origin is discussed in Part 2.1.1. J. Hornibrook [Hornibrook et al. 2014] designed the multiplexing circuit presented in Figure 3.1 (d) (e) and (f), in order to probe a GaAs double quantum dot device. He bonded the coil inductors either to a gate to perform dispersive sensing, or to a quantum point contact (QPC) to perform charge sensing. To bias the gates and the QPCs, he integrated on-chip bias-tees consisting of a coil inductor and an interdigitated capacitor. I. Ahmed [Ahmed et al. 2018] also proposed to use superconducting inductors on a reflectometry setup, in order to dispersively probe the parametric capacitance of Si nanowire field-effect transistors. With the setup presented in Figure 3.1 (a) (b) and (c), he achieved a charge sensitivity of $1.3\ \mu\text{e}/\sqrt{\text{Hz}}$. In the light of these two research works, superconducting coil inductors appeared to be good candidates for the dispersive readout of our Si nanowire quantum dot devices. By modifying the design of the coil inductors, it is possible to reach frequencies ranging from a few tens of megahertz to several gigahertz. This would allow us to explore a wide range of tunnel couplings between QDs.

3.1.2 Microstrip design

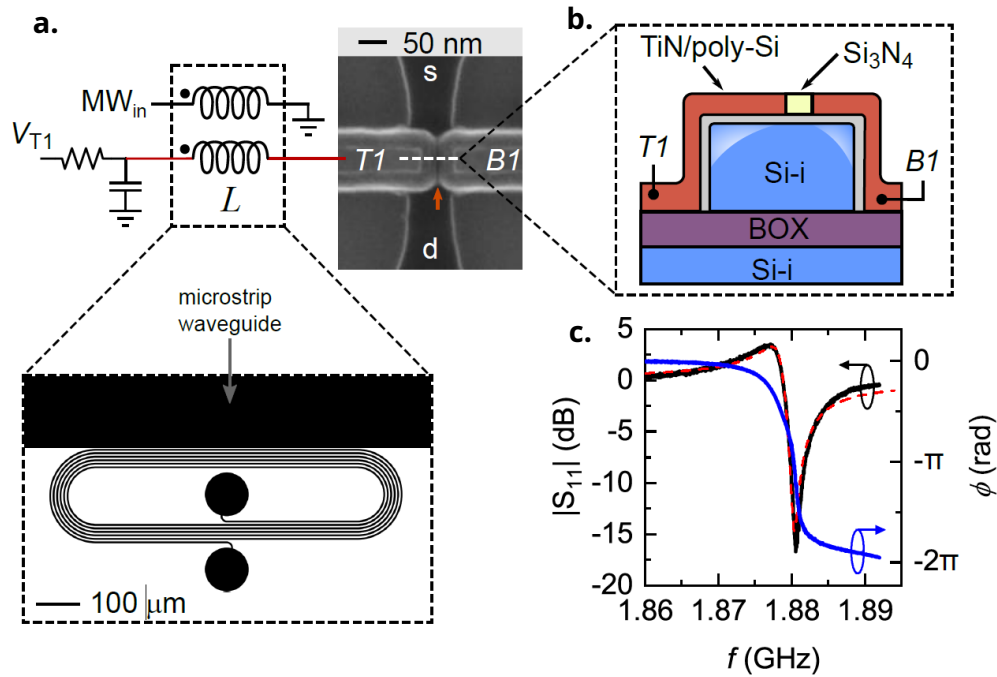


Figure 3.2 – **Coil inductors coupled to a microstrip.** Figure taken from D. Ibberson [Ibberson et al. 2021]. (a) Schematic representation of a coil inductor coupled to a 50Ω-microstrip. The microstrip is read by reflectometry, which explains why one side of the microstrip is bonded to ground. The coil inductor is bonded to a Si nanowire device on one side, and to a DC entry through a bias-tee on the other side. (b) Cross-section schematic of the split-gate Si nanowire device. (c) Reflected signal as a function of the frequency in amplitude (black) and phase (blue).

D. Ibberson proposed to couple superconducting coil inductors to a 50Ω-microstrip¹, as shown in Figure 3.2. The RF-signal is then sent through the microstrip while allowing to probe the coil inductors thanks to the presence of a capacitive and inductive coupling. This design enables the readout of several coil inductors with a single reflectometry setup. Taking up this idea, we could imagine to use a 50Ω-microstrip line to probe several coil inductors in transmission, getting rid of the limited bandwidth of the directional couplers and/or circulators used in reflectometry setups.

In the geometry proposed by D. Ibberson, the coupling between the microstrip and the inductors is partly capacitive, partly inductive. Indeed, the presence of a metallic body close to the microstrip modifies the trajectory of the electric and magnetic field lines as illustrated Figure 3.3. In the case of an inductor not loaded, simulations reveal that the capacitive coupling generally dominates over the inductive coupling. Thus, the coupling can be represented by a capacitor as in Figure 3.3 (e). If the inductor is loaded on both sides, a non-zero current can flow through the entire circuit. As a result, the inductive coupling can take precedence over the capacitive coupling. It can therefore be represented by mutual inductors between the inductance of the microstrip and the inductance of the coil, as shown in Figure 3.3 (f).

1. A metallic ground plane at the back of the resonator sample enables to fix the impedance of the microstrip to 50Ω.

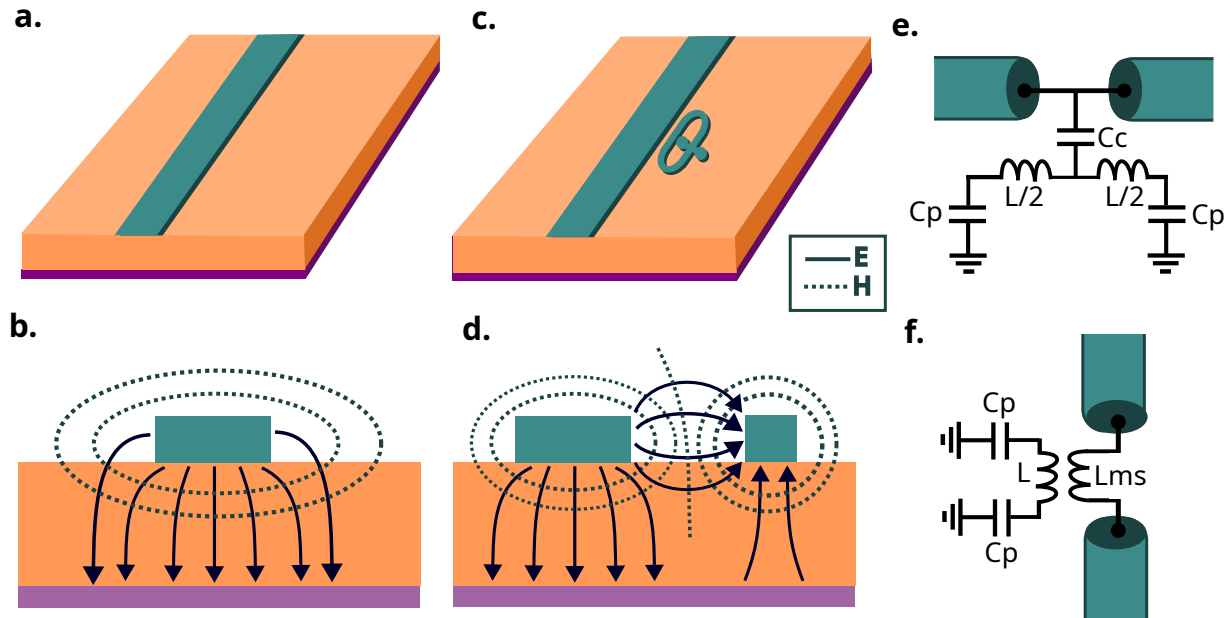


Figure 3.3 – **Microstrip geometry.** (a) Schematic representation of a microstrip design. The microstrip is drawn in green, the substrate in orange and the ground plane in purple. (b) Planar section of the microstrip design in (a) and representation of the electric and magnetic field lines. (c) Schematic representation of an inductor coupled to the microstrip line. (d) Planar section of (c) and field lines. (e) Equivalent schematic of (c), considering that the coupling between the microstrip and the inductor is capacitive. (f) The same, considering an inductive coupling.

3.1.3 Finite-element simulations

Sonnet simulations

The software Sonnet² enables to compute the S-parameters, Z-parameters or Y-parameters of microwave circuits. It allows to extract the resonant frequency and the characteristic impedance of resonators, as well as their quality factors. Sonnet can also be used to calculate the different inductances and capacitances of resonators, using series of pi-models. For the simulations, a virtual substrate has to be defined. Figure 3.4 (b) presents the virtual substrate used for the simulations presented in this section. The NbN layer is defined as a lossless metal with a kinetic inductance, whose value is adjusted to the experimental value measured during the film characterisation. As shown Figure 3.4 (a), one RF port is defined at each extremity of the 50 Ω -microstrip, enabling a two-port simulation. Each face of the box surrounding the design is a ground plane. For microstrip simulations, we want the main ground plane to be the substrate backplane. As a consequence, we have to ensure that the other planes are much further away from the design³.

The internal and external quality factors are key parameters to characterise a resonator. The internal quality factor Q_{int} mostly depends on the substrate and fabrication cleanness and gives information about the internal photon losses. The external quality factor Q_{ext} is given by geometry. It gives information on the coupling between the resonator and its feedlines. If its value is too high,

2. Sonnet Software is an electromagnetic simulation tool based on a finite element method.

3. The top plane is typically placed 10cm from the NbN layer.

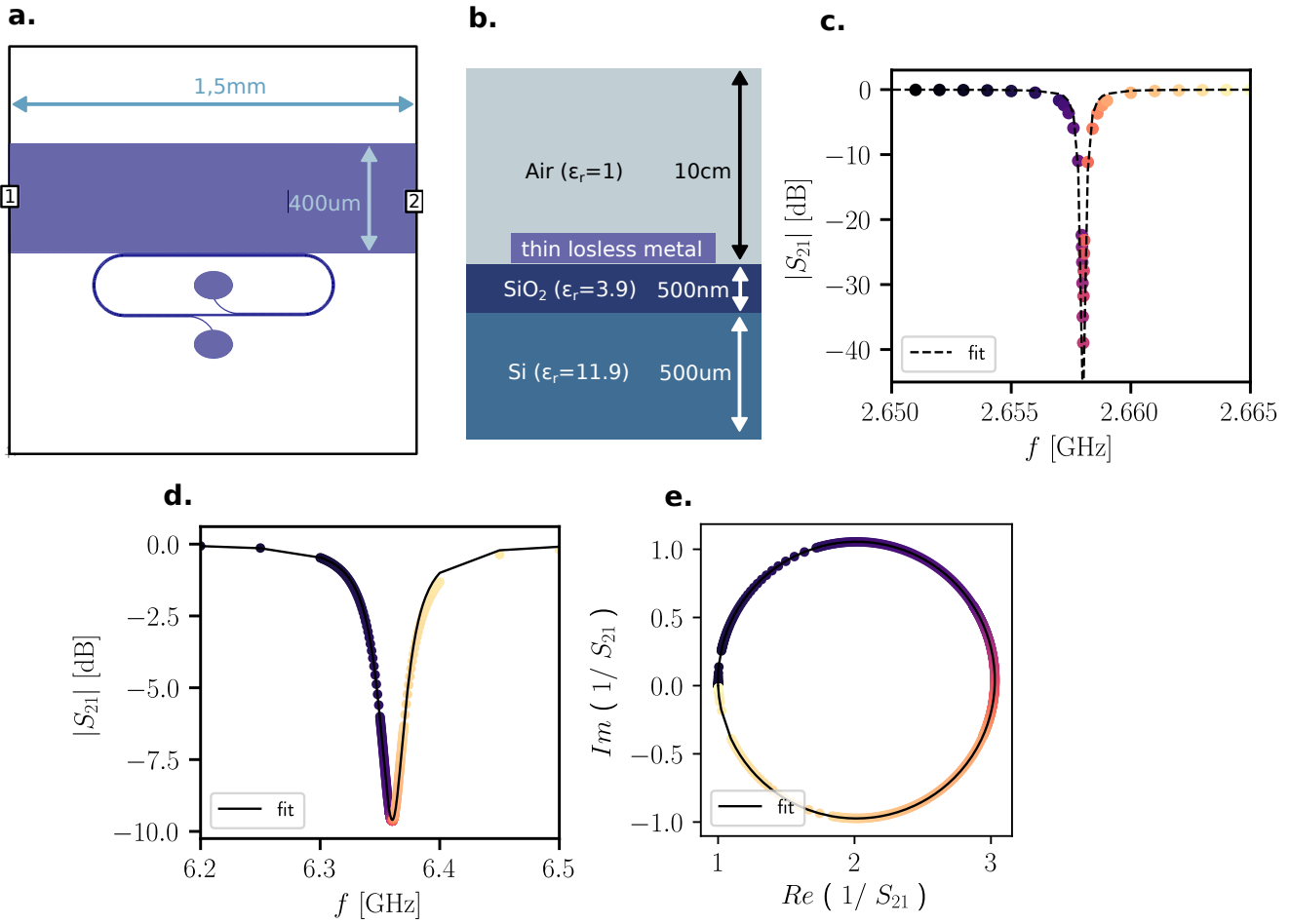


Figure 3.4 – **Finite element simulations using Sonnet.** (a) Typical design of an inductor coupled to a microstrip. Sonnet box size and ports used for the simulations. (b) Virtual substrate defined on Sonnet. (c) Frequency response of a resonator coupled to its microstrip. The scattering parameter $|S_{21}|$ gives the power transmitted from Port 1 to Port 2. It is fitted with a Lorentzian giving the total quality factor. For this simulation and by default, Q_{int} tends to infinity resulting in an infinite deep (in the dB scale). (d) Simulation of a similar design with this time Q_{int} set to a finite value. Hence, the deep has a minimum. (e) The same signal plotted in the IQ-plane (the signal is decomposed into in-phase and quadrature components). Fitting the signal in the IQ-plane enables to properly separate the contributions of Q_{int} and Q_{ext} to the total quality factor.

the resonator and its feedlines are not sufficiently coupled to allow fast photon extraction from the resonator to the feedlines for a fast readout. If its value is too low, photons have not the time to interact within the system before leaking to the feedlines. Q_{ext} can be estimated from Sonnet simulations, while the value of Q_{int} will always tend to infinity in the simulations as the material losses are not taken into account. The easiest way to extract Q_{ext} is to fit the S_{21} response given by Sonnet with a Lorentzian model, as shown in Figure 3.4 (c) and (d). As $Q_{\text{int}} \gg Q_{\text{ext}}$, we can assume that $Q_{\text{tot}} \approx Q_{\text{ext}}$. A more precise method, also valid if $Q_{\text{int}} \sim Q_{\text{ext}}$, is to fit the resonance in the IQ-plane [Megrant et al. 2012] using Formula 3.4, as shown in Figure 3.4 (e). This enables to properly separate Q_{int} and Q_{ext} contributions.

$$y = \left(1 + \frac{Q_{\text{int}} e^{j\Phi}}{1 + 2jQ_{\text{int}} \frac{x-f_0}{f_0}} \right)^{-1} \quad (3.4)$$

Simulations results

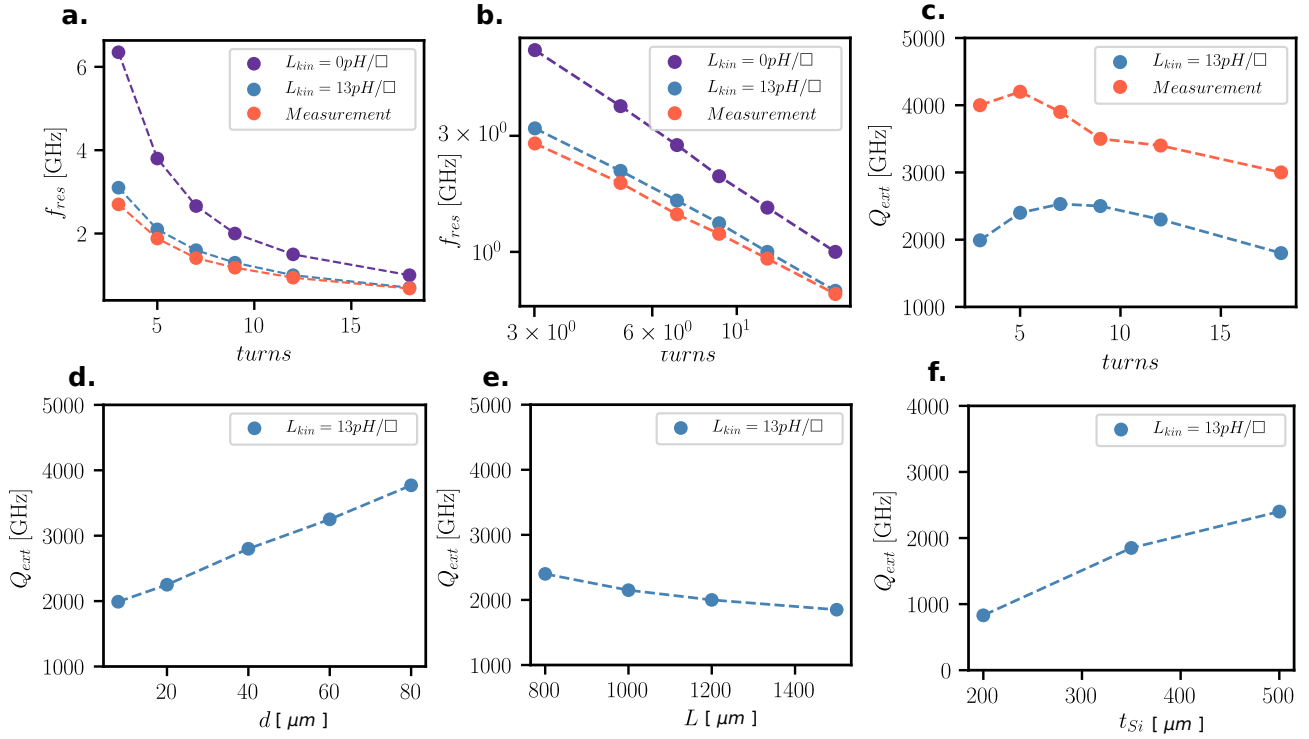


Figure 3.5 – **Simulations results using Sonnet.** (a) Evolution of the resonant frequency with the number of turns the coil have. The orange dots are the points measured experimentally on a NbN film. The purple dots results from Sonnet simulations not taking into account the kinetic inductance of the NbN film. The blue dots are Sonnet simulations obtained with $L_{\text{kin}} = 13 \text{ pH}/\square$. This value of the kinetic inductance has been obtained with a four-probe measurement method detailed below (it is not a fit). (b) The same plot in log-log scale. (c) Evolution of the external quality factor Q_{ext} with the number of turns, simulated (blue dots) and measured (orange dots). (d) Simulated evolution of Q_{ext} with the distance between the bottom of the microstrip and the closest feature of the coil. Q_{ext} increases linearly with the distance. (e) Simulated evolution of Q_{ext} with the total length L of the coil. Q_{ext} decreases while elongating the coil. (f) Simulated evolution of Q_{ext} with the Si substrate thickness. Q_{ext} increases with the substrate thickness. For this simulation, the width of the microstrip is adjusted such that its impedance is maintained at 50Ω while the ground plane is closer.

In order to control the resonant frequency and the external quality factor of resonators by design, we investigated the evolution of f_0 and Q_{ext} with different design parameters. For all simulations, both the conductor width and the spacing are set to $2 \mu\text{m}$ for lithography purposes. Figure 3.5 (a), (b) and (c) present the evolution of f_0 and Q_{ext} with the number of turns a coil has.

It compares the results obtained by simulation with and without taking into account the kinetic inductance of the films, with the results measured experimentally at 4 K in the He probe described later in this Chapter. The resonant frequency increases conversely with the number of turns. It follows a power law of type $f_0 = A \times \text{turns}^k$, as shown in the log-log plot in Figure 3.5 (b). We observe a noteworthy agreement between the measurements and the simulations taking into account the kinetic inductance⁴. In terms of quality factor, we observe variations of Q_{ext} up to 25% when varying the number of turns. However, it does not follow a clear trend. The differences between the measurements and the simulations probably result from an inaccurate modelling of the substrate. In (d), we have simulated the evolution of Q_{ext} with the smallest distance separating the bottom of the microstrip from the top of the coil inductor. Q_{ext} increases linearly with this distance d . We have also studied the evolution of Q_{ext} with the elongation of the coil in (e). We observed a decrease of Q_{ext} with the total length of the coil L . Finally, we looked at Q_{ext} as a function of the Si substrate thickness in (f). We saw an increase of Q_{ext} with the substrate thickness t_{Si} . All these simulations helped us to better understand how to get any $[f_0, Q_{\text{ext}}]$ couple we want by design.

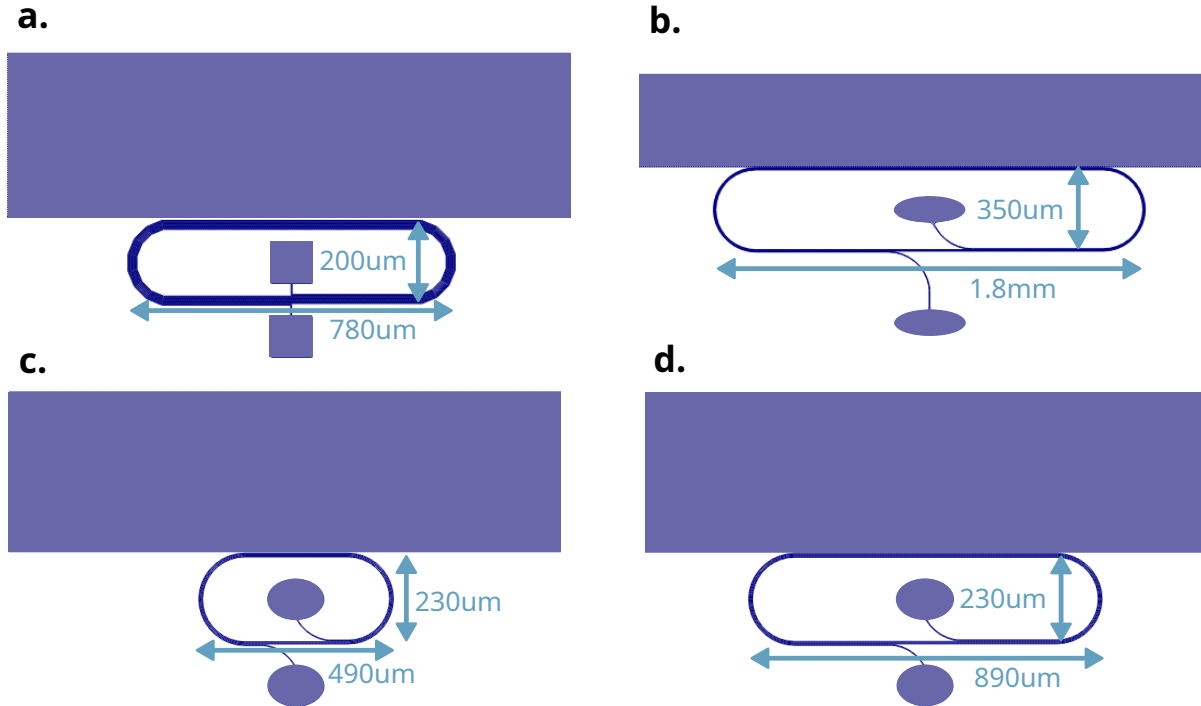


Figure 3.6 – **Evolution of the inductors design with the different batches.** (a) Very first inductor design. (b) Larger size inductors, offering lower values of Q_{ext} . (c) Final design showing large Q_{ext} and large f_0 . (d) Same design with more elongation, allowing for lower Q_{ext} and lower f_0 .

Figure 3.6 shows the evolution of the inductors design within the different batches we produced during this PhD work. For the first designs, presented in (a), the pads were squared shape and the turns of the inductors were drawn from polygons with few bezels. We characterised these inductors unloaded, and we noticed that Q_{ext} was particularly high. To reduce it and to facilitate

4. The remaining difference is due to a rough estimation of the kinetic inductance because the four-probe measurement was done on a sample with a few squares.

the microbonding of the inner pad, we opted for larger inductors as shown in (b). We have also rounded the pads and the inductors turns, assuming that this would help having a better distribution of the electromagnetic field⁵. By coupling the inductors shown in (b) with bias-tees and quantum dot devices on both sides, we noticed a sharp reduction of Q_{ext} , which eventually became too small. We finally found a compromise allowing for reasonably easy microbonding and values of Q_{ext} of a few hundred once the inductor is loaded. Designs shown in (c) and (d) were retained, (c) offering a higher resonant frequency and a larger Q_{ext} than (d).

3.2 Niobium nitride superconducting films

Niobium nitride films are used in our group for years for photonic applications, such as single-photon detection [Sam-Giao et al. 2014] or superconductor-semiconductor Josephson junctions [Grimm et al. 2017]. More recently, the sputtering of NbN films has been developed for the realisation of high-kinetic superconducting inductors integrated on the same chip as silicon nanowires [C. Yu 2022]. These inductors are patterned on 10nm-thick NbN films directly sputtered onto processed SOI wafers. For the realisation of superconducting resonators dedicated to the readout, we chose NbN as well for three main reasons :

- The critical temperature of bulk NbN is around 16 K. For 100nm-thick layers, it remains well above 10 K which allows the characterisation of the films at 4 K in liquid helium.
- The high kinetic inductance of NbN films helps designing high inductance and high characteristic impedance resonators working at a few GHz.
- The critical field of NbN is very high, giving NbN good resilience to magnetic fields. This is a prerequisite for working with spins, as a finite magnetic field of the order of a few hundred mT has to be applied to produce the Zeeman splitting of the energy levels.

3.2.1 Niobium nitride sputtering

In this Section, we detail the sputtering of 50nm-thick and 100nm-thick NbN films on 4" wafers, made from 400 ± 80 nm thermally grown SiO_2 on top of 525 ± 25 μm of p-type silicon. The films are sputtered on a low pressure confocal sputtering machine⁶. First, the surface of the SiO_2/Si wafer is cleaned thanks to a soft 30s argon milling. To grow the NbN, a pure niobium target is bombarded with energetic ions from an argon plasma. An additional nitrogen gas flow transforms the surface of the Nb target into a nitride state. The duration of the target exposure depends on the thickness desired and on the deposition rate. The latter has been evaluated to be in the order of 0.9 nm/s for the set of deposition parameters presented below.

The various sputtering parameters such as the Ar and N_2 flow rates, the target current or the substrate temperature have been optimised by F. Gustavo and C. Yu [Cécile X. Yu et al. 2023]. For this purpose, they measured the variations of the critical temperature T_c when varying the

5. We did not perform simulations to confirm this hypothesis.

6. Plassys MP600S

growth parameters, as for thin films the closer this critical temperature is to the bulk T_c , the better the quality. They first studied the influence of the target current and Ar and N_2 flow rates by measuring the T_c of 50nm-thick films for different sets of parameters. They measured variations from $T_c = 9.5$ K up to $T_c = 11.8$ K. Secondly, they studied the variations of T_c of 10nm-thick films, and obtained T_c varying from 5.6 K up to 10.5 K when changing the substrate temperature from room temperature up to 275 K.

The final set of parameters used for the NbN film deposition is presented Figure 3.1. Between the 50nm-thick and 100nm-thick films only the target exposure time varies. We can note that the N_2 flow rate varies during the target exposition following a bell shape. It starts at 42 %, increases up to 45 %, and then decreases back to 42 %.

Thickness	Exposition time	Target current	Chamber pressure	Ar flow rate	N_2 flow rate
50 nm	55 s	2.0 A	10^{-2} mBar	35 sccm	42-45 %
100 nm	110 s	2.0 A	10^{-2} mBar	35 sccm	42-45 %

Table 3.1 – Sputtering parameters

3.2.2 Film properties

PPMS film characterisation

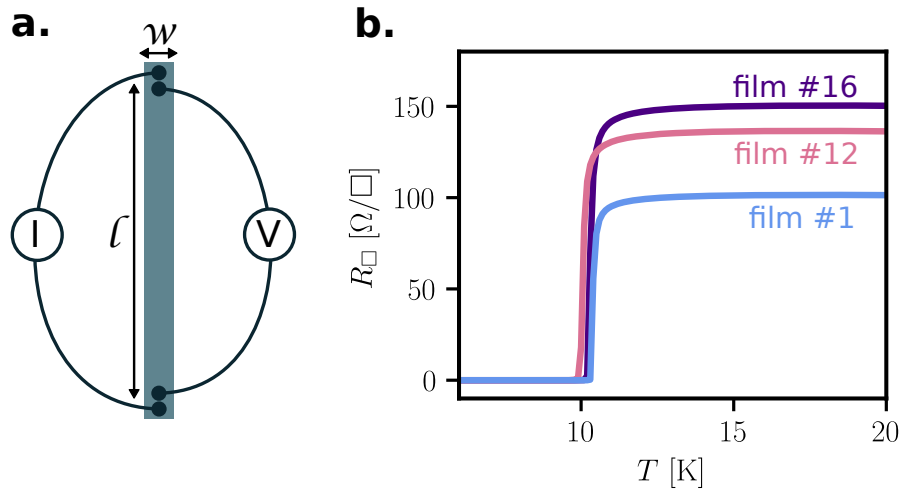


Figure 3.7 – **PPMS measurement of critical temperature and sheet resistivity.** (a) Scheme of the four probe configuration used to measure the film properties with the PPMS. (b) Variation of the film resistivity with temperature, for films #1 #12 and #16. For these three films, the critical temperature T_c is around 10 K. The sheet resistivity is varying from $100 \Omega/\square$ to $150 \Omega/\square$.

We use a physical properties measurement system (PPMS)⁷ to measure the evolution of the film resistivity with the temperature and the magnetic field. From these measurements, it is possible to

7. PPMS from Quantum Design

extract the critical field B_{c2} , the critical temperature T_c and the sheet resistance R_{\square} . These allow for computing the kinetic inductance L_{kin} following the Formula 3.5. To measure the resistivity, a strip of the film is placed on a sample holder and bonded in a four probe configuration, as shown Figure 3.7 (a). It is then inserted in a helium dewar able to go down to 2 K and surrounded by a magnet than can produce an out-of-plane field up to 9 T. At a given temperature, the resistivity of the film suddenly drops to zero. This temperature corresponds to the critical temperature T_c , at which the film becomes superconducting. The film resistivity R before the drop is renormalised as the sheet resistance $R_{\square} = R \frac{l}{w}$.

$$L_{\text{kin}} = \frac{\hbar R_{\square}}{1.76\pi k_B T_c} \quad (3.5)$$

3

Properties of the different films

Table 3.2 summarises the superconducting properties of some NbN films we sputtered using the process described above (#1 to #16), as well as NbN films sputtered by C. Thomas at the CEA Leti (#A to #B). For the films sputtered by us, we observed a certain constancy of the critical temperature $T_c \sim 10$ K and of the sheet resistivity $R_{\square} \sim 100 - 150 \Omega/\square$ with therefore some exceptions. Films #6 and #7 have shown higher T_c which is counterintuitive, as we expect T_c to be larger for 100nm-thick films⁸. Films #9 and #10 have shown higher sheet resistivities resulting in higher kinetic inductances. Finally, film #11 gave a surprising sheet resistivity and we were unable to obtain resonators from it. We evaluated the thickness of three of the NbN films by making a microstrip cross-section cut and observing it under a scanning electron microscope. We reported the values in the table and found that the measured thicknesses were less than the expected thicknesses, especially for #11.

Film	t [nm]	t_{meas} [nm]	T_c [K]	R_{\square} [Ω/\square]	L_{kin} [pH/ \square]	Film tint
#1 (07/2020)	100		10	100	13	cold
#6 (10/2020)	50		12.5	85	9	neutral
#7 (11/2020)	50	50	12.5	70	8	neutral
#9 (01/2021)	50	40	9.5	250	36	cold
#10 (02/2021)	50		10	280	38	cold
#11 (04/2021)	100	65	10.5	1300	168	purple
#12 (07/2021)	100		10	140	19	warm
#13 (09/2021)	100		10	140	19	warm
#14 (11/2021)	100		10.5	120	18	warm
#16 (12/2021)	100		10	150	19	warm
#A (01/2022)	50		12	220	25	warm
#B (03/2022)	100		13.5	100	16	warm

Table 3.2 – NbN films properties

8. As film thickness increases, the superconducting properties are supposed to get closer from bulk ones.

The films #A and #B from CEA Leti shown higher critical temperature and similar sheet resistance than the film we deposited. They were sputtered at a growth temperature of 400° C and a growth rate of 0.2 nm/s on on 300mm-wafers, composed of a 725 μ m-thick highly resistive Si substrate and a 500nm-thick SiO₂ layer. F. Gustavo characterised the superconducting properties of CEA Leti films with various thicknesses, each time taking a sample of 5 films. His results are reported in Table 3.3. We observe a net increase in the critical temperature T_c and critical field $B_{c2}(0)$ between 10nm-thick films and 100nm-thick films [Vasyutin et al. 2016]. For the films we sputtered, we did not measure the evolution of the resistivity with the magnetic field. Therefore, C. Yu characterised a 10nm-thick film sputtered in the same machine using a similar set of parameters [Cécile Xinqing Yu et al. 2021]. She extracted $T_c = 7.4$ K and $B_{c2}(0) = 17.4$ T, as well as a coherence length $\xi(0) = 4.35$ nm. These results are in agreement with those of the CEA Leti films, which nevertheless showed a higher quality. This can be explained by the use of highly resistive substrates together with a semi-industrial sputtering machine allowing for better control of the process.

t [nm]	T_c [K]	$B_{c2}(0)$ [T]	$\xi(0)$ [nm]	Average strain [MPa]
10	9.3	27.4	3.5	/
100	14.3	73.8	2.1	611.5
200	14.6	66.5	2.2	400.8
500	14.7	61.1	2.3	250.0

Table 3.3 – LETI NbN film properties

3.2.3 Magnetic field resilience

For spin qubit experiments, magnetic fields of a few hundred mT are used to lift the degeneracy of the energy levels. Hence, the superconducting resonators that are coupled to the devices have to be resilient to the magnetic field. Several studies have been conducted on the behaviour of thin NbN layers under an external magnetic field [Suzuki et al. 1987]. Among them, A. Kamlapure studied the evolution of the superconducting gap Δ and the penetration depth ξ with film thicknesses varying from 3 nm to 51 nm [Kamlapure, Mondal, et al. 2010]. He shows that increasing the film thickness induces a monotonic increase in T_c and $\Delta(0)$ but a monotonic decrease in ξ . Hence, building resonators on thicker films allows for a higher critical field H_{c2} , but the lower ξ implies that vortices can penetrate even thinner structures.

We have studied the behaviour of a coil inductor made from the 50nm-thick NbN film #8 under an external magnetic field at very low-temperature $T \sim 10$ mK. The results are shown in Figure 3.8. We observe a frequency shift of the order of 1 % for a variation of the in-plane magnetic field of ± 1 T. For out-of-plane fields, it follows a linear trend and the frequency shift is down to 10 % for an applied field of ± 1 T. We also measured the evolution of the internal and external coupling defined as $\kappa_{\text{int}} = 2\pi \frac{f_0}{Q_{\text{int}}}$ and $\kappa_{\text{ext}} = 2\pi \frac{f_0}{Q_{\text{ext}}}$ respectively. We observe that for both in-plane and out-of-plane fields, κ_{ext} varies very little as expected. κ_{int} shows a peak around $B = \pm 0.5$ T, which is the signature of a coupling with magnetic impurities. Using the Formula 3.6, we extracted the Landé g-factor of the magnetic impurities $g \sim 0.1$, which allows us to rule out a coupling with spins. For all results shown Figure 3.8, we did not observe any hysteresis sweeping back and forth

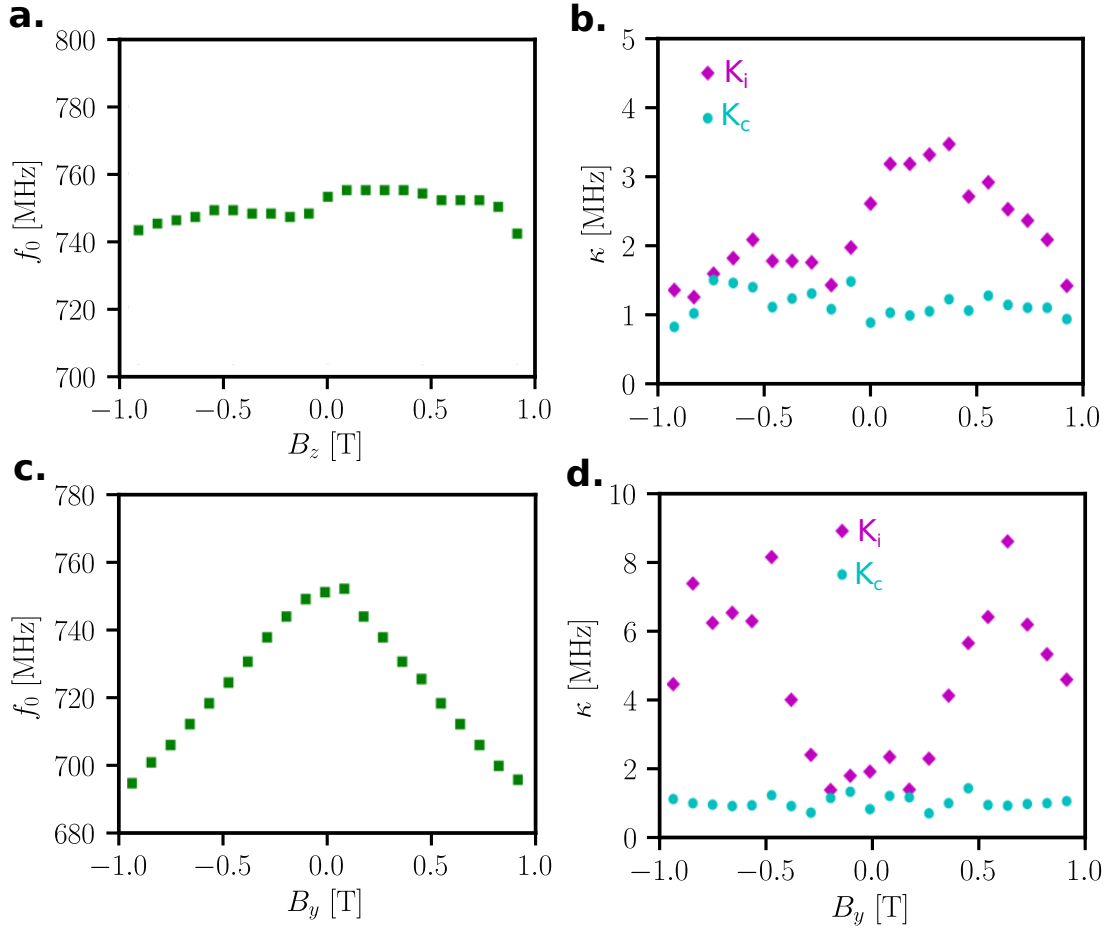


Figure 3.8 – **Resilience of a 50nm-thick NbN film with the magnetic field.** (a) Evolution of the resonant frequency f_0 with the in-plane magnetic field. (b) Evolution of the coupling factors κ_i and κ_c with the in-plane magnetic field. (c) Evolution of the resonant frequency f_0 with the out-of-plane magnetic field. (d) Evolution of the coupling factors κ_i and κ_c with the out-of-plane magnetic field.

the magnetic field.

$$g\mu_B B = \hbar\omega_0 \quad (3.6)$$

Figure 3.9 shows the results of a similar experiment carried out by C. Yu, involving coplanar waveguide resonators from a 10nm-thick NbN layer sputtered in the same machine and under the same conditions as film #8. For three resonators with different characteristic impedances, she observed a good resilience with the in-plane magnetic field up to 6 T. For out-of-plane magnetic fields, she measured a strong decay of the internal quality factor Q_i and the resonant frequency f_0 . Nevertheless, this decay was much less pronounced for the higher impedance resonator with the smaller central conductor width. Indeed, if the conductor width (here 200 nm) is smaller than the London penetration depth the vortices only form in the ground plane, which is less affecting the internal quality factor. Thus, she observed that reducing the conductor width minimises the

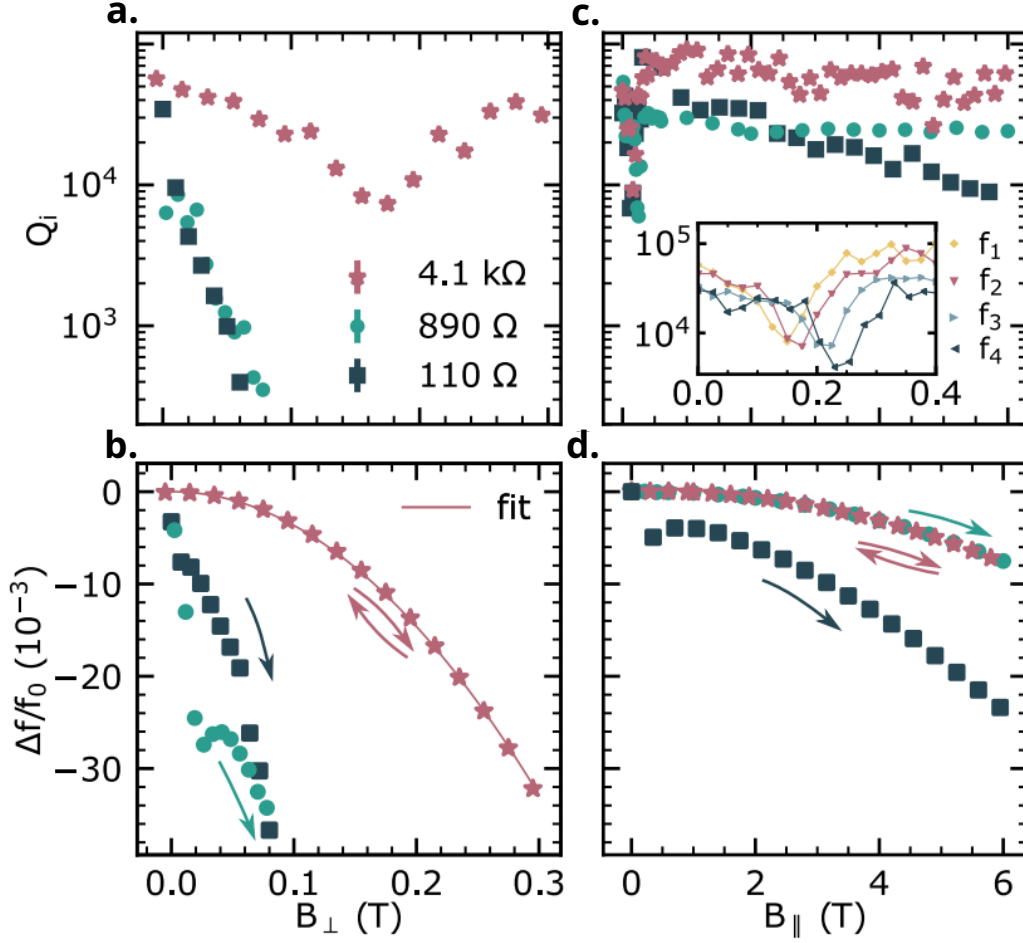


Figure 3.9 – **Resilience of a 10nm-thick NbN film with the magnetic field.** Figure taken from C. Yu [Cécile Xinqing Yu et al. 2021]. (a) Evolution of the internal quality factor Q_i with the out-of-plane magnetic field B_{\perp} , for three resonators with different impedance. (b) Normalised shift of the resonant frequency f_0 while varying B_{\perp} , for the three resonators. (c) Same than (a) for in-plane magnetic field B_{\parallel} . The inset is a zoom around $B_{\parallel} = 200$ mT and concerns four resonators with $Z_c = 4.1$ k Ω . (d) Same than (b) for in-plane magnetic field B_{\parallel} .

vortices creation and dynamics. The inset of Figure 3.9 (c) shows the evolution of Q_i for four 4.1 Ω resonators with different resonant frequencies $f_1 < f_2 < f_3 < f_4$, when sweeping B_{\parallel} around 200 mT. For all four traces, we observe a deep in Q_i signaling a coupling with magnetic impurities. This deep shifts upwards as the resonant frequency of the resonators increases, in agreement with Formula 3.6. The Landé g-factor value extracted from the four traces is $g \sim 2$, corresponding to free electrons.

Both the 50nm-thick film we measured and the 10-nm thick film C. Yu characterised have shown very good resilience with the magnetic field, allowing them to be used in magnetic environments. While the 50nm-thick film benefits from a higher H_{c2} , the 10nm-thick film has a longer penetration depth which prevents the formation of vortices on the condition of designing sufficiently thin conductors. The disorder of the NbN films also plays an important role in the resilience with the magnetic field, as discussed below.

3.2.4 Crystallographic structure and phases

Crystallographic structure of NbN

Niobium nitride is a highly disordered type-II superconductor. Type-II superconductors are used in many applications as they generally benefit from higher T_c than type-I, higher H_{c2} than H_{c1} and possible vortex pinning. It has been demonstrated that the disorder of type-II superconductors increases conversely with the film thickness [Kamlapure, T. Das, et al. 2013]. Accordingly, an increase in the disorder reduces T_c and increases the film resistivity, which has the effect of increasing the film kinetic inductance. The disorder also causes local variations in the superconducting gap [Carbillet et al. 2020], which helps in vortex pinning. Hence, highly disordered films generally show high kinetic inductance and good resilience to the magnetic field.

Depending on its crystalline structure, NbN can have different phases, some of which are superconducting and others normal. The different superconducting phases of NbN are as follows:

- Hexagonal ϵ -phase, with $T_c = 11.6$ K
- Tetragonal λ -phase, with $T_c = 12-15$ K
- Cubic δ -phase, with $T_c \leq 17.3$ K

The normal phases of NbN are :

- Hexagonal δ' -phase (NbN)
- Hexagonal β -phase (Nb₂N)
- Higher order nitride phases (Nb₄N₅, ...)

Several phases can coexist in a thin film of NbN. X-ray diffraction methods allow the precise quantification of the phases that make up a film. Nevertheless, the colour of the film can give a first indication of the phases that are present. The warmer the colour of a film (golden reflections), the more cubic or tetragonal phases it contains. If the colour is cold (bluish-grey), it will be composed mainly of hexagonal phases. We can therefore conclude that a golden tint is a sign of a good superconducting film with high T_c . For ultrathin films, it is important to keep in mind that the colour may also depend on the tint of the substrate underneath.

Dependence on the sputtering parameters

The work of S. Leith [Leith et al. 2021] reveals that the phases composing a film strongly depend on its sputtering parameters. He performed X-ray diffraction on several films obtained by varying the nitrogen percentage or the pressure inside the sputtering chamber. The results for varying the nitrogen percentage are presented in Figure 3.10. In (a) and (b), we clearly observe a change in the grain structure between two films, sputtered with 8 % and 18 % of nitrogen. Further quantitative studies show how the crystallite size and the lattice parameters are actually impacted by the nitrogen percentage. In (c), we observe that the critical temperature T_c and the first entry field H_{en} also vary with this sputtering parameter. The X-rays diffraction patterns in (d) show that the films sputtered with 6 % and 10 % of nitrogen have a majority of cubic δ -phase, which is

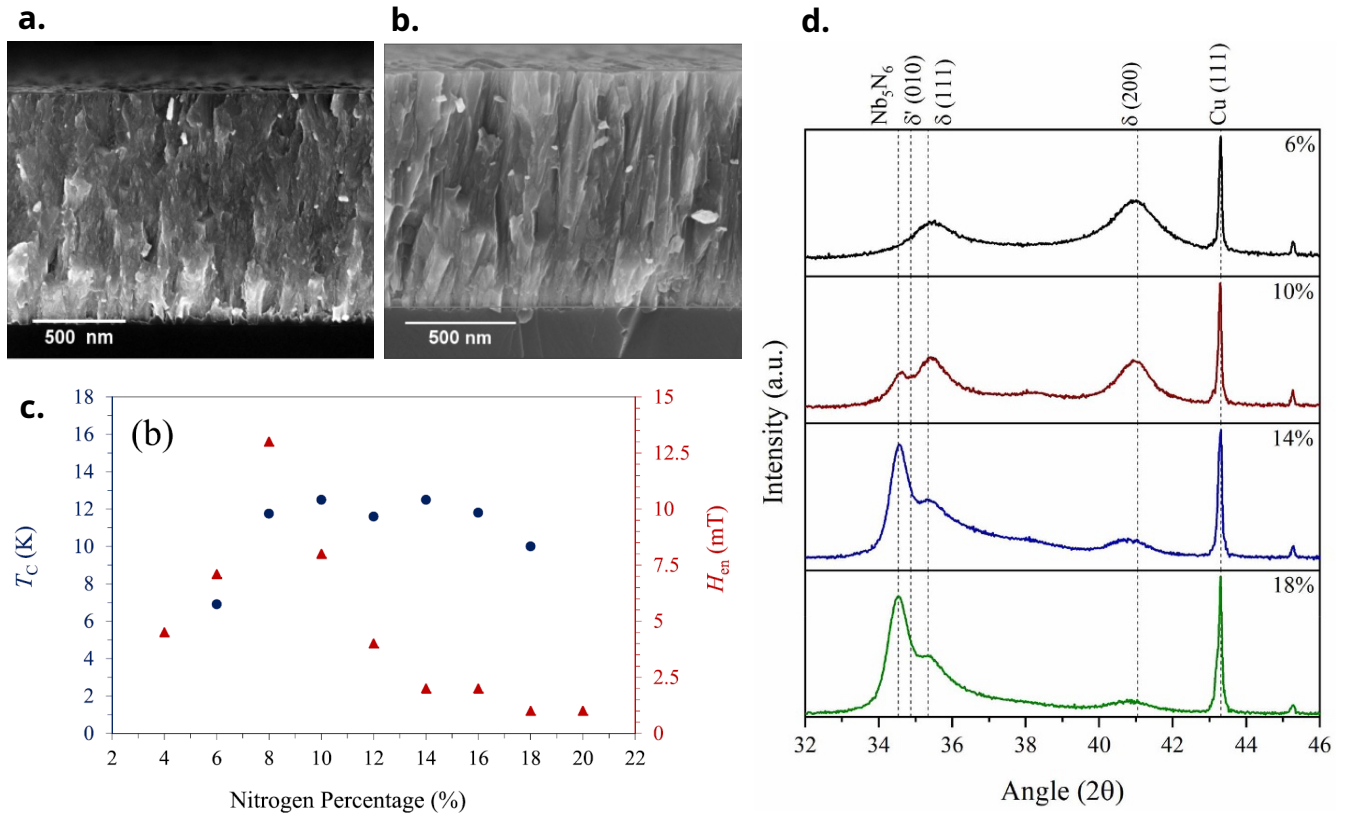


Figure 3.10 – **Evolution of the film phases with the nitrogen percentage.** Figure adapted from S. Leith [Leith et al. 2021]. (a) SEM image of the cross-section of a NbN film sputtered with 8% of N₂. (b) The same for a film sputtered with 18% of N₂. (c) Evolution of T_c and the entry field H_{en} with the nitrogen percentage. (d) X-rays diffraction patterns for different nitrogen percentage.

the superconducting phase with the highest T_c . On the contrary, the films sputtered with 14% and 18% of N₂ have a majority of Nb₅N₆ normal phase and may not have superconducting behaviour. Similar observations have been made by varying the chamber pressure, resulting in films with a majority of superconducting phases or a majority of normal phases.

H. Shao [Shao et al. 2017] studied the evolution of the crystalline orientation of the δ -phase when increasing the sputtering time and so the film thickness, keeping all other parameters constant. He found out that the intensity of the δ -phase (200)-oriented peak increased with the sputtering time, while the intensity of the δ -phase (111)-oriented peak varied randomly. He observed a correlation between the intrinsic stress of the films and the ratio of (200)-oriented and (111)-oriented δ -phase. Looking further at the grain distribution, he concluded that the change of orientation of the δ -phase with the deposition time is due to an anisotropy of both the stress and the grain distribution. Hence, the phases present on a film are influenced by both sputtering time and the sputtering parameters (N₂ percentage, chamber pressure, temperature, ...), which makes NbN film sputtering a key step in the fabrication process of the superconducting resonators.

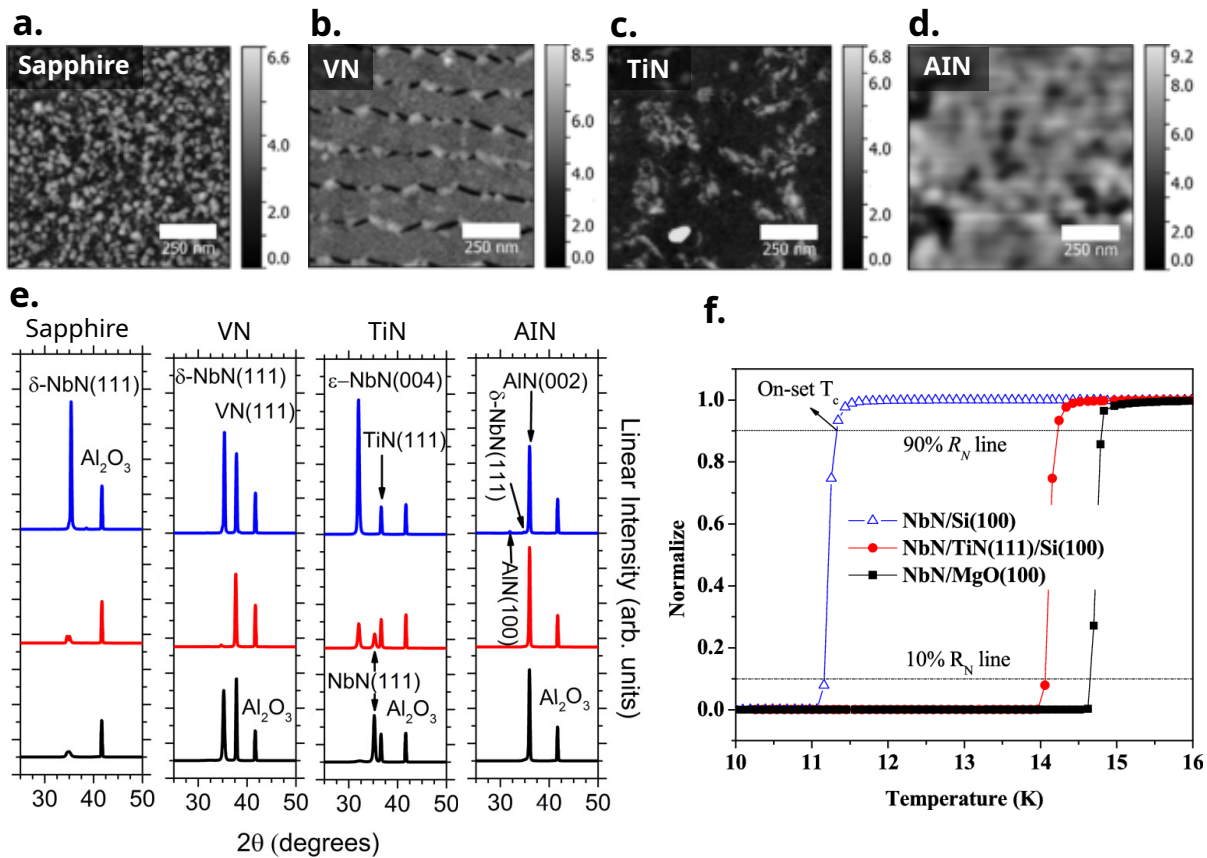


Figure 3.11 – **Evolution of the film phases with the substrate.** Figure adapted from J. Goldsmith [Goldsmith et al. 2018] and J. Zhang [Zhang et al. 2013]. (a) AFM image of a thin NbN layer deposited at 400° C on a sapphire substrate without buffer layer. (b) The same with a VN buffer layer. (c) Same with TiN buffer layer. (d) The same with an AlN buffer layer. (e) X-ray diffraction patterns of four NbN films deposited on a sapphire substrate, without buffer layer, or with VN, TiN or AlN buffer layer. The top pattern (blue) is for a deposition temperature of 840° C, the middle pattern (red) for 600° C, and the bottom pattern (black) for 400° C. (f) PPMS measurement of the resistivity with the temperature for thin NbN layers deposited on Si substrate, TiN buffer layer on Si substrate and MgO substrate.

Dependence on the substrate and buffer layer

The choice of the substrate also has a major influence on phase growth. J. Zhang [Zhang et al. 2013] studied the sputtering of thin NbN layers on different substrates, with or without buffer layers. Buffer layers are generally thin layers growth directly on top of the substrate, chosen so that their lattice parameter is close to the lattice parameter of the NbN phase one want to grow. Thus, if there is a lattice parameter mismatch between the substrate and the desired NbN phase, the addition of an appropriate buffer layer can help to grow the correct phase. Figure 3.11 shows AFM images of the surface of thin NbN layers grown under the same conditions on sapphire without buffer layer (a), with VN buffer layer (b), TiN one (c) and AlN one (d). We observe significant differences in the grain structure and size. The X-ray diffraction patterns of these films, shown in (e), reveal that they are composed of different phases (δ -phase, ϵ -phase or δ' -phase), depending on the buffer layer and the deposition temperature. J. Goldsmith [Goldsmith et al. 2018] made similar observations by studying the evolution of the critical temperature of NbN films when sputtered on

a MgO(100) substrate or on a Si(100) substrate with or without TiN buffer layer. His results are shown in (f), where we see blatantly an increase in T_c when adding a TiN buffer layer or changing the substrate from Si to MgO which has a closer lattice parameter to cubic NbN. As the difference in T_c is very large, it is necessarily explained by a dominant phase change.

3.3 Fabrication of niobium nitride inductors

This Part retraces the full fabrication process of coil inductors and microstrips, including the sputtering of the NbN films described above. The fabrication issues and results are discussed on a second Section, before the characterisation of the inductors fabricated from the different films is presented.

3.3.1 Fabrication recipe

The fabrication process begins with the evaporation of a metallic plane on the back of a SiO₂/Si wafer. This is intended to be the ground plane of the microstrip. Evaporation takes place on a physical vapour deposition machine⁹ including gold, chrome and platinum targets. First, a 10nm-thick Cr layer is deposited as an adhesion layer for platinum. Then, a 100nm-thick Pt layer is deposited to provide the metallic backplane contact.

We deposited Ti(10 nm):Au(90 nm) microstrips on several wafers using the evaporator. The patterning was done using an optical mask exposed with a UV lithography tool¹⁰. The positive photoresist¹¹ is exposed for 35 s in contact mode and developed¹² for 35 s. Lift-off is done in two successive 3 min baths of acetone with ultrasounds and a 3 min cleaning bath of IPA with ultrasounds. For the rest of the wafers, the microstrips are patterned in NbN during the same electronic beam exposure as the inductors.

The NbN is sputtered using the process described in Part 3.2.1. Then, a 1 μm-thick layer of negative photoresist¹³ is spun during 1 min at a speed of 4000 tr/min and an acceleration of 2000 tr/min². A promoter¹⁴ is used to promote its adhesion to the NbN. The resist is annealed at 90° C during 1 min 30. The exposure of the resist is done by J-L. Thomassin in an electronic beam lithography machine¹⁵ (EBEAM) offering high resolution and precise alignment. The accelerating voltage of the electrons is 100 kV and the current is 1 nA. After dose testing, the exposure dose was fixed to 480 μC/cm² for the inductors and 300 μC/cm² for the microstrips. Figure 3.12 shows inductors resulting from underdosed or overdosed exposures. The total exposure time varies from a few hours for inductors alone (12×3 inductors) up to two days for inductors and microstrips (6 microstrips + 6×3 inductors). The resist is developed¹⁶ during 2 min 15 and rinsed with deionised

9. PVD evaporator Plassys - MP700S

10. Manual mask aligner SUSS MicroTec - MJB4

11. Positive photoresist MicroChemicals - AZ 1512 HS

12. Developer MicroChemical - AZ MIF, used in a AZ:DIE [1:1] bath

13. Negative photoresist Micro resist technology - ma-N 2410

14. Adhesion promoter HD MicroSystems - VM652

15. Electronic beam lithography JEOL - JBX-6300FS

16. Developer Megaposit - MF-26A

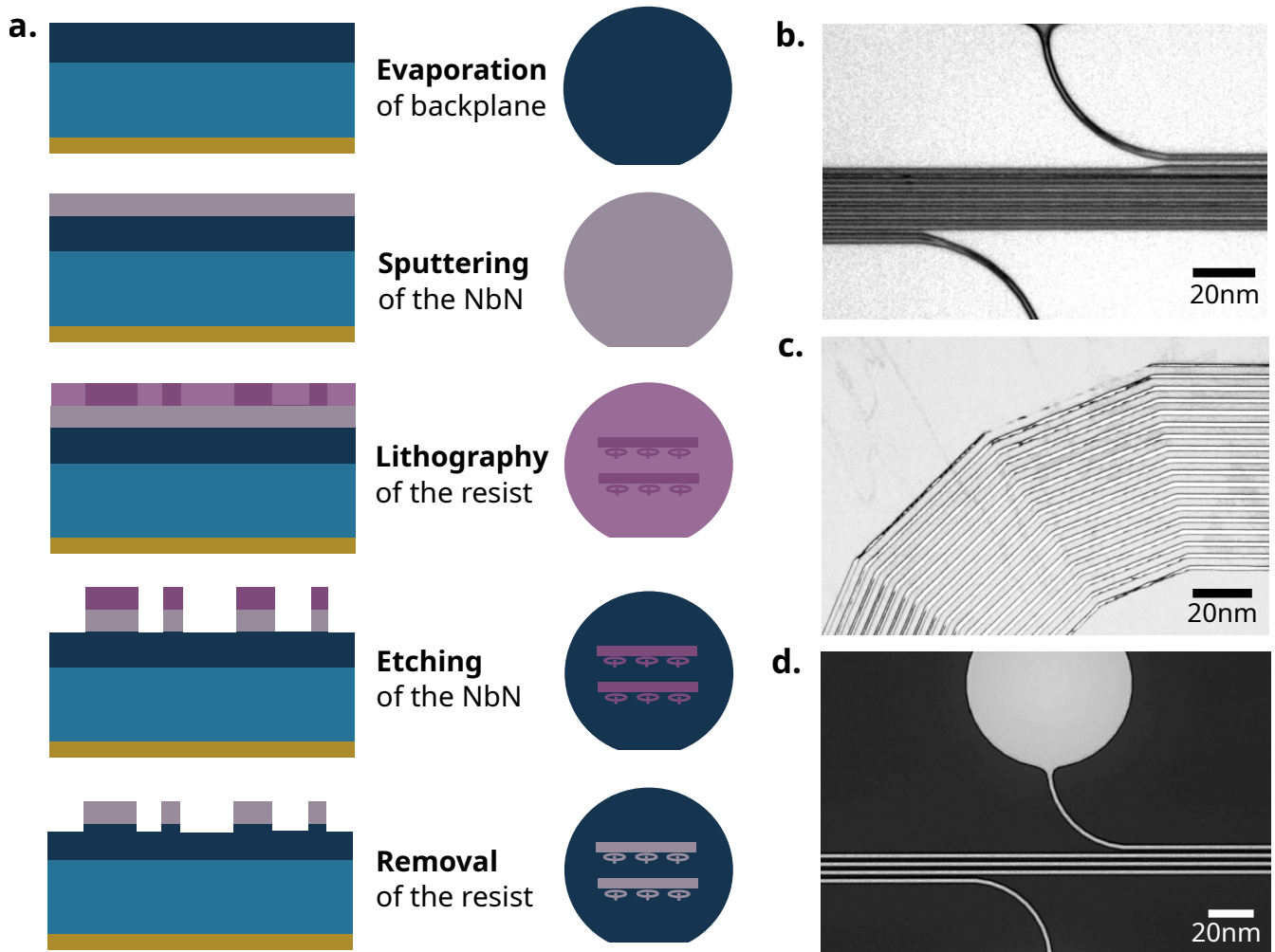


Figure 3.12 – **Fabrication process and dose tests.** (a) Schematic of the wafer during the key steps of the fabrication process. (b) Optical image of underdosed inductors : some features are merged. (c) Optical image of overdosed inductors : some features are missing. (d) Optical image of well-dosed inductor features.

water.

After lithography, the NbN layer is etched on a reactive ion etcher¹⁷ in a $\text{Ar} + \text{SF}_6 + \text{CH}_2\text{F}_2$ plasma. The process starts with a chamber cleaning in an O_2 plasma during 10 min. Then, the chamber is conditioned during 8 min with the $\text{Ar} + \text{SF}_6 + \text{CH}_2\text{F}_2$ plasma used for the etching. The wafer to etch is heated at 30°C and the plasma power is set to 70 W. For 100nm-thick NbN layers, the etch time is divided into $3 \times 50\text{ s}$ to avoid overheating which burn the resist and makes it harder to remove. Part of the SiO_2 layer is also etched away during the process, which is known to increase the internal quality factor. The resist is removed in two 5 min baths of acetone with ultrasounds and a 5 min bath of IPA with ultrasounds followed by a nitrogen blow dry. For 4" wafers, the duration of the acetone baths is extended to 15 min.

17. ICP etcher Oxford Instrument - PLASMALAB100

To preserve them, the resonators are coated with a protective resist¹⁸. They are cleaved in $8\text{ mm} \times 2.5\text{ mm}$ pieces by hand or dice using a diamond saw¹⁹. Before measurement, the resist is removed with two 5 min baths of acetone with ultrasounds and a 5 min bath of IPA with ultrasounds followed by a nitrogen blow dry.

3.3.2 Result of the different batches

Figure 3.13 shows SEM images of inductors and microstrips in NbN after the last step of the fabrication process. We can note the very good resolution of the features and the cleanliness of the surface. Figure 3.14 shows optical images of NbN inductors with gold microstrips. In (b), the inductor is merged with its microstrip due to a poor EBEAM alignment²⁰. To overcome this problem and ensure that the distance between the top of the coil and the bottom of the microstrip remains well controlled, we decided to systematically redo a small part of the microstrip in NbN shifting it slightly downwards, as shown in (c). In (d), we see the overall result which is well resolved and clean. Despite the time added by redoing part of the microstrip, gold microstrips remains very advantageous in terms of exposure time.

Table 3.4 summarises the outcomes of each fabrication batch. In this table, "Size" corresponds to the size of the processed pieces, as the wafers sputtered with NbN are always 4". Most of the batches ended up with a good visual aspect after the last step of the fabrication process. Nevertheless, a batch showed merged features due to a poor adhesion of the resist during its spinning or a wrong dose setting. For the first batches, we had difficulty removing the resist because it was burnt during the etching process and we did not have a suitable 4" ultrasounds bath. The problem was solved by cutting out the etch time and working with smaller wafer pieces.

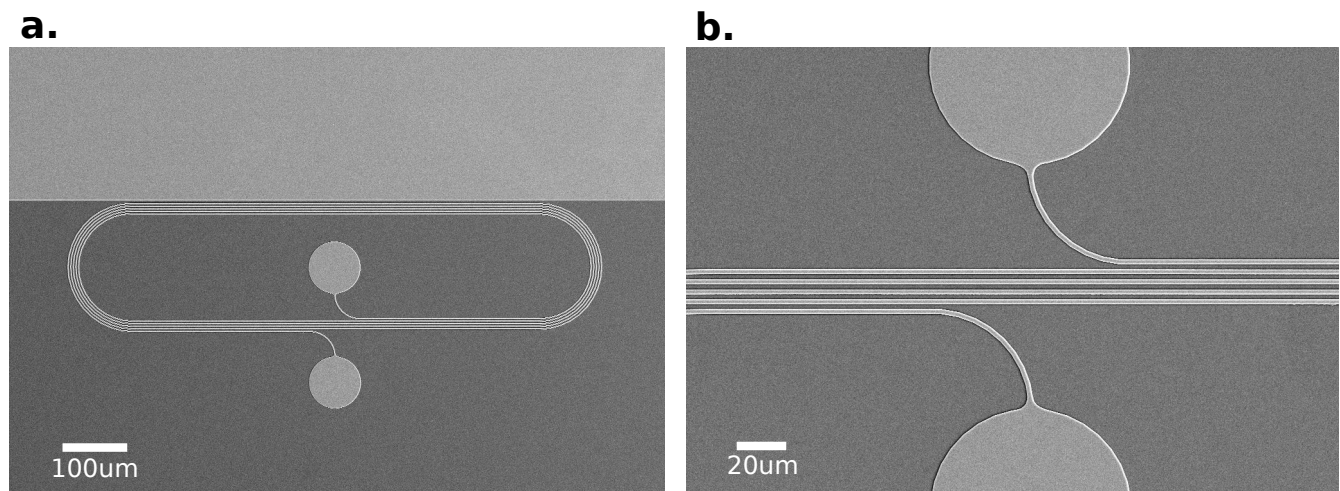


Figure 3.13 – **SEM images of NbN inductor and NbN microstrip.** (a) SEM image of an inductor and its microstrip after the last resist removal. (b) Zoom on the inductor features.

18. Positive photoresist MicroChemicals - AZ 1512 HS

19. Diamond saw DISCO - DAD-321

20. Gold alignment crosses are deposited in the same time as the gold microstrips.

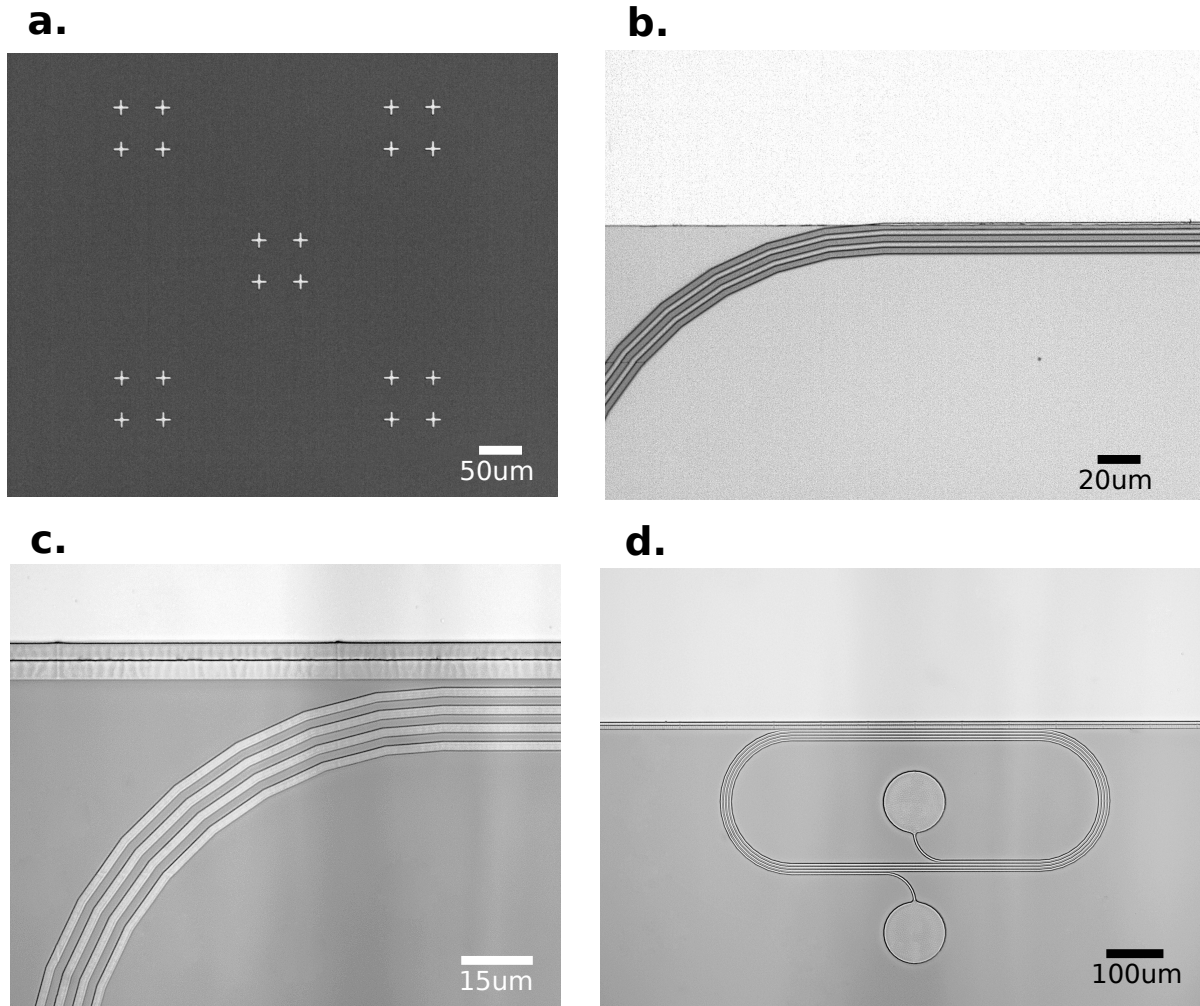


Figure 3.14 – **Optical images of NbN inductors and Au microstrips.** (a) Optical image of Au alignment marks. (b) Optical image of a NbN inductor merged with its Au microstrip. The alignment was not correct. (c) Optical image showing the additional NbN microstrip section on top of the Au microstrip. This ensures the control of the distance between the microstrip and the inductors. (d) Overview of an inductor and its microstrip.

3.3.3 Inductors properties

For each fabrication batch, we measured the frequency response of several inductors and extracted their resonant frequency f_0 and their quality factors Q_{int} and Q_{ext} using IQ-plane fitting. Table 3.5 presents the measurement results for the unloaded²¹ inductors. We observed very deep and narrow resonances for batches #1 #5 #6 #8, with resonant frequencies varying from 0.7 GHz to 3.4 GHz and typical Q_{int} and Q_{ext} above 1500. We further observe deep and narrow resonances for batches #9 and #10, but this time the resonant frequencies were lower than expected due to the relatively high kinetic inductance of these films ($\sim 35\text{pH}/\square$ instead of $\sim 10\text{pH}/\square$). Batch #0 and #11 did not give any results due to the fabrication issues mentioned above. For batch #12, the transmission through the microstrip was very poor and we suspect that the gold was degraded.

Batches #7 #13 #14 and #16 gave rise to weak resonances with very low Q_{int} and variable

21. "Unloaded" is used when both pads of the inductors are not connected.

Film	t	Microstrips	Size	Etching	Cliving	Visual aspect
#0 (06/2020)	100 nm	NbN	4''	4 min 15	hand	✗ acetone dust
#1 (07/2020)	100 nm	NbN	4''	4 min 15	hand	✓
#5 (09/2020)	100 nm	NbN	4''	4 min 15	hand	✓
#6 (10/2020)	50 nm	NbN	4''	2 min 45	hand	✓
#7 (11/2020)	50 nm	NbN	4''	2 min 45	hand	✓
#8 (12/2020)	50 nm	NbN	4''	3 × 50 s	hand	✓
#9 (01/2021)	50 nm	NbN	4''	3 × 50 s	hand	✓
#10 (02/2021)	50 nm	NbN	2 cm × 2 cm	3 × 50 s	hand	✓
#11 (04/2021)	100 nm	Au	2 cm × 2 cm	3 × 45 s	saw	✗ merged inductors
#12 (07/2021)	100 nm	Au	2 cm × 2 cm	3 × 45 s	saw	✓
#13 (09/2021)	100 nm	Au	2 cm × 2 cm	2 × 35 s	saw	✓
#14 (11/2021)	100 nm	Au	2 cm × 2 cm	4 × 35 s	saw	✓
#15 (11/2021)	100 nm	Au	2 cm × 2 cm	4 × 35 s	saw	✓
#16 (12/2021)	100 nm	NbN	4''	4 × 40 s	hand	✓
#A (01/2022)	50 nm	NbN	2 cm × 2 cm	2 × 40 s	hand	✓
#B (03/2022)	100 nm	NbN	2 cm × 2 cm	4 × 40 s	hand	✓

Table 3.4 – Fabrication results.

Q_{ext} . Having long suspected the fabrication process, and in particular the etching step, we now believe that this is due to the superconducting properties of the films. The presence of normal phases within NbN might not have been seen at PPMS, if the superconducting phase shunts the resistivity of the normal phase at low temperature. Moreover, we notice that the NbN films showed different colors, despite the attention we paid to the reproducibility of the sputtering parameters. For example, we could imagine that the batch showing very low Q_{int} has more normal phases, which are then lossy.

3.4 Dispersive readout of charges confined in silicon nanowires

In the previous sections, we discussed the design and fabrication of superconducting resonators and characterised the properties of the inductors alone. We now connect these inductors to a quantum dot device on one side and on a DC line through a bias-tee on the other side. We are studying how these connections affect the properties of the inductors and in particular their resonant frequency and quality factors. We use the resonators to measure the charge states of single and double quantum dot devices and show the measurement results.

3.4.1 Experimental setup

Both resonators and devices have to be operated at very low temperatures. We describe here two measurement setups that allow RF and DC measurements at 4 K or below 10 mK. We present the printed circuit board used for the measurements, on which the resonator chip and the device chip are glued. The quantum dot devices are provided by CEA Leti, and are described in detail in Chapter 1.3.

Film	t [nm]	f_0 [GHz]	Q_{int}	Q_{ext}	Comments
#0 (06/2020)	100	X	X	X	Fabrication issues
#1 (07/2020)	100	0.68-2.7	1200-2300	3000-4200	Deep resonances
#5 (09/2020)	100	0.69-3.4	600-1200	1100-3600	Deep resonances
#6 (10/2020)	50	0.92-1.8	1700-3200	1600-2100	Deep resonances
#7 (11/2020)	50	1.3-2.7	80-250	80-100	Weak resonances
#8 (12/2020)	50	1.3-3.2	1800-3600	1500-3400	Deep resonances
#9 (01/2021)	50	0.7-1.8	420-600	3700-8000	Low f_0 due to large L_{kin}
#10 (02/2021)	50	0.6-1.7	300-1000	2500-3800	Low f_0 due to large L_{kin}
#11 (04/2021)	100	X	X	X	Fabrication issues
#12 (07/2021)	100	X	X	X	Bad microstrips
#13 (09/2021)	100	1.9-4.8	220-450	4500-8000	Weak resonances
#14 (11/2021)	100	1.8-4.3	180-420	5000-7200	Weak resonances
#15 (11/2021)	100	?	?	?	Not measured
#16 (12/2021)	100	1.2-2.4	7-38	35-450	Weak resonances
#A (01/2022)	50	1.4-2.6	2000-3000	11000-14000	Deep resonances
#B (03/2022)	100	2.3-3.2	4000-5700	4000-6200	Deep resonances

Table 3.5 – Unloaded inductors properties.

Printed circuit board

The resonator chip and the Si nanowire chip are glued close together in the centre of a printed circuit board (PCB) called "daughter board". They are glued with silver paste, providing electrical contact between the backplane of the resonators chip and the ground in order to define the 50Ω -microstrip. Both ends of the microstrip are bonded to 50Ω gold pads on the PCB. The connection with the feedlines²² is ensured by two SMP connectors²³. To allow the formation of quantum dots, the Si nanowire gates and leads are bonded to DC gold pads placed all around the gluing area.

The outer pad of each inductor is bonded to a Si nanowire device at one of its gates, as illustrated in Figure 3.15 (a). From a radiofrequency point of view, adding a device mainly adds its differential gate capacitance $C_{\text{gate}} \sim 0.15$ pF, as well as its parametric capacitance $C_q \sim 10$ fF discussed in Chapter 2.1. The inner pad of each inductor is then connected to a bias-tee. This allows a potential to be applied through the inductor to the gate connected to the outer pad, while preventing the RF signal from leaking into the DC lines. The bias-tee is basically an RC filter consisting of a large resistor $R_{\text{bias}} = 1$ M Ω and a large capacitor to the ground $C_{\text{bias}} = 10$ nF. Both are soldered on a "mother board", on which we come to connect the daughter board via an interposer made of gold spring contacts. The mother board further host additional DC and RF filters, as well as additional SMP connectors. Figure 3.15 (c) presents the overall equivalent circuit of an inductor, which is bonded to both a device and a bias-tee.

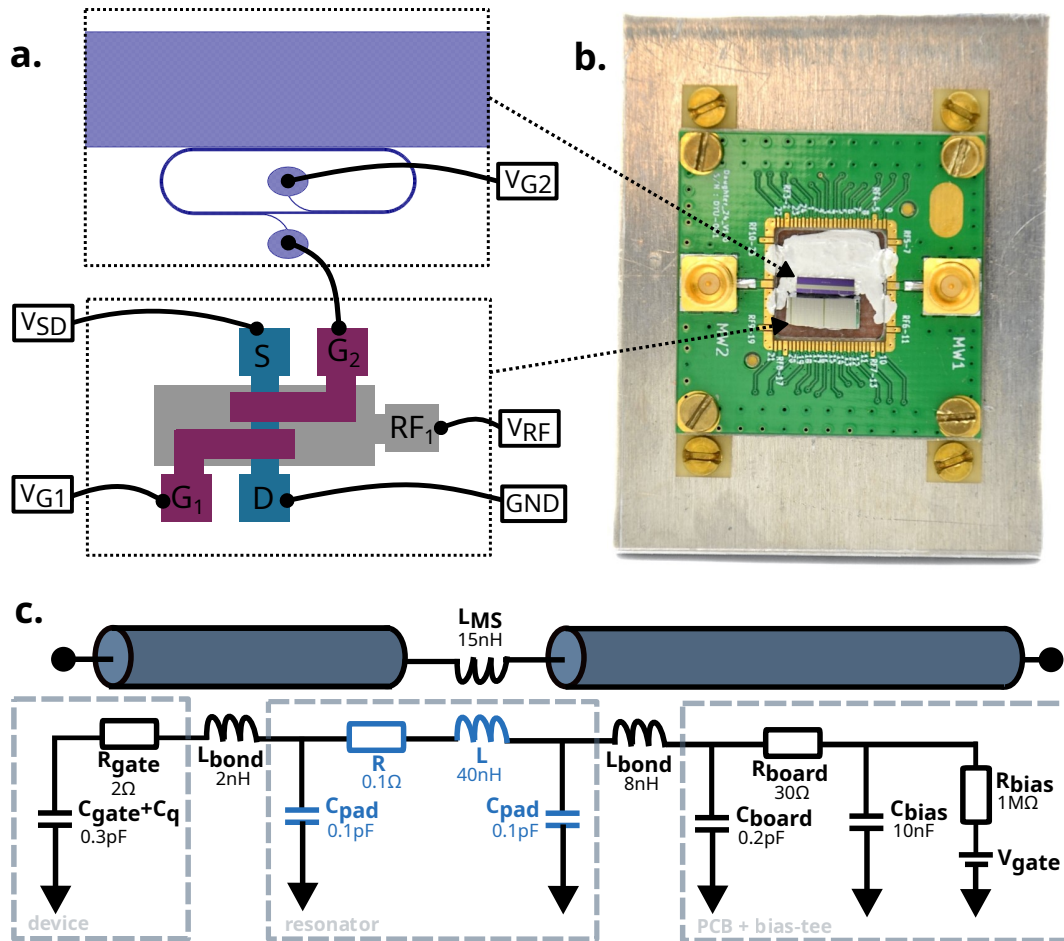


Figure 3.15 – **Setup PCB.** (a) Schematic of the bonding between a coil inductor from the resonator chip and a two-gate pump device from the device chip. (b) Picture of the setup PCB. The resonator chip and the device chip are glued close together in the middle area. (c) Equivalent circuit of the resonator bonded as shown in (a). The values given are orders of magnitude and may vary between two setups.

Helium probe (4 K)

To characterise the inductor properties (f_0 , Q_{int} and Q_{ext}), it is not necessary to work at very low temperatures. In liquid helium it is possible to cool the samples down to 4 K, which is sufficient for the resonators to be in their superconducting phase. Most of the characterisation presented in this Chapter was performed using the 4 K He probe shown in Figure 3.16. The probe is inserted in a vacuum can and pumped until reaching a typical vacuum of 10^{-2} mBar. It is then slowly inserted into the He tank and held in place with a clamp. The entire cooling process usually takes an hour, and warming up also requires an hour.

We designed this probe as a tool for testing superconducting resonators and/or semiconductor quantum dot devices. The mechanical parts were manufactured by M. Boujard and assembled by us. The probe includes a mother board welded to a loom with 24 DC lines driven by digital-

22. Feedlines are 50 Ω coaxial cables

23. SMP connectors from Amphenol RF (ref:SMP-MSSB-PCS15T)

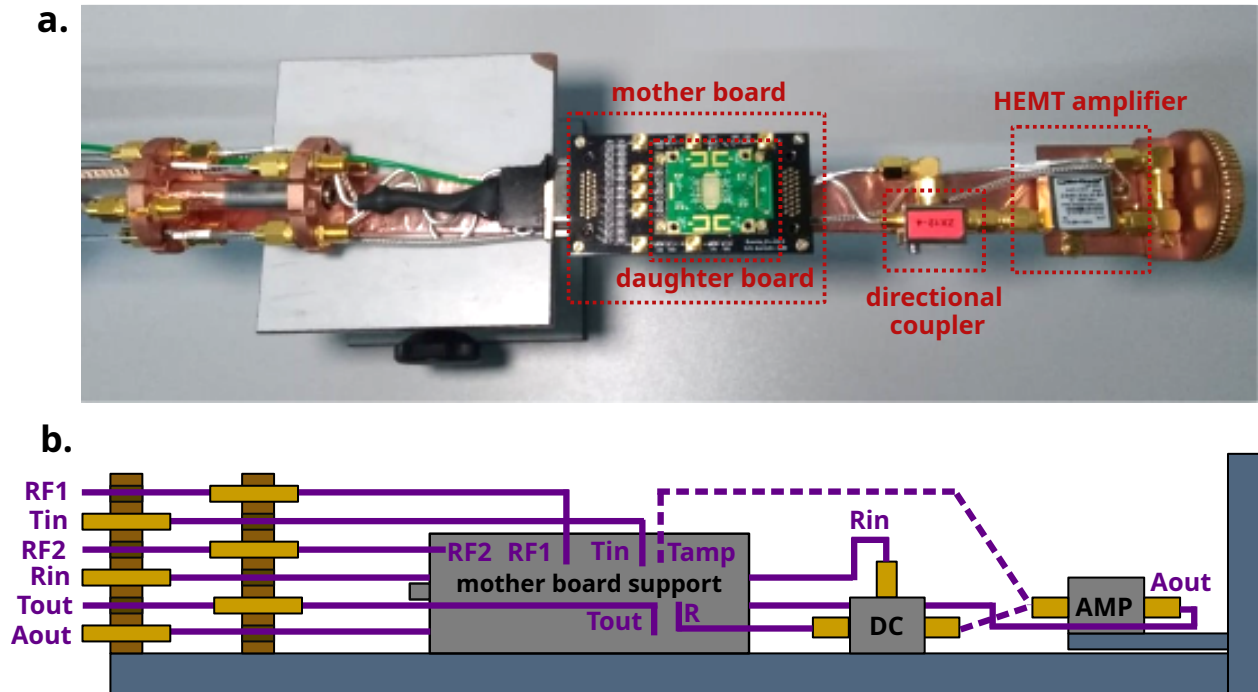


Figure 3.16 – 4K Helium probe. (a) Picture of the 4K He probe. (b) Schematic of the He probe RF wiring.

to-analogue converters²⁴. Two of the 8 RF lines implemented are used for the readout of the resonators in transmission, via the 50 Ω -microstrip. The input and output signals are supplied and read by a network analyser²⁵. The probe can be set to read in transmission or in reflection. A directional coupler has been added for the latter purpose.

Dilution refrigerator (<10 mK)

To form quantum dots in silicon nanowires, the devices have to be operated at very low temperatures to maintain thermal excitation smaller than the Coulomb repulsion. Therefore, we have performed measurements of quantum dot devices coupled to superconducting inductors in a dry dilution refrigerator²⁶, with a base temperature around 7 mK. The cryostat is divided into different temperature stages as shown Figure 3.17. It is equipped with a bottom loader which allows the sample to be changed while the dilution unit remains at 4 K, allowing the sample to be changed in less than a day. To enable spin experiments, the cryostat integrates a 3D-vector magnet thermally and mechanically connected to the 4 K stage. The magnet can generate high magnetic fields up to ± 6 T in the vertical direction and up to ± 1 T in all other directions.

Inside the cryostat, 24 DC lines are connected to the mother board via DC filters. At room temperature, they are connected to digital-to-analogue converters²⁷ through a matrix box hosting electrical switches. The current flowing from the source to the drain of the Si nanowire is

24. DAC from iTEST

25. VNA from Agilent (ref:E5071C)

26. BlueFors LD Dilution Refrigerator System

27. DAC from iTEST

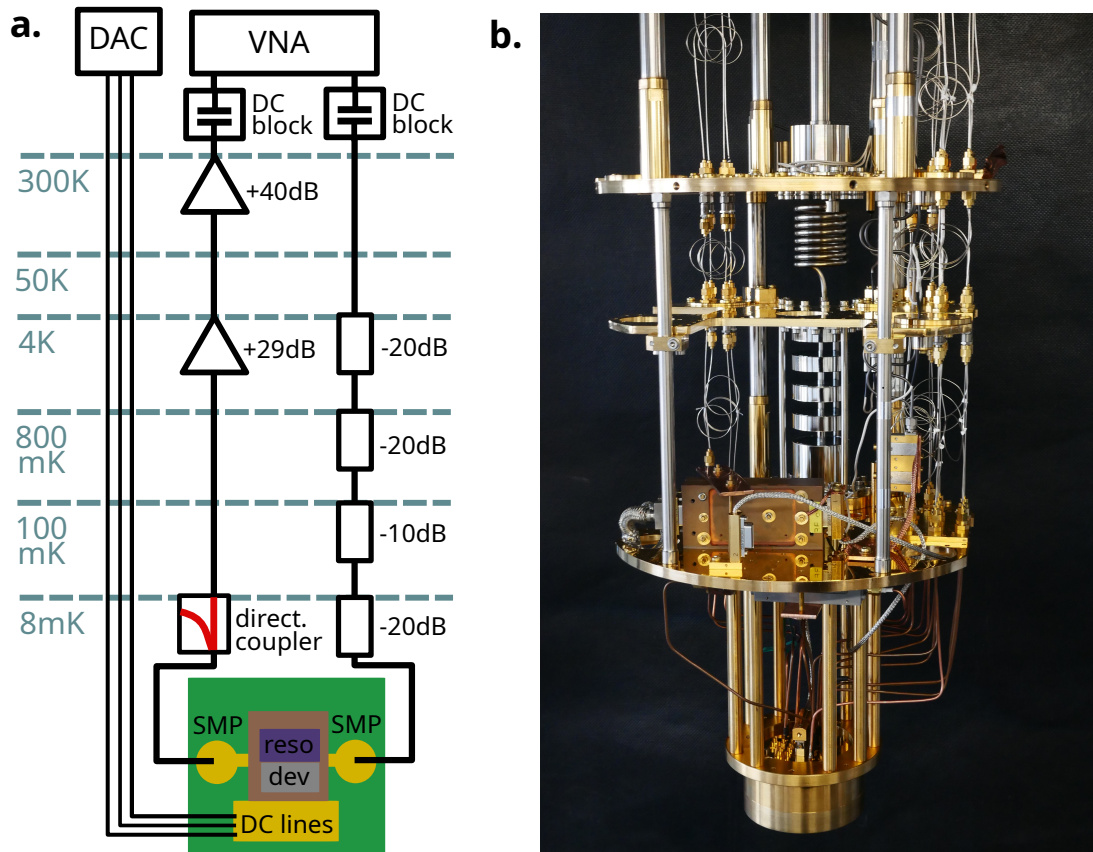


Figure 3.17 – **Dilution refrigerator.** (a) Schematic of the refrigerator wiring for a transmission measurement of a superconducting resonator coupled to a quantum dot device. (b) Picture of the dilution refrigerator.

measured with an IV-converter²⁸. The superconducting resonators are measured in transmission thanks to a two-port network analyser²⁹. The input signal is attenuated by a total of -70 dB along the various refrigerator plates. The output signal passes through the main port of a directional coupler³⁰ and is then amplified with by a high-electron-mobility transistor amplifier³¹ attached to the 4K-plate³². It is further amplified at room temperature. Both input and output lines are protected with 300 K DC-blocks to prevent the formation of ground loops.

3.4.2 Tank circuit characteristics

Having described the setup used for the measurements of Si nanowire devices, we now investigate its influence on the resonance of the coil inductors. We quantify the degradation in resonant frequency and quality factors compared to unloaded coils and propose several solutions to maintain high quality and high frequency resonators.

28. IV-converter from Femto (ref:DLPCA200)

29. VNA from Copper Mountain (ref:M5180)

30. The directional coupler is useless here, it is set for set for other experiments.

31. HEMT amplifier Low-Noise Factory (ref:LNF-LNC0.2-3A)

32. Isolators or circulators placed before the HEMT could help to reduce the noise but they have small bandwidths.

Loaded inductor properties

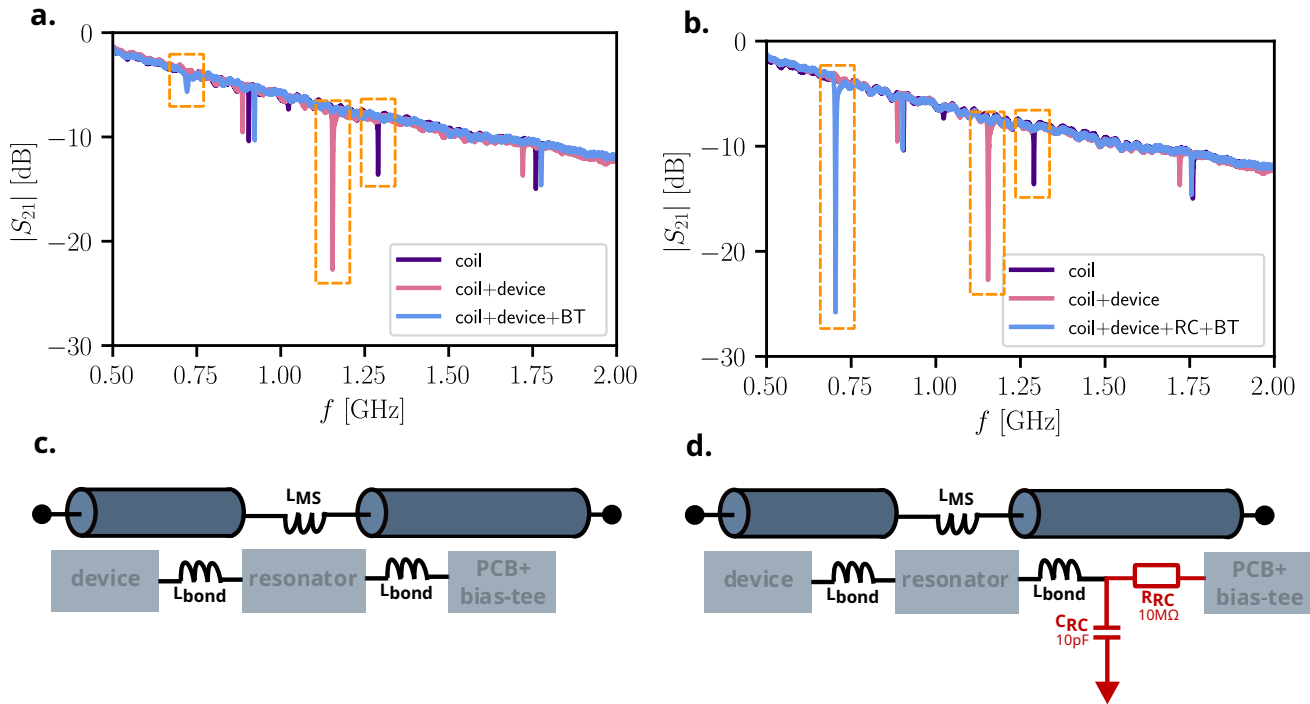


Figure 3.18 – **Loaded inductor properties.** (a) Transmitted signal as a function of frequency for a microstrip coupled to three coil inductors. The purple spectrum corresponds to the measurement of the coil inductors alone (not bonded). For the pink spectrum, the coil inductor whose resonance falls in the centre is bonded to a Si nanowire device. For the blue spectrum, the coil is also bonded to a bias-tee in front of a DC line. (b) Same measurement, but the bias-tee is now preceded by an RC filter placed on the daughter board straight after the bonding wire. (c) Schematic of the setup corresponding to the blue spectrum in (a). The equivalent circuits of the various components are detailed in Figure 3.15 (c). (d) The same for the blue spectrum in (b), showing the addition of the RC filter.

When microbonding a coil inductor to a device and/or to a DC input, they must be taken into account in the equivalent circuit of the resonator (see Figure 3.15) and in the calculations of f_0 , Q_{int} and Q_{ext} . Bonding one pad of the coil inductor to a Si nanowire device adds the inductance of the bonding wire plus the resistance and capacitance of the gate it is bonded to. For a 25 μm -diameter bond wire, the inductance added is on the order of 1 nH/mm and the wirebond is a few mm long. Knowing that the inductance of the coil inductors varies from 100 nH down to 20 nH for resonances aimed at a few GHz, the wirebond inductance is not always negligible. In fact, the more the coil inductor is designed to resonate at high frequency, the more the wirebond inductance will shift down the resonant frequency. The addition of a small gate resistance will mainly affect the internal quality factor, providing a new loss path. Finally, adding the gate capacitance to ground will mainly increase the magnetic coupling between the resonator and the microstrip, enabling a non-zero current to flow through the resonator. This will result in a decrease in the external quality factor. Figure 3.18 and Table 3.6 show the evolution of the resonance when a coil is bonded to a Si nanowire device.

Setup	f_0 [GHz]	Q_{int}	Q_{ext}
coil	1.30	1400	5000
coil+device	1.15	900	800
coil+device+BT	0.670	10	120
coil+device+RC+BT	0.690	500	250

Table 3.6 – Loaded properties of the coil inductor measured on Figure 3.18.

When bonding a coil inductor to the bias-tee implemented on the mother board, it adds to the equivalent circuit the inductance of the wirebond, the PCB capacitance to ground and resistance of the gold track, as well as the RC filter composing the bias-tee (see Figure 3.15). While the resonator and device are glued close together to minimise their bonding distance, the wirebond separating the gold pad of the PCB from the NbN pad of the coil inductor is significantly longer. It can reach several millimetres, and so several nanohenries, strongly shifting down the resonant frequency of the circuit. Before reaching the RC filter, the RF signal has to pass through the daughter board, the interposer and the mother board catching parasitic capacitances and resistances, inducing a strong decay of Q_{int} . Additionally, the RC filter further increases the magnetic coupling between the microstrip and the resonator, decreasing Q_{ext} . Figure 3.18 and Table 3.6 reveal that Q_{int} can drop down to 10 when bonded to the mother board bias-tee, making measurements with this setup very difficult.

To avoid the collapse of Q_{int} , we decided to implement an additional bias-tee on the daughter board, straight after the bonding wire. For this purpose, we simulated and tried different options :

- To put a large CMS resistor such as $1\text{ M}\Omega$ ³³ or $10\text{ M}\Omega$. It perfectly works on simulations but not in the experiment : it is indeed very difficult to have perfect resistors operable at several GHz and at very low temperatures. The ones we tried were lossy, significantly degrading Q_{int} .
- To put a large inductor in front of the CMS resistor to form a RL filter. Again, what worked in the simulations did not work in the experiment. We tried different types of inductors with $L \sim 1\text{ }\mu\text{H}$, including CMS inductors³⁴ and conical inductors³⁵.
- To put a capacitor in front of the CMS resistor to form a RC filter. This option gave good results, with a capacitor of 10 pF ³⁶. In Figure 3.18 and Table 3.6 we can clearly see an improvement in Q_{int} when an RC filter is used before the mother board bias-tee.

On-chip bias-tee

We observed that the implementation of a RC filter on the daughter board straight after the bond wire helped keep the internal quality factor high enough. Yet, the length of the bond wire is responsible for an important frequency shift down which is difficult to control. Indeed, the bond

33. Resistor $1\text{ M}\Omega$ Vishay (ref:MMU01020C1004FB300)

34. High performance inductor 820 nH Coilcraft (ref:0805HP-821XGRB)

35. Broadband conical inductor $1.2\text{ }\mu\text{H}$ Coilcraft (ref:BCL-122JL)

36. Capacitor 10 pF Vishay (ref:VJ0603D100CXPAJ)

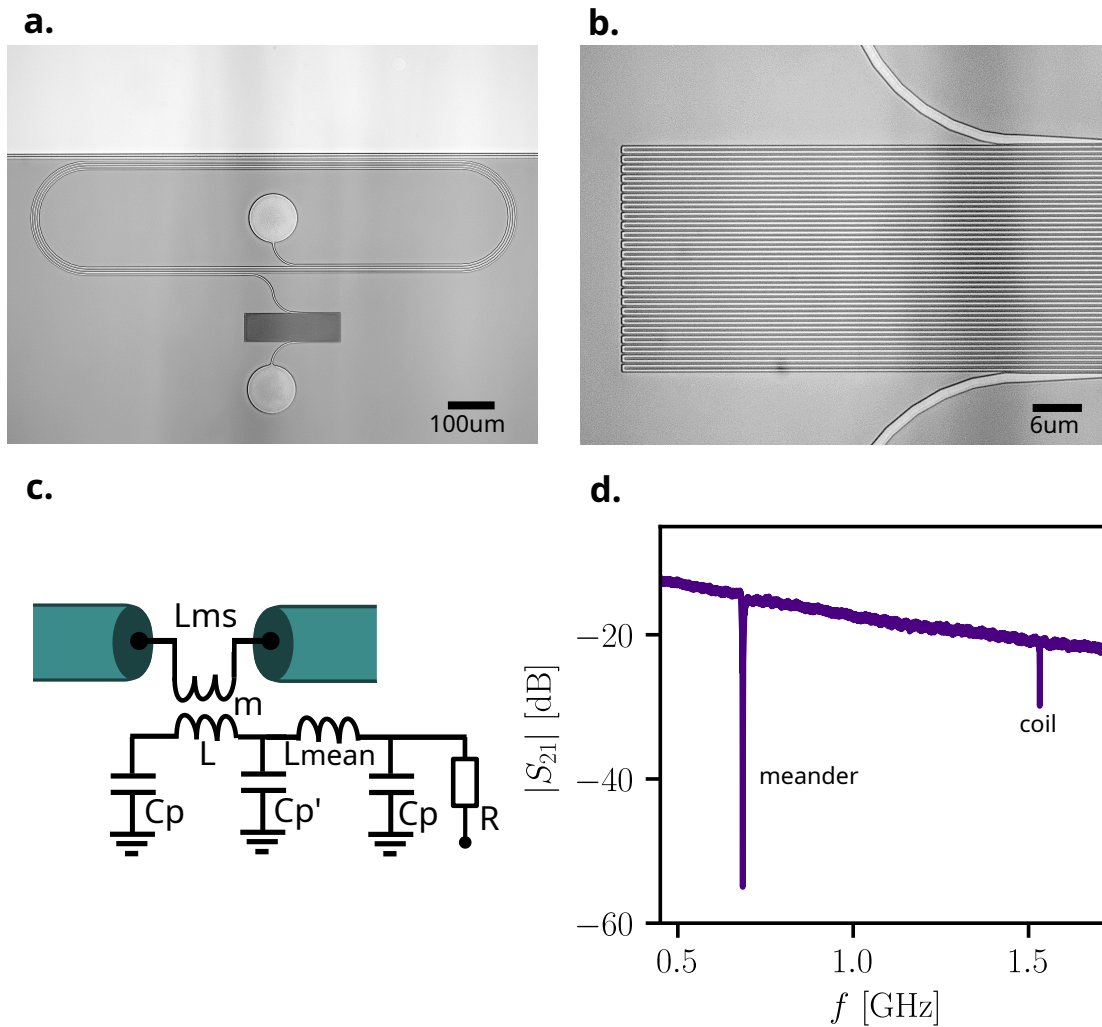


Figure 3.19 – **Superconducting meanders for on-chip bias-tees.** (a) SEM image of an inductor with a bias-tee meander. (b) Zoom in the meander features. The conductor is 500 nm wide. (c) Equivalent circuit of the coil and meander alone. The meander inductance typically varies from 100 nH to 300 nH depending on the number of meander legs and their length. For the inductor shown in (a), it is around 160 nH. (d) Measured $|S_{21}|$ response for the inductor shown in (a). The high frequency deep corresponds to the resonance of the coil inductor, while the low frequency deep corresponds to the meander resonance.

wire length varies according to the gluing of the chips, the bonding plan, the parameters of the microbonding machine, etc... This lack of control makes the estimation of the resonant frequency difficult and can even prevent us from working up to a few GHz. To get rid of this problem and make resonators that can be easily integrated in all setups, we decided to work on the implementation of an on-chip bias-tee. Our efforts focused on the realisation of an RL filter, with an on-chip inductor. The resistor can then be placed anywhere on the daughter board or on the mother board. In simulations, the RL filter is a slightly less efficient than the RC filter, but in practice it is much easier to fabricate an inductor using the kinetic inductance of the films, rather than a capacitor which would add several fabrication steps.

For on-chip bias-tees, we have designed meander inductors whose inductance is mainly due to

the kinetic inductance of the NbN films. They consist of a long wire folded over itself so that it takes up a small area but has a very large number of squares. These meander inductors are fabricated at the same time as the coil inductors. The typical width of the meander conductor is 500 nm, which is large enough to be exposed during the same EBEAM lithography as the coil inductors without changing the usual dose. Figure 3.19 (a) and (b) shows two SEM images of the meander inductors after the last fabrication step. The equivalent circuit of a coil inductor followed by a meander inductor is presented in (c). Its frequency response is presented in (d). The spectrum includes two deeps, one corresponding to the coil inductor and the other to the RL filter. When bonding the pad of the meander to the daughter board where the resistor is soldered, the internal quality factor of the meander peak drops down, without affecting the peak corresponding to the coil inductor. The LR filter is therefore a good biasing solution to allow measurements with coil inductors.

3.4.3 Dispersive charge readout

Single quantum dots

As a proof of concept, we first tried to measure the charge states of single quantum dot (QD) devices using coil inductors with the setup described above. We measured a chip composed by two coil inductors coupled to the same microstrip. The lower frequency coil is bonded to a N-type single quantum dot device, while the upper frequency coil is bonded to a P-type device, similar to those described in Chapter 1.3. At the time this measurement was made, we hadn't worked on the bias-tees yet. Also, the two inductors are bonded to RF+DC inputs only through the bias-tees of the mother board. Figure 3.20 (a) shows the frequency response of the two inductors bonded to the devices and the RF+DC inputs. The two resonances are plotted in the IQ-plane as shown in (b) and (c). These coils inductors, providing from Film #8, demonstrate a fairly high internal quality factor despite the absence of any additional bias-tee.

Figure 3.20 (d), (e) and (f) shows the stability diagram of the N-type device bonded to the lower frequency coil inductor³⁷. Thus, we can compare the signals obtained by measuring the source-drain current, the amplitude of the transmitted signal through the microstrip and its phase. For the last two, we measured the variation in the amplitude or phase of the transmitted signal as it was tuned to the resonant frequency. For all three signals we observe the characteristic Coulomb diamonds, signature of the few electrons regime. We indeed observe a contrast between the regions where the carriers are Coulomb blocked ($I_{SD} = 0$), and the regions where they can flow ($I_{SD} \neq 0$). For the transmitted signal in amplitude and phase, this contrast corresponds to a frequency shift of the resonant frequency of the order of 150 kHz between a blocked state and a passing state.

We measured the evolution of the signal to noise ratio (SNR) of a Coulomb peak belonging to the single quantum dot in the few electrons regime. For this measurement, we defined the SNR as $SNR = \frac{\mu}{\sigma}$, where μ is the mean height of the Coulomb peak and σ is the standard deviation of the background noise. In Figure 3.21, we observe the decrease of the SNR when reducing the integration time t_c . Indeed, σ is expected to linearly decrease with t_c . We extracted a SNR above 3 for $t_c = 1.2 \mu\text{s}$ which allows for fast readout of the single dot charge states.

37. We observed similar Coulomb diamonds for the P-type device bonded to the upper frequency coil inductor.

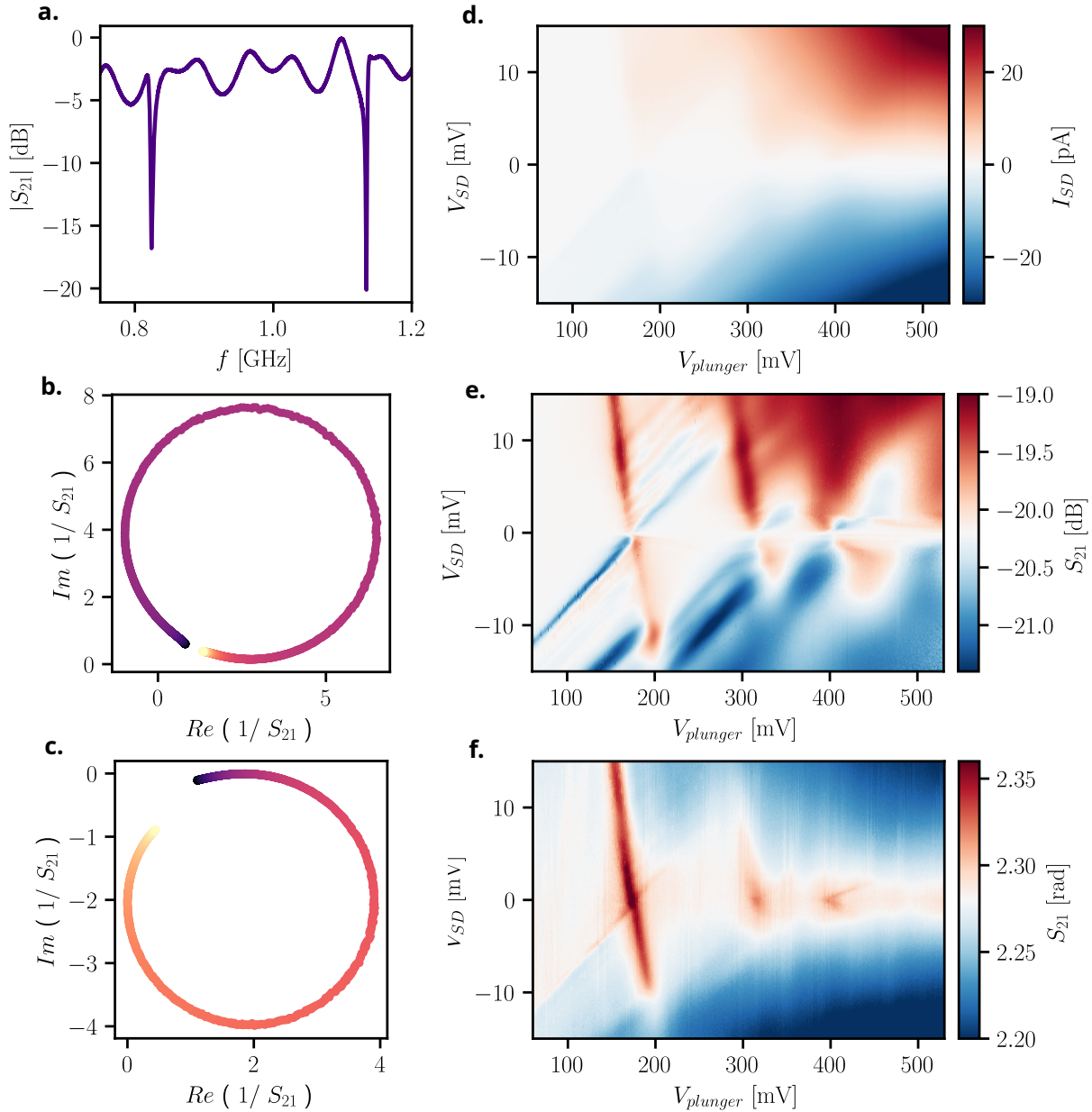


Figure 3.20 – **Stability diagram of a single quantum dot probed with a coil inductor.** (a) Transmitted signal as a function of the frequency. The two deeps correspond to two different coil inductors, one being connected to a N-type device, the other to a P-type device. (b) IQ-plot of the resonance at $f_0 = 766$ MHz. By fitting the circle, we extracted $Q_{\text{int}} = 1010$ and $Q_{\text{ext}} = 130$. (c) IQ-plot of the resonance at $f_0 = 1.08$ GHz. By fitting the circle, we extracted $Q_{\text{int}} = 530$ and $Q_{\text{ext}} = 130$. (d) Stability diagram of an N-type single quantum dot device in the few electrons regime, measured in current. (e) Stability diagram measured in amplitude of the transmitted signal S_{21} at the resonant frequency. For this map, the RF input power is -90 dB and the integration time of each point is 10 ms. (f) The same but with the phase of S_{21} .

The SNR we obtained can be compared with the measurements of G. Zheng [Zheng et al. 2019] presented in Figure 3.22. They have been obtained for a radiofrequency setup where a superconducting resonator is integrated on the same chip as a Si/SiGe double quantum dot device.

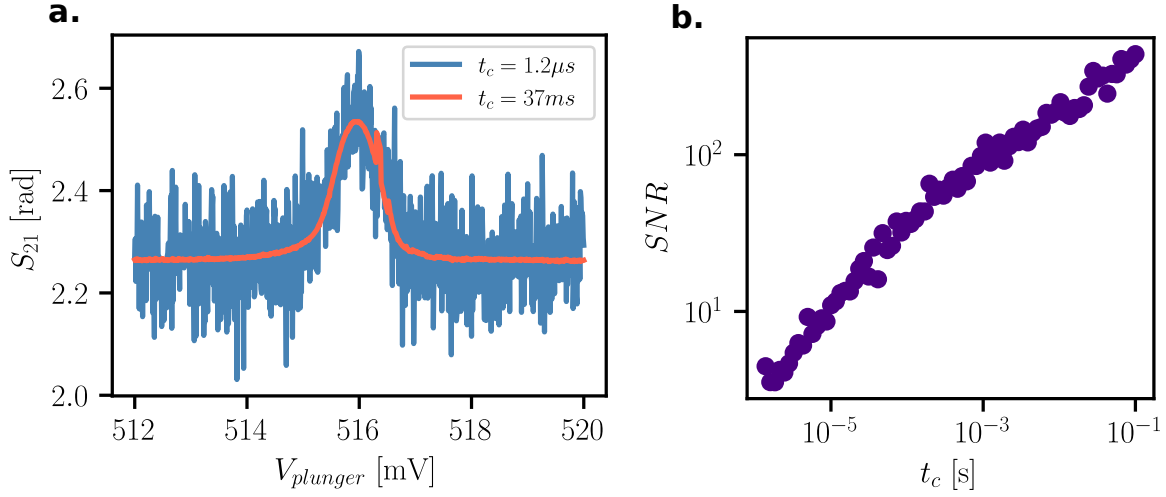


Figure 3.21 – **SNR of a Coulomb peak with the integration time.** (a) Coulomb peak integrated with $t_c = 37 \text{ ms}$, giving a SNR of 184.7. The blue curve is the same Coulomb peak integrated with $t_c = 1.2 \mu\text{s}$ in orange, giving a SNR of 3.018. (b) Evolution of the SNR of the Coulomb peak shown in (a), as a function of the integration time.

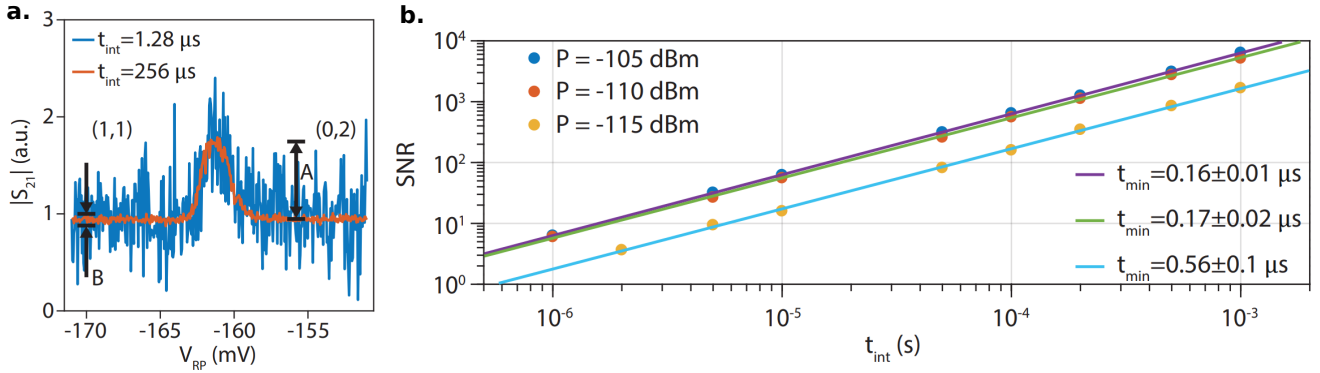


Figure 3.22 – **Evolution of the SNR with the integration time.** Figure adapted from G. Zheng [Zheng et al. 2019]. (a) Coulomb peak integrated with $t_c = 256 \mu\text{s}$ in blue and $t_c = 1.28 \mu\text{s}$ in orange. (b) Evolution of the SNR as a function of the integration time, for different input powers.

The resonator consists in a $\lambda/2$ NbTiN thin wire, with $f_0 = 5.7116 \text{ GHz}$, $Q_{int} = 5780$ and $Q_{ext} = 4730$. Thanks to this setup, G. Zheng was able to achieve a single-shot readout of a two-electron spin state with a fidelity better than 98% for an integration time of $6 \mu\text{s}$.

Double quantum dots

Having observed that it is possible to measure the charge state of a single QD with the dispersive response of coil inductors, we set out to measure double quantum dot devices. Figure 3.23 presents three attempts to measure interdot charge transitions with the phase response of coil inductors coupled to double quantum dot devices :

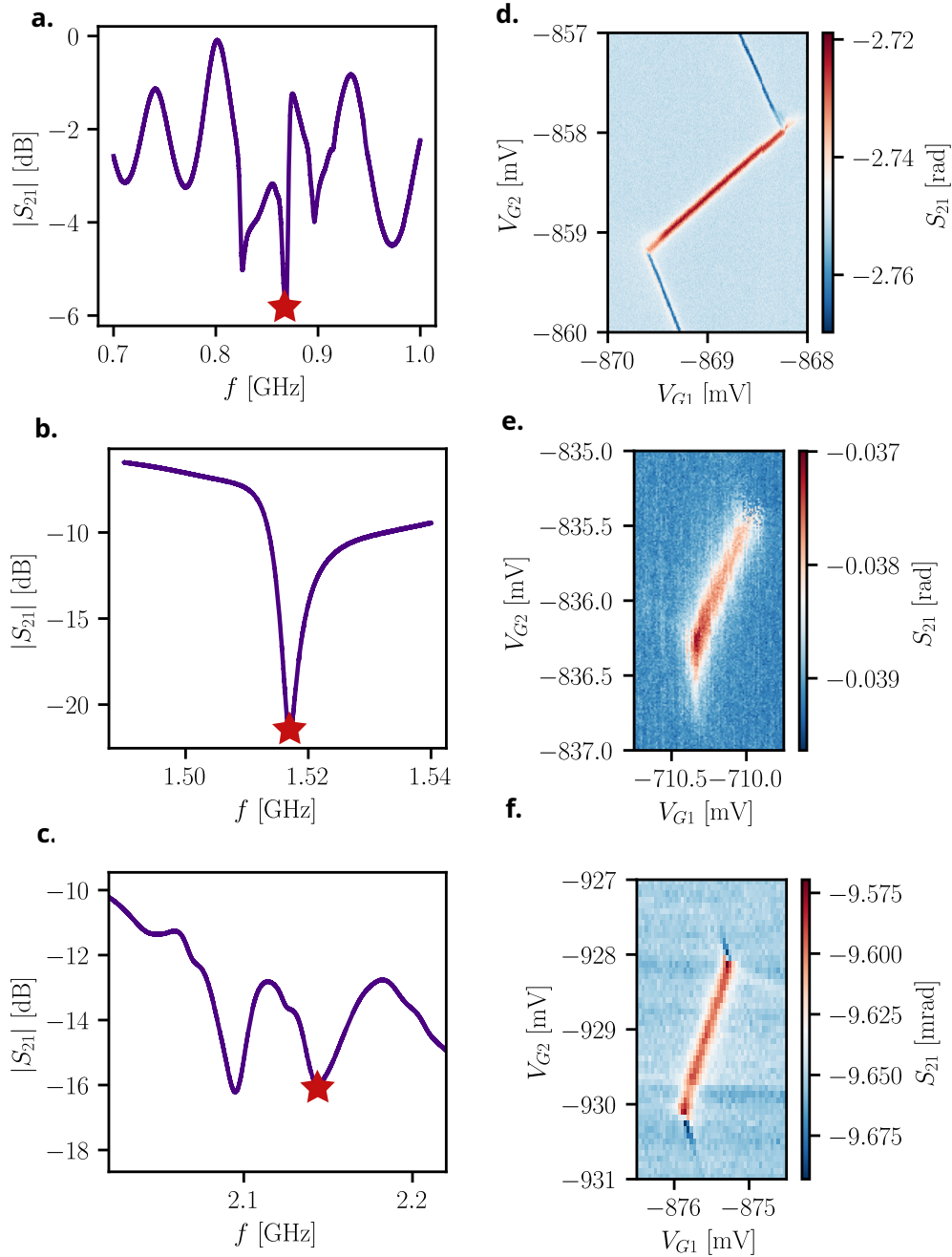


Figure 3.23 – **Interdot charge transitions of DQDs probed with coil inductors.** (a) (b) (c) Transmitted signal versus frequency for three different setups where a coil inductor is bonded to a double quantum dot device. (d) Interdot charge transition in the many hole regime, measured with the setup (a). The integration time of each point is 10 ms and the input power is -105 dB. (e) ICT in the many holes regime, measured with the setup (b). The integration time is 1ms and the power is -110 dB. (f) ICT in the many holes regime, measured with the setup (c). The integration time is 100 ms and the power is -100 dB.

- For the first attempt shown in Figure 3.23 (a) and (d), we measured a 2 gates pump device³⁸

38. CEA Leti reference : batch #T18S0602A, wafer #W23, die #D28 device #2G23

with a top gate and a channel width of 80 nm. The double quantum dot is formed between the right gate (G1) and the left left gate (G2). The resonator is a 4 turns coil inductor fabricated from the NbN film #8. It is bonded to the right gate on one side, and to a DC input on the other side, via the mother board bias-tee.

- For the second attempt shown in Figure 3.23 (b) and (e), we measured a 5 gates pump device³⁹ with a top gate and a channel width of 100 nm. The double quantum dot is formed between the middle gate (G1) and its left neighbour (G2). The resonator is a 6 turns coil inductor fabricated from the NbN film #8. It is bonded to the middle gate on one side, and to an RF+DC input on the other side, protected by an RC filter directly placed on the daughter board after the bonding wire.
- For the third attempt shown in Figure 3.23 (c) and (f), we measured a 5 gates pump device⁴⁰ with a channel width of 100 nm. Again, the double quantum dot is formed between the middle gate (G1) and its left neighbour (G2). The resonator is a 2 turns coil inductor in niobium bonded on one side to the centre gate and on the other side to a DC input via the mother board bias-tee. A second coil inductor is bonded to the drain of the device and to a DC entry. Its resonance is at a lower frequency and is also shown in Figure 3.23 (c).

For all these attempts, we managed to observe interdot charge transitions by measuring the phase of the transmitted signal at the resonant frequency. Dot-lead transitions can also be observed in some measurement maps. Generally, one of the dot-lead transitions is more visible than the other because it involves a dot that is closer to the resonator. Despite our best efforts, we have not been able to reach the few hole regime for the double quantum dots studied. In fact, the long integration time required to observe the weak interdot signals together with the sharpness of their features made the scanning of wide areas of the stability diagrams very time-consuming. Nevertheless, we managed to prove once again that it is possible to detect charge signals using coil inductors. We also took profit of this test phase to study the response of resonators fabricated in niobium, as Nb films should be less resilient with the magnetic field but easier to grow, having a single possible superconducting phase.

3.5 Conclusion

In this Chapter, we studied the implementation of superconducting coil inductors for the dispersive readout of single and double quantum dot devices. We first discussed the choice of geometries and opted for coil inductors coupled to a 50 Ω -microstrip. We performed simulations which led to designs offering high-quality factor and high-frequency resonators. We then motivated the choice of NbN as superconducting material and studied the properties of the films. We noticed several differences between the films, which we attributed to the growth of different NbN phases during the sputtering process, as suggested by the literature. We then established the fabrication recipe of the coil inductors around a key step of EBEAM lithography. We compared the different fabrication outcomes and characterised the properties of the coil inductors providing from the

39. CEA Leti reference : batch #T19S0888, wafer #W4, die #D191 device #5G23

40. CEA Leti reference : batch #T19S0888, wafer #W4, die #D102 device #5G12

different batches. We noticed very large discrepancies in internal quality factors between the different batches, which we explained by the presence of non-superconducting phases in some of the films.

Afterwards, we presented the setups for measuring Si nanowire devices with the coil inductors. We quantified the influence of the devices and DC entries on the resonance properties and compared them with the measurements of the coil inductors alone. We investigated on various biasing solutions to avoid the degradation of the resonances, including on-chip LR filters or RC filters soldered to the PCB. Finally, we showed the measurement of Coulomb diamonds and interdot charge transitions on single and double quantum dot devices using coil inductors.

The major issue we met during this work was the lack of reproducibility of the phases grown during the sputtering of the NbN films, which was the cause of a strong variability in the internal quality factors of the films. To overcome this problem, an important work should be carried out on the sputtering conditions of the machine together with additional tests on the use of alternative substrates and/or buffer layers to facilitate the growth of the desired phases. Unfortunately, we did not have the time necessary for this important fabrication development within the framework of this PhD project. We did try some quick fix ideas, such as sputtering NbN films onto 10 nm thick Nb buffer layers, but failed to see any noticeable improvement. Nevertheless, we had the opportunity to benefit from the deposition of NbN films by the CEA Leti, whose semi-industrial machine allows a very good reproducibility of the grown phases. We could then imagine continuing this collaboration rather than trying to sputter NbN films ourselves. Finally, the designs and recipes that we have implemented and presented in this Chapter could also be applied to niobium films, and hence be used for many applications that do not require external magnetic fields. We have sputtered and fabricated several batches of Nb resonators⁴¹, all of which showing high internal quality factors.

41. Not shown in this manuscript.

TAKEAWAY MESSAGES:

- Superconducting coil inductors coupled to a 50Ω -microstrip allow the simultaneous readout of several devices in transmission.
- The resonance of a resonator can be characterised with its resonant frequency, its internal quality factor associated with losses and its external quality factor associated with the coupling to its environment.
- Electromagnetic simulations based on finite elements allow to compute the resonant frequency and the external quality factor of a resonator with great accuracy.
- NbN is a superconducting material renowned for its resilience with the magnetic field and its high critical temperature.
- The crystallographic structure of NbN films and the phases that compose them strongly depend on the sputtering parameters and the lattice parameters of the substrate. Consequently, we observed large variations in the internal quality factors of the coil inductors within the different fabrication batches.
- The bonding of the coil to a device and a DC input leads to a degradation of the internal quality factor and a shift down of the resonant frequency. It can be compensated by adding a proper bias-tee, consisting of an on-chip RL filter or an RC filter on the PCB.
- The variations in phase or amplitude of the transmitted signal at the coil inductor resonant frequency enable to detect the charge states of single and double quantum dots.
- Thanks to the coil inductors, it is possible to detect a Coulomb peak with an integration time of $1.2\mu\text{s}$ with a SNR above 3.

CHARGE SENSING READOUT OF GE QUANTUM DOTS

Contents

4.1	Charge sensing readout circuit	82
4.1.1	Device and experimental setup	82
4.1.2	Simulations of the readout circuit	84
4.1.3	Circuit matching and sensitivity	87
4.1.4	Properties of the measured readout circuit	89
4.2	Charge sensing measurements and performances	90
4.2.1	Charge sensor tuning	90
4.2.2	Charge sensitivity of the sensor	91
4.2.3	Sensor signal and charge noise	93
4.3	Charge sensing of a double quantum dot	97
4.3.1	Double quantum dot design and experimental setup	97
4.3.2	Double quantum dot tuning and stability diagram	99
4.3.3	Charge sensitivity to the double quantum dot	101
4.3.4	Double quantum dot charge noise	102
4.4	Conclusion	102

Ascent of Pointe de l'Echelle by the N ridge, with D. Fraudet

Vanoise massif, France - July 15th 2022

Ge/SiGe planar heterostructures are ergonomic platforms for spin manipulation in double quantum dots, benefiting from large hole mobility, reduced hyperfine interaction and large level spacing. In Chapter 2.1, we saw that the geometry of the devices made on Ge/SiGe heterostructures is such that charge sensing is the most suitable readout solution. Here, we introduce a radiofrequency setup enabling for the readout of single hole transistors (SHT) used as charge sensors (CS). These single quantum dot systems are integrated within the design of the Ge/SiGe heterostructure devices described in Chapter 1.2.3. We start by presenting an equivalent circuit of the readout setup, including the capacitances and resistances of the SHT, and work on its matching with the feedlines. Then, we discuss on the tuning of a single quantum dot device and characterise its charge sensitivity and charge noise. Finally, we extend our study to the sensing of a double quantum dot (DQD). We evaluate the sensitivity of the CS to the DQD and discuss different noise sources.

4.1 Charge sensing readout circuit

In this Part, we focus on the implementation of a radiofrequency setup dedicated to the readout of SHTs used as charge sensors. We establish the equivalent circuit of the system under study, including the resistive and capacitive environment of the SHT, the LC-resonator, and the different filters. Through numerical simulations we improve the matching of the LC-resonator with the feedlines and its sensitivity to the SHT channel resistance. Finally, we characterise the LC-circuit implemented experimentally and compare its characteristics with the model.

4.1.1 Device and experimental setup

Single quantum dot device

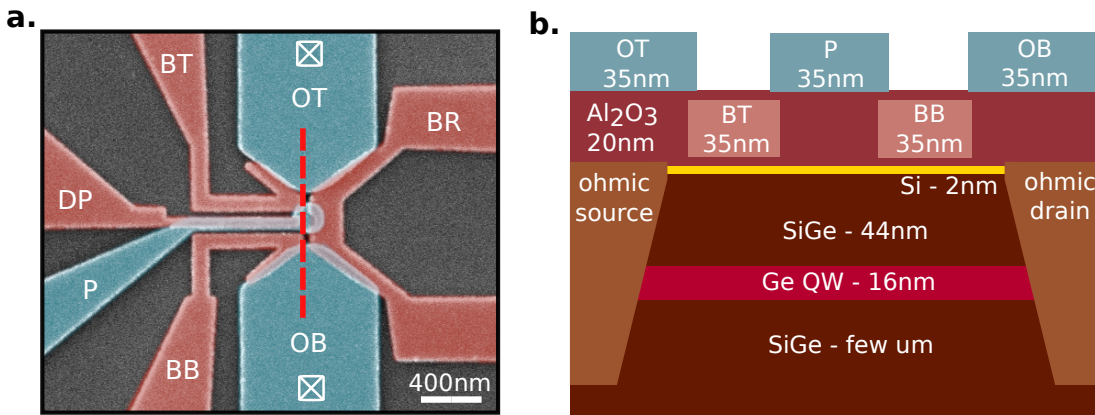


Figure 4.1 – **Gate layers and layer stack of the charge sensor** (a) SEM picture of the charge sensor gate layers. The barrier gates (first gate layer) are red-coloured and the accumulation gates (second gate layer) are blue-colored. (b) Transverse view of the layer stack along the red dashed line in (a). The heterostructure is described in detail in Chapter 1.2.1.

The gate layer and the layer stack of the SHT charge sensor under study are presented in Figure 4.1. A set of barrier and accumulation gates enables the formation of a quantum dot under

the plunger gate P. The gates BR and DP help controlling the lateral confinement of the dot. The gates BT and BB control the coupling with the source and drain two-dimensional electron gases (2DHGs) accumulated below the gates OT and OB, respectively. These largely accumulated 2DHGs are connected to metallic ohmic contacts, hundreds of micrometers away from the dot.

Experimental setup

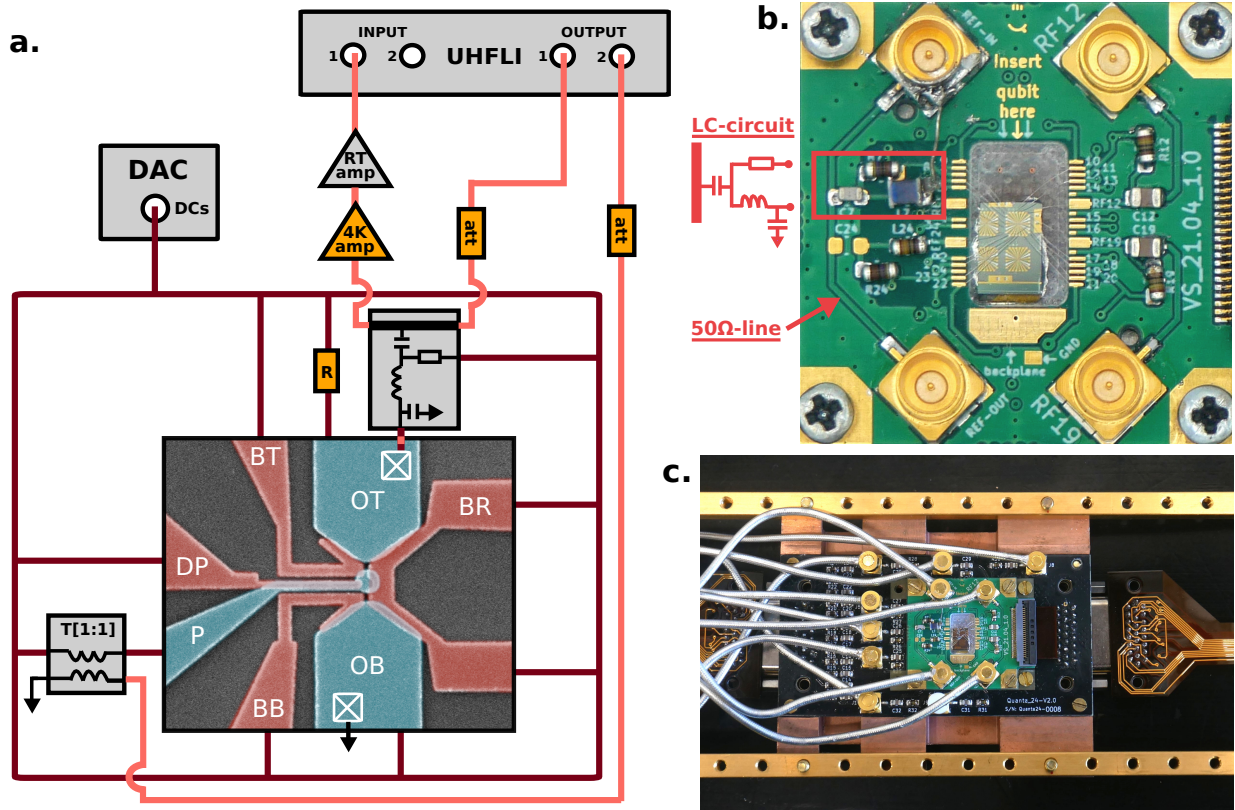


Figure 4.2 – **Experimental setup.** (a) Schematic of the setup used to characterise the charge sensor. The brown wire is a DC bundle that splits to power the gates. (b) Picture of the PCB with the sample chip in the middle, surrounded by the LC circuit, two bias-tees and four RF-connectors. (c) Picture of the full circuit placed in the mixing chamber of the dilution refrigerator, including the PCB shown in (b) and the mother board.

To probe the SHT, we implemented the setup presented Figure 4.2 (a). The device is glued on a PCB and each of its gates and ohmics are microbonded to DC-ports. The resonant circuit used for radiofrequency readout is composed by an SMD inductor and a SMD capacitor soldered to the same PCB, as shown in Figure 4.2 (b). The resonant circuit is microbonded to the device with an aluminium wire of 25 μm diameter. An interposer made of gold springs connects the PCB to a mother board, containing all the RC-filters for the DC-lines^{1,2} and the bias-tees for the RF-lines^{3,4}, see Figure 4.2 (c). The RC-filters ensure that signals passing through the DC-lines are filtered

1. Resistor 2k Ω Vishay (ref:MMU01020C2001FB300)
2. Capacitor 10 nF Kemet (ref:C0805X103J5GACAUTO)
3. Resistor 1M Ω Vishay (ref:MMU01020C1004FB300)
4. Capacitor 10 nF Kemet (ref:C0805X103J5GACAUTO)

above 50 kHz. The bias-tees allow the RF-signals to be mixed with the DC-signals. Their RC time constant is about 10 ms, allowing for a fast control of the gates through the RF-lines. This setup is placed at the mixing chamber of a commercial dilution refrigerator⁵. An high-electron-mobility transistor amplifier⁶ is attached to the 4K-stage of the dilution refrigerator to amplify the output signal reflected from the resonant circuit. Several attenuators are mounted on the various cooling plates along the input line of the RF-circuit to provide a total attenuation of 70 dB. At room temperature, the DC-signals are generated by digital analog converters⁷. The RF-signals are sent and read using a high frequency lock-in amplifier⁸. A low frequency voltage modulation can also be sent to the plunger gate P thanks to an isolating transformer⁹.

4.1.2 Simulations of the readout circuit

In 2021, Liu et al. [Liu et al. 2021] presented the implementation of a radiofrequency readout setup for the charge sensing of Si/SiGe double quantum dot devices using a single electron transistor (SET). In particular, they wondered where to place the readout system to get the largest charge signal. They demonstrate that placing the LC-resonator either on an ohmic contact, or on an accumulation gate of their SET can lead to fast readout possibilities. In the following, we transpose these two different approaches¹⁰ to our system and comment on their differences.

Resistances and capacitances proper to the device

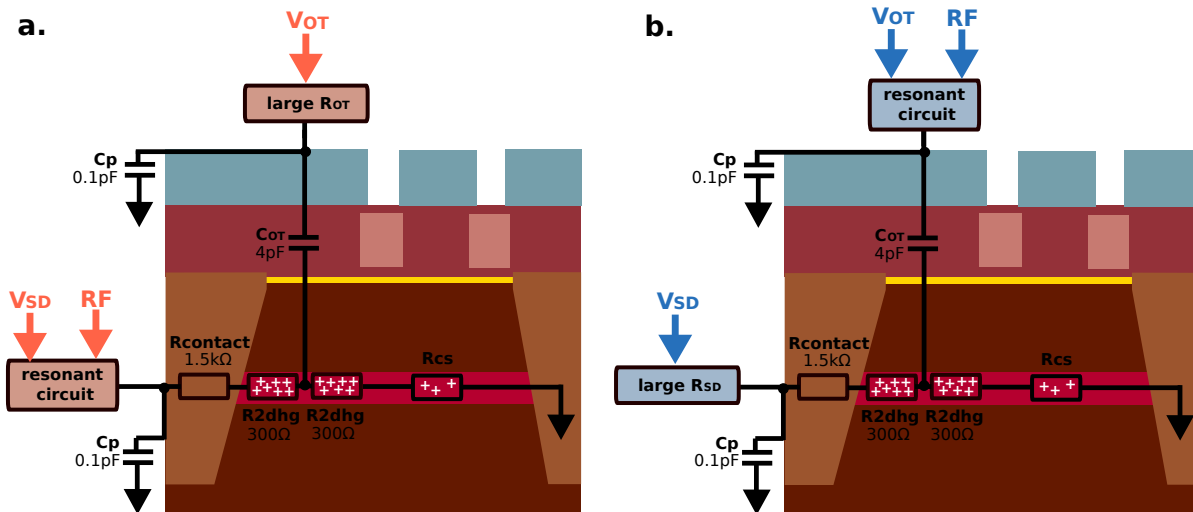


Figure 4.3 – **Ohmic and accumulation approaches.** (a) Simplified schematic of the readout circuit for the ohmic approach, where the resonant circuit is connected to an ohmic contact. (b) Simplified schematic of the readout circuit for the accumulation approach, where the resonant circuit is connected to the accumulation gate OT.

5. BlueFors LD Dilution Refrigerator System with bottom-loader
6. HEMT amplifier Low-Noise Factory (ref:LNF-LNC0.2-3A)
7. DAC from iTEST
8. UHF Lock-In Amplifier from Zurich Instrument
9. Isolating Transformer (1:1) from Physics Basel (ref:SP921a)
10. Namely, the ohmic approach and the accumulation approach.

Figure 4.3 schematises the two different approaches and the parasitic capacitances and resistances of the single quantum dot device. For both approaches, the ohmic contact or the accumulation gate that is not connected to the readout setup must be protected by a large resistor to prevent parallel RF paths from shunting the signal to ground.

In the ohmic approach, the LC circuit is directly bonded to the ohmic contact. The RF-signal reaches the device via the contact resistance of the ohmic contact with the heterostructure R_{contact} . A low value of R_{contact} is sign of a good quality of the interface between the aluminium and the germanium. It can vary between $100\ \Omega$ and $100\ \text{k}\Omega$ depending on the fabrication process. The RF-signal propagates afterwards through the 2DHG of resistance $R_{2\text{DHG}}$ formed under the accumulation gate OT. The value of $R_{2\text{DHG}}$ has been estimated to be around $600\ \Omega$ from previous work [Fernandez-Bada 2023]. The 2DHG has a parallel capacitance to the gate OT C_{OT} estimated around $4\ \text{pF}$. OT has itself a parasitic capacitance to ground C_P of $0.1\ \text{pF}$ due to the bonding pad. We added a large resistor to OT R_{OT} ¹¹ to filter out the parasitic resistances and capacitances of the circuit used to power the gate. The 2DHG is then directly connected to sensing dot, which we model as a resistor R_{CS} .

For the accumulation approach shown in Figure 4.3 (b), the RF-signal arrives on the device chip through C_{OT} . It is then split into two paths. The first, passing through half of the 2DHG resistance $R_{2\text{DHG}}$ goes to the contact resistance with the ohmic R_{contact} , and then to a DC-input protected by a large resistor R_{SD} , in parallel with a parasitic capacitance to ground C_p . The second path, passes through half of the 2DHG resistance $R_{2\text{DHG}}$ and directly goes to the resistance of the sensing dot R_{CS} . By choosing $R_{SD} = 1\ \text{M}\Omega$ we avoid the RF signal being shunted to ground at the ohmic contact.

Equivalent circuit of the full radiofrequency setup

For both ohmic and accumulation approaches, the LC-circuit is implemented on the PCB. It is composed by an inductor L ¹² and a capacitor C_{match} ¹³ in parallel of the parasitic board capacitance C_{board} . The values chosen for these components are discussed in the following Section. The LC-circuit is coupled to a $50\ \Omega$ transmission line on the PCB through a coupling capacitor C_c ¹⁴. The capacitor enables to read the resonant circuit response by measuring $|S_{21}|$ through the transmission line while allowing to isolate the RF lines from the DC biasing of the resonator. A bias resistor R_{SD} or R_{OT} ¹⁵ is soldered before the resonant circuit to allow DC biasing through the resonator. Simplified equivalent circuits of the full radiofrequency setup for the two approaches are presented in Figure 4.4 (a) and (c). Many resistances, inductances and capacitances are not shown as their influence on the simulated frequency response is negligible.

The resonant readout circuit is designed to be as sensitive as possible to variations of the sensing dot channel resistance R_{CS} . Simulations¹⁶ of the sensitivity to R_{CS} are shown in Figure 4.4, for

-
11. Resistor $1\ \text{M}\Omega$ Vishay (ref:MMU01020C1004FB300)
 12. High-performance inductor $820\ \text{nH}$ Coilcraft (ref:0805HP-821XGRB)
 13. Capacitor $3.9\ \text{pF}$ Vishay (ref:VJ0603D3R9CXP AJ)
 14. Capacitor $220\ \text{pF}$ Vishay (ref:VJ0603D22IKXAAJ)
 15. Resistor $4,7\ \text{k}\Omega$ Vishay (ref:MMU01020C4701FB300)
 16. The simulations have been performed on QUCS (open-source Quite Universal Circuit Simulator).

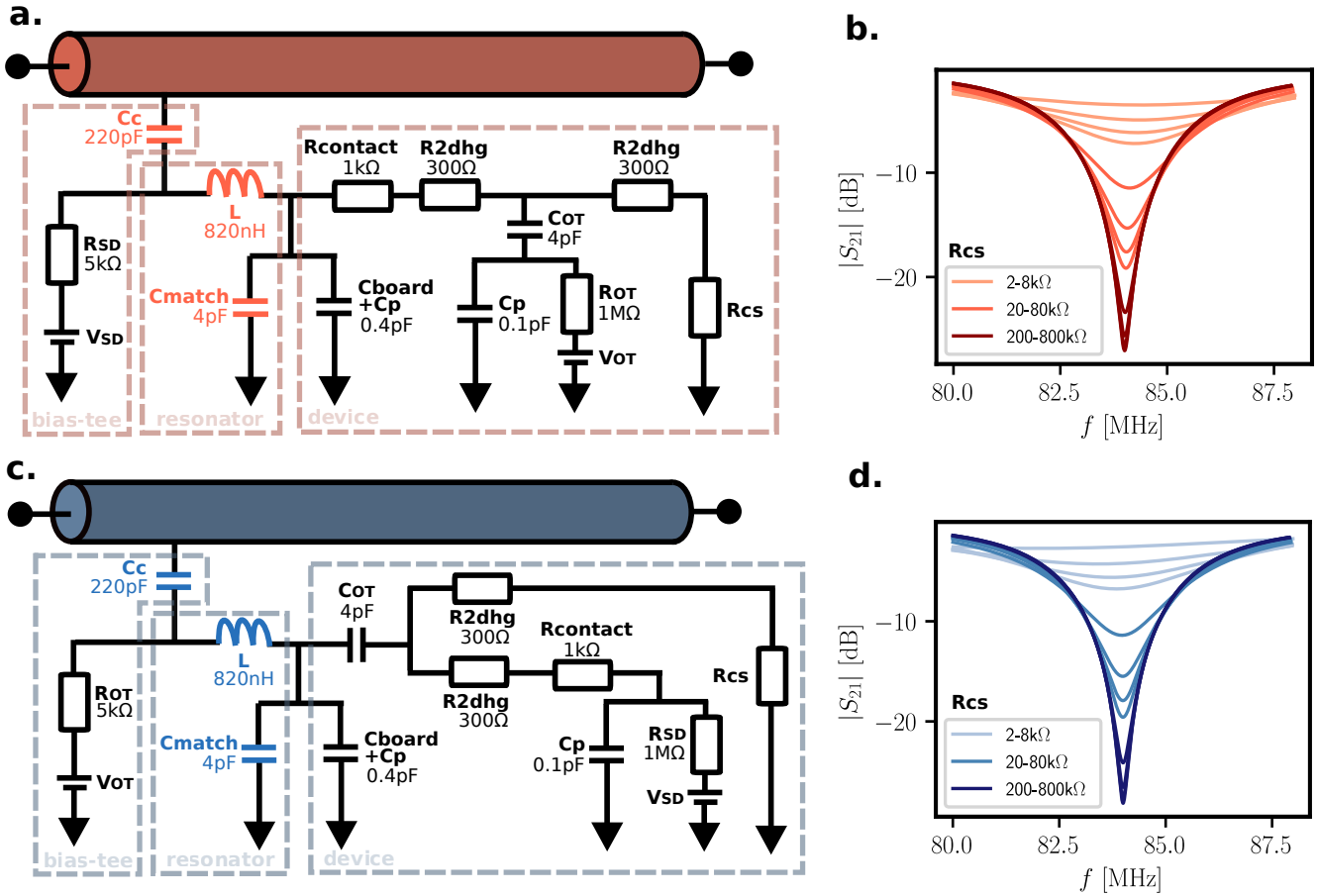


Figure 4.4 – **Equivalent readout circuit for the ohmic and accumulation approaches.** (a) Equivalent readout circuit when the radiofrequency setup is implemented on the ohmic contact of a lead. (b) Simulated frequency response of the circuit (a) for different ranges of variations of the dot resistance. The lightest colour is used for values of R_{CS} of 2 k Ω , 4 k Ω , 6 k Ω and 8 k Ω , the medium-tone colour for values of R_{CS} of 20 k Ω , 40 k Ω , 60 k Ω and 80 k Ω , and the darkest colour for values of R_{CS} of 200 k Ω , 400 k Ω , 600 k Ω and 800 k Ω . (c) Equivalent readout circuit when the radiofrequency setup is implemented on the accumulation gate of a lead. (d) Simulated frequency response of the circuit (c) for different ranges of variations of the dot resistance.

both ohmic (b) and accumulation (d) approaches. One can easily highlight the quasi-equivalence of the two approaches for the geometry of our devices and the typical values of L and C_{match} we are working with. We chose to implement the ohmic approach, which is the most common in the literature [Nico W. Hendrickx et al. 2021]. In the two graphs, the depth of the resonance strongly varies for values of R_{CS} in the range 20 – 80 k Ω , while it is less pronounced for higher values of R_{CS} in the range 200 – 800 k Ω . This is nevertheless the regime of interest, since we expect the resistance of the QD to be around a few hundred of k Ω . In the following section we will discuss how far it is possible to improve the matching of the readout circuit and what limits its sensitivity to high values of R_{CS} .

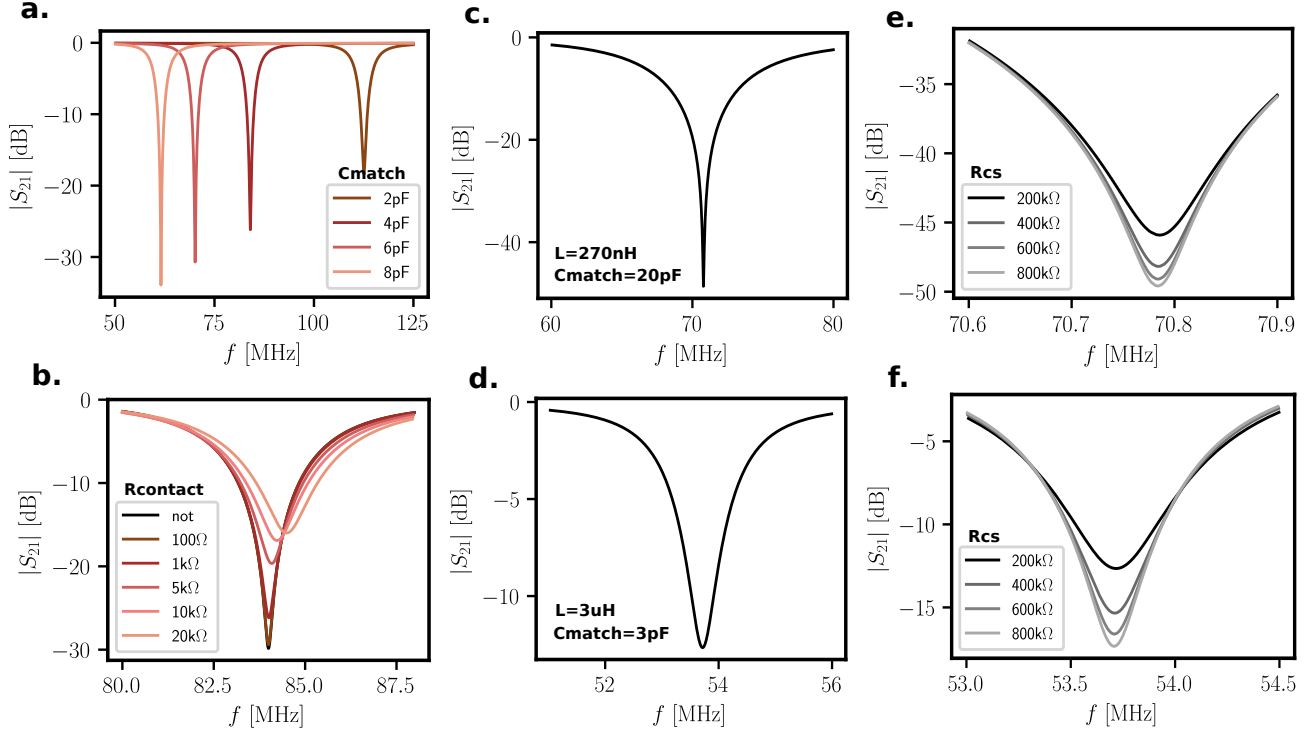


Figure 4.5 – **Circuit matching and sensitivity to the QW resistance.** (a) Influence of C_{match} on readout circuit matching and on the resonant frequency, for $R_{CS} = 800 \text{ k}\Omega$. (b) Evolution of the readout circuit matching with R_{contact} , for $R_{CS} = 800 \text{ k}\Omega$. (c) A well-matched readout circuit obtained with $L=270 \text{ nH}$ and $C_{\text{match}}=20 \text{ pF}$. Here, $R_{CS} = 800 \text{ k}\Omega$. (d) A less-matched readout circuit obtained with $L=3 \text{ uH}$ and $C_{\text{match}}=3 \text{ pF}$. Here, $R_{CS} = 800 \text{ k}\Omega$. (e) Sensitivity to changes in R_{CS} for the well-matched readout circuit (c). (f) Sensitivity to changes in R_{CS} for the less-matched readout circuit (d).

4.1.3 Circuit matching and sensitivity

Matching improvements and effects on sensitivity

One way to improve the matching of the readout circuit to the feedlines is to add a matching capacitor to ground C_{match} in parallel with the inductance. By adjusting its value to the chosen inductance L , we can change the impedance of the resonant circuit seen from the feedlines Z_{circuit} such that it drops to zero at resonance. Since the impedance of the readout circuit is in parallel to the transmission line, we can apply the Formula 4.1. It establishes [Pozar 2005] that the transmitted signal $|S_{21}| \rightarrow 0$ when $Z_{\text{circuit}} \rightarrow 0$. In Figure 4.5 (a), we can observe the influence of C_{match} on the matching, for a given $L = 820 \text{ nH}$. As we increase the value of C_{match} , the resonance becomes deeper and deeper until a certain threshold and then it degrades again. The resonant frequency gets lower when we increase C_{match} as $f_r \propto 1/\sqrt{LC_{\text{match}}}$. As a consequence, the addition of a large C_{match} can be a bottleneck due to the limited bandwidth of the amplifiers and filters used to perform the radiofrequency measurement.

$$|S_{21}| = \frac{2Z_{\text{circuit}}}{2Z_{\text{circuit}} + Z_0} \quad (4.1)$$

Matching is not the only limiting factor in increasing the sensitivity of the readout circuit to large values of the sensing dot resistance R_{CS} . We simulated two radiofrequency circuits in the ohmic approach for two couples of L and C_{match} . The matching obtained with the first circuit, in Figure 4.5 (c), is greater than the matching obtained with the second circuit, in Figure 4.5 (d). However, these two circuits show the same sensitivity in dB to variations of R_{CS} in the range 200 – 800 k Ω , as plotted Figures 4.5 (e) and (f). The resistive and capacitive environment around R_{CS} plays a direct role in the maximum sensitivity of the readout circuit. Simulations shown that decreasing R_{contact} and $R_{2\text{DHG}}$ down to 500 Ω helps to increase the sensitivity. Reducing the parasitic capacitance of the accumulation gate to ground C_p below 1 pF also helps increasing the sensitivity. To prevent a strong decrease of the sensitivity, we found that the resistor protecting the DC-input of the accumulation gate R_{OT} has to be set above 100 k Ω , and that the capacitance of the 2DHG to the accumulation gate C_{OT} has to be maintained on the order of a few pF. All these parameters imposed by the properties of the device act on the sensitivity but also on the matching. Figure 4.5 (b) highlights the deterioration of the matching with the increase of the contact resistance R_{contact} .

Resonant frequency and effects on sensitivity

For a given set of R_{contact} , $R_{2\text{DHG}}$, C_{gate} and C_p imposed by the properties of the device, the sensitivity is maximum in a certain range of frequencies. Indeed, it occurs when L and C_{match} are such that the impedance of the full readout circuit drops to zero for the values of R_{CS} we are interested to work with. Figure 4.6 shows the evolution of the sensitivity with the resonant frequency of the readout circuit. We simulated the frequency response for three different couples of L and C_{match} , resulting in readout circuits resonating at 20 MHz, 80 MHz and 300 MHz. These simulations were extended to many other L and C_{match} couples. We observed the best sensitivities for frequencies below 100 MHz. The largest variations of the resonance depth are about 5 dB for a variation of R_{CS} from 200 k Ω to 800 k Ω . The sensitivity of the readout circuit at 20 MHz is slightly better than the one at 80 MHz, but its bandwidth is smaller. The readout circuit at 300 MHz shows a very low sensitivity to R_{CS} in the 200 – 800 k Ω range, as the impedance of the circuit shows a saturation for this range of resistances. Different couples of L and C_{match} allow to reach good sensitivities under 100 MHz, with L starting from a few hundred of nH up to tens of μH . Table 4.1 proposes several couples of standard inductor values with their C_{match} associated. In the table, f_r is the resonant frequency of the full circuit, $|S_{21}|_{\text{min}}$ is the depth of the resonance enabling to evaluate the matching quality, and $\Delta|S_{21}|_{R_{CS}=200-800\text{k}\Omega}$ is the variation of the depth for R_{CS} starting from 200 k Ω to 800 k Ω which allows to quantify the sensitivity.

L [nH]	C_{match} [pF]	f_r [MHz]	$ S_{21} _{\text{min}}$ [dB]	$\Delta S_{21} _{R_{CS}=200-800\text{k}\Omega}$ [dB]
270	20	71	-49	5
470	8	81	-37	5
820	4	84	-27	5
3000	3	54	-18	5

Table 4.1 – Several couples of L and C_{match} allowing for the maximum sensitivity.

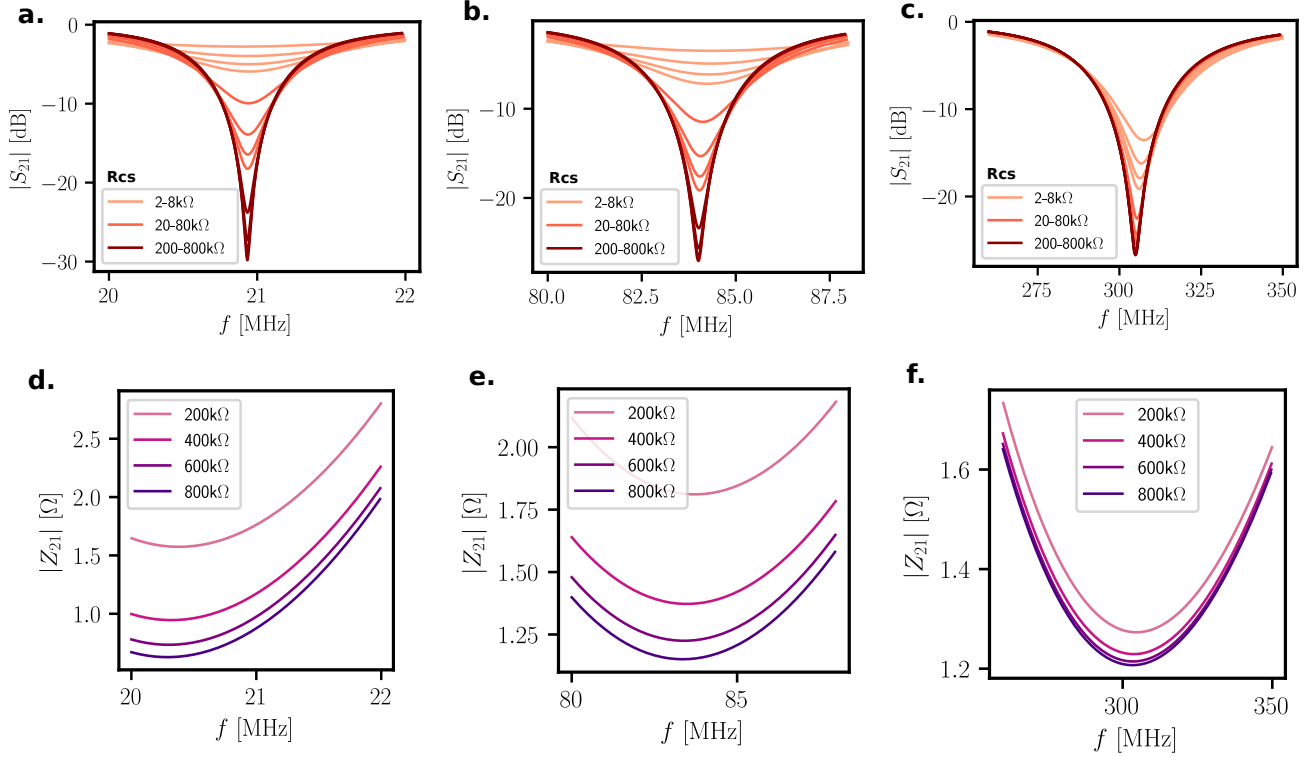


Figure 4.6 – **Evolution of the sensitivity with the resonant frequency.** (a) (b) (c) Simulated frequency response of readout circuits design to resonate at 20 MHz, 80 MHz and 300 MHz respectively, for different ranges of variations of the dot resistance. The lightest colour is used for values of R_{CS} of 2 k Ω , 4 k Ω , 6 k Ω and 8 k Ω , the medium-tone colour for values of R_{CS} of 20 k Ω , 40 k Ω , 60 k Ω and 80 k Ω , and the darkest colour for values of R_{CS} of 200 k Ω , 400 k Ω , 600 k Ω and 800 k Ω . (d) (e) (f) Impedance of the readout circuit around the resonance for values of R_{CS} of 200 k Ω , 400 k Ω , 600 k Ω and 800 k Ω .

4.1.4 Properties of the measured readout circuit

Following the simulations we performed, we decided to implement the readout circuit schematised Figure 4.4 (a) on the setup presented Figure 4.2 (a). We measured the transmitted signal $|S_{21}|$ as a function of the frequency of the input RF-signal, ensuring that no current circulates in the device. Figure 4.7 (a) highlights the agreement between the resonance estimated in advance from the simulations, and the resonance effectively measured at base temperature. This confirms our overall equivalent circuit for the ohmic approach, and the estimates of the different resistances and capacitances specific to the device. The measured resonant frequency is 83.7 MHz, which is at the limit of the bandwidth of the amplifiers used in the setup¹⁷.

By fitting the resonance in the IQ-plane as shown Figure 4.7 (b), we can determine the internal quality factor $Q_{\text{int}} = 165$ and the external quality factor $Q_{\text{ext}} = 10$ of the readout circuit. As $Q_{\text{int}} > Q_{\text{ext}}$, the internal losses are smaller than the coupling to the 50 Ω -feedlines. This is a suitable regime for radiofrequency readout because the signal photons can be read before they are lost in the resonant circuit.

17. The HEMT is designed to be used between 200 MHz and 3 GHz

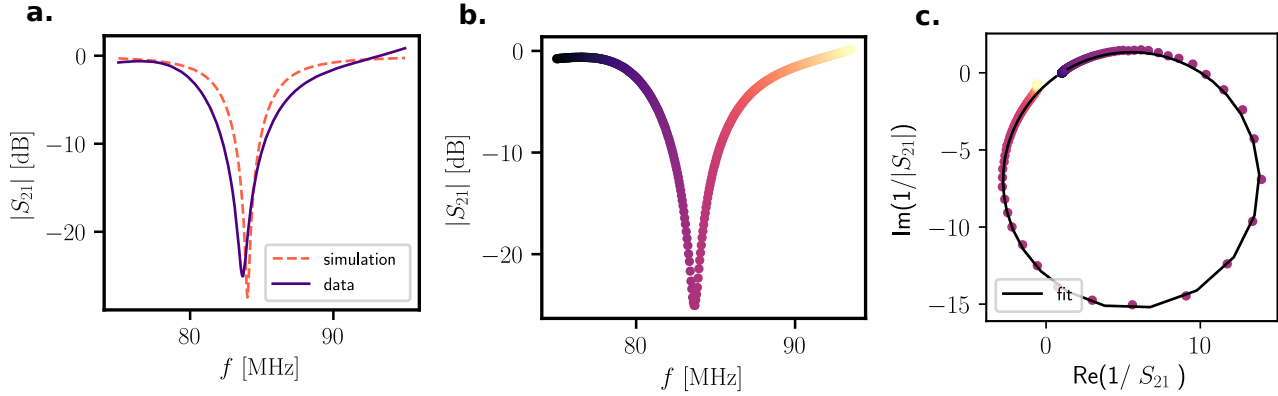


Figure 4.7 – **Resonance of the readout circuit.** (a) The measured resonance (in the purple solid line) and the simulated resonance (in the orange dashed line) from the circuit shown in Figure 4.4 (a). (b) The measured resonance. (c) IQ-plane plot and fit of the resonance in (b).

4.2 Charge sensing measurements and performances

The sensitivity of a single hole transistor is maximal when it is operated on the flank of a Coulomb peak, where $\delta I/\delta V$ is maximal. In this Part, we detail the tuning process required to form a single quantum dot to be used as a charge sensor. We characterise its charge sensitivity to an induced charge modulation, and we evaluate its charge noise. We comment on its performance and compare it with the literature.

4.2.1 Charge sensor tuning

To form a quantum dot under the plunger gate P, we need to carefully tune all the gates surrounding it to the appropriate regime. The first step in this process is to look at the threshold voltage of the different accumulation gates to work in saturation, in order to be sure that the leads are sufficiently accumulated. In Figure 4.8 (a), we can observe that the plunger P and the accumulation gates covering the ohmics OB and OT have a similar threshold voltage and opening characteristics. To tune the barriers, we record a 2D colour plot of the current, while sweeping the two barriers surrounding the dot. For this measurement, OB and OT are largely accumulated, P is set straight after its threshold voltage and the both BR and DP are set in depletion mode. From the map Figure 4.8 (b), one can determine BB and BT so that the amplitude of the Coulomb peaks is maximum. Finally, the bias voltage can be adjusted in order to obtain well separated Coulomb peaks.

Figure 4.8 (c) shows the Coulomb peaks of the sensing dot, measured in current and with the radiofrequency setup. All three signals arises from a variation of the resistance of the dot depending on its chemical potential alignment with source and drain. This explains the similarities between the signals. We built our radiofrequency setup such that a change of the dot resistance induces a change of the quality factor of the resonance. Thus, the amplitude of the transmitted signal at the resonant frequency varies with the dot resistance. We also observed some phase signal for the same reason, but the system is optimised to work with the amplitude of $|S_{21}|$. In the simulations performed on the previous Part, we estimated the maximum variation of the resonance depth to be around 5 dB for expected values of R_{CS} in the range 200 – 800 k Ω . In Figure 4.8 (c), we observe

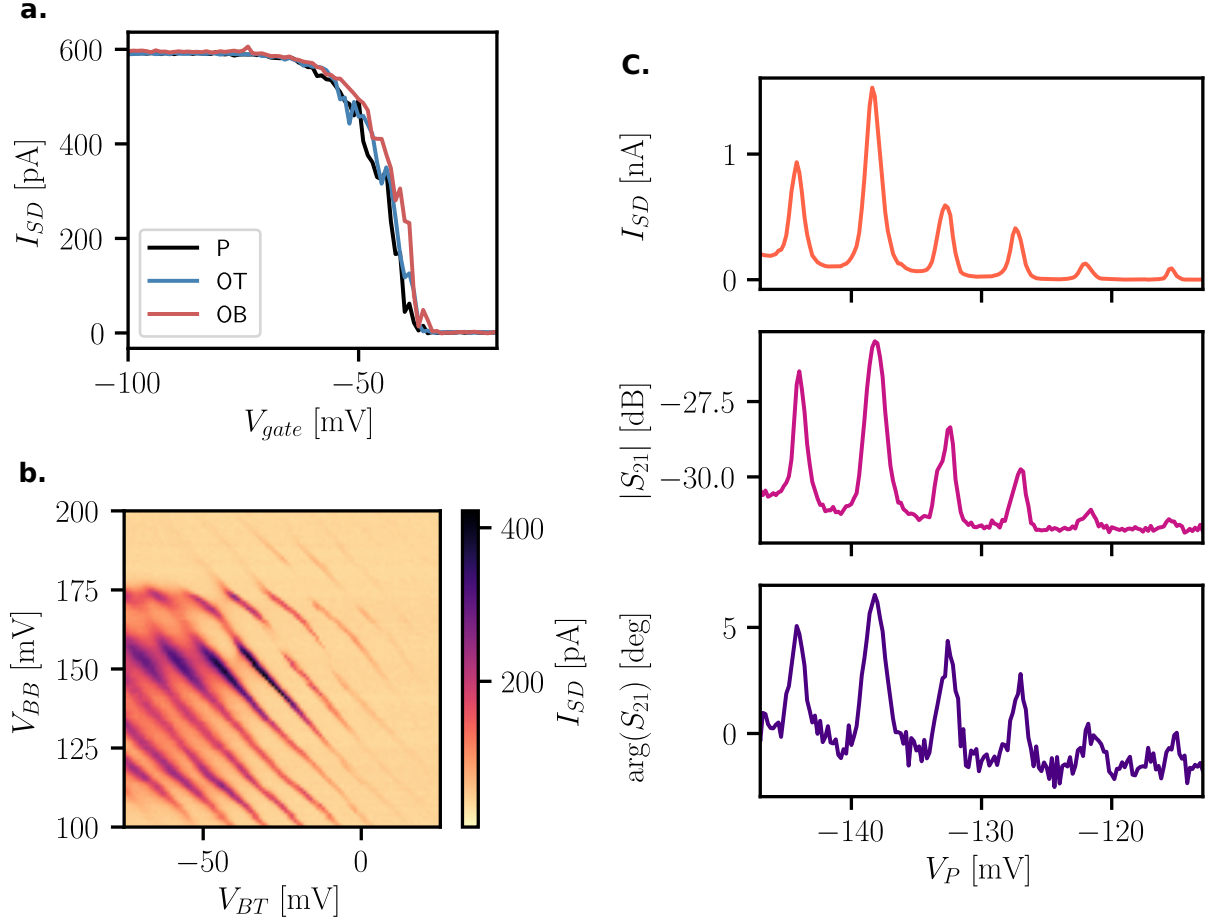


Figure 4.8 – **Tuning of the charge sensor.** (a) Source-drain current versus gate voltage for P, OT and OB. (b) 2D colour plot of the source-drain current while opening the barriers BB and BT. (c) Coulomb peaks of the dot formed under P, measured in current and in radiofrequency (amplitude and phase signals).

that the height of the Coulomb peaks measured in amplitude of the radiofrequency signal can reach almost 5 dB, which is in agreement with these simulations. Furthermore, if we plot the resistance corresponding to the IV-characteristic shown Figure 4.8 (c), we observe that it is varying in the range of a few hundreds of $k\Omega$ as predicted.

4.2.2 Charge sensitivity of the sensor

One approach to measure the charge sensitivity of our system is to apply a voltage modulation on the plunger gate P [Ahmed et al. 2018]. We first set the sensor on the side of a Coulomb peak and we excite the corresponding gate by sending a sinusoidal voltage modulation at a frequency f_m . This will induce a displacement of the Coulomb peak equivalent to a shift arising from the charging of a device measured by the charge sensor. The measurement presented Figure 4.9 (c) enables us to determine the equivalent charge variation Δq [e] for a given amplitude of the voltage modulation V_{mod} [V]. We varied amplitude of the voltage modulation and measured the shift of the Coulomb peaks in plunger gate voltage. We observed that a voltage modulation of 300 mV induces a shift from one charge, i.e. $\Delta q/|e| = \beta V_{mod}$ with $\beta = 0.3 \text{ V}^{-1}$. The result of the mod-

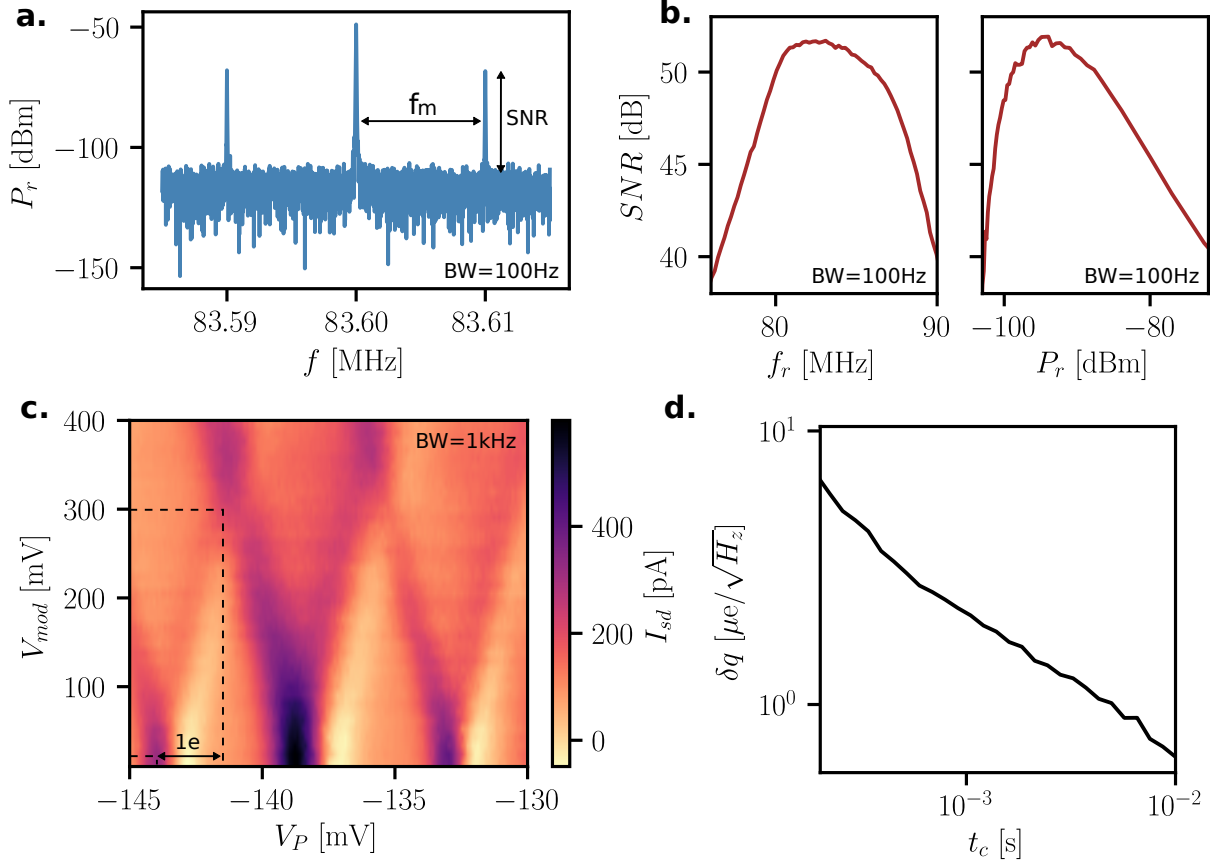


Figure 4.9 – **SNR optimisation and charge sensitivity.** (a) Frequency spectrum of the transmitted signal, measured with an integration time $t_c = 10$ ms and a voltage modulation $V_{\text{mod}} = 35$ mV (equivalent to 80 μV after attenuation). The two side peaks correspond to the voltage modulation applied to the plunger gate P. (b) Evolution of the SNR with the readout frequency and the power applied on the resonant circuit, measured with an integration time $t_c = 10$ ms. (c) Shift of the Coulomb peaks as a function of the amplitude of the voltage modulation V_{mod} applied on P. This graph enables to convert V_{mod} into an equivalent charge modulation. It is measured with an integration time $t_c = 1$ ms. (d) Charge sensitivity as a function of the integration time. It follows a square root trend.

ulation is the appearance of two side peaks in the frequency spectrum of the transmitted signal, as observed Figure 4.9 (a). They are detuned by $\pm f_m$ from the peak at the resonant frequency of the radiofrequency circuit. The height of the side peaks compared to the noise floor directly gives the signal-to-noise ratio for a given charge variation. We observe that this SNR is maximum if the readout is performed at the resonant frequency and with a power close to -90 dBm (see Figure 4.9 (b)).

$$\delta q = \frac{\Delta q}{\sqrt{2RBW} \times 10^{\text{SNR}/20}} \quad (4.2)$$

From the SNR measured for a given charge variation, we can compute the charge sensitivity of

the readout circuit using the Formula 4.2. The resolution bandwidth RBW is the inverse of the integration time required to measure the signal. Figure 4.9 (d) shows the evolution of the charge sensitivity with the integration time of the UHF t_c . We observe that δq is inversely proportional to $\sqrt{t_c}$ in the range $t_c = 0.2 - 10$ ms, which is in accordance with the Formula 4.2. For longer values of t_c , we expect the 1/f-noise to limit the increase of sensitivity. The table 4.2 brings a comparison between our results and sensitivities of other setups based on RF-SET or gate-sensing. For a RBW of 1 kHz, we measured a charge sensitivity $\delta q = 2.1 \mu\text{e}/\sqrt{\text{Hz}}$. It is in the same order of magnitude of the other values gathered in the table. A fine comparison between setups is complicated because the measurements are not made using the same RBW. It could be tricky to interpolate the different values, as the sensitivities may not fit into $\sqrt{t_c}$ for all setups.

Material	Readout	f_r [MHz]	δq [$\mu\text{e}/\sqrt{\text{Hz}}$]	RBW [Hz]	Reference
Ge	RF-SHT	83	2.1	1000	this work
Al	RF-SET	1700	12	23	[Schoelkopf et al. 1998]
Al	RF-SET	345	1	15000	[Brenning et al. 2006]
Si	Gate-sensing	330	7.7	10	[Ahmed et al. 2018]
Si	Gate-sensing	730	1.3	20	[Ahmed et al. 2018]

Table 4.2 – State-of-the-art charge sensitivities

4.2.3 Sensor signal and charge noise

Sensor signal and maximum SNR

The displacement of a Coulomb peak from half a charge gives the maximum SNR we can get from the sensing setup. Hence, by comparing the signal obtained in the flank of a peak and in the noise floor, as indicated Figure 4.10 (a), one can extract the maximum SNR at a given integration time. To perform this time measurement, we set the sensor on the flank of a Coulomb peak, and measure the transmitted signal for a certain time without applying any excitation on the system. We repeat this measurement setting the sensor in its noise floor. By plotting the two signals in the IQ-plane, as shown Figure 4.10 (c), we can extract the maximum SNR using the Formula 4.3, where d is the distance between the centres of the signals and σ is the standard deviation. We measured a maximum SNR = 13 for an integration time $t_c = 100 \mu\text{s}$ and a full measurement time close to the second. In the following Part, we compare this maximum SNR value with the effective SNR obtained when sensing a DQD. This helps to assess how well the charge sensor can be integrated into a more complex design.

$$\text{SNR} = \frac{d^2}{\sigma^2} \quad (4.3)$$

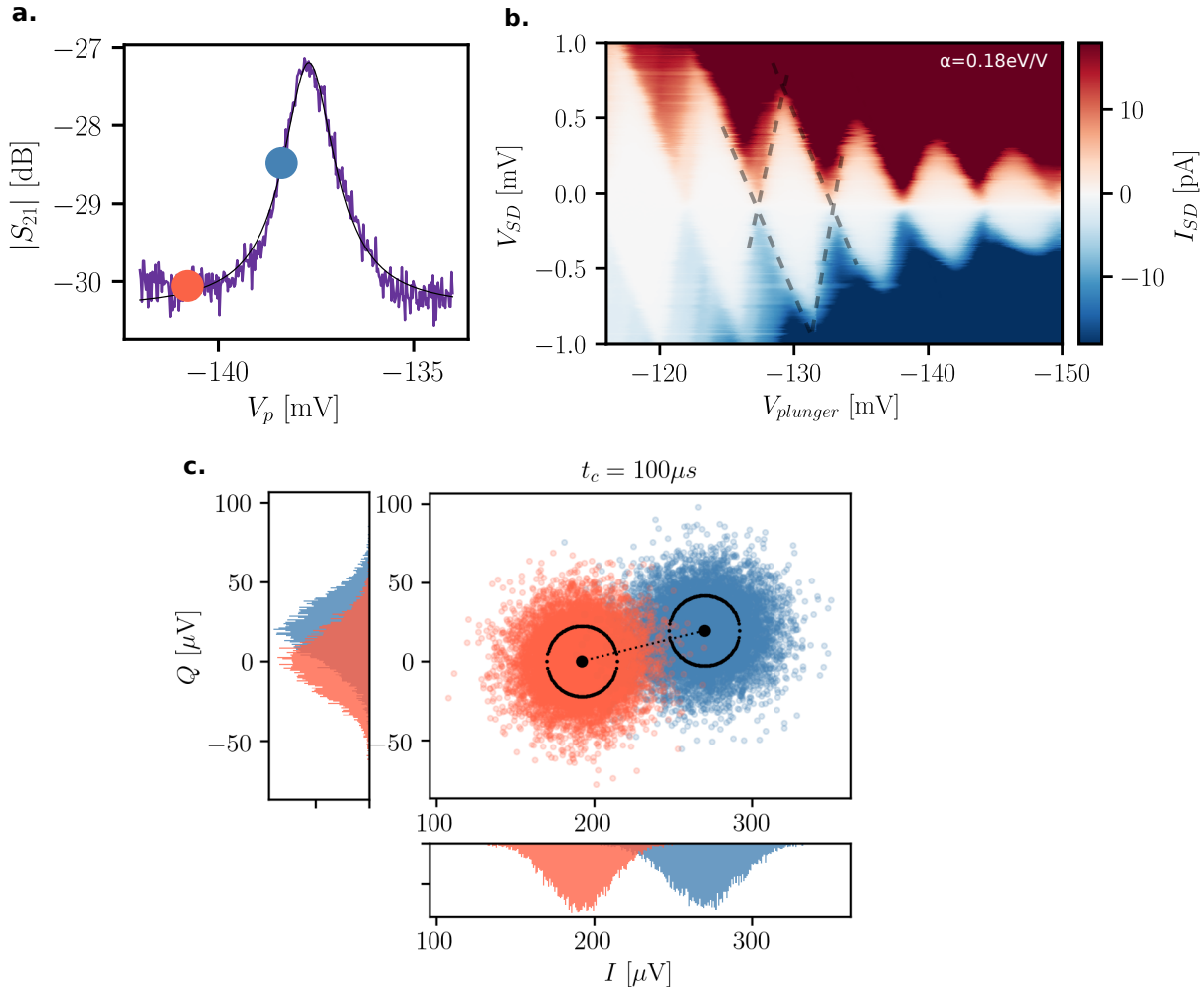


Figure 4.10 – **Maximum SNR and lever-arm.** (a) Zoom on the Coulomb peak on which the maximum SNR and charge noise measurements are performed. The time traces are recorded on the flank of the peak (orange dot), or on the background (blue dot). (b) Coulomb diamonds when sweeping the plunger and the source drain voltages. (c) Difference between the signals on the flank of the peak and on the background plotted in the IQ-plane. The separation between the signals gives the maximum SNR that can be obtained with the setup for an integration time of 100 μ s.

Time measurement and charge noise

The time signal measured on the flank of the peak has more noise than the time signal measured on the background, as we can observe in Figure 4.11 (a). This is the signature of the charge noise. Using the Formula 4.4, we can convert the fluctuations of the transmitted signal in volts $V_{S_{21}}$ into dot energy fluctuations δ_μ . To process, we need to use two different renormalisation factors $|dV_{S_{21}}/dV_P|$ and α . $|dV_{S_{21}}/dV_P|$ correspond to the slope of the Coulomb peak at the measurement point. It allows the transmitted signal in volts to be converted to a gate voltage signal. We measured a slope of $0.16 V_{S_{21}}/V_P$ from the Coulomb peak plotted Figure 4.10 (a). α is the lever arm of the plunger gate. It allows to convert a gate voltage signal into a variation of the dot energy. From the measurement presented Figure 4.10 (d), we extracted the lever arm of the plunger gate $\alpha = 0.18 \text{ eV}/V_P$ from the slope of a Coulomb diamond formed by sweeping the plunger gate and the source-drain voltages. The resulting dot energy fluctuations are plotted Figure 4.11 (b). For

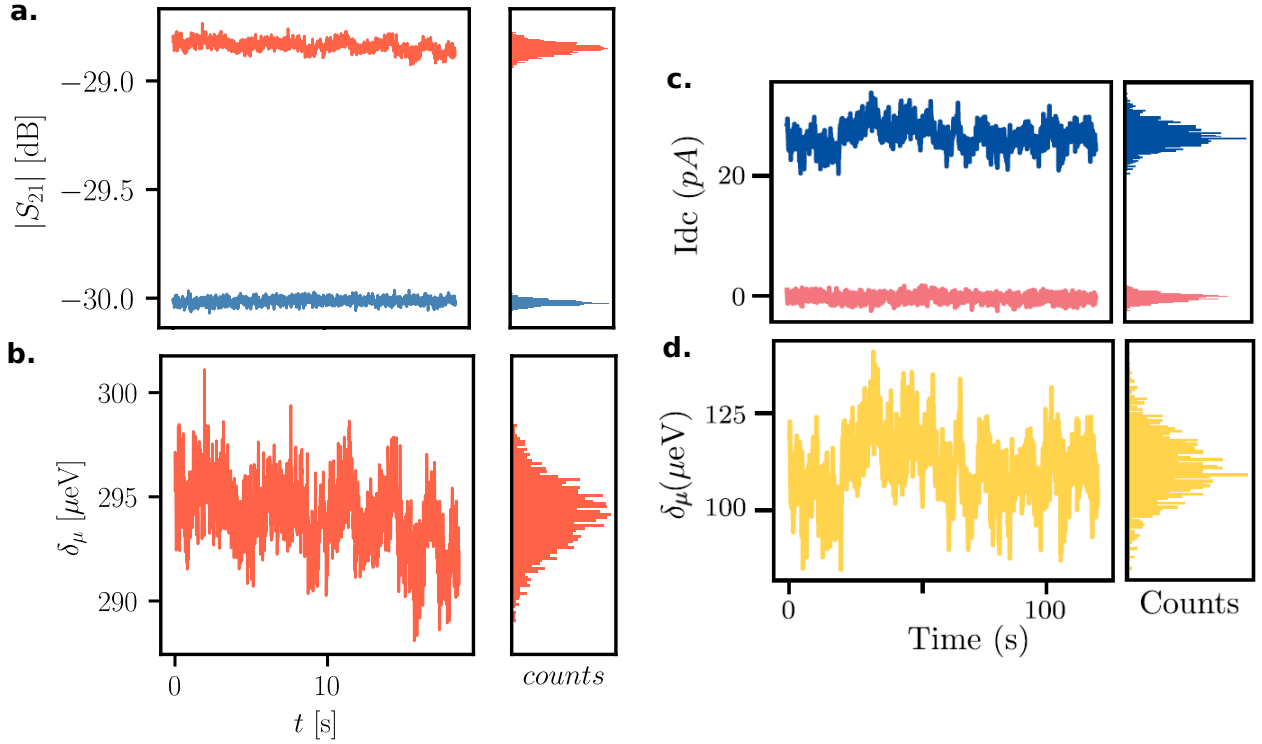


Figure 4.11 – **Time measurement of the charge.** (a) Time measurement of the transmitted signal at the two points represented Figure 4.10 (a). It highlights that the noise on the flank of the peak is larger than the background noise. (b) Equivalent time variations of the charge, measured on the flank of the peak. The voltage signal has been normalised by the slope of the Coulomb peak and the lever-arm. (c) Similar time measurement performed on a comparable device by current sensing by G. Troncozo [Fernandez-Bada 2023]. The blue curve corresponds to the current signal measured on the flank of the peak, while the pink curve corresponds to the current signal measured on the background. (d) Equivalent time variations of the charge on the flank of the peak, renormalised by G. Troncozo.

purposes of comparison, Figures 4.11 (c) and (d) present time measurements performed by G. Troncozo [Fernandez-Bada 2023] on a similar device from a different fabrication batch. It is clear that the charge fluctuations are larger for the device measured by G. Troncozo.

$$\delta_\mu = \frac{1}{|dV_{S_{21}}/dV_P|^2} \alpha^2 V_{S_{21}} \quad (4.4)$$

$$S_\mu = \frac{1}{|dV_{S_{21}}/dV_P|^2} \alpha^2 S_{V_{S_{21}}} \quad (4.5)$$

Figure 4.12 (a) shows the power spectral density (PSD) of the time signals measured on the flank of the Coulomb peak and on the background. For frequencies below a few Hz, the background noise is constant with the frequency, while the noise on the flank of the peak follows a $1/f$ trend as expected for charge noise. At higher frequencies, the signals are distorted by the RF-filters of

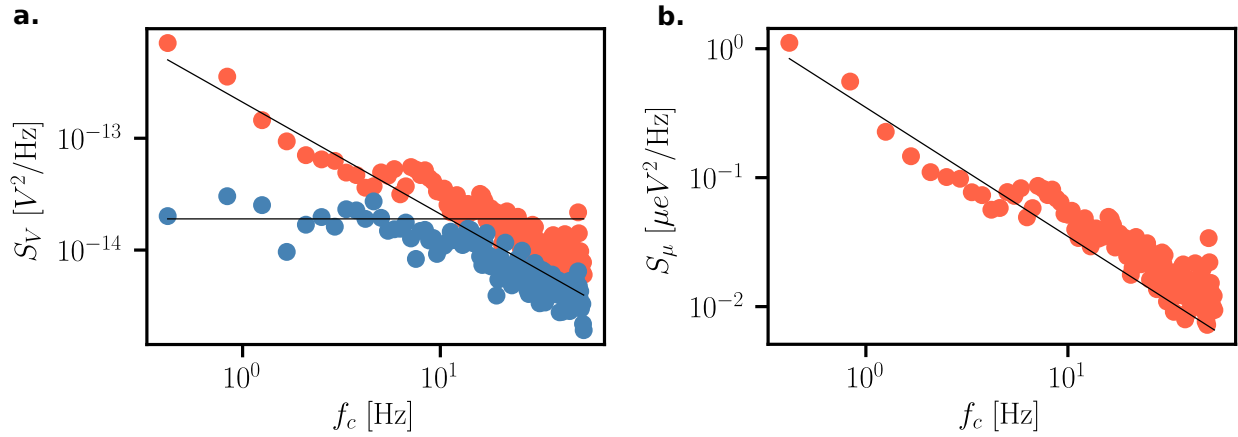


Figure 4.12 – **Low-frequency charge noise.** (a) Power spectral density of the transmitted signal in the flank of the peak (orange) and in the background (blue). The noise in the flank of the peak is fitted with a $1/f$ trend, while the noise in the background is constant. (b) Equivalent charge noise on the flank of the Coulomb peak, fitted with a $1/f$ trend. The voltage signal has been normalised by the slope of the peak and the lever-arm.

the setup (-3 dB at 100 Hz). We use the Formula 4.5 to convert the transmitted signal PSD S_V into an energy PSD S_μ , plotted in Figure 4.12 (b). The charge noise at 1 Hz is a common figure of merit of the devices. From Figure 4.12 (b), we extracted $S_\mu(1 \text{ Hz}) = 0.5 \mu\text{eV}/\sqrt{\text{Hz}}$. In such complex devices, the noise sources are multiple and their predominance is not clearly established. Yet, many studies suggest that the charge noise mainly arises from the charges trapped inside and at the interfaces of the Al_2O_3 [Connors, JJ Nelson, et al. 2019]. These charges are responsible for measuring a non-zero current while all the gates are grounded. They can reach densities of up to $10^{12} - 10^{13} \text{ cm}^{-2}$ [Jordan et al. 2016]. A fraction of this charges are mobile due to the proximity with the ohmic contacts (or traps) and the natural displacement of the amorphous insulator bindings. These mobile charges can generate charge noise when distributed around the Fermi level of the dot. As a consequence, the charge noise is strongly dependent on the polarisation point. Other candidates for charge noise include the presence of charged dislocations in the heterostructure.

Table 4.3 resumes the lowest charge noise measured on different semiconductor devices. The charge noise we measured on our SHT charge sensor is comparable to the state-of-the-art charge noise reported for germanium [Mario Lodari et al. 2021]. It is from an order of magnitude lower than the charge noise measured on a similar device by G. Troncoso [Fernandez-Bada 2023]. This difference might be explained by a better quality of the interface between the SiGe and the Al_2O_3 and the very different polarisation point we worked with. In Figure 4.11 (b) and (d), we clearly observe that the charge variations are at least 5 times larger for the device measured by G. Troncoso on a similar time range. The work carried out by B. Paquelet Wuetz [Paquelet Wuetz et al. 2023] highlights the variability of the charge noise between measurements performed on the same device but on different Coulomb peaks (different polarisation points). We have not tried to optimise the charge noise by looking at other Coulomb peaks or by changing the tuning of the device. This would be an interesting optimisation work.

Material	Readout	$S_{\mu}(1 \text{ Hz})$ [$\mu\text{eV}/\sqrt{\text{Hz}}$]	Reference
Ge	RF	0.5	this work
Ge	current	8.1	[Fernandez-Bada 2023] (similar device)
Ge	current	0.6	[Mario Lodari et al. 2021]
Ge	current	1.4	[N. W. Hendrickx, D. Franke, et al. 2018]
SiMOS	RF	0.5	[Connors, J. Nelson, et al. 2022]
Si/SiGe	current	0.8	[Freeman et al. 2016]
Si/SiGe	current	0.3	[Paquelet Wuetz et al. 2023]
GaAs	current	0.5	[You et al. 2015]

Table 4.3 – State-of-the-art charge noise for SETs or SHTs

4.3 Charge sensing of a double quantum dot

We have integrated a double quantum dot together with an SHT charge sensor, which is similar to the one we studied in the previous Part. We discuss here the perilous tuning process of such devices including many gates. We characterise the signal difference between two charge states of the DQD stability diagram and comment on the integration time required for their differentiation. We finally study the different noise sources and their predominance.

4.3.1 Double quantum dot design and experimental setup

Double quantum dot device

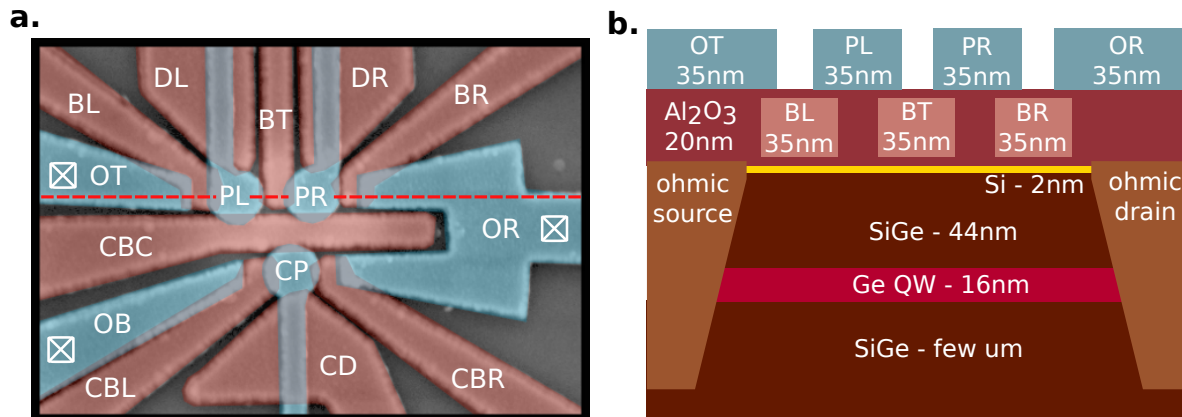


Figure 4.13 – **Gate layers and layer stack of the DQD devices** (a) SEM picture of the DQD gate layers. The barrier gates (first gate layer) are red-coloured, while the accumulation gates (second gate layer) are blue-coloured. (b) Transverse view of the layer stack along the red dashed line. The heterostructure is described in detail in Chapter 1.2.1.

The device layout integrating both a double quantum dot and a charge sensor is presented Figure 4.13. Similar to the single quantum dot devices, it has two gate layers, one dedicated to the barrier gates and one to the accumulation gates. A set of barrier and accumulation gates enables

board containing the RC-filters and the bias-tees. The whole is placed in the mixing chamber of the dilution refrigerator. In total, we used 18 DC-lines to control the gate voltages, 2 RF-lines for the radiofrequency readout, and 9 RF-lines to apply fast pulses to the gates, which could be used to manipulate the DQD. At room temperature, we added an Arbitrary Waveform Generator (AWG) in order to deliver fast pulses¹⁸. It is triggered with the UHF, enabling for time-resolved measurements.

4.3.2 Double quantum dot tuning and stability diagram

DQD and CS tuning process

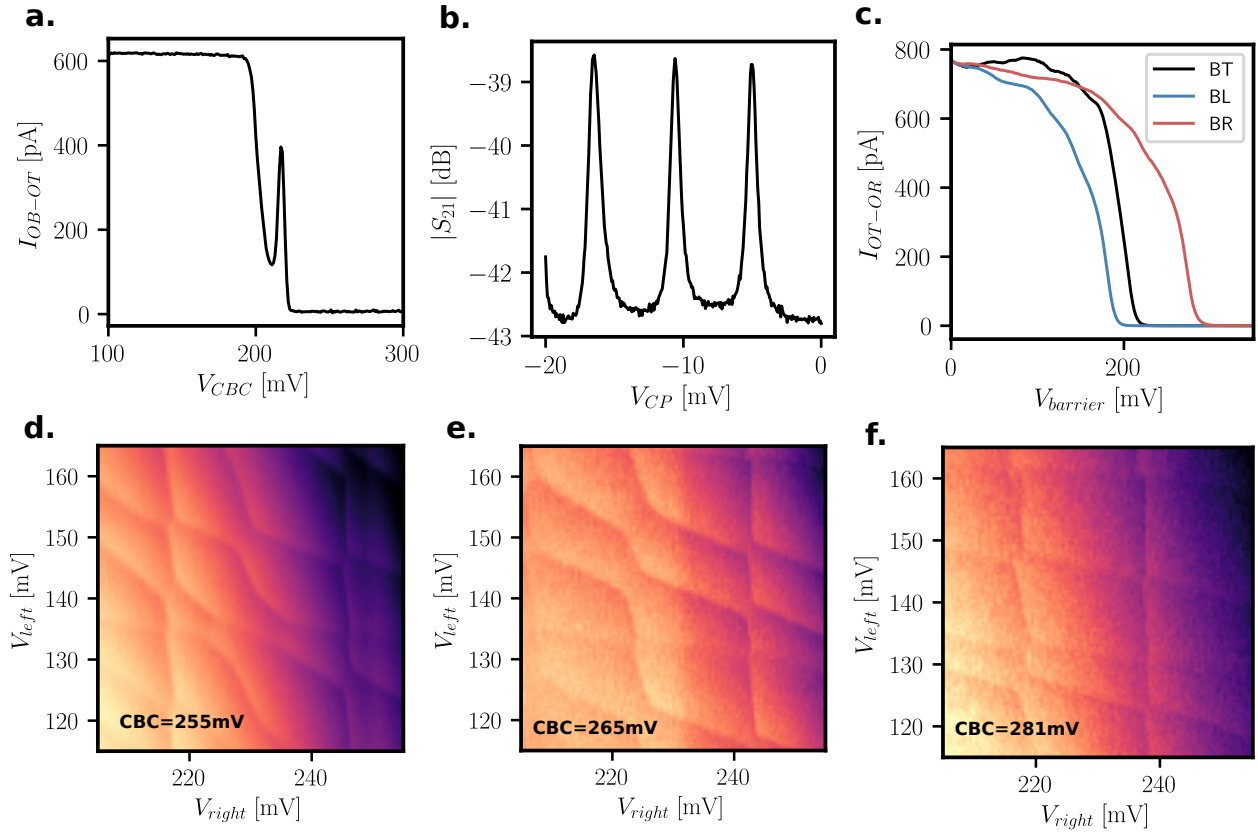


Figure 4.15 – **Double quantum dot tuning.** (a) Current-voltage characteristic of CBC, the barrier separating the double quantum dot from the charge sensor. (b) Coulomb peaks of the charge sensor. (c) Current-voltage characteristic of the barriers used to confine the double quantum dot. (d) (e) (f) Stability diagrams in the few hole regime recorded with the Video Mode, for different values of CBC.

To set the double quantum dot and the charge sensor in a working regime, we have to first isolate both entities. We start by closing all the current paths within the device by setting all gates to a positive voltage $V = 300$ mV. Then, we apply a bias voltage $V_{OB-OT} = 1$ mV between the ohmic contacts OB and OT, and we set a negative voltage $V = -200$ mV on their associated gates to accumulate charges. We progressively open CBC, the barrier separating the double quantum

18. AWG from Tektronix (ref: AWG5202)

dot from the charge sensor, and we measure the current flowing from OB to OT. From this current-voltage characteristic, presented in Figure 4.15 (a), we deduce the opening point of CBC and we ensure to work well above it. The next step is to tune the charge sensor as detailed in the previous section. We end up with the Coulomb peaks shown Figure 4.15 (b). The last step is to apply a bias voltage between the ohmic contacts under OT and OR to tune the DQD. We adjust the barriers first (Figure 4.15 (c)) and then the accumulation gates, until we obtain a stability diagram.

Video Mode and stability diagram

The large number of gates, the proximity of the DQD with the sensor and the small difference between the potentials applied on the barriers and the accumulations make possible the formation of parasitic dots. They can strongly disturb the stability of the double quantum dot, leading to a complex stability diagram. In order to make it more textbook, an intensive tuning process involving each gate has to be done. Indeed, the modification of the voltage of one gate usually requires a complete retuning of the DQD and the charge sensor. To speed up the process, we made extensive use of the Video Mode [Ezzouch 2021]. This measurement method enables to get rid of the communication time with the instruments between consecutive measurement points. It consists of continuously scanning the amplitude of the transmitted signal with the UHF, while sending voltage modulations on the gates with the AWG. Using this technique, it takes only a few seconds to record a map of 100×100 points. Hence, by recording several maps of the stability diagram while sweeping one of the gates and stitching them together, we can create a video that allows us to understand the role of the gate on the stability diagram of the complete system. We created videos for all the gates, for different configurations, which helped us to improve the confinement of the double quantum dot.

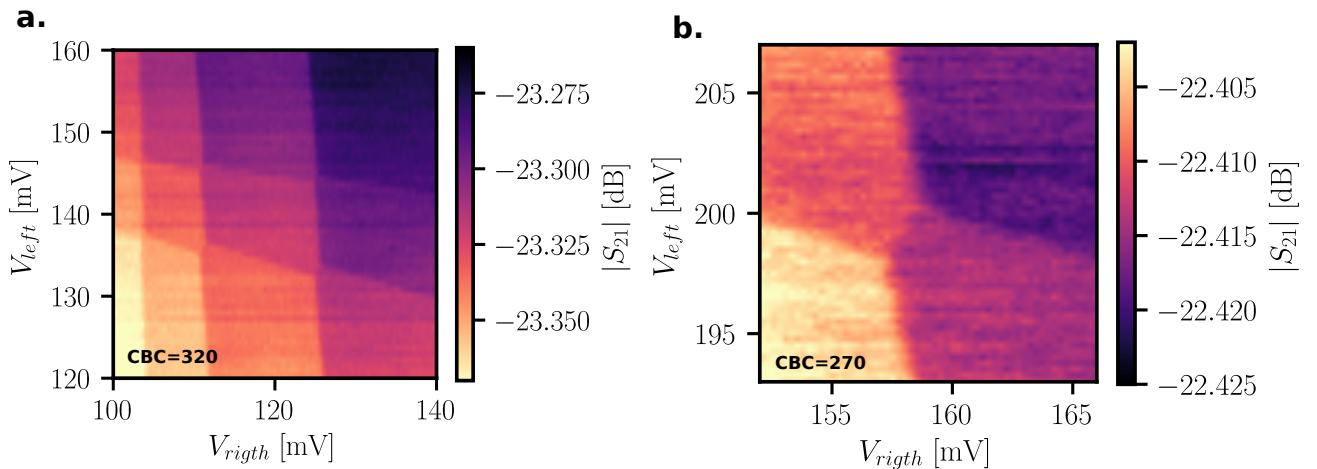


Figure 4.16 – **Stability diagram of the DQD.** (a) Stability diagram obtained after the tuning of the DQD and the charge sensor, with $CBC=320$ mV. (b) Zoom on an interdot transition, obtained with $CBC=270$ mV. We observe a better contrast between the charge states having the same total number of charges.

Figure 4.15 (d) (e) and (f) present three extracts of a video recorded with the Video Mode, highlighting the effect of CBC. Particular attention has been paid to this barrier as it governs the

coupling between the charge sensor and the DQD. On the one hand, lowering this barrier disturbs the stability diagram. On the other hand, it helps to increase the amplitude of the charge sensor signal and the contrast between the charge states, as shown Figure 4.16. A compromise must be found.

4.3.3 Charge sensitivity to the double quantum dot

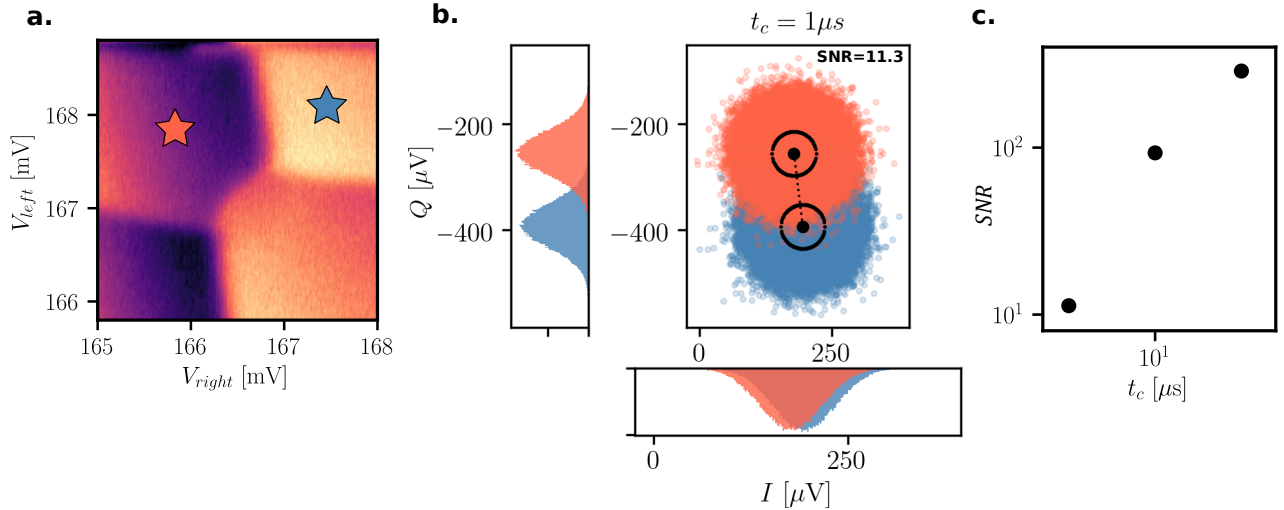


Figure 4.17 – **Signal difference between two charge states of the DQD.** (a) Stability diagram around a similar interdot recorded with the Video Mode. The blue and orange stars indicate the measurement points used to differentiate the two charge states around the interdot. (b) Histogram giving the signal separation of the two charge states for an integration time of 1 μs . The IQ signal is measured for 10 s. (c) Evolution of the signal separation for three different integration times.

The tuning of the DQD and the charge sensor strongly influences the contrast between the charge states. The ability to discriminate between two different charge states within a short time is required for many different measurements. To characterise this measurement efficiency, we studied the signal-to-noise ratio between two charge regions around a dot-lead transition. For this purpose, we recorded time traces in the two charge states for 10 s, for several integration times t_c . We plotted the time traces in the IQ-plane, as shown Figure 4.17 (b) for $t_c = 1 \mu s$. Then, we extracted the SNR for the different t_c using the Formula 4.3. The results are plotted in Figure 4.17 (c). We observe that the SNR increases linearly with t_c . As a matter of fact, the gap between the means of the signals remains constant but the standard deviation decreases when we increase the integration time. This results in a better differentiation of the two signals.

In the previous Part, we characterised the maximum signal we could get with such a sensor. This corresponds to the situation where the sensor shifts from half a Coulomb peak between two charge states. We found a maximum signal-to-noise ratio SNR=13.0 for $t_c = 100 \mu s$, whereas for the two charge states around the interdot mapped Figure 4.17 (a) we measured a SNR=11.3 for $t_c = 1 \mu s$. This strong improvement of the CS sensitivity could be explained by three reasons. First, the radiofrequency setup is more sensitive to variations of R_{CS} because the contact resistance of the ohmic is lower for the DQD device than for the single QD device, resulting from another fabrication

batch. Second, the sensor charge noise of the DQD device is lower¹⁹. Thirdly, the sensing dot integrated with the DQD is more sensitive to charge modulations than the sensor characterised alone, as we managed to form sharper and higher Coulomb peaks resulting in a larger slope $\delta I/\delta V$. In Figure 4.17 (b), we can note that the voltage separation between the centres of the signals is small compared to the voltage height of the sensor Coulomb peak used for the measurement. This means that the shift of the sensor Coulomb peak between two different charge regions is small. It could be increased by lowering the separation barrier or reworking on the integration of the CS with respect to the DQD. This is one way to further improve the readout speed.

4.3.4 Double quantum dot charge noise

The charge noise of the sensor and the charge noise induced by a charge transition of the DQD can greatly increase the integration time required to discern two charge states. To evaluate and compare these two noise sources, we recorded time traces in and out of a dot-lead charge transition (DLCT). At the DLCT, the noise spectrum contains the contribution of both the charge noise of the sensor and the charge noise acting on a charge transition of the DQD. Out of the DLCT, we only measure the charge noise of the sensor. Hence, by comparing the two signals, we can separate the noise contributions. We measured two time traces in and out the DLCT during 9 minutes, as shown Figure 4.18 (a). We plotted the PSD of both signals in and out the interdot in Figure 4.18 (c). We observe that the noise of both traces is very similar at high frequencies. At low frequencies under 5Hz, the noise recorded on the DLCT becomes larger as the frequency decreases. The charge noise acting on the DQD is therefore not negligible. It results from the charge fluctuations caused by the tunnelling events through the barrier.

We used the Formula 4.5 to compare the charge noise at 1 Hz for both signals in and out the DLCT. We extracted the slope of the sensor Coulomb peak at the measurement point and we obtained $|dV_{S_{21}}/dV_{CP}| = 0.5 V_{S_{21}}$. From the Coulomb diamonds plotted Figure 4.18 (b), we extracted the lever arm $\alpha = 0.21 \text{ eV}/V_{CP}$. Finally, we obtained a charge noise at 1 Hz $S_{\mu_{CB}}(1 \text{ Hz}) = 0.13 \mu\text{eV}/\sqrt{\text{Hz}}$ out of the DLCT²⁰, and $S_{\mu_{DLCT}}(1 \text{ Hz}) = 0.15 \mu\text{eV}/\sqrt{\text{Hz}}$ in the DLCT. These values are lower than the charge noise measured on the single QD device.

4.4 Conclusion

In this Chapter, we presented the experimental setup and the charge sensing readout circuit used to measure single and double quantum dot devices fabricated from a Ge heterostructure. We designed the readout circuit and investigated where it should be placed in order to maximise its sensitivity to the charge sensor resistance. We found out that the best sensitivities were obtained for LC readout circuit composed by an inductor and a parallel matching capacitor, the whole resonating around a few tens of MHz. This readout circuit should ideally be placed either on the ohmic contact of a lead, or on its accumulation gate. In a second time, we worked on the tuning of the many gates of the devices and established the stability diagram of a DQD. Among all the gates, we paid particular attention to the role of CBC, the barrier separating the DQD from the

19. We will verify this hypothesis in the next Session.

20. Namely in the Coulomb blocked region.

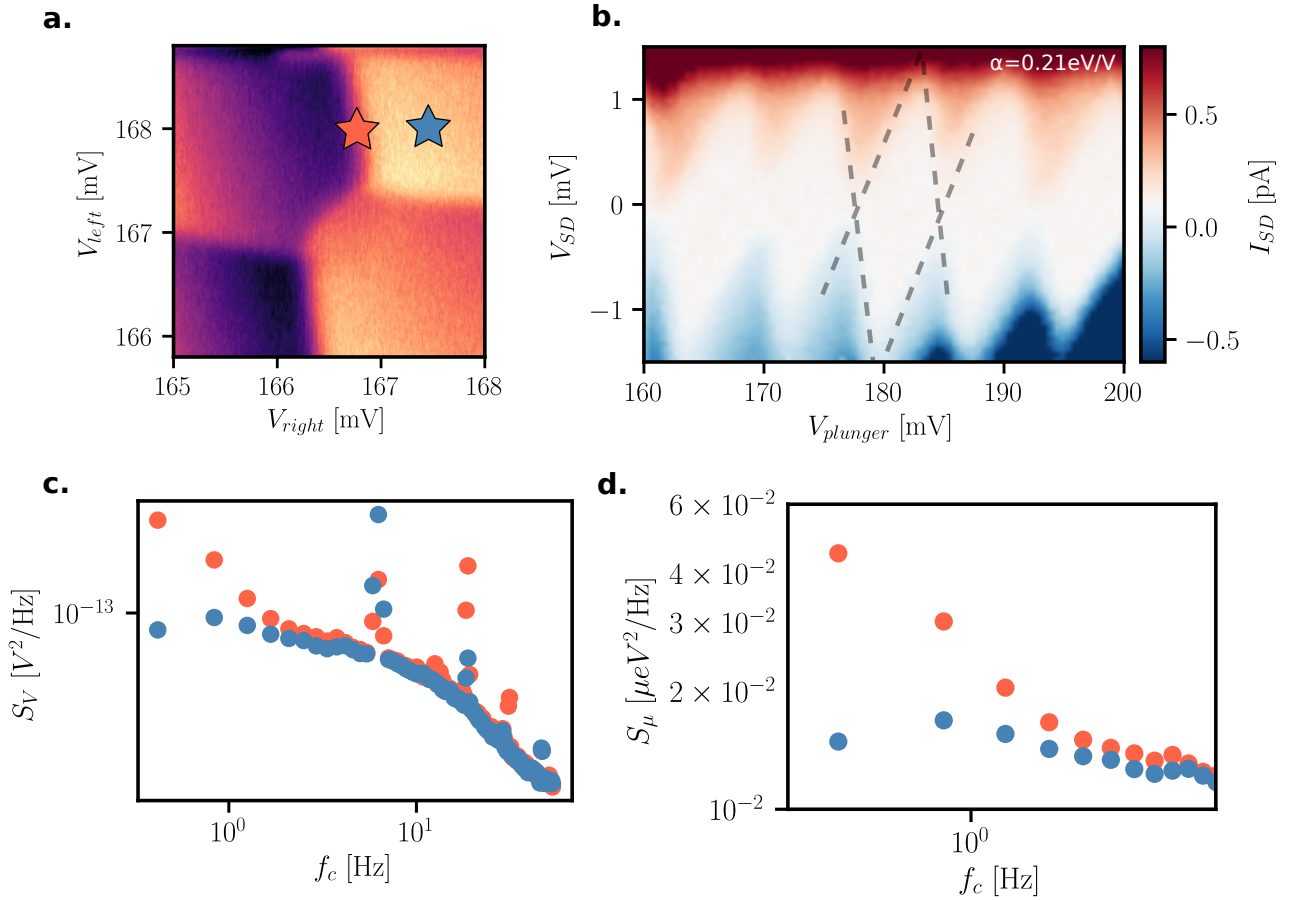


Figure 4.18 – **Tunnelling noise and sensor noise.** (a) Stability diagram around an interdot transition recorded with the Video Mode. At the point indicated by the blue star, the noise is coming from the sensor. At the point indicated by the orange star, the noise contains the sensor noise, the DQD charge noise and the tunnelling noise. (b) Coulomb diamonds obtained by measuring the current when sweeping V_{SD} and $V_{plunger}$. From the slope of the diamonds, we extracted the lever-arm $\alpha = 0.21 \text{ eV/V}$. (c) Power spectral density of the transmitted signal at a dot-lead transition (orange) and in a blockade state (blue). (d) Equivalent charge noise on the dot-lead transition and in the blockade state. The voltage signal has been normalised by the slope of the sensor Coulomb peak and the lever-arm.

CS. This gate has a strong influence on the contrast between the charge states, but also on the stability of the DQD.

We finally characterise the performances of the charge sensor. We studied the charge noise by looking at the signal in and out a sensor Coulomb peak. We extracted the charge noise at 1 Hz and found $S_\mu(1 \text{ Hz}) = 0.15 \text{ } \mu\text{eV}/\sqrt{\text{Hz}}$, which is state of the art for Ge. We also investigated on the time required to discriminate between two neighbouring charge states of the DQD and measured a separation of the signals of more than 10 for an integration time $t_c = 1 \text{ } \mu\text{s}$, allowing a fast readout of the charge states.

TAKEAWAY MESSAGES:

- For the geometry of our devices, putting the radiofrequency on the ohmic contact of a lead or on its accumulation gate is quasi equivalent.
- Increasing the quality factor of the readout circuit does not necessarily increase its sensitivity to variations in the resistance of the charge sensor.
- The charge noise of our sensor is state of the art for Ge. We have extracted $S_{\mu}(1Hz) = 0.15 \mu\text{eV}/\sqrt{\text{Hz}}$.
- We use the video mode extensively to tune the DQD to a suitable regime.
- Tuning the barrier separating the DQD from the CS is key. Opening it improves the contrast between the charge states, but affects the stability of the DQD.
- Our sensor can discriminate between two charge states with an SNR of ten in less than a microsecond.
- There is an additional charge noise at the DQD charge transitions, on top of the charge sensor noise, due to random tunnelling events between charge states.

SPINS IN GE QUANTUM DOTS

Contents

5.1 Last holes regime	106
5.1.1 Stability diagram	106
5.1.2 Lever arms and interdot properties	108
5.2 Pauli Spin Blockade signature	109
5.2.1 Pulse sequence	110
5.2.2 Video mode scanning	111
5.3 Spin states and relaxation	112
5.3.1 Relaxation time T_1	112
5.3.2 Landau-Zener spectroscopy	115
5.4 Conclusion	119

Ascent of Aiguille de la Vanoise by Desmaison route, with G. Schiano

Vanoise massif, France - August 13th 2023

Spin states in quantum dots are more coherent than charge states because of their weak sensitivity to the electric field fluctuations. To use them as spin qubits, it is necessary to work in a regime where the spin states are a few and well known. For this purpose, we have to operate the quantum dots in the few charge regime, and if possible in the configuration where there is a single spin in each dot. The direct readout of these spin states being difficult, a spin-to-charge conversion method has to be implemented. By the means of Pauli Spin Blockade (PSB) [Hanson, L. P. Kouwenhoven, et al. 2007], we can induce spin dependent charge transitions and thus access the spin states of the system. We report in this Chapter spin and charge measurements performed on a double quantum dot (DQD) device integrated with a charge sensor (CS). We first study the last hole regime and the interdots properties in the few hole regime. We then explore how the Pauli spin blockade principle can be exploited to perform spin-to-charge conversion. Finally, we characterise the different spin states of the system and their relaxation time T_1 .

5.1 Last holes regime

In this section, we focus on the process that allows working in the last hole regime. We study the properties of several interdot transitions involving few charges. Moreover, we characterise the tunnelling rate between two charge states and the lever arm of the gates on the DQD.

5.1.1 Stability diagram

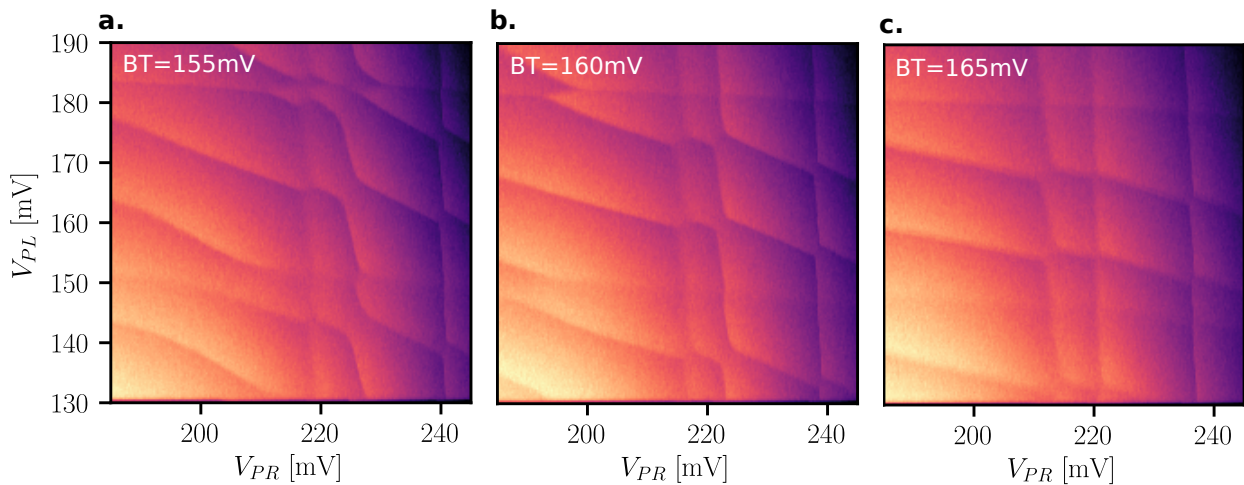


Figure 5.1 – **Evolution of the stability diagram with the tunnel barrier BT.** (a) (b) (c) Stability diagram in the few charge regime for $BT=155$ mV, $BT=160$ mV and $BT=165$ mV respectively. The measurements are recorded with an integration time $t_c = 30$ ms. They reveal the presence of two different DQDs in the system, as some lines are sensitive to BT and others are not.

The device under investigation and the experimental setup are described in detail in Chapter 4.3.1. In Chapter 4.3.2, we presented the tuning process enabling for the formation of a DQD and we highlighted the role of the barrier CBC, separating the DQD from the CS. We observed that opening increased the sensitivity of the CS to the DQD, but also decreased the stability of the DQD. It was not the only charged source that disturbed the DQD. We therefore used the video

mode extensively to remove these perturbations and make the stability diagram more textbook.

While trying to set in the last hole regime, we figured out that we were measuring two different DQDs participating to the stability diagram. In Figure 5.1, we can observe that some charge transition lines strongly move with BT, the barrier separating the two plunger gates. Other horizontal and vertical lines are quasi insensitive to changes in BT, which suggests that they belong to a DQD that is not located under the plunger gates. By changing the potentials applied on the different barriers surrounding the plunger gates, we managed to separate the two objects and work in a more standard DQD regime.

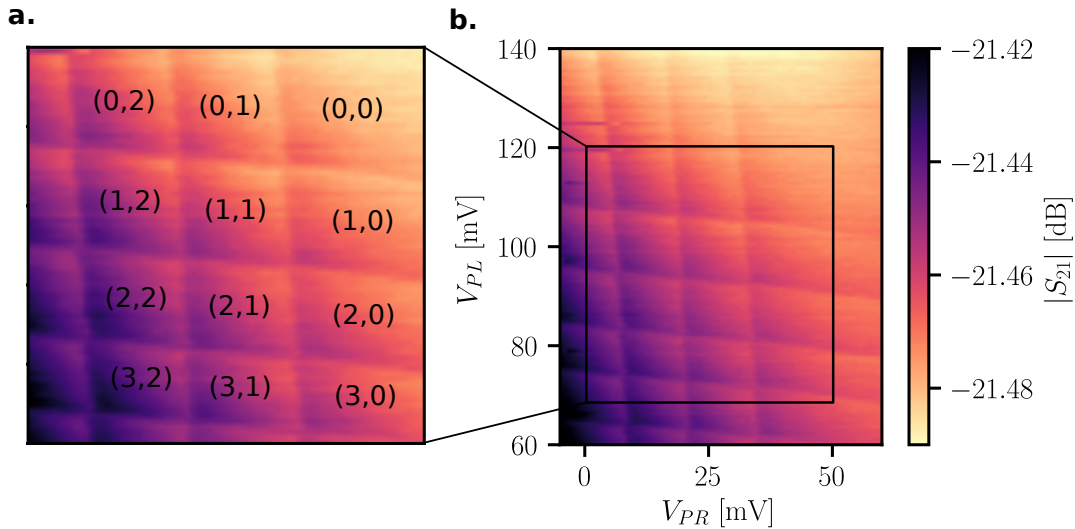


Figure 5.2 – **The last hole regime.** (a) Zoom in the first charge states of the stability diagram. The charges present in the two dots are indicated for each region. (b) Stability diagram of the last hole regime, recorded with the classical manner and an integration time $t_c = 30$ ms. No further lines have been observed above 140 mV for PL and 60 mV for PR.

By progressively sweeping PL and PR we have reached the last hole regime. This means that no other charge transition can be observed by sweeping PR and PL to higher values. The associated stability diagram is presented in Figure 5.2 (b). In this figure, the charge state in the upper right corner is the (0,0) where both dots are completely empty. By sweeping down PR in order to cross the first charge transition, we can load a charge in the right dot and thus reach the (0,1) charge state. Conversely, by sweeping down PL we will load a charge in the left dot and end up in the (1,0) state. The other charge states of the DQD are annotated in Figure 5.2 (a).

Figure 5.3 shows the stability diagram in the last hole regime measured with the Video Mode (a) and with the classical manner (b). For the classical manner, we set a value of PL and we sweep the whole line of PR. We repeat this procedure for each value of PL. As a consequence, each time we change PL we jump from one state to another without charging it correctly. This explains the jumps we can observe at the left of the plot, along the axis PL. For the same charging reason, the stability diagram in Video Mode is distorted on its edges. Despite the similarities between the two graphs, the slope of several transition lines is different. This can be explained by the fast axis of the Video Mode, where the scan can be faster than the tunnelling rate between the different charge

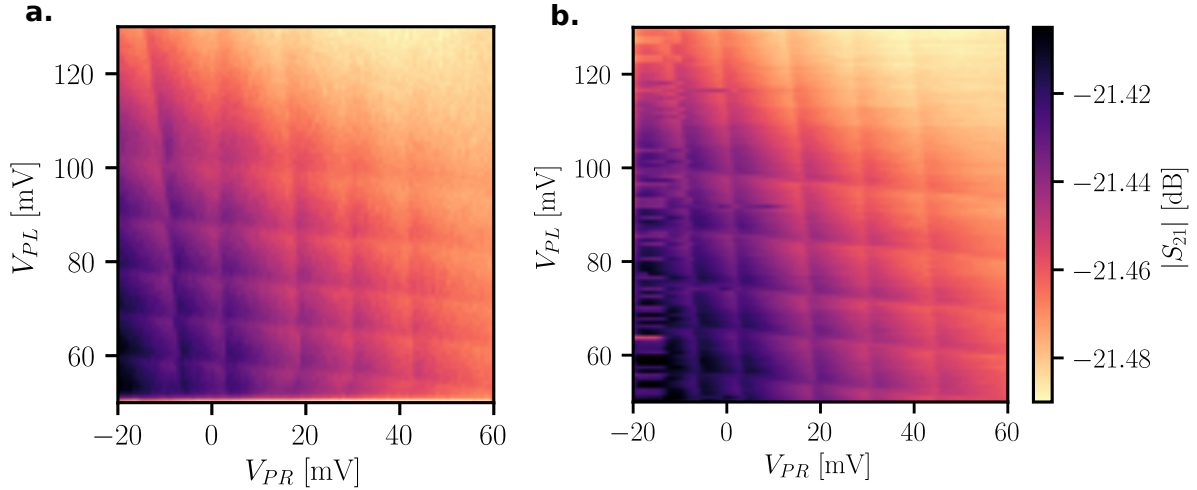


Figure 5.3 – **Stability diagram recorded with two different measurement methods.** (a) Stability diagram of the last hole regime recorded with the Video Mode, with $t_c = 30$ ms. (b) Stability diagram recorded with the same gate potentials but using the classical manner, also with $t_c = 30$ ms.

states, causing some delay in the transitions. In the classical manner, the scan is slow enough to allow the DQD to successfully cross each tunnel barrier in time.

5.1.2 Lever arms and interdot properties

Some charge transitions of the stability diagram require a charge to move from one dot to another by passing through a tunnel barrier. They do not involve the leads as the total number of charges occupying the DQD stays constant. They are called interdot charge transitions (ICTs). Two Video Mode images of the same interdot region are shown Figure 5.4 (a) and (b). Between these two images, only BT has varied from 2 mV. We observe a clear enlargement of the ICT while reducing BT, highlighting the role of this barrier gate on the coupling between the two dots forming the DQD. We recorded several 1D-traces along the ICT and fit them using Formula 5.1, where g_0 is the mean signal, ϵ is the energy detuning and T_e is the electronic temperature. This enabled us to determine the variations of the tunnelling rate with BT and with the magnetic field B applied in-plane along the DQD. Figure 5.4 (c) and (d) shows the 1D-traces and their fit for BT=169 mV and BT=178 mV respectively. We observed that the tunnelling rate was reduced by 2 by lowering BT from 10 mV. Figure 5.4 (e) shows that the tunnelling rate is not clearly influenced by B . On the other hand, BT strongly influences the tunnelling rate, as shown Figure 5.4 (f). As a result, we can finely control the tunnelling coupling of the two dots.

$$S_{21} = g_0 + \Delta g \frac{\epsilon}{\Omega} \tanh\left(\frac{\Omega}{2k_B T_e}\right) + \Delta g \epsilon, \text{ with } \Omega = \sqrt{\epsilon^2 + h^2 t^2} \quad (5.1)$$

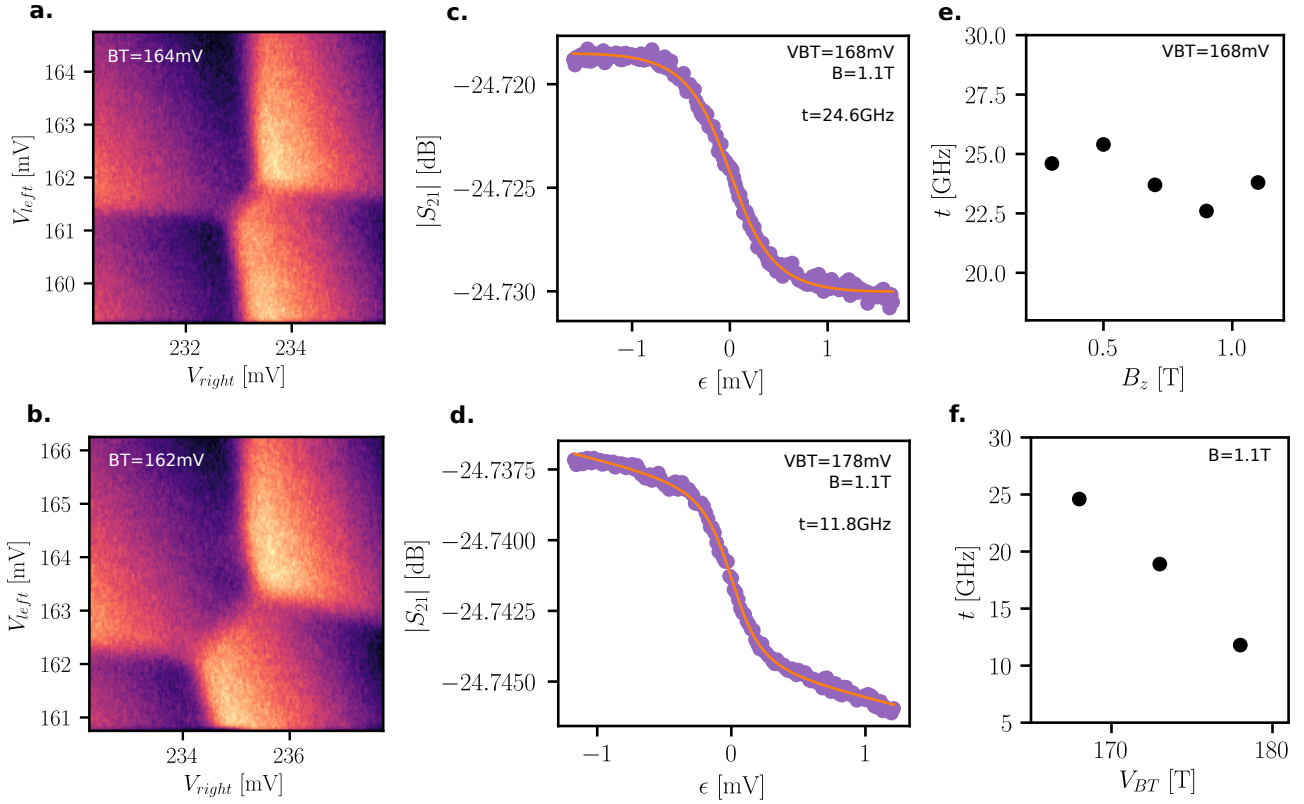


Figure 5.4 – **Tunability of the interdot tunnelling rate.** (a) Stability diagram around an interdot recorded with the Video Mode, with $t_c = 30$ ms and $BT = 164$ mV. (b) The same measurement with $BT = 162$ mV. We observe an enlargement of the interdot characteristic of the augmentation of the tunnelling rate. (c) Cut perpendicular to the interdot for $BT = 168$ mV and fit. (d) Same measurement with $BT = 178$ mV. The fit shows a reduction of the tunnelling rate by a factor 2. (e) Evolution of the tunnelling rate with the in-plane magnetic field B_z , for a fixed $BT = 168$ mV. (f) Evolution of the tunnelling rate with the gate voltage applied on BT, for a fixed $B_z = 1.1$ T.

By applying a voltage difference between the source and the drain, we can circulate some current through the DQD. Inelastic tunnelling results in the appearance of bias triangles at the triple points of the interdots [Hanson, L. P. Kouwenhoven, et al. 2007]. As the bias window increases, so does the size of the triangle. Thus, we can extract the lever-arms of the gates on the DQD from the scaling of the triangles with the bias voltage [Jirovec et al. 2021]. In Figure 5.5, we clearly observe that the bias triangles grow proportionally with the bias voltage applied. We extracted a lever arm $\alpha_{PL} = 0.15$ eV/V for the left dot and $\alpha_{PR} = 0.18$ eV/V for the right dot, which is consistent with other values reported in similar Ge heterostructures [Lawrie et al. 2020].

5.2 Pauli Spin Blockade signature

Pauli Spin Blockade (PSB) can be used as a spin-to-charge conversion method, and is commonly used in the field of spin qubits [Seedhouse et al. 2021]. Chapter 1.4.3 presents the PSB principle

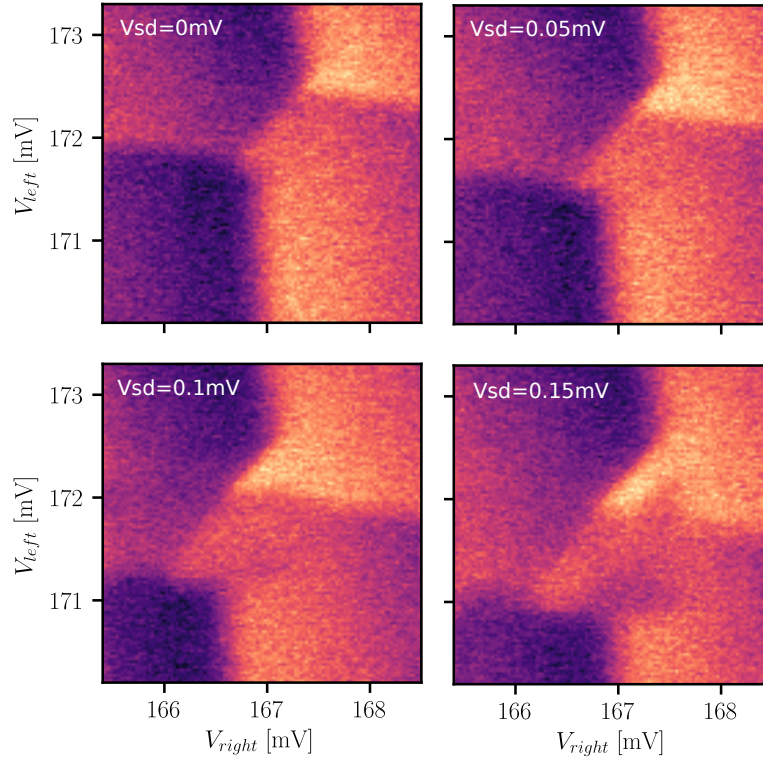


Figure 5.5 – **Bias triangles.** Evolution of the bias triangles when raising the source-drain bias voltage. The four plots are recorded with the Video Mode, with $t_c = 30ms$.

and how we can use it to convert a spin state into a measurable charge state. In the case of a DQD, a charge transition can be Pauli spin blocked if it involves a charge state having an odd number of charges in the two dots together with a charge state having an even number of charges in one of the two dots.

5.2.1 Pulse sequence

To observe Pauli Spin Blockade, we have to cross an interdot charge transition (ICT) that can be blocked. The first ICT of the stability diagram that is subject to PSB is the (1,1)-(0,2). Thus, if we initialise the DQD in the (1,1) charge state and quickly pulse to the (0,2) charge state, we should be able to observe that the transition is blocked in a fraction of the cases. This requires the pulse to be faster than the spin relaxation time and the tunnelling rate. In order to observe blockage in a fraction of the transitions, we need to initialise the (1,1) charge state with different spin states. Consequently, we start with a first pulse from the (0,1) to the (1,1) charge state in order to load a charge with a random spin on the left dot. The resulting (0,1)→(1,1)→(0,2) sequence is illustrated Figure 5.6 (a). By repeating this sequence for a certain time for each point of the stability diagram around the (1,1)-(0,2) transition, we should observe a partially blocked region on the (0,2) charge state close to the interdot.

Figures 5.6 (b) and (c) result from the pulse sequence described Figure 5.6 (a), repeated several times and averaged over the first 15 μs for (b) and the first 50 μs for (c). In both maps, we observe the appearance of a blockade region on the (0,2) charge state close to the interdot. It has

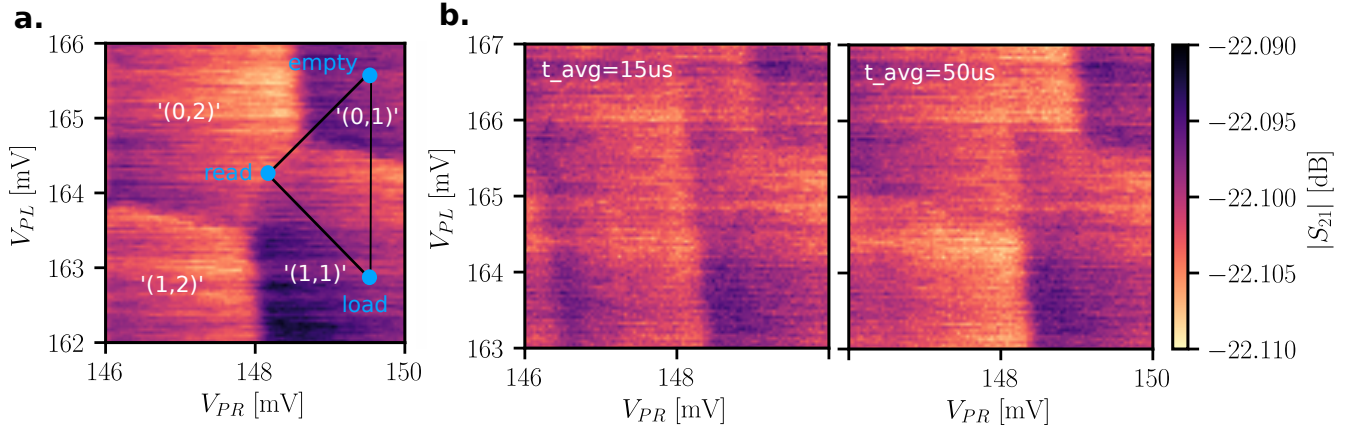


Figure 5.6 – **PSB signature and pulse sequence.** (a) Schematic of the pulse sequence applied to evidence PSB. The background map of the interdot is recorded using the classical manner, with $t_c = 30$ ms. (b) *left* Map resulting from the pulse sequence, integrated over the first $15 \mu s$. We note the appearance of a blockade triangle. *right* The same measurement, integrated over the first $50 \mu s$. The blockade triangle is even clearer.

a triangular shape because the crossing of the dot-lead transitions leverages the blockade. The triangle seems to be clearer for the map integrated over $50 \mu s$, which suggests that the lifetime of the spin state is on the same order of magnitude or even longer.

5.2.2 Video mode scanning

Video mode allows fast scanning along a given axis in a given direction. The scan time of a single raw along the fast axis is set at $t_{scan} = 20 \mu s$. If we work around the (1,1)-(0,2) transition (or an equivalent transition), scanning the stability diagram from the top to the bottom or from the left to the right is then equivalent to pulsing from the (0,2) to the (1,1) charge state in less than $20 \mu s$. This has no effect on the stability diagram as there is no reason for the transition to be blocked. Contrariwise, scanning the stability diagram from the bottom to the top or from the right to the left is equivalent to pulsing from the (1,1) to the (0,2) charge state. In this case, the Pauli Spin Blockade principle applies and the transition is blocked in part of the cases.

Figure 5.7 shows the same interdot scanned in four different directions. It corresponds to a (0,2)-(1,1) equivalent transition with a few more charges, probably about five in each dot. We observe a signature of the Pauli Spin Blockade when the stability diagram is scanned from bottom to top or from right to left¹. This results in the appearance of a blockade triangle at the interdot [Lawrie et al. 2020; N. W. Hendrickx, D. P. Franke, et al. 2020; Jirovec et al. 2021], whose colour is a mixture between the colours of the two charge states. As expected, this triangle is no longer visible when the stability diagram is scanned from top to bottom or from left to right². The clarity of the triangle in the blockade region suggests that the relaxation time T_1 of the spin state is longer than the scan time of a raw $t_{scan} = 20 \mu s$.

1. This corresponds to pulsing from the (1,1) to the (0,2).

2. It is equivalent to pulsing from the (0,2) to the (1,1).

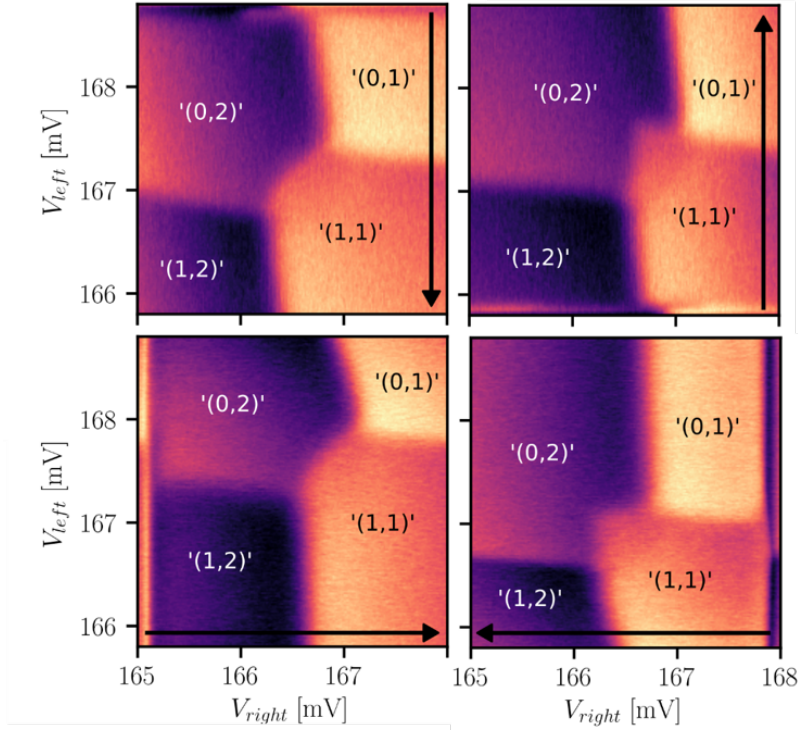


Figure 5.7 – **PSB signature with the Video Mode.** Interdot scanned with the Video Mode in four different directions indicated by a black arrow. The measurement time of a raw along the fast axis is set to $t_{\text{scan}} = 20 \mu\text{s}$.

5.3 Spin states and relaxation

In this Part, we try to dress the spin states of the system and their lifetimes. We mainly focus on an interdot involving about five charges in each dot, which exhibits a Pauli Spin Blockade signature. We start by measuring the relaxation times T_1 of the different relaxation mechanisms that led to the leverage of the spin blockade. We then perform Landau-Zener spectroscopy to observe the different energy levels involved and their interactions.

5.3.1 Relaxation time T_1

To measure the relaxation time of the spin states responsible for PSB, we implemented the sequence presented Figure 5.8 (a) and (b). We start by pulsing from the (0,2) to the (1,1) state in order to have one spin in each dot. We pulse back to the (0,2) state near the interdot (inside the blockade triangle) and we look at the evolution of the reflectometry signal with the time. The decay can be fitted with one exponential or a sum of exponentials giving the different spin relaxation times T_1 of the system. Figure 5.8 (c) shows a measurement of the transmission coefficient along the different steps of the sequence. The sequence was subsequently optimised to improve the measurement time. In particular, we studied how T_1 was affected by the addition of ramps while varying PR and PL. We ended up with a sequence very similar to the one represented Figure 5.8 (b), but with shorter 'start' and 'load' steps.

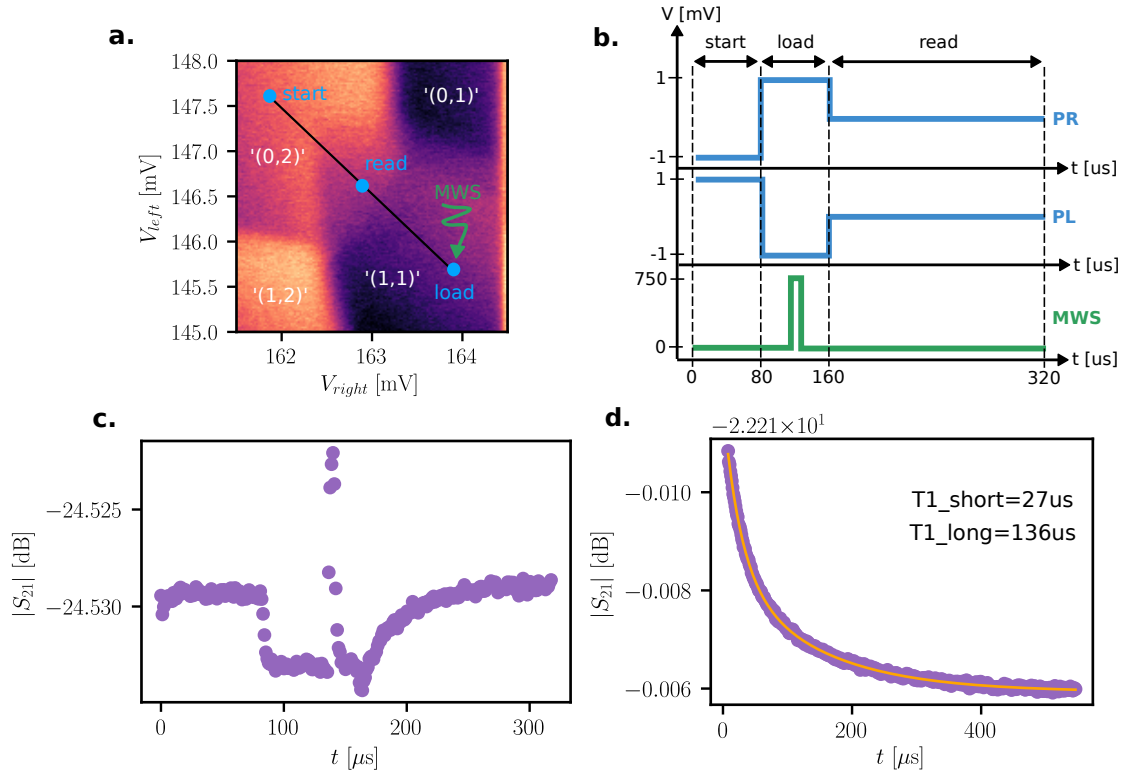


Figure 5.8 – **Pulse sequence for the measurement of T_1 .** (a) Schematic of the pulse sequence applied to measure the relaxation time T_1 . The background map of the interdot is recorded with the Video Mode, with an integration time $t_c = 30$ ms. (b) Sequence delivered by the AWG to PR, PL and the microwave source (MWS). The microwave burst during the load phase has no effects on T_1 as it is not spin-resonant. It has been set for another experiment aiming for electrically driven spin resonance (EDSR). (c) Evolution of the transmitted signal $|S_{21}|$ averaged 20000 times, during the pulse sequence. The signal remains constant during the "start" phase. During the "load" phase, we observe a peak that correspond to the microwave burst. In the "read" phase, we observe the relaxation decay of the blockade states. (d) The longest decay measured on the interdot presented in (a), with in-plane $B = 0.4$ T. It is fitted (orange curve) with a sum of two exponentials, giving $T_{1_short} = 27 \mu s$ and $T_{1_long} = 136 \mu s$ respectively.

$$|S_{21}|(t) = A_{short} \times e^{-t/T_{1_short}} + A_{long} \times e^{-t/T_{1_long}} + C \quad (5.2)$$

The longest spin decay observed is presented in Figure 5.8 (c). It has been measured on the interdot shown Figure 5.8 (a), involving around 5 charges in each dot. The curve is fitted with a sum of two exponentials according to the Formula 5.2. It gives rise to two different T_1 , a short one $T_{1_short} = 27 \mu s$ and a longer one $T_{1_long} = 136 \mu s$. This highlights the coexistence of at least two relaxation mechanisms. Looking at the amplitudes of the exponentials, we found a ratio $|A_{short}/A_{long}| = 1.31$. This means that statistically there are more prepared states corresponding to the short mechanism than to the long mechanism. We do not benefit from a model for the spin states of an interdot involving about 10 charges, which makes it difficult to identify the blockade mechanisms. Nevertheless, we can think that T_{1_long} may correspond to a transition similar to a

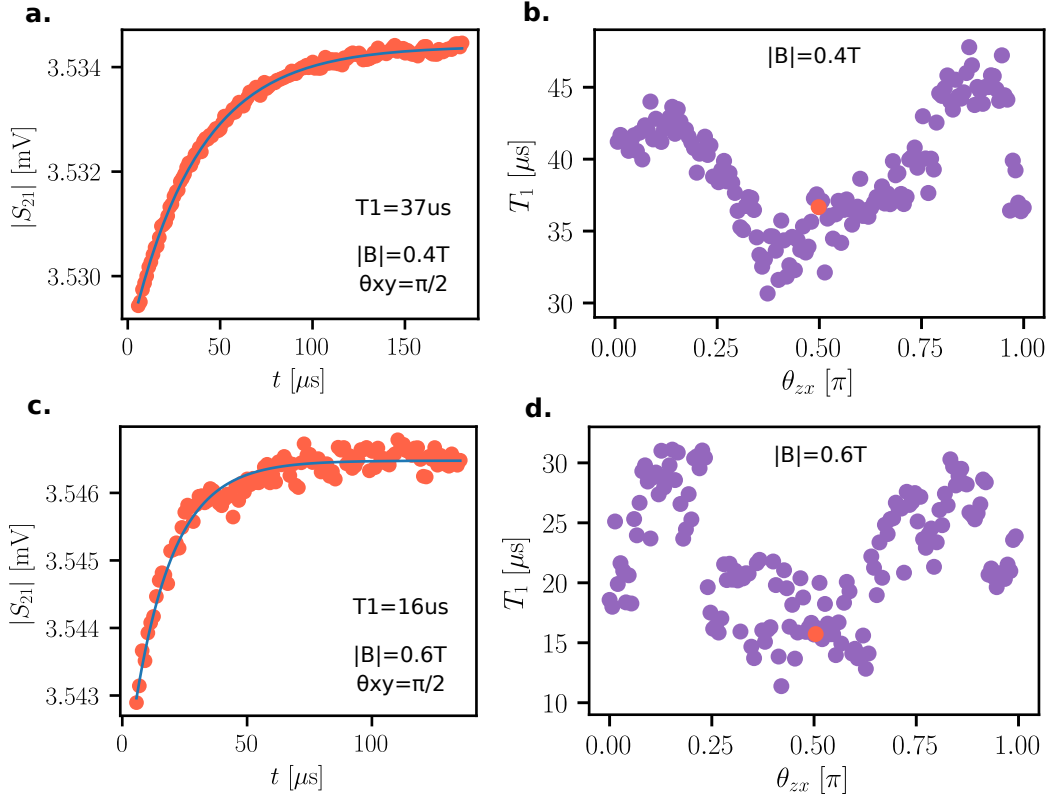


Figure 5.9 – T_1 as a function of the angle of the in-plane magnetic field. (a) Decay of the transmitted signal in the blockade region, measured using a pulse sequence similar to the one presented Figure 5.8. The magnetic field is applied in the plane perpendicular to the DQD axis, and has an amplitude $|B| = 0.4$ T. It is fitted (blue curve) with an exponential giving $T_1 = 37 \mu\text{s}$. (b) T_1 as a function of the angle θ_{zx} of the in-plane magnetic field, for $|B| = 0.4$ T. The orange point corresponds to the measurement fitted in (a). (c) Same as (a) for $|B| = 0.6$ T. (d) Same as (b) for $|B| = 0.6$ T.

singlet-triplet transition ($T^-(1,1) \rightarrow S(2,0)$)³. Hence, the $T_{1\text{long}}$ we measured is comparable to the singlet-triplet relaxation time $T_{ST} = 103 \mu\text{s}$ reported by W. Lawrie [Lawrie et al. 2020] on another planar Ge/SiGe heterostructure. Higher T_1 , such as $T_1 = 32$ ms for a single hole occupancy and $T_1 = 1.2$ ms for a five hole occupancy, have been reported using different loading protocols and minimising the reservoir-dot coupling.

The relaxation time T_1 evolves with the angle of the magnetic field. We setup the DQD in a spin blockade region, where the spin decay can be fitted with a single exponential. We extracted T_1 as a function of the in-plane field angle and plotted the results in Figure 5.9 (b) and (d) for $|B| = 0.4$ T and $|B| = 0.6$ T respectively. An angle of 0 or π corresponds to the case where the magnetic field is applied along the DQD axis. The angle $\pi/2$ corresponds to a magnetic field applied perpendicular to the DQD axis, still in the plane. We observe variations of T_1 on the order of $15 \mu\text{s}$, and maxima for angles close to $\pm\pi/4$. The averaged T_1 is larger for the measurement with $|B| = 0.4$ T than $|B| = 0.6$ T as expected. Indeed, when increasing the magnetic field, we increase

3. A diagram showing the transitions for DQDs with even charge configurations can be found in Chapter 1.4.2.

the Zeeman energy which allows more relaxation phenomena. As a consequence, the extraction of T_1 for the curves with $|B| = 0.6$ T is less precise, leading to a larger dispersion of the points.

5.3.2 Landau-Zener spectroscopy

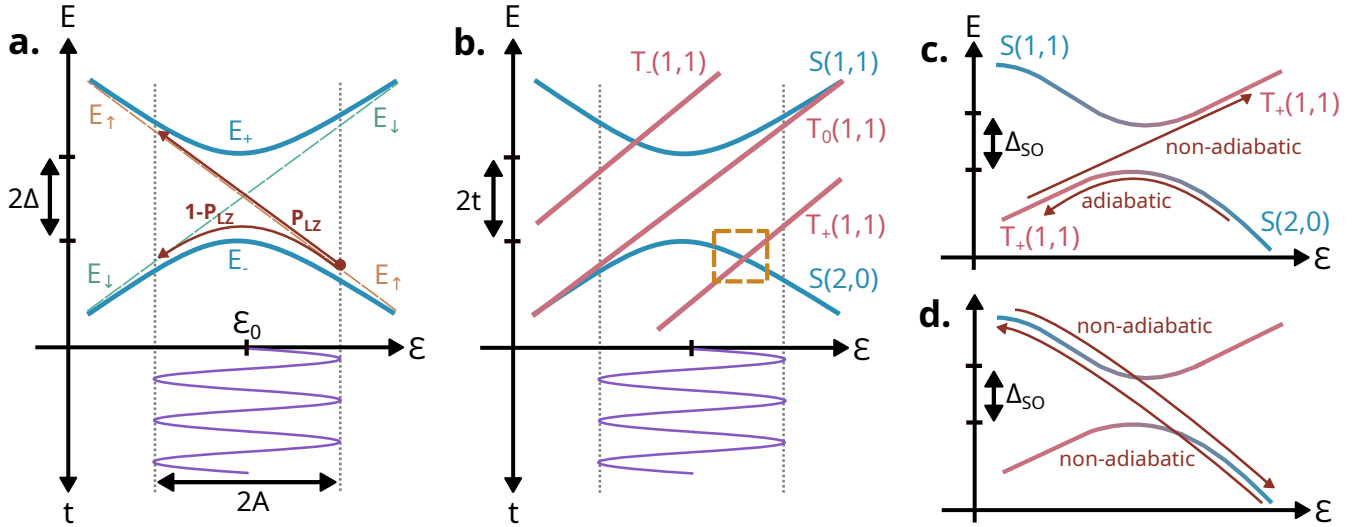


Figure 5.10 – **Landau-Zener interferometry applied to a singlet-triplet qubit.** Figure adapter from S. Shevchenko [Shevchenko et al. 2010] and H. Ribeiro [Ribeiro and Burkard 2009]. (a) Illustration of an anticrossing in the general case, with the energy E of the levels on the y-axis and an external driving parameter ϵ on the x-axis. The latter oscillates around the anticrossing with an amplitude of $2A$, as illustrated by the purple sine curve. The blue solid curves represent the two adiabatic energy levels E_{\pm} which exhibit an anticrossing with energy splitting 2Δ . The orange and green dashed lines show the corresponding crossing non-adiabatic levels $E_{\uparrow\downarrow}$. The probabilities of the non-adiabatic transition P_{LZ} and adiabatic transition $1 - P_{LZ}$ are represented in red. (b) Transposed illustration for the case of singlet-triplet states, belonging to a double quantum dot with an even number of charges. (c) (d) Zoom on the orange box in (b), showing possible transitions.

Two-level systems often exhibit anticrossings between their two energy levels when an external parameter is varied. By driving this parameter fast enough, the system can cross the anticrossing region, resulting in a non-adiabatic transition between the two energy levels [Landau 1932; Zener 1932]. The probability that this transition occurs is given by the Landau-Zener probability. Figure 5.13 (a) shows the general case of an anticrossing of two energy levels E_{\pm} , when a parameter ϵ varies. The Hamiltonian of such system is given in Formula 5.3. The probability that a non-adiabatic transition between the energy levels E_{\pm} occurs is given by the Formula 5.4, where $\nu = |d(E_1 - E_2)/dt|$ is the Landau-Zener level velocity. The parameter ϵ is driven periodically with a large amplitude, such that the system goes back and forth across the anticrossing, allowing for Landau-Zener-Stückelberg-Majorana interferometry [Leggett et al. 1987]. Figure 5.13 (b) transposes the general case to the case of a singlet-triplet spin qubit [Ribeiro and Burkard 2009]. Figures 5.13 (c) and (d) show the possible adiabatic and non-adiabatic transitions that can occur around the anticrossing between the singlet $S(2,0)$ and the triplet $T_+(1,1)$.

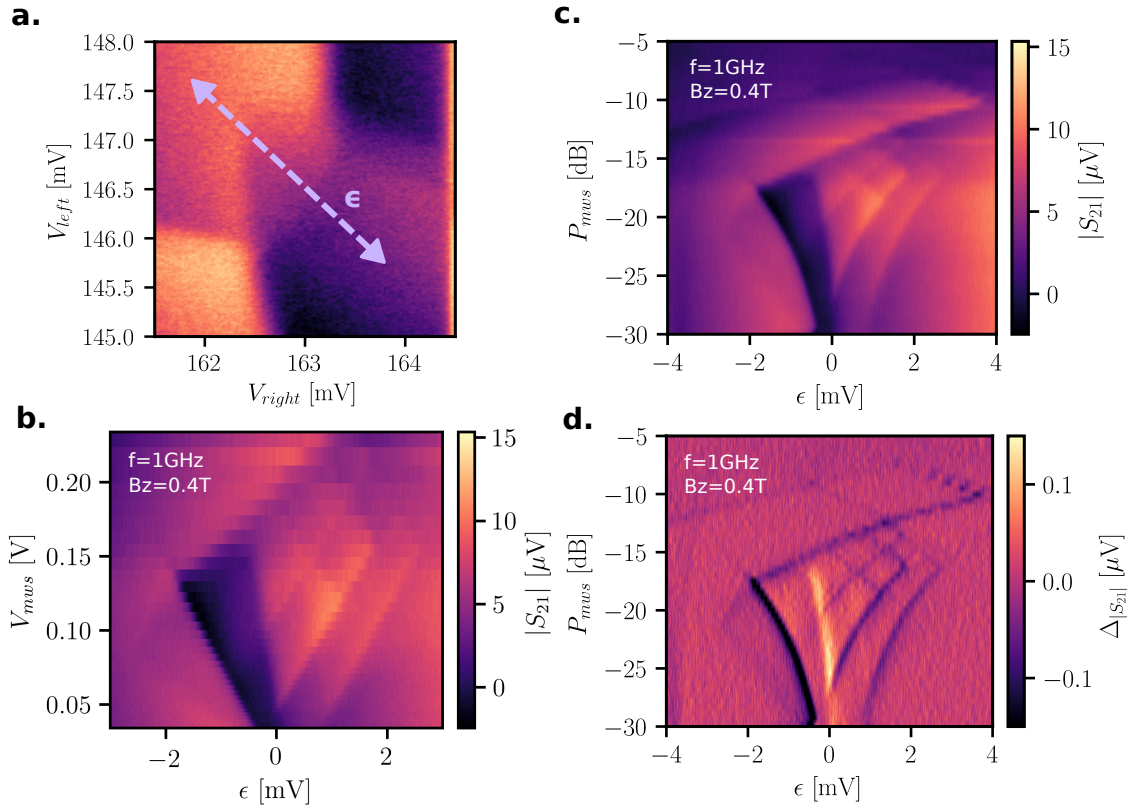


Figure 5.11 – **Landau-Zener spectroscopy of an interdot.** (a) Detuning axis ϵ used for the Landau-Zener spectroscopy, defined perpendicular to the interdot. The background map of the interdot is recorded with the Video Mode, with an integration time $t_c = 30$ ms. (b) Transmitted signal along ϵ for the interdot plotted (a), when varying the output voltage of the microwave source signal V_{MWS} . The latter is plotted in the linear scale. The map is measured for a microwave source frequency $f = 1$ GHz, an in-plane magnetic field $B_z = 0.4$ T and an integration time $t_c = 30$ ms. (c) The same measurement as in (b), plotted in the logarithmic scale with the power V_{MWS} . (d) Same measurement than (b), showing the differential of $|S_{21}|$ according to ϵ and P_{MWS} .

$$\mathcal{H} = \begin{pmatrix} \epsilon & \Delta \\ \Delta & -\epsilon \end{pmatrix} \quad (5.3)$$

$$P_{LZ} = e^{-\frac{2\pi\Delta^2}{h\nu}} \quad (5.4)$$

For the experiment presented in Figure 5.11 (a), we excited the gate BT with an external microwave source, delivering a sinusoidal signal at a frequency f_{MWS} and a power P_{MWS} , corresponding to an output voltage V_{MWS} . We performed the spectroscopy along the detuning axis of the interdot shown Figure 5.11 (a) with about 5 charges in each dot. Figure 5.11 (b) shows the the spectroscopy of the interdot as a linear function of the output voltage V_{MWS} , for $B_z = 0.4$ T and $f_{\text{MWS}} = 1$ GHz. Figures 5.11 (c) and (d) show the same measurement plotted in the log-

arithmetic scale with the power of the microwave source P_{MWS} , (d) being the differentiate of (c). We observe that increasing the power of the microwave source makes it possible to access new Landau-Zener transitions, as we scan the anticrossing with increasing amplitude. We performed similar measurements to investigate on the influence of the microwave source frequency on the LZ transitions. We observed very similar transition lines even at very low frequencies such as 500 kHz. This means that the tunnelling rate is lower than this value and that the power is mainly driving the LZ transitions we observe.

On Figure 5.11 (b), we see that at low power all the transition lines are contained into a main V-shape feature. The latter corresponds to the scanning of the ground state of the DQD. The left arm corresponds to a transition equivalent to $(1,0) \rightarrow (0,1)$, reached when sitting on the state equivalent to $(1,0)$. The right arm corresponds to the same transition reached when sitting in the equivalent $(0,1)$. The more we increase the power of the microwave source, the more the arms spread out as the equivalent $(1,0) \rightarrow (0,1)$ transition can be reached by sitting further away from the interdot. Once and only once this transition is passed, higher energy Landau-Zener transition can be achieved. This explains why there is only lines inside the V-shape and why they are not continuous. At higher power, around $V_{\text{MWS}} = 150 \text{ mV}$, another branch coming from the left appears. It arises from another charge transition located at approximately 5 mV from the interdot under study. For the following we will only consider the low power region ($V_{\text{MWS}} < 150 \text{ mV}$), where this parasitic transition has no influence.

Simulations performed by Y-M. Niquet and presented in Figure 5.12 (a) and (b) show the energy level spectrum of a single hole spin in a Ge DQD and the evolution of the energy required to induce state transitions as a function of the detuning. The latter simulation is performed by adding thermal excitation to the system. As a result, the anticrossings appearing in Figure 5.12 (a) can be reached without the need for others to be reached first. This is why the lines appear to be continuous in the thermal excitation simulation (Figure 5.12 (b)), while they were not in the Landau-Zener excitation experiment. On both simulation and experiment it is difficult to observe the Zeeman splitting of the energy levels. This is because the g-factor in the in-plane directions is expected to be small and the applied field $|B| = 0.4 \text{ T}$ is not strong enough to compensate for small g. We performed additional LZ measurements varying the amplitude of the magnetic field from 0 T up to 2 T, but we still did not observe any significant splitting of the LZ transitions.

Since we know the lever arms of the gates responsible for the sweep along epsilon, we can convert the level spacing along epsilon into an energy level spacing. In Figure 5.12 (d), we extracted the energy difference between the ground state E_1 and the first and second excited states E_2 and E_3 . We found $E_2 - E_1 = 0.149 \text{ meV}$ and $E_3 - E_1 = 0.314 \text{ meV}$. Figure 5.12 (c) shows the wave function of a single hole in a Ge quantum dot, as a function of the energy level it occupies. The first energy level E_1 can be associated with an s-orbital ($n=1, l=0, m=0$), and the other two with p-orbital with ($n=2, l=1, m=0$) for E_2 and ($n=2, l=1, m=1$) for E_3 . The anisotropy of the dot is responsible for the lifting of the degeneracy between E_2 and E_3 . The simulations presented Figure 5.12 (c) are released considering a single hole, whereas the energy level spacings we extracted from Figure 5.12 (d) are for a DQD with around 10 charges inside. This mainly explains why we found smaller energy spacings experimentally.

We performed Landau-Zener spectroscopy on different interdots involving a few charges and present an overview of the results on Figure 5.13. Due to latched charge transitions in the few hole

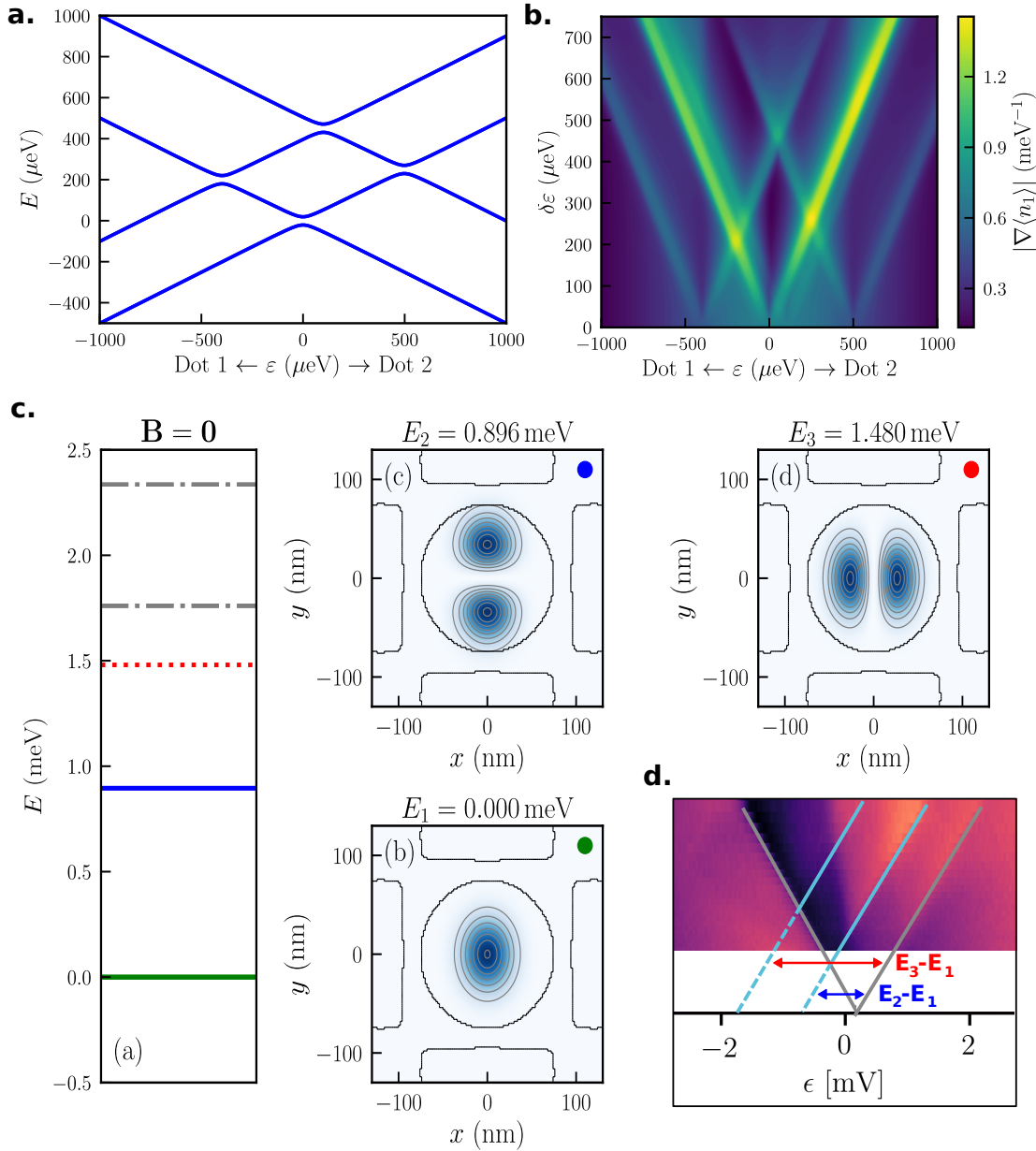


Figure 5.12 – **Energy levels and wave function of a single hole.** Figure adapted from the simulation results of Y.-M. Niquet. **(a)** Simulation of the energy level spectrum of a single hole in a Ge DQD in the absence of an external magnetic field. **(b)** Thermal energy required to induce state transitions as function of the detuning. The simulation is done for the energy level spectrum shown in (a). **(c)** Simulation of the energy level spacing and shape of the wave function of a single hole in an anisotropic Ge well. For this simulation, a positive gate voltage is applied to the left and right gates, the top and bottom gates are biased and a negative voltage is applied to the plunger gate. **(d)** Energy level spacing of the states experimentally probed by Landau-Zener spectroscopy on Figure 5.11.

regime, we were not able to evaluate with certainty the charge states corresponding to each interdot studied. Nevertheless, we are sure that all the interdots involved in this figure have lower charges than the interdot presented in Figure 5.11 (a). The features we observe on the different plots seem

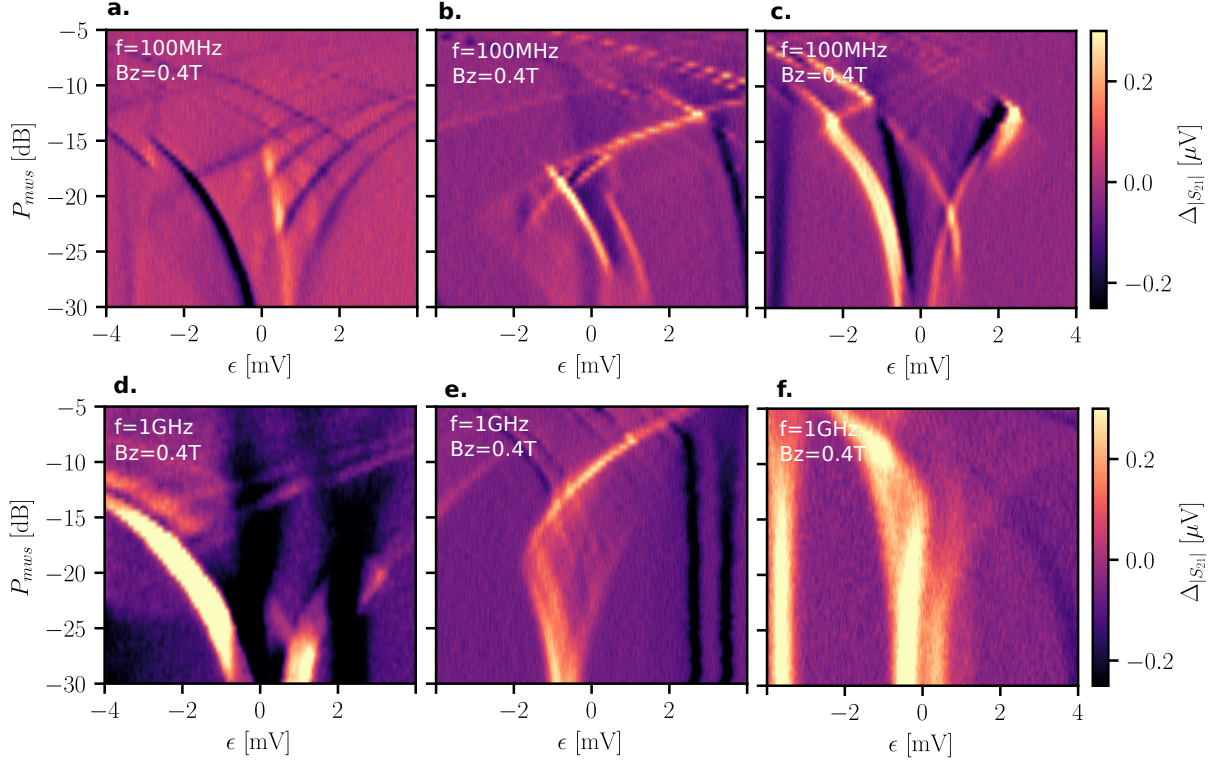


Figure 5.13 – **Landau-Zener spectroscopy on different interdots.** (a) Signal differentiation along ϵ , a perpendicular section of an interdot containing a few charges, as the power of the microwave source signal P_{MWS} is varied. The map is measured for a microwave source frequency $f = 100$ MHz, an in-plane magnetic field $B_z = 0.4$ T and an integration time $t_c = 30$ ms. (b) (c) (d) (e) (f) The same measurement on five other interdots involving a few charges, with $f = 100$ MHz or $f = 1$ GHz.

to be quite similar to the one previously studied, with more or less an outer V-shape each time corresponding to the lowest energy states. Inside the V-shape we can also observe other partial lines corresponding to higher energy states accessible by Landau-Zener. The presence of neighbouring charge transitions or other energy states makes a precise analysis of such measurements difficult.

5.4 Conclusion

In this chapter we have shown that it is possible to deplete a DQD to the last hole. We extracted the lever arms of the gates on the electrostatic potential of the dots and managed to fine-tune the tunnelling rate between two dots. We observed a Pauli Spin Blockade signature on several interdot charge transitions, either by applying a well-defined pulse sequence or by taking advantage of the Video Mode. We measured the lifetime of the blockade spin states and pointed out the coexistence of a blockade state with a short relaxation time and a another with a long relaxation time, which can exceed $T_1 > 100 \mu\text{s}$. We finally performed Landau-Zener spectroscopy to understand better the different states involved in our system.

Once the PSB signature was found, we also tried to induce electrically driven spin rotation (EDSR) on the spin that is loaded during the pulse sequence described in Figure 5.8. This phe-

nomenon occurs when the microwave burst photon energy matches the Zeeman splitting between the two spin states of a doublet. As a consequence, the loaded spin will be always in the same state and so the (1,1)-(2,0) transition will be either always Pauli spin blocked or never. Thereby, when varying the frequency of the microwave burst one can hope to observe a peak or a deep in the charge sensor response. To increase the chance of finding EDSR, it is possible to sweep the magnetic field in addition to varying the microwave burst frequency. Indeed, as the Zeeman energy linearly varies with B , it is possible to observe EDSR transition lines [Corna et al. 2018] (see Formula 5.5). Measuring these 2D-maps generally takes a long time because it requires a high resolution in the frequency axis. In our case, the charge sensor response is averaged over the first tens of microseconds to enhance any EDSR signal while staying below T_1 .

$$hf_{\text{MWS}} = g\mu_B B \quad (5.5)$$

Our charge sensor and setup is not optimal for EDSR lines observation. First, we suffer from measurement difficulties. Because of the sensor noise ($\sigma \sim 3 \mu\text{V}$), we have to do a large average of each point⁴. Therefore, the measurement time for a wide frequency range is very long, and the sensor could jump during this time. This involves a systematic repositioning on the PSB region of the interdot. Second, although it should be possible to observe EDSR lines at arbitrary fields, the other groups working with Ge heterostructures only found EDSR lines for small fields $B < 0.1 \text{ T}$ [Jirovec et al. 2021]. It is not possible for us to work in this region because the charge contrast of the sensor is not sufficient at such low fields. Despite these obstacles, we have tried to find EDSR lines for :

- multiple field directions in the plane
- multiple field amplitudes from $B = 0.15 \text{ T}$ to $B = 2 \text{ T}$
- for microwave source frequencies starting from 10 MHz to 10 GHz
- for placing the microwave source on different gates such as DR, DL, BT, PL and PR

This consistent work enabled us to cover a very wide range of possible g-factors, but we did not succeed in finding the EDSR.

4. On the order of 10^3 repetitions.

TAKEAWAY MESSAGES:

- The DQD can be depleted to the last hole.
- The tunnelling rate between the two dots can be fine-tuned thanks to the BT barrier.
- The lever arms of the gates on the electrostatic potential of the dots are $\alpha_{PR} = 0.18 \text{ eV/V}$ and $\alpha_{PL} = 0.15 \text{ eV/V}$.
- Pauli Spin Blockade signature has been observed on an interdot charge transition equivalent to the (1,1)-(0,2).
- The lifetime of a spin blockade state can be as large as $T_1 = 136 \mu\text{s}$.
- T_1 evolves with the magnetic field angle and has maxima for angles close to $\pm\pi/4$.
- Landau-Zener spectroscopy helps to understand the energy states of the system under study.

CONCLUSION

It's a funny thing about coming home. Looks the same, smells the same, feels the same. You'll realize what's changed is you! - F. Scott Fitzgerald

Illustration of the Aiguilles d'Arves (Maurienne valley, France)

The development of compact spin qubits readout architectures enabling for fast readout will allow to take a further step towards scalability. It will additionally provide new tools for better understanding of the hole spin physics. This Manuscript was dedicated to the implementation of radiofrequency circuits for two readout methods for the detection of spin states in double quantum dots. We first presented the implementation of an RF gate-based dispersive circuit for the readout of Si nanowire devices. We then focused on an RF charge sensing circuit dedicated to the readout of Ge/SiGe heterostructure devices. For both circuits we demonstrated that it is possible to probe charge signals within the microsecond range.

To push the limits of gate-based dispersive readout, we investigated on the fabrication of superconducting resonators. We designed NbN coil inductors coupled to a 50Ω -microstrip enabling for radiofrequency readout in transmission. Hence, we obtained resonators with high internal quality factors $Q_{\text{int}} > 1000$, resonant frequencies varying from $f_0 \sim 500$ MHz to $f_0 \sim 5$ GHz and external quality factors adjustable by design. Once the resonators bonded to Si nanowire devices, we managed to maintain high quality factors by adding appropriate bias-tees. The resonators further demonstrated a good resilience with the magnetic field, allowing them to be used for spin experiments whose require the application of an external magnetic field. The ability to probe the parametric capacitance of hole spin qubits with high-frequency and high-quality resonators opens the way to explore higher tunnelling rate regimes or investigate on spin-photon coupling regimes.

On another side, the implementation of a RF transmission setup dedicated to the readout of charge sensors in Ge/SiGe heterostructures also lead to promising results. We performed simulations to improve the matching of the readout circuit with the feedlines and its sensitivity to the charge sensor resistance. We achieved high charge sensitivity together with low charge noise $S_\mu(1 \text{ Hz}) \sim 0.2 \mu\text{eV}/\sqrt{\text{Hz}}$. With such setup, we probed the stability diagram of a double quantum dot up to the last hole regime. By applying an external magnetic field, we observed the signature of the Pauli Spin Blockade permitting spin-to-charge conversion. We measured the relaxation of the blockade states and eventually found $T_1 > 100 \mu\text{s}$. This opens the path to electrically driven coherent manipulation and further investigation of the qubit driving mechanisms [N. W. Hendrickx, Massai, et al. 2023].

This manuscript presents the highlights as well as the problems we encountered with both systems. On one hand, we faced to reproducibility issues in the sputtering of the NbN films for the superconducting inductors. Indeed, the phases of NbN grown strongly depend on the sputtering parameters and the substrates. Possible solutions include extensive work on the calibration of the sputtering machine or a partnership with CEA Leti, which has provided us with films of remarkable quality. On the other hand, we have not been able to electrically drive the hole spins in our Ge/SiGe heterostructure devices. Due to a lack of sensor contrast at low magnetic fields, we had to work at fields above $B > 0.1 \text{ T}$. Despite efforts to explore a wide range of possible gyromagnetic factors, we did not observe the characteristic electrically driven spin resonance lines. Apart from these two major difficulties, this PhD project allowed us to make progress in many aspects of the readout of silicon and germanium quantum dot devices.

This PhD work mainly focusing on readout was integrated into a larger work on hole spin qubits carried out in the Lateqs group at CEA Grenoble. Recent studies have been carried on the strong spin-photon coupling [C. Yu 2022] between a hole spin in a Si nanowire and a microwave photon from a NbN $\lambda/2$ -resonator. In particular, this project targets the long-range spin-spin interaction [Borjans et al. 2020]. Other investigations on Si nanowires focus on optimal operating points to enhance both operation speed and coherence time [Piot et al. 2022]. In parallel, we have a growing interest in germanium. This material is CMOS compatible and allows spin qubits to be co-integrated with other quantum objects based on superconductivity or possible topologically protected states. The ability we have now to fabricate our own Ge/SiGe quantum dot device [Fernandez-Bada 2023] allows to test different architectures and different integration schemes towards scalable quantum platforms. Other prospects we are working on include the cooling of the hole electronic temperature using Maxwell demons [Koski et al. 2015] or the study of topological states in semiconductor superconductor devices [Vigneau, Mizokuchi, et al. 2019]. For all these projects a fast and high fidelity spin or charge readout method is of paramount importance. The work developed in this PhD project will certainly provide a strong basis for radiofrequency readout of semiconducting nanostructures.

BIBLIOGRAPHY

- Ahmed, Imtiaz, James A. Haigh, Simon Schaal, Sylvain Barraud, Yi Zhu, Chang-min Lee, Mario Amado, Jason W. A. Robinson, Alessandro Rossi, John J. L. Morton, and M. Fernando Gonzalez-Zalba (July 19, 2018). « Radio-Frequency Capacitive Gate-Based Sensing ». In: *Physical Review Applied* 10.1. Publisher: American Physical Society, p. 014018. DOI: [10.1103/PhysRevApplied.10.014018](https://doi.org/10.1103/PhysRevApplied.10.014018) (cit. on pp. 46, 91, 93).
- Averin, D. V. and K. K. Likharev (Feb. 1, 1986). « Coulomb blockade of single-electron tunneling, and coherent oscillations in small tunnel junctions ». In: *Journal of Low Temperature Physics* 62.3, pp. 345–373. ISSN: 1573-7357. DOI: [10.1007/BF00683469](https://doi.org/10.1007/BF00683469) (cit. on p. 30).
- Baibich, M. N., J. M. Broto, A. Fert, F. Nguyen Van Dau, F. Petroff, P. Etienne, G. Creuzet, A. Friederich, and J. Chazelas (Nov. 21, 1988). « Giant Magnetoresistance of (001)Fe/(001)Cr Magnetic Superlattices ». In: *Physical Review Letters* 61.21. Publisher: American Physical Society, pp. 2472–2475. DOI: [10.1103/PhysRevLett.61.2472](https://doi.org/10.1103/PhysRevLett.61.2472) (cit. on p. 2).
- Binasch, G., P. Grünberg, F. Saurenbach, and W. Zinn (Mar. 1, 1989). « Enhanced magnetoresistance in layered magnetic structures with antiferromagnetic interlayer exchange ». In: *Physical Review B* 39.7. Publisher: American Physical Society, pp. 4828–4830. DOI: [10.1103/PhysRevB.39.4828](https://doi.org/10.1103/PhysRevB.39.4828) (cit. on p. 2).
- Björk, Mikael T., Claes Thelander, Adam E. Hansen, Linus E. Jensen, Magnus W. Larsson, L. Reine Wallenberg, and Lars Samuelson (Sept. 1, 2004). « Few-Electron Quantum Dots in Nanowires ». In: *Nano Letters* 4.9. Publisher: American Chemical Society, pp. 1621–1625. ISSN: 1530-6984. DOI: [10.1021/nl049230s](https://doi.org/10.1021/nl049230s) (cit. on p. 3).
- Borjans, F., X. G. Croot, X. Mi, M. J. Gullans, and J. R. Petta (Jan. 2020). « Resonant microwave-mediated interactions between distant electron spins ». In: *Nature* 577.7789. Number: 7789. Publisher: Nature Publishing Group, pp. 195–198. ISSN: 1476-4687. DOI: [10.1038/s41586-019-1867-y](https://doi.org/10.1038/s41586-019-1867-y) (cit. on p. 124).
- Borsoi, Francesco, Nico W. Hendrickx, Valentin John, Marcel Meyer, Sayr Motz, Floor van Riggelen, Amir Sammak, Sander L. de Snoo, Giordano Scappucci, and Menno Veldhorst (Aug. 28, 2023). « Shared control of a 16 semiconductor quantum dot crossbar array ». In: *Nature Nanotechnology*. Publisher: Nature Publishing Group, pp. 1–7. ISSN: 1748-3395. DOI: [10.1038/s41565-023-01491-3](https://doi.org/10.1038/s41565-023-01491-3) (cit. on pp. 5, 31, 35).

BIBLIOGRAPHY

- Brenning, Henrik, Sergey Kafanov, Tim Duty, Sergey Kubatkin, and Per Delsing (Dec. 13, 2006). « An ultrasensitive radio-frequency single-electron transistor working up to 4.2K ». In: *Journal of Applied Physics* 100.11, p. 114321. ISSN: 0021-8979. DOI: [10.1063/1.2388134](https://doi.org/10.1063/1.2388134) (cit. on pp. 31, 93).
- Broderick, Christopher (Sept. 1, 2020). « Electronic structure of lonsdaleite SiGe alloys ». In: (cit. on p. 10).
- Bychkov, Yu. A. and É. I. Rashba (Jan. 1, 1984). « Properties of a 2D electron gas with lifted spectral degeneracy ». In: *Soviet Journal of Experimental and Theoretical Physics Letters* 39. ADS Bibcode: 1984JETPL..39...78B, p. 78. ISSN: 0021-3640 (cit. on p. 4).
- Camenzind, Leon C., Simon Geyer, Andreas Fuhrer, Richard J. Warburton, Dominik M. Zumbühl, and Andreas V. Kuhlmann (Mar. 2022). « A hole spin qubit in a fin field-effect transistor above 4 kelvin ». In: *Nature Electronics* 5.3. Number: 3 Publisher: Nature Publishing Group, pp. 178–183. ISSN: 2520-1131. DOI: [10.1038/s41928-022-00722-0](https://doi.org/10.1038/s41928-022-00722-0) (cit. on p. 4).
- Carbillet, C., V. Cherkez, M. A. Skvortsov, M. V. Feigel'man, F. Debontridder, L. B. Ioffe, V. S. Stolyarov, K. Ilin, M. Siegel, D. Roditchev, T. Cren, and C. Brun (July 2, 2020). « Spectroscopic evidence for strong correlations between local superconducting gap and local Altshuler-Aronov density of states suppression in ultrathin NbN films ». In: *Physical Review B* 102.2. Publisher: American Physical Society, p. 024504. DOI: [10.1103/PhysRevB.102.024504](https://doi.org/10.1103/PhysRevB.102.024504) (cit. on p. 58).
- Cassidy, M. C., A. S. Dzurak, R. G. Clark, K. D. Petersson, I. Farrer, D. A. Ritchie, and C. G. Smith (Nov. 27, 2007). « Single shot charge detection using a radio-frequency quantum point contact ». In: *Applied Physics Letters* 91.22, p. 222104. ISSN: 0003-6951. DOI: [10.1063/1.2809370](https://doi.org/10.1063/1.2809370) (cit. on p. 33).
- Ciorga, M., A. S. Sachrajda, P. Hawrylak, C. Gould, P. Zawadzki, S. Jullian, Y. Feng, and Z. Wasilewski (June 15, 2000). « Addition spectrum of a lateral dot from Coulomb and spin-blockade spectroscopy ». In: *Physical Review B* 61.24. Publisher: American Physical Society, R16315–R16318. DOI: [10.1103/PhysRevB.61.R16315](https://doi.org/10.1103/PhysRevB.61.R16315) (cit. on p. 3).
- Colless, J. I., A. C. Mahoney, J. M. Hornibrook, A. C. Doherty, H. Lu, A. C. Gossard, and D. J. Reilly (Jan. 25, 2013). « Dispersive Readout of a Few-Electron Double Quantum Dot with Fast rf Gate Sensors ». In: *Physical Review Letters* 110.4. Publisher: American Physical Society, p. 046805. DOI: [10.1103/PhysRevLett.110.046805](https://doi.org/10.1103/PhysRevLett.110.046805) (cit. on p. 30).
- Connors, Elliot J., J. Nelson, Lisa F. Edge, and John M. Nichol (Feb. 17, 2022). « Charge-noise spectroscopy of Si/SiGe quantum dots via dynamically-decoupled exchange oscillations ». In: *Nature Communications* 13.1. Number: 1 Publisher: Nature Publishing Group, p. 940. ISSN: 2041-1723. DOI: [10.1038/s41467-022-28519-x](https://doi.org/10.1038/s41467-022-28519-x) (cit. on pp. 5, 97).
- Connors, Elliot J., JJ Nelson, Haifeng Qiao, Lisa F. Edge, and John M. Nichol (Oct. 23, 2019). « Low-frequency charge noise in Si/SiGe quantum dots ». In: *Physical Review B* 100.16. Publisher: American Physical Society, p. 165305. DOI: [10.1103/PhysRevB.100.165305](https://doi.org/10.1103/PhysRevB.100.165305) (cit. on p. 96).
- Corna, Andrea, Léo Bourdet, Romain Maurand, Alessandro Crippa, Dharmraj Kotekar-Patil, Heorhii Bohuslavskiy, Romain Laviéville, Louis Hutin, Sylvain Barraud, Xavier Jehl, Maud Vinet,

- Silvano De Franceschi, Yann-Michel Niquet, and Marc Sanquer (Feb. 2, 2018). « Electrically driven electron spin resonance mediated by spin–valley–orbit coupling in a silicon quantum dot ». In: *npj Quantum Information* 4.1. Number: 1 Publisher: Nature Publishing Group, pp. 1–7. ISSN: 2056-6387. DOI: [10.1038/s41534-018-0059-1](https://doi.org/10.1038/s41534-018-0059-1) (cit. on p. 120).
- Crippa, Alessandro, Romain Maurand, Léo Bourdet, Dharmraj Kotekar-Patil, Anthony Amisse, Xavier Jehl, Marc Sanquer, Romain Laviéville, Heorhii Bohuslavskiy, Louis Hutin, Sylvain Barraud, Maud Vinet, Yann-Michel Niquet, and Silvano De Franceschi (Mar. 30, 2018). « Electrical Spin Driving by g-Matrix Modulation in Spin-Orbit Qubits ». In: *Physical Review Letters* 120.13. Publisher: American Physical Society, p. 137702. DOI: [10.1103/PhysRevLett.120.137702](https://doi.org/10.1103/PhysRevLett.120.137702) (cit. on p. 23).
- Dabbousi, B. O., J. Rodriguez-Viejo, F. V. Mikulec, J. R. Heine, H. Mattoussi, R. Ober, K. F. Jensen, and M. G. Bawendi (Nov. 1, 1997). « (CdSe)/ZnS Core-Shell Quantum Dots: Synthesis and Characterization of a Size Series of Highly Luminescent Nanocrystallites ». In: *The Journal of Physical Chemistry B* 101.46. Publisher: American Chemical Society, pp. 9463–9475. ISSN: 1520-6106. DOI: [10.1021/jp971091y](https://doi.org/10.1021/jp971091y) (cit. on p. 3).
- Datta, Supriyo and Biswajit Das (Feb. 12, 1990). « Electronic analog of the electro-optic modulator ». In: *Applied Physics Letters* 56.7, pp. 665–667. ISSN: 0003-6951. DOI: [10.1063/1.102730](https://doi.org/10.1063/1.102730) (cit. on p. 2).
- Dirac, P. A. M. (1928). « The Quantum Theory of the Electron ». In: *Proceedings of the Royal Society of London. Series A, Containing Papers of a Mathematical and Physical Character* 117.778, pp. 610–624. ISSN: 09501207 (cit. on p. 2).
- Dobbie, A., M. Myronov, R. J. H. Morris, A. H. A. Hassan, M. J. Prest, V. A. Shah, E. H. C. Parker, T. E. Whall, and D. R. Leadley (Oct. 23, 2012). « Ultra-high hole mobility exceeding one million in a strained germanium quantum well ». In: *Applied Physics Letters* 101.17, p. 172108. ISSN: 0003-6951. DOI: [10.1063/1.4763476](https://doi.org/10.1063/1.4763476) (cit. on pp. 3, 11).
- Dresselhaus, G. (Oct. 15, 1955). « Spin-Orbit Coupling Effects in Zinc Blende Structures ». In: *Physical Review* 100.2. Publisher: American Physical Society, pp. 580–586. DOI: [10.1103/PhysRev.100.580](https://doi.org/10.1103/PhysRev.100.580) (cit. on p. 4).
- Elzerman, J. M., R. Hanson, J. S. Greidanus, L. H. Willems van Beveren, S. De Franceschi, L. M. K. Vandersypen, S. Tarucha, and L. P. Kouwenhoven (Apr. 30, 2003). « Few-electron quantum dot circuit with integrated charge read out ». In: *Physical Review B* 67.16. Publisher: American Physical Society, p. 161308. DOI: [10.1103/PhysRevB.67.161308](https://doi.org/10.1103/PhysRevB.67.161308) (cit. on p. 30).
- Elzerman, J. M., R. Hanson, L. H. Willems van Beveren, B. Witkamp, L. M. K. Vandersypen, and L. P. Kouwenhoven (July 2004). « Single-shot read-out of an individual electron spin in a quantum dot ». In: *Nature* 430.6998. Number: 6998 Publisher: Nature Publishing Group, pp. 431–435. ISSN: 1476-4687. DOI: [10.1038/nature02693](https://doi.org/10.1038/nature02693) (cit. on p. 25).
- Ezzouch, Rami (June 9, 2021). « Gate reflectometry as readout and spectroscopy tool for silicon spin qubits ». PhD thesis. Université Grenoble Alpes [2020-....] (cit. on p. 100).

BIBLIOGRAPHY

- Fernandez-Bada, Gonzalo Troncoso (Mar. 20, 2023). « Hole Quantum Dots in Strained Ge/SiGe Quantum-Well Heterostructures ». PhD thesis. Université Grenoble Alpes [2020-....] (cit. on pp. 13, 85, 95–97, 124).
- Foronda, J., C. Morrison, J. E. Halpin, S. D. Rhead, and M. Myronov (Dec. 2014). « Weak antilocalization of high mobility holes in a strained Germanium quantum well heterostructure ». In: *Journal of Physics: Condensed Matter* 27.2. Publisher: IOP Publishing, p. 022201. ISSN: 0953-8984. DOI: [10.1088/0953-8984/27/2/022201](https://doi.org/10.1088/0953-8984/27/2/022201) (cit. on p. 13).
- Freeman, Blake M., Joshua S. Schoenfeld, and HongWen Jiang (June 22, 2016). « Comparison of low frequency charge noise in identically patterned Si/SiO₂ and Si/SiGe quantum dots ». In: *Applied Physics Letters* 108.25, p. 253108. ISSN: 0003-6951. DOI: [10.1063/1.4954700](https://doi.org/10.1063/1.4954700) (cit. on p. 97).
- Gao, Fei, Jian-Huan Wang, Hannes Watzinger, Hao Hu, Marko J. Rančić, Jie-Yin Zhang, Ting Wang, Yuan Yao, Gui-Lei Wang, Josip Kukučka, Lada Vukušić, Christoph Kloeffer, Daniel Loss, Feng Liu, Georgios Katsaros, and Jian-Jun Zhang (2020). « Site-Controlled Uniform Ge/Si Hut Wires with Electrically Tunable Spin–Orbit Coupling ». In: *Advanced Materials* 32.16. _eprint: <https://onlinelibrary.wiley.com/doi/pdf/10.1002/adma.201906523>, p. 1906523. ISSN: 1521-4095. DOI: [10.1002/adma.201906523](https://doi.org/10.1002/adma.201906523) (cit. on p. 3).
- Gerlach, Walther and Otto Stern (Dec. 1, 1922). « Das magnetische Moment des Silberatoms ». In: *Zeitschrift für Physik* 9.1, pp. 353–355. ISSN: 0044-3328. DOI: [10.1007/BF01326984](https://doi.org/10.1007/BF01326984) (cit. on p. 2).
- Goldsmith, John H., Ricky Gibson, Tim Cooper, Thaddeus J. Asel, Shin Mou, Dave C. Look, John S. Derov, and Joshua R. Hendrickson (Sept. 18, 2018). « Influence of nitride buffer layers on superconducting properties of niobium nitride ». In: *Journal of Vacuum Science & Technology A* 36.6, p. 061502. ISSN: 0734-2101. DOI: [10.1116/1.5044276](https://doi.org/10.1116/1.5044276) (cit. on p. 60).
- Gonzalez-Zalba, M. Fernando, Sergey N. Shevchenko, Sylvain Barraud, J. Robert Johansson, Andrew J. Ferguson, Franco Nori, and Andreas C. Betz (Mar. 9, 2016). « Gate-Sensing Coherent Charge Oscillations in a Silicon Field-Effect Transistor ». In: *Nano Letters* 16.3. Publisher: American Chemical Society, pp. 1614–1619. ISSN: 1530-6984. DOI: [10.1021/acs.nanolett.5b04356](https://doi.org/10.1021/acs.nanolett.5b04356) (cit. on p. 36).
- Grimm, A., S. Jebari, D. Hazra, F. Blanchet, F. Gustavo, J.-L. Thomassin, and M. Hofheinz (Aug. 2017). « A self-aligned nano-fabrication process for vertical NbN–MgO–NbN Josephson junctions ». In: *Superconductor Science and Technology* 30.10. Publisher: IOP Publishing, p. 105002. ISSN: 0953-2048. DOI: [10.1088/1361-6668/aa8007](https://doi.org/10.1088/1361-6668/aa8007) (cit. on p. 52).
- Hanson, R., L. H. Willems van Beveren, I. T. Vink, J. M. Elzerman, W. J. M. Naber, F. H. L. Koppens, L. P. Kouwenhoven, and L. M. K. Vandersypen (May 17, 2005). « Single-Shot Readout of Electron Spin States in a Quantum Dot Using Spin-Dependent Tunnel Rates ». In: *Physical Review Letters* 94.19. Publisher: American Physical Society, p. 196802. DOI: [10.1103/PhysRevLett.94.196802](https://doi.org/10.1103/PhysRevLett.94.196802) (cit. on p. 5).
- Hanson, R., L. P. Kouwenhoven, J. R. Petta, S. Tarucha, and L. M. K. Vandersypen (Oct. 1, 2007). « Spins in few-electron quantum dots ». In: *Reviews of Modern Physics* 79.4. Publisher:

- American Physical Society, pp. 1217–1265. DOI: [10.1103/RevModPhys.79.1217](https://doi.org/10.1103/RevModPhys.79.1217) (cit. on pp. 3, 106, 109).
- Hartmann, Jean-Michel, Nicolas Bernier, Francois Pierre, Jean-Paul Barnes, Vincent Mazzocchi, Julia Krawczyk, Gabriel Lima, Elyjah Kiyooka, and Silvano De Franceschi (May 19, 2023). « Epitaxy of Group-IV Semiconductors for Quantum Electronics ». In: *ECS Transactions* 111.1. Publisher: IOP Publishing, p. 53. ISSN: 1938-5862. DOI: [10.1149/11101.0053ecst](https://doi.org/10.1149/11101.0053ecst) (cit. on p. 11).
- Hendrickx, N. W., D. Franke, A. Sammak, M. Kouwenhoven, D. Sabbagh, L. Yeoh, R. Li, M. L. V. Tagliaferri, M. Virgilio, G. Capellini, G. Scappucci, and M. Veldhorst (July 19, 2018). « Gate-controlled quantum dots and superconductivity in planar germanium ». In: *Nature Communications* 9.1. Number: 1 Publisher: Nature Publishing Group, p. 2835. ISSN: 2041-1723. DOI: [10.1038/s41467-018-05299-x](https://doi.org/10.1038/s41467-018-05299-x) (cit. on pp. 3, 97).
- Hendrickx, N. W., D. P. Franke, A. Sammak, G. Scappucci, and M. Veldhorst (Jan. 2020). « Fast two-qubit logic with holes in germanium ». In: *Nature* 577.7791. Number: 7791 Publisher: Nature Publishing Group, pp. 487–491. ISSN: 1476-4687. DOI: [10.1038/s41586-019-1919-3](https://doi.org/10.1038/s41586-019-1919-3) (cit. on pp. 5, 111).
- Hendrickx, N. W., W. I. L. Lawrie, L. Petit, A. Sammak, G. Scappucci, and M. Veldhorst (July 10, 2020). « A single-hole spin qubit ». In: *Nature Communications* 11.1. Number: 1 Publisher: Nature Publishing Group, p. 3478. ISSN: 2041-1723. DOI: [10.1038/s41467-020-17211-7](https://doi.org/10.1038/s41467-020-17211-7) (cit. on p. 5).
- Hendrickx, N. W., L. Massai, M. Mergenthaler, F. Schupp, S. Paredes, S. W. Bedell, G. Salis, and A. Fuhrer (May 24, 2023). *Sweet-spot operation of a germanium hole spin qubit with highly anisotropic noise sensitivity*. DOI: [10.48550/arXiv.2305.13150](https://doi.org/10.48550/arXiv.2305.13150) (cit. on pp. 4, 124).
- Hendrickx, Nico W., William I. L. Lawrie, Maximilian Russ, Floor van Riggelen, Sander L. de Snoo, Raymond N. Schouten, Amir Sammak, Giordano Scappucci, and Menno Veldhorst (Mar. 2021). « A four-qubit germanium quantum processor ». In: *Nature* 591.7851. Number: 7851 Publisher: Nature Publishing Group, pp. 580–585. ISSN: 1476-4687. DOI: [10.1038/s41586-021-03332-6](https://doi.org/10.1038/s41586-021-03332-6) (cit. on pp. 5, 34, 86).
- Hornibrook, J. M., J. I. Colless, A. C. Mahoney, X. G. Croot, S. Blanvillain, H. Lu, A. C. Gossard, and D. J. Reilly (Mar. 12, 2014). « Frequency multiplexing for readout of spin qubits ». In: *Applied Physics Letters* 104.10, p. 103108. ISSN: 0003-6951. DOI: [10.1063/1.4868107](https://doi.org/10.1063/1.4868107) (cit. on pp. 35, 46).
- Hu, Yongjie, Ferdinand Kuemmeth, Charles M. Lieber, and Charles M. Marcus (Jan. 2012). « Hole spin relaxation in Ge–Si core–shell nanowire qubits ». In: *Nature Nanotechnology* 7.1. Number: 1 Publisher: Nature Publishing Group, pp. 47–50. ISSN: 1748-3395. DOI: [10.1038/nnano.2011.234](https://doi.org/10.1038/nnano.2011.234) (cit. on p. 3).
- Hutin, L., B. Bertrand, R. Maurand, M. Urdampilleta, B. Jadot, H. Bohuslavskyi, L. Bourdet, Y.-M. Niquet, X. Jehl, S. Barraud, C. Bauerle, T. Meunier, M. Sanquer, S. De Franceschi, and M. Vinet (May 2017). « SOI CMOS technology for quantum information processing ». In: *2017 IEEE International Conference on IC Design and Technology (ICICDT)*. Conference

Name: 2017 IEEE International Conference on IC Design and Technology (ICICDT) ISBN: 9781509045020 Place: Austin, TX, USA Publisher: IEEE, pp. 1–4. DOI: [10.1109/ICICDT.2017.7993523](https://doi.org/10.1109/ICICDT.2017.7993523) (cit. on p. 16).

- Ibberson, David J., Theodor Lundberg, James A. Haigh, Louis Hutin, Benoit Bertrand, Sylvain Barraud, Chang-Min Lee, Nadia A. Stelmashenko, Giovanni A. Oakes, Laurence Cochrane, Jason W.A. Robinson, Maud Vinet, M. Fernando Gonzalez-Zalba, and Lisa A. Ibberson (May 5, 2021). « Large Dispersive Interaction between a CMOS Double Quantum Dot and Microwave Photons ». In: *PRX Quantum* 2.2. Publisher: American Physical Society, p. 020315. DOI: [10.1103/PRXQuantum.2.020315](https://doi.org/10.1103/PRXQuantum.2.020315) (cit. on pp. 39, 47).
- Jirovec, Daniel, Andrea Hofmann, Andrea Ballabio, Philipp M. Mutter, Giulio Tavani, Marc Boffill, Alessandro Crippa, Josip Kukucka, Oliver Sagi, Frederico Martins, Jaime Saez-Mollejo, Ivan Prieto, Maksim Borovkov, Jordi Arbiol, Daniel Chrastina, Giovanni Isella, and Georgios Katsaros (Aug. 2021). « A singlet-triplet hole spin qubit in planar Ge ». In: *Nature Materials* 20.8. Number: 8 Publisher: Nature Publishing Group, pp. 1106–1112. ISSN: 1476-4660. DOI: [10.1038/s41563-021-01022-2](https://doi.org/10.1038/s41563-021-01022-2) (cit. on pp. 5, 109, 111, 120).
- Johnson, A. C., J. R. Petta, C. M. Marcus, M. P. Hanson, and A. C. Gossard (Oct. 5, 2005). « Singlet-triplet spin blockade and charge sensing in a few-electron double quantum dot ». In: *Physical Review B* 72.16. Publisher: American Physical Society, p. 165308. DOI: [10.1103/PhysRevB.72.165308](https://doi.org/10.1103/PhysRevB.72.165308) (cit. on p. 26).
- Jordan, Paul M., Daniel K. Simon, Thomas Mikolažick, and Ingo Dirnstorfer (June 6, 2016). « Trapped charge densities in Al₂O₃-based silicon surface passivation layers ». In: *Journal of Applied Physics* 119.21, p. 215306. ISSN: 0021-8979. DOI: [10.1063/1.4953141](https://doi.org/10.1063/1.4953141) (cit. on p. 96).
- Kamlapure, Anand, Tanmay Das, Somesh Chandra Ganguli, Jayesh B. Parmar, Somnath Bhattacharyya, and Pratap Raychaudhuri (Oct. 17, 2013). « Emergence of nanoscale inhomogeneity in the superconducting state of a homogeneously disordered conventional superconductor ». In: *Scientific Reports* 3.1. Number: 1 Publisher: Nature Publishing Group, p. 2979. ISSN: 2045-2322. DOI: [10.1038/srep02979](https://doi.org/10.1038/srep02979) (cit. on pp. 45, 58).
- Kamlapure, Anand, Mintu Mondal, Madhavi Chand, Archana Mishra, John Jesudasan, Vivas Bagwe, L. Benfatto, Vikram Tripathi, and Pratap Raychaudhuri (Feb. 17, 2010). « Measurement of magnetic penetration depth and superconducting energy gap in very thin epitaxial NbN films ». In: *Applied Physics Letters* 96.7, p. 072509. ISSN: 0003-6951. DOI: [10.1063/1.3314308](https://doi.org/10.1063/1.3314308) (cit. on p. 55).
- Keith, D., M. G. House, M. B. Donnelly, T. F. Watson, B. Weber, and M. Y. Simmons (Oct. 3, 2019). « Single-Shot Spin Readout in Semiconductors Near the Shot-Noise Sensitivity Limit ». In: *Physical Review X* 9.4. Publisher: American Physical Society, p. 041003. DOI: [10.1103/PhysRevX.9.041003](https://doi.org/10.1103/PhysRevX.9.041003) (cit. on pp. 33, 34).
- Kloeffel, Christoph, Marko J. Rančić, and Daniel Loss (June 13, 2018). « Direct Rashba spin-orbit interaction in Si and Ge nanowires with different growth directions ». In: *Physical Review B* 97.23. Publisher: American Physical Society, p. 235422. DOI: [10.1103/PhysRevB.97.235422](https://doi.org/10.1103/PhysRevB.97.235422) (cit. on pp. 16, 17).

- Kloeffel, Christoph, Mircea Trif, and Daniel Loss (Nov. 9, 2011). « Strong spin-orbit interaction and helical hole states in Ge/Si nanowires ». In: *Physical Review B* 84.19. Publisher: American Physical Society, p. 195314. DOI: [10.1103/PhysRevB.84.195314](https://doi.org/10.1103/PhysRevB.84.195314) (cit. on p. 16).
- Koski, J. V., A. Kutvonen, I. M. Khaymovich, T. Ala-Nissila, and J. P. Pekola (Dec. 30, 2015). « On-Chip Maxwell's Demon as an Information-Powered Refrigerator ». In: *Physical Review Letters* 115.26. Publisher: American Physical Society, p. 260602. DOI: [10.1103/PhysRevLett.115.260602](https://doi.org/10.1103/PhysRevLett.115.260602) (cit. on p. 124).
- Kouwenhoven, L. P., D. G. Austing, and S. Tarucha (June 2001). « Few-electron quantum dots ». In: *Reports on Progress in Physics* 64.6, p. 701. ISSN: 0034-4885. DOI: [10.1088/0034-4885/64/6/201](https://doi.org/10.1088/0034-4885/64/6/201) (cit. on pp. 2, 20).
- Kouwenhoven, Leo P., Gerd Schön, and Lydia L. Sohn (1997). « Introduction to Mesoscopic Electron Transport ». In: *Mesoscopic Electron Transport*. Ed. by Lydia L. Sohn, Leo P. Kouwenhoven, and Gerd Schön. NATO ASI Series. Dordrecht: Springer Netherlands, pp. 1–44. ISBN: 978-94-015-8839-3. DOI: [10.1007/978-94-015-8839-3_1](https://doi.org/10.1007/978-94-015-8839-3_1) (cit. on p. 19).
- Landau, L.D. (1932). « On the Theory of Transfer of Energy at Collisions II ». In: *Physikalische Zeitschrift der Sowjetunion* 2, pp. 46–51 (cit. on p. 115).
- Lauterbur, P. C. (Mar. 1973). « Image Formation by Induced Local Interactions: Examples Employing Nuclear Magnetic Resonance ». In: *Nature* 242.5394. Number: 5394 Publisher: Nature Publishing Group, pp. 190–191. ISSN: 1476-4687. DOI: [10.1038/242190a0](https://doi.org/10.1038/242190a0) (cit. on p. 2).
- Lawrie, W. I. L., N. W. Hendrickx, F. van Riggelen, M. Russ, L. Petit, A. Sammak, G. Scappucci, and M. Veldhorst (Oct. 14, 2020). « Spin Relaxation Benchmarks and Individual Qubit Addressability for Holes in Quantum Dots ». In: *Nano Letters* 20.10. Publisher: American Chemical Society, pp. 7237–7242. ISSN: 1530-6984. DOI: [10.1021/acs.nanolett.0c02589](https://doi.org/10.1021/acs.nanolett.0c02589) (cit. on pp. 109, 111, 114).
- Leggett, A. J., S. Chakravarty, A. T. Dorsey, Matthew P. A. Fisher, Anupam Garg, and W. Zwerger (Jan. 1, 1987). « Dynamics of the dissipative two-state system ». In: *Reviews of Modern Physics* 59.1. Publisher: American Physical Society, pp. 1–85. DOI: [10.1103/RevModPhys.59.1](https://doi.org/10.1103/RevModPhys.59.1) (cit. on p. 115).
- Leith, S., M. Vogel, J. Fan, E. Seiler, R. Ries, and X. Jiang (Jan. 2021). « Superconducting NbN thin films for use in superconducting radio frequency cavities ». In: *Superconductor Science and Technology* 34.2. Publisher: IOP Publishing, p. 025006. ISSN: 0953-2048. DOI: [10.1088/1361-6668/abc73b](https://doi.org/10.1088/1361-6668/abc73b) (cit. on pp. 58, 59).
- Liu, Y.-Y., S.G.J. Philips, L.A. Orona, N. Samkharadze, T. McJunkin, E.R. MacQuarrie, M.A. Eriksson, L.M.K. Vandersypen, and A. Yacoby (July 23, 2021). « Radio-Frequency Reflectometry in Silicon-Based Quantum Dots ». In: *Physical Review Applied* 16.1. Publisher: American Physical Society, p. 014057. DOI: [10.1103/PhysRevApplied.16.014057](https://doi.org/10.1103/PhysRevApplied.16.014057) (cit. on pp. 34, 84).
- Lodari, M., A. Tosato, D. Sabbagh, M. A. Schubert, G. Capellini, A. Sammak, M. Veldhorst, and G. Scappucci (July 31, 2019). « Light effective hole mass in undoped Ge/SiGe quantum wells ». In: *Physical Review B* 100.4. Publisher: American Physical Society, p. 041304. DOI: [10.1103/PhysRevB.100.041304](https://doi.org/10.1103/PhysRevB.100.041304) (cit. on p. 11).

BIBLIOGRAPHY

- Lodari, Mario, Nico W. Hendrickx, William I. L. Lawrie, Tzu-Kan Hsiao, Lieven M. K. Vandersypen, Amir Sammak, Menno Veldhorst, and Giordano Scappucci (Jan. 2021). « Low percolation density and charge noise with holes in germanium ». In: *Materials for Quantum Technology* 1.1. Publisher: IOP Publishing, p. 011002. ISSN: 2633-4356. DOI: [10.1088/2633-4356/abcd82](https://doi.org/10.1088/2633-4356/abcd82) (cit. on pp. 96, 97).
- Loss, Daniel and David P. DiVincenzo (Jan. 1, 1998). « Quantum computation with quantum dots ». In: *Physical Review A* 57.1. Publisher: American Physical Society, pp. 120–126. DOI: [10.1103/PhysRevA.57.120](https://doi.org/10.1103/PhysRevA.57.120) (cit. on pp. 4, 25).
- Luttinger, J. M. and W. Kohn (Feb. 15, 1955). « Motion of Electrons and Holes in Perturbed Periodic Fields ». In: *Physical Review* 97.4. Publisher: American Physical Society, pp. 869–883. DOI: [10.1103/PhysRev.97.869](https://doi.org/10.1103/PhysRev.97.869) (cit. on p. 8).
- Maurand, R., X. Jehl, D. Kotekar-Patil, A. Corna, H. Bohuslavskiy, R. Laviéville, L. Hutin, S. Barraud, M. Vinet, M. Sanquer, and S. De Franceschi (Nov. 24, 2016). « A CMOS silicon spin qubit ». In: *Nature Communications* 7.1. Number: 1 Publisher: Nature Publishing Group, p. 13575. ISSN: 2041-1723. DOI: [10.1038/ncomms13575](https://doi.org/10.1038/ncomms13575) (cit. on pp. 4, 15, 16).
- Megrant, A., C. Neill, R. Barends, B. Chiaro, Yu Chen, L. Feigl, J. Kelly, Erik Lucero, Matteo Mariantoni, P. J. J. O’Malley, D. Sank, A. Vainsencher, J. Wenner, T. C. White, Y. Yin, J. Zhao, C. J. Palmstrøm, John M. Martinis, and A. N. Cleland (Mar. 15, 2012). « Planar superconducting resonators with internal quality factors above one million ». In: *Applied Physics Letters* 100.11, p. 113510. ISSN: 0003-6951. DOI: [10.1063/1.3693409](https://doi.org/10.1063/1.3693409) (cit. on p. 49).
- Mizuta, R., R. M. Otxoa, A. C. Betz, and M. F. Gonzalez-Zalba (Jan. 18, 2017). « Quantum and tunneling capacitance in charge and spin qubits ». In: *Physical Review B* 95.4. Publisher: American Physical Society, p. 045414. DOI: [10.1103/PhysRevB.95.045414](https://doi.org/10.1103/PhysRevB.95.045414) (cit. on p. 35).
- Mutter, Philipp M. and Guido Burkard (Feb. 26, 2021). « Natural heavy-hole flopping mode qubit in germanium ». In: *Physical Review Research* 3.1. Publisher: American Physical Society, p. 013194. DOI: [10.1103/PhysRevResearch.3.013194](https://doi.org/10.1103/PhysRevResearch.3.013194) (cit. on p. 23).
- Ono, K., D. G. Austing, Y. Tokura, and S. Tarucha (Aug. 23, 2002). « Current Rectification by Pauli Exclusion in a Weakly Coupled Double Quantum Dot System ». In: *Science* 297.5585. Publisher: American Association for the Advancement of Science, pp. 1313–1317. DOI: [10.1126/science.1070958](https://doi.org/10.1126/science.1070958) (cit. on p. 25).
- Pakkiam, P., A. V. Timofeev, M. G. House, M. R. Hogg, T. Kobayashi, M. Koch, S. Rogge, and M. Y. Simmons (Nov. 26, 2018). « Single-Shot Single-Gate rf Spin Readout in Silicon ». In: *Physical Review X* 8.4. Publisher: American Physical Society, p. 041032. DOI: [10.1103/PhysRevX.8.041032](https://doi.org/10.1103/PhysRevX.8.041032) (cit. on p. 35).
- Paquelet Wuetz, Brian, Davide Degli Esposti, Anne-Marije J. Zwerver, Sergey V. Amitonov, Marc Botifoll, Jordi Arbiol, Amir Sammak, Lieven M. K. Vandersypen, Maximilian Russ, and Giordano Scappucci (Mar. 13, 2023). « Reducing charge noise in quantum dots by using thin silicon quantum wells ». In: *Nature Communications* 14.1. Number: 1 Publisher: Nature Publishing Group, p. 1385. ISSN: 2041-1723. DOI: [10.1038/s41467-023-36951-w](https://doi.org/10.1038/s41467-023-36951-w) (cit. on pp. 96, 97).

- Pauli, W. (Feb. 1, 1925). « Über den Zusammenhang des Abschlusses der Elektronengruppen im Atom mit der Komplexstruktur der Spektren ». In: *Zeitschrift für Physik* 31.1, pp. 765–783. ISSN: 0044-3328. DOI: [10.1007/BF02980631](https://doi.org/10.1007/BF02980631) (cit. on p. 2).
- Petersson, K. D., L. W. McFaul, M. D. Schroer, M. Jung, J. M. Taylor, A. A. Houck, and J. R. Petta (Oct. 2012). « Circuit quantum electrodynamics with a spin qubit ». In: *Nature* 490.7420. Number: 7420 Publisher: Nature Publishing Group, pp. 380–383. ISSN: 1476-4687. DOI: [10.1038/nature11559](https://doi.org/10.1038/nature11559) (cit. on p. 35).
- Piot, N., B. Brun, V. Schmitt, S. Zihlmann, V. P. Michal, A. Apra, J. C. Abadillo-Uriel, X. Jehl, B. Bertrand, H. Niebojewski, L. Hutin, M. Vinet, M. Urdampilleta, T. Meunier, Y.-M. Niquet, R. Maurand, and S. De Franceschi (Oct. 2022). « A single hole spin with enhanced coherence in natural silicon ». In: *Nature Nanotechnology* 17.10. Number: 10 Publisher: Nature Publishing Group, pp. 1072–1077. ISSN: 1748-3395. DOI: [10.1038/s41565-022-01196-z](https://doi.org/10.1038/s41565-022-01196-z) (cit. on pp. 4, 18, 124).
- Pozar, David M (2005). *Microwave engineering; 3rd ed.* Hoboken, NJ: Wiley (cit. on p. 87).
- Rashba, E. I. (1960). « Cyclotron and combined resonances in a perpendicular field ». In: *Sov. Phys. Solid State* (2), pp. 1109–1122 (cit. on p. 2).
- Reilly, D. J., C. M. Marcus, M. P. Hanson, and A. C. Gossard (Oct. 15, 2007). « Fast single-charge sensing with a rf quantum point contact ». In: *Applied Physics Letters* 91.16, p. 162101. ISSN: 0003-6951. DOI: [10.1063/1.2794995](https://doi.org/10.1063/1.2794995) (cit. on p. 33).
- Ribeiro, Hugo and Guido Burkard (May 28, 2009). « Nuclear State Preparation via Landau-Zener-Stückelberg Transitions in Double Quantum Dots ». In: *Physical Review Letters* 102.21. Publisher: American Physical Society, p. 216802. DOI: [10.1103/PhysRevLett.102.216802](https://doi.org/10.1103/PhysRevLett.102.216802) (cit. on p. 115).
- Sam-Giao, Diane, Stéphanie Pouget, Catherine Bougerol, Eva Monroy, Alexander Grimm, Salha Jebari, Max Hofheinz, J.-M. Gérard, and Val Zwiller (Oct. 13, 2014). « High-quality NbN nanofilms on a GaN/AlN heterostructure ». In: *AIP Advances* 4.10, p. 107123. ISSN: 2158-3226. DOI: [10.1063/1.4898327](https://doi.org/10.1063/1.4898327) (cit. on p. 52).
- Scappucci, Giordano, Christoph Kloeffel, Floris A. Zwanenburg, Daniel Loss, Maksym Myronov, Jian-Jun Zhang, Silvano De Franceschi, Georgios Katsaros, and Menno Veldhorst (Oct. 2021). « The germanium quantum information route ». In: *Nature Reviews Materials* 6.10. Number: 10 Publisher: Nature Publishing Group, pp. 926–943. ISSN: 2058-8437. DOI: [10.1038/s41578-020-00262-z](https://doi.org/10.1038/s41578-020-00262-z) (cit. on pp. 11, 17).
- Schoelkopf, R. J., P. Wahlgren, A. A. Kozhevnikov, P. Delsing, and D. E. Prober (May 22, 1998). « The Radio-Frequency Single-Electron Transistor (RF-SET): A Fast and Ultrasensitive Electrometer ». In: *Science* 280.5367. Publisher: American Association for the Advancement of Science, pp. 1238–1242. DOI: [10.1126/science.280.5367.1238](https://doi.org/10.1126/science.280.5367.1238) (cit. on pp. 30, 31, 93).
- Seedhouse, Amanda E., Tuomo Tantt, Ross C.C. Leon, Ruichen Zhao, Kuan Yen Tan, Bas Hensen, Fay E. Hudson, Kohei M. Itoh, Jun Yoneda, Chih Hwan Yang, Andrea Morello, Arne Laucht, Susan N. Coppersmith, Andre Saraiva, and Andrew S. Dzurak (Jan. 7, 2021). « Pauli Block-

- ade in Silicon Quantum Dots with Spin-Orbit Control ». In: *PRX Quantum* 2.1. Publisher: American Physical Society, p. 010303. DOI: [10.1103/PRXQuantum.2.010303](https://doi.org/10.1103/PRXQuantum.2.010303) (cit. on p. 109).
- Shao, Hong Yang, Kan Zhang, Yi Dan Zhang, Mao Wen, and Wei Tao Zheng (2017). « NbN Thin Film of Alternating Textures ». In: *Materials Science Forum* 898. Publisher: Trans Tech Publications Ltd, pp. 1431–1437. ISSN: 1662-9752. DOI: [10.4028/www.scientific.net/MSF.898.1431](https://doi.org/10.4028/www.scientific.net/MSF.898.1431) (cit. on p. 59).
- Shevchenko, S. N., S. Ashhab, and Franco Nori (July 1, 2010). « Landau–Zener–Stückelberg interferometry ». In: *Physics Reports* 492.1, pp. 1–30. ISSN: 0370-1573. DOI: [10.1016/j.physrep.2010.03.002](https://doi.org/10.1016/j.physrep.2010.03.002) (cit. on p. 115).
- Simmons, Christie, J. R. Prance, Madhu Thalakulam, B. M. Rosemeyer, B. J. Van Bael, Donald E. Savage, Max G. Lagally, R. Joynt, Mark Friesen, S. N. Coppersmith, and M. A. Eriksson (Oct. 1, 2010). « (Invited) Toward Si/SiGe Quantum Dot Spin Qubits: Gated Si/SiGe Single and Double Quantum Dots ». In: *ECS Transactions* 33.6. Publisher: IOP Publishing, p. 639. ISSN: 1938-5862. DOI: [10.1149/1.3487594](https://doi.org/10.1149/1.3487594) (cit. on p. 3).
- Sprinzak, D., Yang Ji, M. Heiblum, D. Mahalu, and Hadas Shtrikman (Apr. 12, 2002). « Charge Distribution in a Kondo-Correlated Quantum Dot ». In: *Physical Review Letters* 88.17. Publisher: American Physical Society, p. 176805. DOI: [10.1103/PhysRevLett.88.176805](https://doi.org/10.1103/PhysRevLett.88.176805) (cit. on pp. 30, 31).
- Suzuki, Mitsumasa, Masahiro Baba, and Takeshi Anayama (Jan. 1, 1987). « Critical Magnetic Fields of Superconducting NbN Films Prepared by Reactive Sputtering ». In: *Japanese Journal of Applied Physics* 26 (S3-2). Publisher: IOP Publishing, p. 947. ISSN: 1347-4065. DOI: [10.7567/JJAPS.26S3.947](https://doi.org/10.7567/JJAPS.26S3.947) (cit. on p. 55).
- Takeda, Kenta, Akito Noiri, Takashi Nakajima, Leon C. Camenzind, Takashi Kobayashi, Amir Sammak, Giordano Scappucci, and Seigo Tarucha (Aug. 31, 2023). *Rapid single-shot parity spin readout in a silicon double quantum dot with fidelity exceeding 99 %*. DOI: [10.48550/arXiv.2309.00225](https://doi.org/10.48550/arXiv.2309.00225) (cit. on p. 31).
- Terrazos, L. A., E. Marcellina, Zhanning Wang, S. N. Coppersmith, Mark Friesen, A. R. Hamilton, Xuedong Hu, Belita Koiller, A. L. Saraiva, Dimitrie Culcer, and Rodrigo B. Capaz (Mar. 15, 2021). « Theory of hole-spin qubits in strained germanium quantum dots ». In: *Physical Review B* 103.12. Publisher: American Physical Society, p. 125201. DOI: [10.1103/PhysRevB.103.125201](https://doi.org/10.1103/PhysRevB.103.125201) (cit. on p. 14).
- Uhlenbeck, G. E. and S. Goudsmit (Nov. 1, 1925). « Ersetzung der Hypothese vom unmechanischen Zwang durch eine Forderung bezüglich des inneren Verhaltens jedes einzelnen Elektrons ». In: *Die Naturwissenschaften* 13.47, pp. 953–954. ISSN: 1432-1904. DOI: [10.1007/BF01558878](https://doi.org/10.1007/BF01558878) (cit. on p. 2).
- Urdampilleta, Matias, David J. Niegemann, Emmanuel Chanrion, Baptiste Jadot, Cameron Spence, Pierre-André Mortemousque, Christopher Bäuerle, Louis Hutin, Benoit Bertrand, Sylvain Barraud, Romain Maurand, Marc Sanquer, Xavier Jehl, Silvano De Franceschi, Maud Vinet, and Tristan Meunier (Aug. 2019). « Gate-based high fidelity spin readout in a CMOS device ».

- In: *Nature Nanotechnology* 14.8. Number: 8 Publisher: Nature Publishing Group, pp. 737–741. ISSN: 1748-3395. DOI: [10.1038/s41565-019-0443-9](https://doi.org/10.1038/s41565-019-0443-9) (cit. on p. 38).
- Vasyutin, M. A., N. D. Kuz'michev, and D. A. Shilkin (Feb. 1, 2016). « Upper critical field of niobium nitride thin films ». In: *Physics of the Solid State* 58.2, pp. 236–239. ISSN: 1090-6460. DOI: [10.1134/S1063783416020311](https://doi.org/10.1134/S1063783416020311) (cit. on p. 55).
- Veldhorst, M., J. C. C. Hwang, C. H. Yang, A. W. Leenstra, B. de Ronde, J. P. Dehollain, J. T. Muhonen, F. E. Hudson, K. M. Itoh, A. Morello, and A. S. Dzurak (Dec. 2014). « An addressable quantum dot qubit with fault-tolerant control-fidelity ». In: *Nature Nanotechnology* 9.12. Number: 12 Publisher: Nature Publishing Group, pp. 981–985. ISSN: 1748-3395. DOI: [10.1038/nnano.2014.216](https://doi.org/10.1038/nnano.2014.216) (cit. on p. 18).
- Venitucci, Benjamin and Yann-Michel Niquet (Mar. 27, 2019). « Simple model for electrical hole spin manipulation in semiconductor quantum dots: Impact of dot material and orientation ». In: *Physical Review B* 99.11. Publisher: American Physical Society, p. 115317. DOI: [10.1103/PhysRevB.99.115317](https://doi.org/10.1103/PhysRevB.99.115317) (cit. on p. 8).
- Vigneau, Florian, Federico Fedele, Anasua Chatterjee, David Reilly, Ferdinand Kuemmeth, M. Fernando Gonzalez-Zalba, Edward Laird, and Natalia Ares (June 1, 2023). « Probing quantum devices with radio-frequency reflectometry ». In: *Applied Physics Reviews* 10.2, p. 021305. ISSN: 1931-9401. DOI: [10.1063/5.0088229](https://doi.org/10.1063/5.0088229) (cit. on p. 35).
- Vigneau, Florian, Rasei Mizokuchi, Dante Colao Zanuz, Xuhai Huang, Susheng Tan, Romain Maurand, Sergey Frolov, Amir Sammak, Giordano Scappucci, Francois Lefloch, and Silvano De Franceschi (Feb. 13, 2019). « Germanium Quantum-Well Josephson Field-Effect Transistors and Interferometers ». In: *Nano Letters* 19.2. Publisher: American Chemical Society, pp. 1023–1027. ISSN: 1530-6984. DOI: [10.1021/acs.nanolett.8b04275](https://doi.org/10.1021/acs.nanolett.8b04275) (cit. on p. 124).
- Voisin, Benoit, Viet-Hung Nguyen, Julien Renard, Xavier Jehl, Sylvain Barraud, François Triozon, Maud Vinet, Ivan Duchein, Yann-Michel Niquet, Silvano de Franceschi, and Marc Sanquer (Apr. 9, 2014). « Few-Electron Edge-State Quantum Dots in a Silicon Nanowire Field-Effect Transistor ». In: *Nano Letters* 14.4. Publisher: American Chemical Society, pp. 2094–2098. ISSN: 1530-6984. DOI: [10.1021/nl500299h](https://doi.org/10.1021/nl500299h) (cit. on p. 3).
- Vukušić, Lada, Josip Kukučka, Hannes Watzinger, Joshua Michael Milem, Friedrich Schäffler, and Georgios Katsaros (Nov. 14, 2018). « Single-Shot Readout of Hole Spins in Ge ». In: *Nano Letters* 18.11. Publisher: American Chemical Society, pp. 7141–7145. ISSN: 1530-6984. DOI: [10.1021/acs.nanolett.8b03217](https://doi.org/10.1021/acs.nanolett.8b03217) (cit. on p. 5).
- Watanabe, Koki, Keiji Yoshida, and Takeshi Aoki Kohjiro (Oct. 1, 1994). « Kinetic Inductance of Superconducting Coplanar Waveguides ». In: *Japanese Journal of Applied Physics* 33.10. Publisher: IOP Publishing, p. 5708. ISSN: 1347-4065. DOI: [10.1143/JJAP.33.5708](https://doi.org/10.1143/JJAP.33.5708) (cit. on p. 45).
- Wees, B. J. van, H. van Houten, C. W. J. Beenakker, J. G. Williamson, L. P. Kouwenhoven, D. van der Marel, and C. T. Foxon (Feb. 29, 1988). « Quantized conductance of point contacts in a two-dimensional electron gas ». In: *Physical Review Letters* 60.9. Publisher: American Physical Society, pp. 848–850. DOI: [10.1103/PhysRevLett.60.848](https://doi.org/10.1103/PhysRevLett.60.848) (cit. on pp. 30, 31).

- West, Anderson, Bas Hensen, Alexis Jouan, Tuomo Tanttu, Chih-Hwan Yang, Alessandro Rossi, M. Fernando Gonzalez-Zalba, Fay Hudson, Andrea Morello, David J. Reilly, and Andrew S. Dzurak (May 2019). « Gate-based single-shot readout of spins in silicon ». In: *Nature Nanotechnology* 14.5. Number: 5 Publisher: Nature Publishing Group, pp. 437–441. ISSN: 1748-3395. DOI: [10.1038/s41565-019-0400-7](https://doi.org/10.1038/s41565-019-0400-7) (cit. on p. 38).
- Wiel, W. G. van der, S. De Franceschi, J. M. Elzerman, T. Fujisawa, S. Tarucha, and L. P. Kouwenhoven (Dec. 17, 2002). « Electron transport through double quantum dots ». In: *Reviews of Modern Physics* 75.1. Publisher: American Physical Society, pp. 1–22. DOI: [10.1103/RevModPhys.75.1](https://doi.org/10.1103/RevModPhys.75.1) (cit. on p. 21).
- Winkler, Roland (Jan. 1, 2003). « Spin–Orbit Coupling Effects in Two-Dimensional Electron and Hole Systems ». In: *Springer Tracts in Modern Physics* 191. ISSN: 978-3-540-01187-3. DOI: [10.1007/b13586](https://doi.org/10.1007/b13586) (cit. on p. 9).
- You, Jie, Hai-Ou Li, Ke Wang, Gang Cao, Xiang-Xiang Song, Ming Xiao, and Guo-Ping Guo (Dec. 7, 2015). « Suppression of low-frequency charge noise in gates-defined GaAs quantum dots ». In: *Applied Physics Letters* 107.23, p. 233104. ISSN: 0003-6951. DOI: [10.1063/1.4937271](https://doi.org/10.1063/1.4937271) (cit. on p. 97).
- Yu, Cécile (Sept. 15, 2022). « Hybrid circuit quantum electrodynamics with a hole spin in silicon ». PhD thesis. Université Grenoble Alpes [2020-....] (cit. on pp. 52, 124).
- Yu, Cécile X., Simon Zihlmann, José C. Abadillo-Uriel, Vincent P. Michal, Nils Rambal, Heimanu Niebojewski, Thomas Bedecarrats, Maud Vinet, Étienne Dumur, Michele Filippone, Benoit Bertrand, Silvano De Franceschi, Yann-Michel Niquet, and Romain Maurand (July 2023). « Strong coupling between a photon and a hole spin in silicon ». In: *Nature Nanotechnology* 18.7. Number: 7 Publisher: Nature Publishing Group, pp. 741–746. ISSN: 1748-3395. DOI: [10.1038/s41565-023-01332-3](https://doi.org/10.1038/s41565-023-01332-3) (cit. on p. 52).
- Yu, Cécile Xinqing, Simon Zihlmann, Gonzalo Troncoso Fernández-Bada, Jean-Luc Thomassin, Frédéric Gustavo, Étienne Dumur, and Romain Maurand (Feb. 2, 2021). « Magnetic field resilient high kinetic inductance superconducting niobium nitride coplanar waveguide resonators ». In: *Applied Physics Letters* 118.5, p. 054001. ISSN: 0003-6951. DOI: [10.1063/5.0039945](https://doi.org/10.1063/5.0039945) (cit. on pp. 55, 57).
- Zener Clarence and Fowler, Ralph Howard (1932). « Non-adiabatic crossing of energy levels ». In: *Proceedings of the Royal Society of London. Series A, Containing Papers of a Mathematical and Physical Character* 137.833, pp. 696–702. DOI: [10.1098/rspa.1932.0165](https://doi.org/10.1098/rspa.1932.0165) (cit. on p. 115).
- Zhang, J. J., Xiaodong Su, L. Zhang, L. Zheng, X. F. Wang, and Lixing You (Mar. 2013). « Improvement of the superconducting properties of NbN thin film on single-crystal silicon substrate by using a TiN buffer layer ». In: *Superconductor Science and Technology* 26.4. Publisher: IOP Publishing, p. 045010. ISSN: 0953-2048. DOI: [10.1088/0953-2048/26/4/045010](https://doi.org/10.1088/0953-2048/26/4/045010) (cit. on p. 60).
- Zheng, Guoji, Nodar Samkharadze, Marc L. Noordam, Nima Kalhor, Delphine Brousse, Amir Sammak, Giordano Scappucci, and Lieven M. K. Vandersypen (Aug. 2019). « Rapid gate-based spin read-out in silicon using an on-chip resonator ». In: *Nature Nanotechnology* 14.8. Number:

8 Publisher: Nature Publishing Group, pp. 742–746. ISSN: 1748-3395. DOI: [10.1038/s41565-019-0488-9](https://doi.org/10.1038/s41565-019-0488-9) (cit. on pp. 35, 39, 74, 75).

Zwanenburg, Floris A., Cathalijn E. W. M. van Rijmenam, Ying Fang, Charles M. Lieber, and Leo P. Kouwenhoven (Mar. 11, 2009). « Spin States of the First Four Holes in a Silicon Nanowire Quantum Dot ». In: *Nano Letters* 9.3. Publisher: American Chemical Society, pp. 1071–1079. ISSN: 1530-6984. DOI: [10.1021/nl803440s](https://doi.org/10.1021/nl803440s) (cit. on p. 3).